Inheritance of dust from cores to disks

Measurements of dust properties through the infalling envelopes of young protostars

Luca Cacciapuoti

München 2024

Inheritance of dust from cores to disks

Measurements of dust properties through the infalling envelopes of young protostars

Luca Cacciapuoti

Dissertation
der Fakultät für Physik
der Ludwig-Maximilians-Universität
München

vorgelegt von
Luca Cacciapuoti
aus Neapel - Italien

München, den 09 September 2024

Erstgutachter: Prof. Dr. Barbara Ercolano
Zweitgutachter: Prof. Dr. Tilman Birnstiel
Tag der mündlichen Prüfung: October 23rd, 2024

"Dicette 'o pappice vicino 'a noce:
damme 'o tiempo ca te spertose"

Neapolitan saying

Contents

List of Figures

List of Tables

List of Abbreviations

ACA: Atacama Comapct Array
ALMA: Atacama Large Millimeter/submillimeter Array
ATCA: Australia Telescope Compact Array
CALYPSO: Continuum and Lines in Young Protostellar Objects
CARTA: Cube Analysis and Rendering Tool for Astronomy
CASA: Common Astronomical Software Applications
COBE: Cosmic Background Explorer
ESO: European Southern Observatory
FAUST: Fifty AU STudy of the chemistry in the disk/envelope systems of Solar-like protostars
IRAS: InfraRed Astronomical Satellite
ISM: Interstellar Medium
ISO: Infrared Space Observatory
JAO: Joint ALMA Observatory
JCMT: James Clerk Maxwell Telescope
JWST: James Webb Space Telescope
LTE: Local Thermal Equilibrium
MET: Mechanican Torques (theory, ndr.)
MRN: Mathis-Rumpl-Nordsiek (dust model, ndr.)
NAOJ: National Astronomical Observatory of Japan
NOEMA: Northern Extended Millimeter Array (formerly PdBI, ndr.)
NRAO: National Radio Astornomy Observatory
PAH: Policyclic Aromatic Hydrocarbons
PdBI: Plateau de Bure Interferometer
RAT: Radiative Torque Alignment (theory, ndr.)
SED: Spectral Energy Distribution
SMA: Submillimeter Array
SOFIA: Stratospheric Observatory for Infrared Astronomy
TIPSY: Trajectory of Infalling Particles in Streamers around Young stars
VLA: Very Large Array
VLT: Very Large Telescope
YSO: Young Stellar Object

Abstract

It has been long understood that star and planet formation starts from the collapse of dense cores of material embedded in the more diffuse interstellar medium. As these collapse under the force of gravity, their inner densities and their initial rotation increase. This collapse will thus produce a protostar at the centre, a compact object that will keep accreting mass from an infalling envelope and via a flattened disk that forms due to conservation of angular momentum.

While only accounting for 1% of the total infalling material, mostly dominated by molecular gas, dust grains play crucial roles in the evolution of forming systems. Dust grains represent the initial reservoir to form the cores of giant planets and the bulk of terrestrial planets. Dust grains also carry volatiles in the form of icy mantles to the proto-planetary disk, where they will be released and possibly incorporated in the atmospheres of new exoplanets. Even more strinkingly, due to their coupling to magnetic fields, charged dust grains contribute to the transport of angular momentum within the collapsing system. If dust is well coupled, it can remove significant amounts of angular momentum from it and hinder the formation of a rotationally supported circumstellar disk or, more generally, shape its extent. The efficiency of this phenomenon, called magnetic breaking, depends on the properties of dust and in particular on the dust size distribution.

For these reasons, characterizing dust particles in the infalling envelopes of young protostellar systems becomes a critical task. Since envelopes are very dense and collapse from 10,000 au to 100 au circa, radiointerferometry offers our best chance at studying them. Dust at envelope scales thermally emits in the submillimetre regime because of its low temperatures and it is thus detectable in the radio spectral regime. Moreover, the intrinsic multi-scale nature of the problem requires an "adjustable" resolution in order to trace possible evolution of dust properties from the outer to the inner envelope.

In this Thesis work, I thus utilize data from state-of-the-art radiointerferometers to constrain the dust size distribution in the infalling envelopes of young protostars, by measuring the spectral index of their spectral energy distribution. I find that envelopes are characterized by a variety of spectral indices. These can be explained with the presence of sub-micron dust particles much similar to the ones of the interstellar medium in some cases, and by some degree of dust evolution and perhaps optical depth effects in other

instances. I find that a tentative correlation might exist between these spectral indices and the outflows mass loss rates of some systems, suggesting observational evidence for a possible mechanism in which dust grains evolve in protoplanetary disks and are then lifted via outflows to the natal envelope in a recycling pattern. Finally, I present the first constraints of the dust grain size distribution in an infalling "streamer", an asymmetric event of episodic infall much like the many that the community is detecting more and more often, a reminder that star and planet formation is an instrinsically intricate, multi-scale, and multi-stage process.

This Thesis represents an effort to deepen our understanding of dust properties across the infalling envelopes that embed young protoplanetary disks and protostars. It contributes to largely extend the number of objects for which more and stricter constraints are available; it required to develop methodologies that enable a refined analysis of this problem with respect to the past; and it presents original observational evidences for the life cycle of dust around young stellar forming systems.

Zusammenfassung

Es ist seit langem bekannt, dass die Entstehung von Sternen und Planeten mit dem Kollaps dichter Kerne von Material beginnt, die in dem weniger dichten interstellaren Medium eingebettet sind. Während diese unter dem Einfluss der Schwerkraft kollabieren, nehmen ihre inneren Dichten und ihre anfängliche Rotation zu. Dieser Kollaps führt dazu, dass sich im Zentrum ein Protostern bildet, ein kompaktes Objekt, das weiterhin Masse aus einer einfallenden Hülle und über eine abgeflachte Scheibe akkretiert, die sich aufgrund der Erhaltung des Drehimpulses bildet.

Obwohl sie nur etwa 1% des gesamten einfallenden Materials ausmachen, das hauptsächlich aus molekularem Gas besteht, spielen Staubkörner eine entscheidende Rolle in der Entwicklung von entstehenden Systemen. Staubkörner stellen das ursprüngliche Reservoir zur Bildung der Kerne von Gasriesen und den Großteil der terrestrischen Planeten dar. Staubkörner transportieren auch flüchtige Stoffe in Form von eisigen Hüllen in die protoplanetare Scheibe, wo sie freigesetzt und möglicherweise in die Atmosphären neuer Exoplaneten eingebaut werden. Noch bemerkenswerter ist, dass geladene Staubkörner durch ihre Kopplung an Magnetfelder zum Transport von Drehimpuls innerhalb des kollabierenden Systems beitragen. Wenn Staub gut gekoppelt ist, kann er erhebliche Mengen an Drehimpuls aus dem System entfernen und die Bildung einer rotatorisch gestützten zirkumstellaren Scheibe verhindern oder allgemeiner deren Ausdehnung beeinflussen. Die Effizienz dieses Phänomens, das als magnetische Bremsung bezeichnet wird, hängt von den Eigenschaften des Staubs und insbesondere von der Größenverteilung der Staubkörner ab.

Aus diesen Gründen wird die Charakterisierung von Staubpartikeln in den einfallenden Hüllen junger protostellarer Systeme zu einer kritischen Aufgabe. Da die Hüllen sehr dicht sind und von etwa 10.000 AU auf etwa 100 AU kollabieren, bietet die Radiointerferometrie die beste Möglichkeit, sie zu untersuchen. Staub in diesen Hüllen emittiert aufgrund seiner niedrigen Temperaturen thermische Strahlung im Submillimeterbereich und ist daher mit Radiointerferometern nachweisbar. Darüber hinaus erfordert die inhärente Multi-Skalen-Natur des Problems eine “anpassbare” Auflösung, um eine mögliche Evolution der Staubeigenschaften von der äußeren bis zur inneren Hülle zu verfolgen.

In dieser Dissertation nutze ich daher Daten von hochmodernen Radiointerferometern, um die Größenverteilung von Staub in den einfallenden Hüllen junger Proto-

sterne zu bestimmen, indem ich den Spektralindex ihrer Spektralenergiedichte messe. Ich stelle fest, dass die Hüllen durch eine Vielzahl von Spektralindizes gekennzeichnet sind. Diese können in einigen Fällen durch das Vorhandensein von submikronischen Staubpartikeln, die denjenigen im interstellaren Medium sehr ähnlich sind, erklärt werden und in anderen Fällen durch eine gewisse Staubevolution und möglicherweise durch optische Tiefeffekte. Ich finde, dass möglicherweise eine Korrelation zwischen diesen Spektralindizes und den Massenverlusten durch Ausflüsse bei einigen Systemen besteht, was auf Beobachtungsbelege für einen möglichen Mechanismus hindeutet, bei dem Staubkörner in protoplanetaren Scheiben evolvieren und dann über Ausflüsse in die ursprüngliche Hülle zurückgeführt werden, in einem Recyclingmuster. Schließlich präsentiere ich die ersten Einschränkungen der Staubkorn-Größenverteilung in einem einfallenden "Streamer", einem asymmetrischen Ereignis episodischen Einfalls, ähnlich den vielen, die in der Gemeinschaft immer häufiger entdeckt werden – eine Erinnerung daran, dass die Entstehung von Sternen und Planeten ein von Natur aus komplexer, vielschichtiger und mehrstufiger Prozess ist.

Diese Dissertation stellt einen Beitrag zur Vertiefung unseres Verständnisses der Staubeigenschaften in den einfallenden Hüllen dar, die junge protoplanetare Scheiben und Protosterne umgeben. Sie trägt dazu bei, die Anzahl der Objekte, für die genauere und strengere Einschränkungen verfügbar sind, erheblich zu erweitern; sie erforderte die Entwicklung von Methoden, die eine verfeinerte Analyse dieses Problems im Vergleich zur Vergangenheit ermöglichen; und sie präsentiert originale Beobachtungsbelege für den Lebenszyklus von Staub um junge sternenbildende Systeme.

1

Introduction

1.1 A brief journey from ISM to planets

Star formation takes place in dense, sub-parsec-scale cores within parsec-scale clouds of dust and gas. The process of formation starts with gravitational collapse: when the cores mass exceeds a threshold value called Jeans mass (M_J), the material starts converging towards a centre. The threshold is set by the condition that the outwards gas pressure cannot counter balance the central gravitational pull. Requesting this condition for a spherical cloud, one can obtain the Jeans mass formula (Jeans, 1902):

$$M_J = \left(\frac{5kT}{G\mu m_H}\right)^{3/2}\left(\frac{3}{4\pi\rho}\right)^{1/2} \tag{1.1}$$

The equation shows how the critical mass has a super-linear dependence on the temperature T and a radical one on ρ. In a formation event, the collapsing region gets denser and denser as material particles are compressed in smaller and smaller regions. Since the cloud is transparent to radiation, the collapse is nearly isothermal in this first stage. Local increases in density forces the Jeans mass to decrease so that some sectors begin an individual collapse in a hierarchical fragmentation process, which might end up with the formation of multiple stars within the core. Indeed, most systems are observed to be formed in binary or multiple configurations (Offner et al., 2023). The collapse proceeds if no force can counteract gravity. When the inner regions of collapse become dense enough that radiation cannot escape and that temperatures reach 10^2 K, it is the surrounding dust that absorbs light and radiates at longer wavelengths, thus cooling the medium and allowing for further contraction. At even higher temperatures of 10^3 K, the endothermic dissociation of molecular hydrogen converts the energy of collapse, which can proceed even further. Only when the central core reaches final equilibrium between gas pressure and external gravity, the collapse comes to a halt and a "protostar" is said to be formed. Sources at these stages of evolution are referred to as young stellar objects (YSOs). During this stage, accretion of material continues via a protostellar envelope and a circumstellar disk, and leads to the formation of bipolar jets and outflows. Indeed, during collapse of a rotating core, the angular velocity of the material increases as it contracts around the centre of mass, due to conservation of angular momentum. At scales of tens of Astronomical Units (1 au = 1.5 x 10^{11} m), a rotationally supported disk is formed and

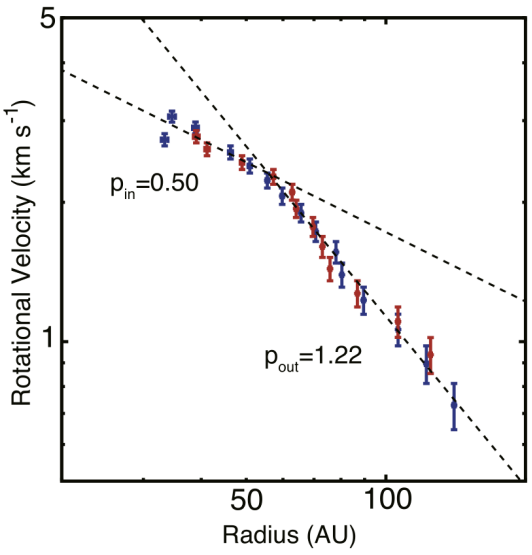

Figure 1.1: Velocity break between the disk and envelope structure of the protostar L1527 IRS (Aso et al., 2017).

fed by the envelope. Both the disk and the envelope transport material onto the central object, dragging the core's magnetic field inwards in a hourglass shape (Maury et al. 2018, Girart et al. 2008). The dragging of magnetic field lines has two main effects. First, the drag slows down the rotation of the collapsing material, a mechanism called "magnetic braking", and can prevent the formation of rotationally supported disks. This magnetic braking "catastrophe" has been attenuated by studies in which the effect of non-ideal magnetohydrodynamics, turbulence and the misalignment between disk and magnetic fields are considered (e.g., Maury et al. 2022, Kuffmeier 2024, and references therein). Indeed, a completely disk-disruptive magnetic braking effect would be in contrast with observations showing many instances of early protoplanetary disks with sizes of about 50 au (e.g., Maury et al. 2019). Second, the pinching of magnetic field lines leads to the ejection of material as the magnetic energy is freed. While the second effect is confirmed by observations, with bipolar outflows and jets commonly detected around young protostars (e.g., Podio et al. 2021).

The circumstellar disk is also referred to as a protoplanetary disk, since we today know that planet formation takes place in this structure. During the early stages of collapse, gas and dust are very well coupled and the disk is very puffed (e.g., Ahmad et al. 2024). However, as time goes by the dust starts to settle towards a midplane, the gas circularizes and its velocity pattern becomes keplerian. The observational distinction between a disk and its embedding envelope becomes clearer by the different velocity profiles of the two (Fig. 1.1, Aso et al. 2017). Since the dusty disk absorbs radiation and emits it at longer wavelengths, protoplanetary disks have been discovered based on the detected infrared excess in near-infrared surveys (e.g., Dunham et al. 2015). Counting disk fractions in stellar clusters of different ages, one can derive the average expected disk lifetime (Ribas et al. 2014; or Fig. 1.2 from Pfalzner et al. 2022), which results in mean disk lifetimes of less than ten million years. It is thus within this period of star formation that we expect disks to form planets. Whether these planets are formed via further gravitational collapse within the disk or via a bottom-up core accretion process is still debated and both could be options depending on the system-specific conditions (Ormel et al. 2017, Drążkowska & Dullemond 2018, Terry et al. 2022, Longarini et al. 2024). It is likely that both processes happen and lead to very different planetary systems. However, in which stage of star formation does planet formation occur it is still a very debated topic and one that is gathering more and more attention in recent years. Since "classes" are used to refer to particular stages of star formation, I will briefly introduce them in the next section.

Finally, it is important in the context of this Thesis work to note that thanks to recent observations, the community has been discovering more and more cases of asymmetric, channel-like infall onto protoplanetary disks (Pineda et al. 2020, Valdivia et al. 2019, Gupta et al. 2023, Bianchi et al. 2023). The discovery of these events is shifting the traditional exemplification of star formation as a process proceeding with the spherical collapse of a cloud in the first few 10^5 yr towards a much more asymmetric and episodic panorama. "Streamers", as these infalling structures have been called, were expected from both sim-

ulations and observations in the early stages of star formation (e.g., Tobin et al. 2010b, Lebreuilly et al. 2020) and are now appearing as clear features that connect protostellar systems with the surrounding enviornment thanks to observations in the submillimetre. However, it is still rather unclear how frequent streamers are and how significant their role is in shaping the history of more evolved protostar/disk systems, i.e. how much mass, angular momentum and fresh chemical material these late-infall events can bring onto evolved planet-forming systems (Winter et al. 2024, Pelkonen et al. 2024).

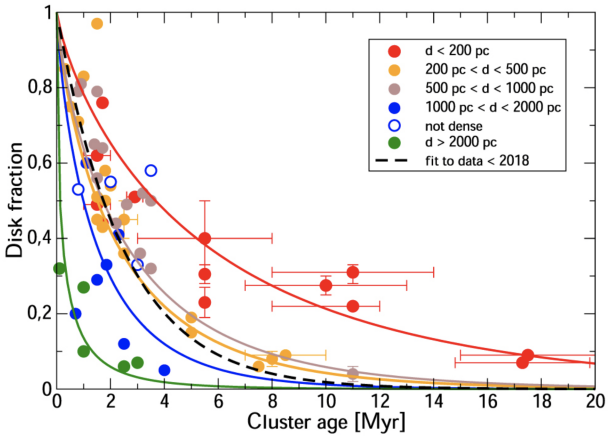

Figure 1.2: The fraction of detected protoplanetary disks in different star-forming regions as function of their age. Image from Pfalzner et al. 2022

1.1.1 The classification of young stellar objects

Traditionally, YSOs have been categorized based on the slope of their near-infrared spectral index $\alpha = d\log(\lambda F_\lambda)/d\log\lambda$. Initially, they were divided into three groups (Lada, 1987): Class I exhibiting a rising near-infrared spectrum ($\alpha > 0$), Class II with a gradual decline (0 $< \alpha <$ -3), and Class III showing a rapid decline ($\alpha <$ -3). This classification was thought to correspond to distinct components: a large dusty envelope around the protostar (Class I), a milder infrared excess from a dusty disk (Class II), and a minimal excess from a very faint debris disk (Class III). Later on, Flat Spectrum sources were added to the framework, with -0.3 $< \alpha <$ 0.3, thought to represent a transitional phase between Class I and Class II.

A significant addition to this system is the inclusion of Class 0 sources (Andre et al., 1993): these are heavily enshrouded protostars, thus challenging to detect in near-infrared observations but highly luminous at (sub-)millimeter wavelengths. The proposed criterion for Class 0 was $L_{submm}/L_{bol} > 0.005$. In this context, the bolometric luminosity (L_{bol}) is empirically measured by integrating the observed Spectral Energy Distribution (SED), without adjustments for obscured optical and UV emissions, as these are expected to be absorbed and re-emitted by the envelope and disk. In practice, L_{bol} is often measured

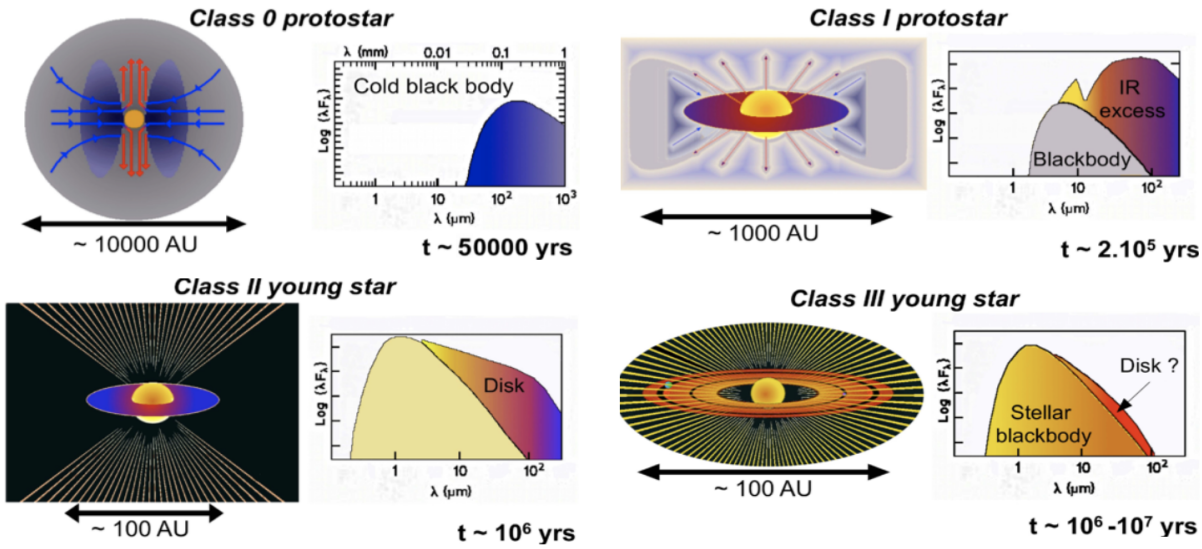

Figure 1.3: Schematics of young stellar object evolution and their division in "classes", from younger to older. Image credits: A. Maury & B. Commerçon.

between ∼1 μm and ∼3 mm wavelengths. For L_{submm}, on the other hand, one typically begins integration at 350 μm. However, it is imperative to keep in mind that the relationship between L_{bol} and total luminosity can be intricate, contingent upon the protostar's inclination and envelope opacity. A complementary classification method is done by bolometric temperature (T_{bol}; Myers & Ladd 1993, Chen et al. 1995), representing the temperature of a blackbody that best reproduces the SED. Chen et al. (1995) delineated the T_{bol}-based classifications as follows:

- Class 0: 70K > T_{bol} > 20K
- Class I: 650K > T_{bol} > 70K
- Class II: 2800K > T_{bol} > 650K
- Class III: T_{bol} > 2800 K

The T_{bol} classification system is not exempt from its own set of caveats. The determination of the boundary for Class 0 in T_{bol} was somewhat arbitrary, as it was chosen based on where the majority of known Class 0s fell according to the L_{submm}/L_{bol} criteria. A comprehensive comparison of T_{bol} and L_{submm}/L_{bol} criteria was presented in (Dunham et al., 2014), indicating a reasonable alignment between the two definitions, although enhancing consistency might be achievable by reducing the upper limit of T_{bol} for Class 0. Additionally, there exists a small yet noteworthy subset of protostars exhibiting L_{submm}/L_{bol} consistent with Class 0, yet T_{bol} consistent with Class I. Furthermore, the accuracy of both criteria depends on the sampling of the Spectral Energy Distribution (SED) across wavelengths, which has

markedly improved over the past two decades but remains a limitation. Nevertheless, the intention behind these criteria was to follow the evolution of sources in time from earlier, more embedded stages in which the protostar is embedded in an infalling envelope to more evolved and cases in which a residual disk (or none) remains (Fig. 1.3). While the introduced systems might not be perfect as described, it is still common practice to classify the sources based on these methods and I will refer to Class 0, I, II in the rest of this Thesis to objects as classified with these schemes. In particular, I will focus on the study of Class 0 and Class I sources.

1.2 Not just a nuisance: cosmic dust

Interstellar dust grains have historically represented a problem for astronomers. Dusty regions absorb or deflect light coming from background objects as seen by the observer and thus either cause dimming of celestial sources or completely hide them at certain wavelengths. However, while this is still a problem to face when e.g., accurate stellar parameters or source number counts are main goals of a certain study, a lot can also be learnt on the properties of dust itself through its interaction with light.

Even though dust grains only amount to about a percent of the total material in the ISM, they play unquestionably important roles in the evolution of star forming regions and entire galaxies. Dust acts as a coolant of the interstellar medium during the collapse that will form new stars, it offers a favorable role for atoms to form molecules that would be otherwise impossible to synthesize in the gas phase (e.g., Ceccarelli et al. 2022), it represents the building block of the cores of planets (e.g., Drążkowska & Dullemond 2018), it couples with magnetic fields to regulate angular momentum transport during cloud collapse and more (e.g., Hennebelle & Ciardi 2009). For these reasons, dust plays a crucial role in the evolution of star-forming regions at all scales, from the diffuse medium down to the scale of planetary cores, and it thus deserve utmost attention.

1.2.1 A brief view on the life cycle of dust

The refractory elements that build up an interstellar dust grain are produced in the interiors of stars during their evolution along the Hertzsprung-Russel diagram. Low-mass stars evolve by means of nuclear fusion in their interiors that start with proton-proton reactions and lead to the formation of helium. When helium accumulates in the nucleus of the star, a burning shell of hydrogen surrounds it, feeds it with even more helium and increases its temperature as a result of the increase in pressure towards the centre. When the centre reaches $\sim 10^8$ K, helium fusion starts to produce carbon and accumulating it in the centre. Until the central temperature is high enough for carbon to fuse, an helium shell around it burns. After the helium shell runs out of fuel, the star derives its energy from the hydrogen shell, which compresses the helium shell. Over periods of tens or hundreds of kilo-years, the helium shell ignites explosively, in what are called helium shell "flashes". During these

episodes, the star suffers from heavy mass loss (10^{-8}-$10^{-5} M_{\odot}$/yr; Fig. 1.4) in which also the refractory materials are expelled, cool off and condense into dust grains. This evolutionary stage of a low-mass star is thought to be one of the most prominent sources of dust production in the Universe. Nuclear fusion proceeds in the giant star element-by-element, producing oxygen (O), neon (N), magnesium (Mg), sulfur (S), silicon (Si), phophorus (P), and finally iron (Fe). Up to this point, the nuclear reactions were exothermic, thus freeing energy with which the star is uphold against gravitational collapse over billions of years. However, the fusion of iron atoms is endothermic, and thus seize that very sustaining energy from the star, which is doomed to collapse. The gravitational collapse might then end in a supernova explosion, the shocks of which will form even heavier elements that will be spread out the surrounding ISM. Recent JWST observations, for example, detected large amounts of dust mass - as high as 5,000 $M_{\oplus}$ - expelled by two supernovae (Shahbandeh et al. 2023). Once dust is injected in the surrounding ISM by AGB stars and supernovae,

Figure 1.4: Expanding shells of an AGB star as imaged by ALMA in CO gas emission (Maercker et al., 2016).

a myriad of processes will govern its evolution in the diffuse medium. Dust grains can interact with radiation, gas and among themselves. When interacting with photons, dust grains can release atoms or molecules off their surfaces, either keeping their physical state ("desorption") or changing from solid to gas phase ("sublimation"). On the other hand, gas-grain collisions can lead to "adsorption", in which gas molecules stick to the grain surface because of electromagnetic forces, and "icing", when a thin layer of condensed gas wraps the grain. However, gas-grain collisions can be disruptive if the exchanged angular momentum is high, and lead to "sputtering", the freeing of gas molecules off the grain surface due to impacts of another molecule. While photon-grain and gas-grain interactions have the potential to free a few molecules off the surface, or build and disrupt thin ice layers, grain-grain collisions are much more efficient when it comes to change the grain

size distribution. Impacts between two grains can in fact lead to growth by "coagulation", in which two grains stick together by means of electromagnetic forces and geometrical porosity; or they can produce a distribution of smaller grains if the energy of the impact is above a certain threshold, "shattering".

Eventually, when collapsing pockets of the diffuse medium start to compress under the effect of gravity towards the central overdensities that will become stars, dust follows the gas in its way to the newly forming object. An observational view of the evolution of dust during collapse is at the centre of this Thesis and thus discussed further in Sections 1.5.1, 1.5.2, and 1.5.3. Generally, however, dust will be entrained by the gas flow in a circumstellar disk that will be partially accreted onto the star and partly dispersed in a few million years. Within the disk, part of the dust will form planets and minor bodies like comets and asteroids, and another fraction will drift towards the star where it will meet a $\sim$1200 K sublimation barrier where the grains will return into their atomic components and they will infall onto the star or be ejected from the system by protostellar jets and outflows and enter again the cycle of the ISM.

1.2.2 Early dust observations and models

In 1785, William Herschel noticed a black patch in the sky while running observations towards the Scorpius constellation. This patch was mistakenly explained as a lack of stars in the specific region (e.g., Clerke, 1903), and only about twenty years later it came to be recognized as the effect of an obscuring material between the observer and the stars by Barnard (1919). In 1874, astronomer Friederich Struve realized that stellar counts in the Galaxy would diminish in density when observing larger and larger volumes, which could be explained by means of a cumulative distribution of an obscurant material along the line of sight. Struve (1847) computed a mean extinction of about 1mag/kpc, within a factor of 2 of today's value. Studies of Russell (1922) and Trumpler (1930) allowed for a conclusive interpretation of extinction as an effect due to dust, since they recognized two more effects: (i) the distribution of stellar colors towards these dark patches appears much redder than the surroundings, and (ii) the derived photometric distances and diameter distances towards a sample of stellar clusters do not match since the photometric distances are biased by the reddening of which above. Thus, within the 1930s the facts were that some dark patches on the sky were present, and that these "markings" would redden background stars. A set of studies then began to characterize extinction at different wavelength ranges, but within the limits imposed by atmospheric transmission. The extinction curves looked mostly similar along many lines of sight with a $1/\lambda$ profile, and were interpreted as the presence of particles that would scatter light efficiently at those wavelengths. Based on optics theory, the particles should have been of the order of 0.03-0.1μm. Only in the 1960s the UV range of the electromagnetic spectrum became available with spaceborn missions and two new facts came along: (i) different lines of sight display different slope of the optical-UV extinction, and (ii) the existence of a bump at 2175Å in the extinction curves was discovered (Fig. 1.5).

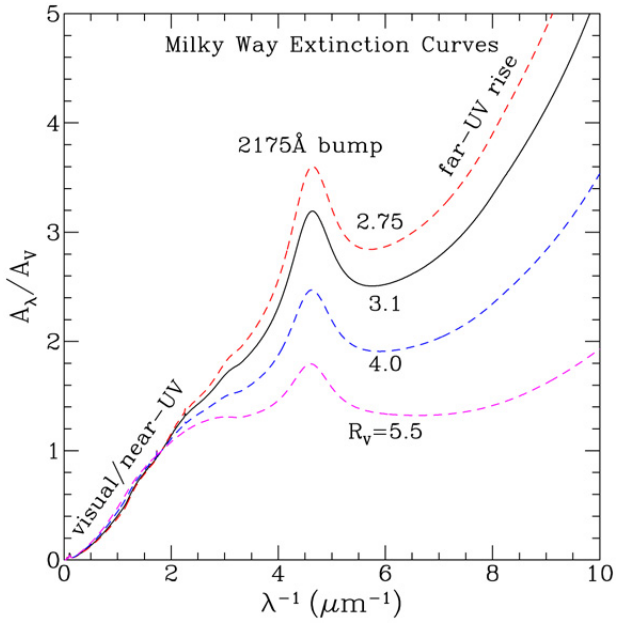

Figure 1.5: Dust extinction curves as a function of wavelength along lines of sight with different densities in the Galaxy. At 2175Å, enhanced extinction is caused by graphite.

The first models of interstellar dust thus had to explain the observed extinction curves and their main features, like the UV rise along some lines of sight and the 2175Å bump. First dust models would thus make assumptions on dust based on the size constraints from the multi-wavelength observations of which above and using meteorites as a guide to what interstellar solid material could be like in terms of composition (e.g., Oort & van de Hulst 1946). Moreover, a strong constraint from the shape of the extincion, the 2175 Å bump suggested grains bulk to be made of policyclic aromatic hydrocarbons (PAHs) and graphite (Donn, 1968). The first model to fit the general shape of the extinction curve of the Milky Way, by assuming a mix of dust grains made of silicates and carbonaceous material (graphite), is the *MRN* model (Mathis et al., 1977), in which the dust size distribution is approximated by a power law of the form $dN/da \propto a^{-3.5}$ for a in the range [0.005,1] μm for graphite grains and [0.025,0.25] μm for the silicate component. Empirically, we today conveniently describe to UV-optical-NIR extinction curve based the work of Cardelli et al. (1989), who provided an empirical fit in different spectral ranges to the observed extinction curve along different lines of sight in the milky way, from more diffuse to denser. The general profile shows that more diffuse environments presents a stronger UV-rise with respect to the denser one. This effect is due to the presence of larger amount of smaller dust grains relative to the larger ones in the diffuse medium (Fig. 1.5).

With the advent of infrared missions that allowed to look at the sky under a different light, other features of dust have been studied thanks to observatories like “The Infrared Astronomical Satellite” (IRAS, launched in 1983), the “Cosmic Background Ex-

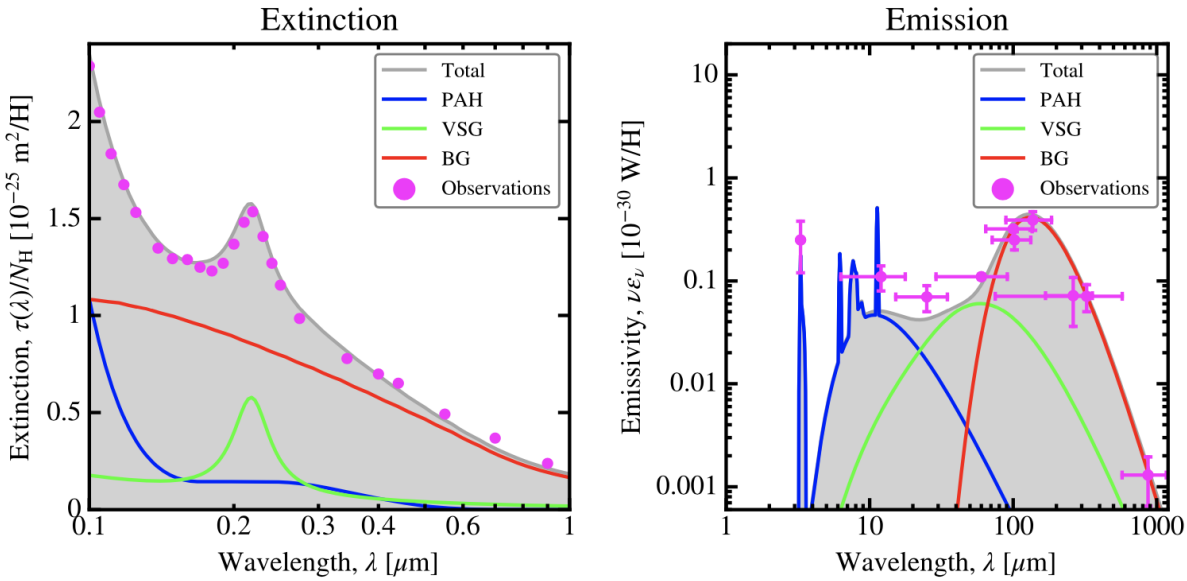

Figure 1.6: The Desert et al. (1990) dust model, the first to fit both dust extinction and emission across wavelenghts by combining the properties of very small grains (VSG), PAHs, and big grains (BG). Image credits: Galliano (2022).

plorer" (COBE, 1989), and the "Infrared Space Observatory" (ISO, 1995). These missions largely contributed to characterize dust with both their spectroscopic capabilities and by adding additional constraints to the coarse SEDs of young stellar objects. For example, absorption bands at 9.7 and 18 μm further constrained the bulk of dust grains as mainly composed of astro-silicates (McCarthy et al. 1980, Demyk et al. 1999); and the water bands at 3 μm, along with the CO and CO_2 bands around 4μm unveiled the compositions of the bulk of the ice mantles (Pontoppidan et al. 2004, Boogert et al. 2015). On the continuum emission side, the wavelengths probed by these observations allowed to observe the dust continuum excess in the far infrared, due to the warm envelopes and disks embedding them (e.g., Lada 1987, Andre et al. 1993). The excess emission at far-infrared, and subsequently observed down to mm/cm wavelengths by modern radiointerferometers down to circumstellar disk scales (e.g., Beckwith & Sargent 1991, Testi et al. 2001), necessarily required larger carbonaceous grains to reproduce the observed SEDs (Fig. 1.6).

Complex models aiming to fit the whole extent of the dust spectrum thus needed to reproduce the UV-NIR-optical extinction curves, the PAH-induced bump, the mid-infrared absorption bands, and the far-infrared emission. Examples of such models were presented by Desert et al. (1990), Ossenkopf (1993), Draine & Li (2007), Köhler et al. (2015), Guillet et al. (2018). An example of comparison between model and observations is given in Fig. 1.6, for the model by Desert et al. (1990). A full discussion on early and more recent dust models is out of the scope of this Thesis, and we refer to Galliano (2022) for an extended recent review. However, it is here important to understand that, in order to go from

assumptions on dust composition, size distribution, and physical parameters to a model that can fit the extinction and emission of dust in interstellar space, radiative transfer has to be computed for the grain distribution. Thus, the next Section is devoted to understand how grains interact with light, and how one can interpret observations in terms of dust properties.

1.3 Dust-light interactions

Observations that allow us to learn about the properties of dust in the interstellar medium are naturally possible because dust grains interact with light in several ways. From this interaction, we can constrain the properties of grains by comparing observations to models that predict the behavior of light when passing through a dusty media. Generally, dust can be absorbed or scattered away from the observer's line of sight, causing extinction; and emit light at wavelengths that are longer than the absorbed ones, in both an unpolarized and polarized fashion.

1.3.1 Grain cross section

A fundamental quantity in the interaction of light and dust, cross-section is a measure of the effective interaction area between the beam of light and the grain. If a plane parallel wave reaches a grain, it will be scattered in several directions. How much of it, depends on the grain scattering cross-section C_{sca}. Moreover, the particle will absorb part of the incident radiation with an absorption cross-section C_{abs}. The total extinction cross section will thus be given by:

$$C_{ext} = C_{sca} + C_{abs} \tag{1.2}$$

In a more explicit form, the scattering cross section is the ratio between the incoming radiation flux (Poynting vector) and the re-radiated power by the particle:

$$C_{sca} = \frac{W_{rad}}{\vec{P}} = \frac{\omega^4 e^2 x_0^2}{12\pi\epsilon_0 c^3} \times \frac{2E_0^2}{\epsilon_0 c}, \tag{1.3}$$

where ϵ_0 is the dielectric constant in vacuum, c is the speed of light and E_0 the modulus of the electric field of the electromagnetic wave. Here, W_{rad} is the power radiated by a classic harmonic oscillating dipole, with $x_0 = \frac{eE_0}{m_e\sqrt{\omega_0^2-\omega^2+\gamma^2\omega^2}}$ its amplitude and ω its frequency. In turn, $\omega_0 = k_e/m_e$ is the natural frequency, ratio of the "elastic" constant and electron mass; and $\gamma = b/m_e$ is the damping constant, the ratio between a dissipation constant and the electron mass which appears in the dissipation force $\vec{F} = -m_e\gamma\dot{\vec{x}}$ of a damped oscillator.

The absorption cross-section is instead the ratio between the dissipated energy in

the grain over the same Poynting vector:

$$C_{abs} = \frac{W_{dis}}{\vec{P}} = \frac{m_e \gamma \omega^2 x_0^2}{2} \times \frac{2E_0^2}{\epsilon_0 c}. \tag{1.4}$$

One can then explicit the terms in the equations above to obtain:

$$C_{sca} = \frac{C_1 \omega^3}{(\omega^2 - \omega_0^2)^2 + \gamma^2 \omega^2} \tag{1.5}$$

for the scattering cross-section, where the constant $C_1 = 8\pi/3 \times (\frac{e^2}{4\pi\epsilon_0 m_e c^2})^2$. And:

$$C_{abs} = \frac{\gamma \omega^2}{(\omega^2 + \omega_0^2)^2 + \gamma^2 \omega^2} \tag{1.6}$$

for the absorption cross-section, with the constant $C_2 = \frac{e^2}{m_e \epsilon_0 c}$. By considering the limit cases when $\omega \ll \omega_0$, $\omega \gg \omega_0$, $\omega \sim \omega_0$, one can derive simplified forms for the cross-sections (see, e.g., Galliano 2022 for the explicit forms).

The cross sections can also be expressed, conveniently, per unit area (cm^{-2}), mass (g^{-1}) or volume (cm^{-3}) of dust. In particular, the so called "extinction efficiency" is defined as the ratio of the cross section C_{ext} to the geometrical cross section of a grain, which is πa^2 for spherical particles, $Q_{ext} = C_{ext}/\pi a^2$. The (e.g., absorption) cross-section per unit mass, κ_{abs}, can be defined as:

$$\kappa_{abs} = \frac{C_{abs}(a, \lambda)}{4/3\pi a^3 \rho} \tag{1.7}$$

where ρ is the dust grain density. This quantity is often referred to as "dust absorption opacity", and its scattering counterpart is defined similarly.

1.3.2 Scattering and absorption

Scattering and absorption contribute to remove photons from a beam of light incident onto a dusty media. Their combined effect is thus the extinction of light. Such extinction can be written as:

$$dI/I = -n_d C_{ext} dL, \tag{1.8}$$

where dI/I is the fractional variation of the light beam along its path, n_d is the number density of scattering/absorbing particles, C_{ext} is the grain cross section and dL the unit length of material through which light passes. Integrating Eq. 1.8, one obtains the specific intensity of the light beam after passage through the material:

$$I = I_0 e^{-\tau}, \tag{1.9}$$

where I_0 is the intensity before interaction and the optical depth:

$$\tau = \int n_d C_{ext} dL \tag{1.10}$$

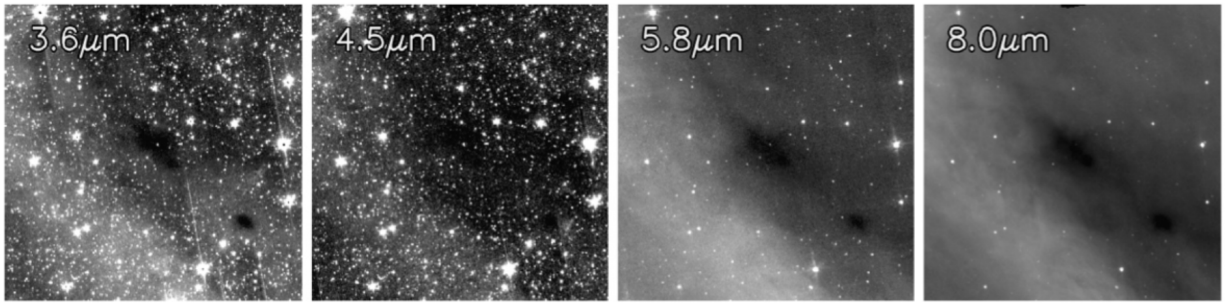

Figure 1.7: Spitzer Space Telescope observations of dust scattering from a dense core. As the wavelength increases, so does the efficiency of grains at scattering light, suggesting the presence of micron-sized grains in the medium. Image from Pagani et al. (2010).

is the optical depth of the medium. Expressing the variation of brightness in magnitudes, one finds that the extinction is proportional to the optical depth as $A_\lambda = 1.086\tau$. If instead of a fixed grain size, the extinction is caused by a dust distribution:

$$A_\lambda = \pi L \int a^2 Q_{ext}(a) n(a) da, \tag{1.11}$$

where n(a) is the dust size distribution, usually assumed to be a power law.

The problem of describing the extinction law as a function of wavelength thus become a problem of determining the efficiencies Q_{sca} and Q_{abs} as a function of wavelength. These in turn depend on the size of dust relative to the incoming radiation, and on its composition. This is because absorption and scattering are microscopically dependent on the type of material that makes up the grain, and thus on its specific dielectric and magnetic permittivities. One of the most widely used theories that describes the scattering of light by dust particles is the "Mie Theory" (Mie, 1908), in which a dust grain is assumed spherical and homogeneous. Depending on the relative size of the spherical grains with respect to the incident wavelength, three regimes can be defined: the geometrical, the Mie and the Rayleigh regimes. When particles are much larger than the observing wavelength ($x >> 1$), Mie theory predicts $Q_{sca} = Q_{abs} = 1$. In this regime, the grains are efficient forward scatterers. When instead the particle size is comparable to the incoming wavelength ($x \sim 1$), the efficiencies can have complex shapes depending on their composition. An example is the presence of peaks in the efficiencies due to the microscopic-level interactions between light and the structure of matter, which cause the absorption bands we discussed previously, such as the one of graphite at 2175 Å. Moreover, while forward scattering is still preferred, its angle can largely vary across the full solid angle. Finally, when the particles are much smaller than the incoming radiation's wavelength ($x << 1$), the efficiencies can be expressed as power laws of the wavelength. In particular, it can be proven that $Q_{abs} \propto \lambda^{-1}$ and $Q_{sca} \propto \lambda^{-4}$.

Dust extinction observations have been historically employed to retrieve the properties of dust in the diffuse ISM, where background stars are more easily detected, as

described in Section 1.2.2. Moreover, scattering observations have largely been employed to constrain the geometry of protoplanetary disks as well the presence of substructure in their dust surface brightness as traced by small and porous grains (e.g., Krist et al. 2000, Mouillet et al. 2001, Takami et al. 2013), and the environment in which they are embedded which has revealed a variety of spirals and streamers (e.g., Ginski et al. 2021, Ginski et al. 2022, Garufi et al. 2024). Finally, the properties of the dust grains that cause the scattering in these observations are encoded in both the intensity and the fraction of polarization of the reflected light, as well as in their wavelength dependence, e.g., Fig. 1.7.

1.3.3 Thermal emission

When dust is hit by radiation, it heats up. The absorbed energy needs to be re-radiated to achieve thermal balance, and the grain acquires an equilibrium temperature T_d. In local thermodynamical equilibrium (LTE), the ratio between the emissivity ϵ_ν and absorption opacity κ_ν of a body is a function of the frequency and temperature only, i.e. the Planck function. While a grain in the interstellar medium is not in LTE conditions, it possess many possible energy levels because of its complexity and thus, when a photon impinges onto it, a wide distribution of energy states is populated according to the Boltzmann function. For this reason, the emission of a dust grain can also be expressed as $\epsilon_\nu = \kappa_\nu \times \mathrm{B}_\nu(\mathrm{T}_d)$. Consider a spherical grain of radius a located at a certain distance from a light source of specific intensity $I(\nu)$. The absorbed and emitted energy must then be equal:

$$\pi a^2 \int\int I_\nu Q_{abs}(a,\nu) d\nu d\Omega = 4\pi a^2 \int\int Q_{em}(a,\nu) \pi B_\nu(T_d) d\nu d\Omega, \tag{1.12}$$

where the absorbed and emitted radiation is modulated by the absorption and emission efficiencies Q_{abs} and Q_{em} and the area over which light is absorbed/emitted, proportional to the grain size a^2. $\mathrm{B}(\mathrm{T}_d)$ is the Planck function. To a first order approximation, the equation above becomes:

$$\frac{L}{4\pi d^2} < Q_{abs} >= 4 < Q_{em} > \sigma T_d^4, \tag{1.13}$$

which leads to a simple expression for the equilibrium temperature of a dust grain:

$$T_d = \left(\frac{< Q_{abs} >}{< Q_{em} >}\right)^{0.25} \left(\frac{L}{16\pi\sigma d^2}\right)^{0.25}. \tag{1.14}$$

Typical temperatures for dust grains of 0.1μm are of the order of 20 K, which means that their emission dominates the mid- and far-infrared spectrum. If any other radiation source is present, like an external radiation field, the equations above should be modified to account for it.

Real dust grains emit as modified black bodies since they do not absorb perfectly at all wavelengths, and their temperature, along with size, composition and porosity, drive the way they emit light. The emission of a dusty medium is thus linked to the fundamental

properties of dust. At sub-millimeter wavelengths, the emission of the dust is regulated by the dust opacity κ_ν:

$$\kappa = \frac{\int_{a_{min}}^{a_{max}} da(dn/da)C_{abs}(a,\nu)}{\int_{a_{min}}^{a_{max}} da(dn/da)4/3\pi\rho a^3} \tag{1.15}$$

which is thus defined as the mass-averaged absorption cross section of a dust grains population defined by a certain range of sizes [a_{min},a_{max}] distributed as a power law $n(a) \propto a^{-p}$. Indeed, the intensity emitted by the dust grain distribution is:

$$I_\nu = B_\nu\left(1-\exp\left(-\tau_\nu\right)\right) = B_\nu \times \begin{cases} 1 & \text{for } \tau_\nu \gg 1 \\ \tau_\nu & \text{for } \tau_\nu \ll 1, \end{cases} \tag{1.16}$$

where B_ν is the Planck function and τ_ν is the optical depth along the line of sight. The optical depth depends on the absorption cross-section per gram of dust - i.e., its absorption opacity, as $\tau_\nu \propto \Sigma_d\kappa$, with Σ_d the dust surface density. In the submillimeter regime, the flux decreases as a power law $F_\nu \propto \nu^\alpha$ and the dust opacity can approximated by a power law $\kappa_\nu \propto \nu^\beta$. Thus, Eq. 1.16 leads to the fact that the flux scales as $F_\nu \propto \nu^{\beta+2}$, if the emission is optically thin and if the Rayleigh-Jeans approximation holds ($h\nu/k_BT << 1$). It thus results clear how measuring the spectral index α of the submillimeter emission of a source can yield a constraint on β, the exponent of the dust absorption opacity. In turn, β carries information on the characteristics of the dust grains, such as porosity, composition and, particularly, size (Fig. 1.8). In particular, it can be shown that the exponent of the dust opacity, β, strongly depends on the particle size with $\beta \sim 1.6$ for very small grains ($a_{max} < 10$ μm) and $\beta < 1$ for much larger grains ($a_{max} > 1mm$) - e.g., Natta et al. (2007), Testi et al. (2014), Ysard et al. (2019). Observations have confirmed such predictions both in the ISM, where diffuse dust is expected to be small (Schwartz 1982, Weingartner & Draine 2001, Li & Draine 2001), and in disks where higher densities and longer timescales promotes dust growth into larger pebbles (e.g., Ricci et al. 2010, Tazzari et al. 2021).

On the other hand, the spectral index cannot always be used in such a simple way to derive β. First, when the emission is (even partially) optically thick, $\alpha \sim 2$ and the dependence on β is hidden (e.g. Ricci et al. 2012, Delussu et al. 2024). In this case, it becomes impossible to constrain dust properties based merely on α and τ, while T and β have to be determined self-consistently (e.g., Sierra & Lizano 2020). Moreover, if the Rayleigh-Jeans approximation does not hold, which could be the case in cold media at relatively high frequencies, the non-approximated form for the dust opacity spectral index is:

$$\beta = \frac{d\log\tau}{d\log\nu} = \alpha - \frac{d\log B_\nu(T)}{d\log\nu}, \tag{1.17}$$

instead of the simple $\beta = \alpha - 2$. Besides, if scattering is important for a given source, it will increase the intensity in the optically thin spectral regime (long wavelengths) and reduce the intensity of the optically thick regime (short wavelengths). This will naturally decrease the spectral slope, and even yield $\alpha < 2$ in some cases (Liu, 2019). Finally, if one measures spectral indices using millimeter-to-radio data, great care should be taken in considering the

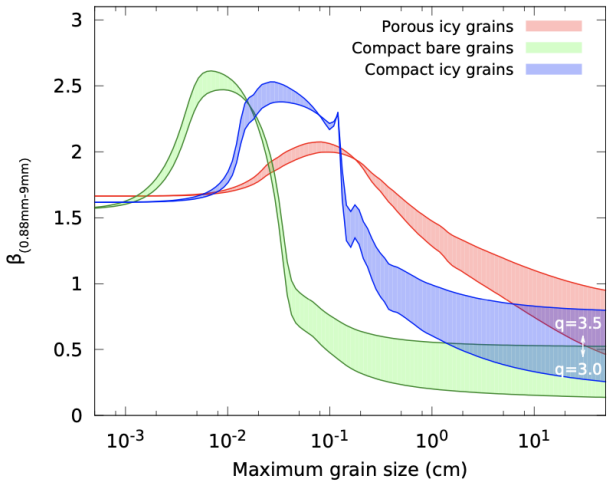

Figure 1.8: The dependence of the dust opacity spectral index β on composition, porosity and the grain size distribution parameters (a_{max}, q) for three different models (Testi et al., 2014).

effects of free-free, synchrotron and anoumalous microwave emission. These contributions are important at cm wavelengths, but can significantly contribute to the mm-wavelength observations contaminating the dust thermal emission contribution and thus have to be disentangled and characterized on their own (e.g., Curone et al. 2023, Rota et al. 2024). In general, multi-wavelength observations can be used in order to provide enough degrees of freedom in the problem of deriving physical properties and dust characteristics from a spectrum. For example, using the spectral range covered by ALMA and VLA detectors, several authors have fitted the spectrum of protoplanetary disks to obtain their Σ_d, τ_d, β simultaneously (e.g., Isella et al. 2009, Tazzari et al. 2016, Macías et al. 2021, Guidi et al. 2022). It is noteworthy in this context that all multi-wavelength studies have been carried out for protoplanetary disks, when the signal-to-noise ratio is high at all wavelengths. Dust thermal emission is in fact much weaker further away from the protostar as it gets colder, and thus studies of dust continuum emission protostellar envelopes are rare and somewhat limited in sensitivity, resolution and spectral range as performed on data taken with few-antenna interferometers as SMA, ATCA, PdBI (Miotello et al. 2014, Galametz et al. 2019, Agurto-Gangas et al. 2019a). Today, the much greater sensitivity, resolution and spectral coverage of ALMA allows for studies such as the ones presented in Chapters 3 and 5.

1.3.4 Polarization

Light is an electromagnetic wave that has both an electric and a magnetic field component. When the electric and magnetic fields oscillate in numerous planes, the light is said to be unpolarized. However, if light propagates on a preferential plane, it is said to be polarized. Microscopically, the difference is due to the oscillations of the charges that produce the

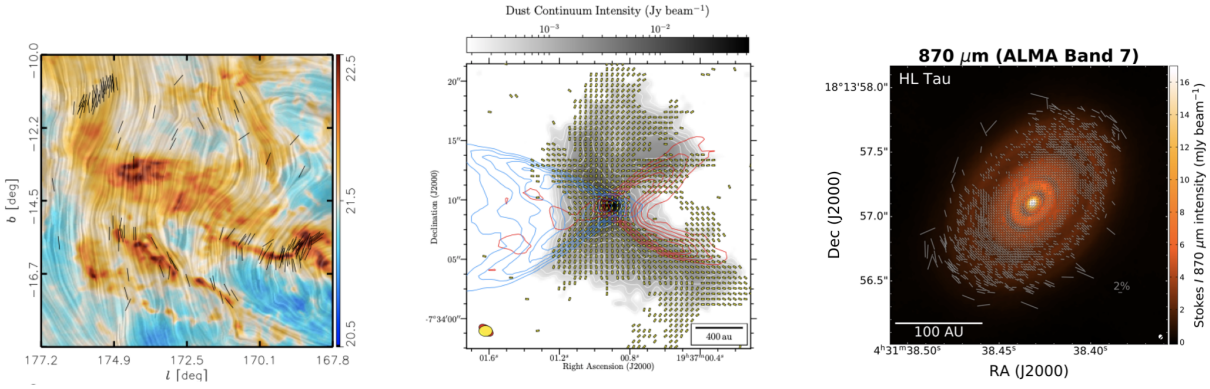

Figure 1.9: Examples of polarization observations. Planck observations of the magnetic field orientation (drapey pattern) of the Taurus star-forming region (left, Soler et al. 2016) overplotted on the gas column density (color scale). ALMA view of the magnetic field vectors overplotted on the dust continuum (gray) and outflow emission (colored) for the isolated protostar B335 (centre, Le Gouellec et al. 2020). A very high resolution polarization observation of the HL Tau disk with ALMA at 0.88mm (right, Stephens et al. 2023).

wave. If these vibrate over a preferential plane, so will the light they emit. Polarized light can thus be observed to be emitted, transmitted or scattered by grains that preferentially align along a given direction. Polarization in transmission is essentially caused by the already mentioned extinction, but with different extinctions efficiencies when one considers the directions parallel ($Q_{\parallel}$) and perpendicular ($Q_{\perp}$) to the grain alignment axis. In one direction, indeed, light will encounter a larger fraction of the grain than in the other, thus resulting in light being more efficiently scattered or absorbed, i.e. $Q_{\parallel} > Q_{\perp}$. In the Milky Way, this effect is observed towards stars that are in the background with respect to certain regions of the ISM. The alignment of dust grains that is necessary to polarize light is thought to be arranged by galactic magnetic fields. Polarized light can also be observed in emission when the emitting dust grains are aligned. The principle behind the emission process are the same as described in the previous section, while the polarization of light is once again granted by the preferential direction of the grains in space. While light polarization itself is well understood and perfectly described by the formalism of the Maxwell's equations, it is not yet clear what is the mechanism for grain alignment itself in the interstellar medium. A widely accepted theory that describes how grains align is the Radiative Alignment Torques one (RATs, Dolginov & Mitrofanov 1976). In this scenario, non-spherical and irregular grains have different cross-sections for clockwise and counterclockwise circularly polarized light. Thus, scattering on the grains inputs a net torque that spins the grain. Then, if these grains have paramagnetic inclusions, their rotation will precess and the grain align with the magnetic field. Other theories describe alternative scenarios, such as the so-called mechanical torques (or METs, Lazarian & Hoang 2007). Instead of the effect of photons, as in the RAT paradigm, METs arises from the scattering of gas atoms by the grain surface that drifts through the ambient gas and it is

thought to be especially important in denser environments like protostellar envelopes due to its need for a relatively dense gas flow (Hoang et al., 2022).

The observation of polarized light across scales in the ISM has historically been challenging due to the low levels of polarization fractions and thus the need to accurately calibrate instruments and get precise measurements. However, thanks to advancements in both space missions at high frequencies and ground-based interferometry at lower ones, the sky has now been largely mapped at several scales in polarization (Fig. 1.9). Through polarization of light at 100-350 GHz, due to dust-light interactions, the plane-of-the-sky galactic magnetic field has been reconstructed (Planck Collaboration et al., 2016), and traced down to star-forming region scales (Soler et al., 2016). At even smaller scales, the 2D orientation of magnetic fields have been reconstructed for denser cores (Li et al. 2022, Lin et al. 2024a) with JCMT, SOFIA observations; and even protostellar envelopes (Girart et al. 2008, Galametz et al. 2018) and outflows (Maury et al. 2018, Le Gouellec et al. 2019a) with submillimeter interferometry. Finally, thanks to the advent of ALMA, polarization has been mapped in a resolved fashion in protoplanetary disks, yielding strong constraints on both magnetic fields morphology and dust grain size (Kataoka et al. 2016, Lin et al. 2024b, Lin et al. 2024c, Stephens et al. 2023).

1.4 Dust in star and planet formation

However scarce, the presence of dust in the interstellar medium plays crucial roles in the evolution of a system. First, dust grains are responsible for the cooling of a collapsing dense core. When a core exceeds the critical mass for gravitational collapse, it contracts under its own gravity. The cloud, however, will only keep collapsing as long as it can release the energy built up by the compression, which is mainly lost through radiation. Eventually, when the cloud becomes opaque to its own radiation, it necessitates an alternative method of energy dissipation. Dust particles within the cloud heat up to temperatures between 20–100 K, radiating energy at far-infrared wavelengths where the cloud remains transparent. This allows the dust to facilitate the ongoing collapse of the cloud and thus a denser core to be formed.

Second, dust provides a site for the formation of molecules that would otherwise by hindered in space. The most abundant molecule in space, H_2, is indeed thought to be formed on icy interstellar grains, as its abundance could not be explained by simple gas-phase reactions and given the relative ease to which molecular hydrogen is photodissociated by UV radiation (e.g., van de Hulst 1946, Wakelam et al. 2017). Not only the simplest, but also much more complex molecules find their best forming conditions on the surfaces of dust grains. In fact, the same UV radiation that could easily photodissociate gas-phase molecules, can help the formation of complex ones (molecules with six or more atoms, and at least one carbon) in the ices that wrap dust grains (Schutte et al., 1992). Even pre-biotic molecules such as amino acids and nucleobases are today thought to possibly formed in similar pathways that necessitate grain surfaces (e.g., Oba et al. 2019).

For a full review on the importance on dust grains in astrochemistry, see Ceccarelli et al. (2022).

Third, dust grains play a driving role when it comes to the very formation of rotationally supported circumstellar disks. A protoplanetary disk is the direct consequence of the conservation of angular momentum for infalling and rotating particles. A collection of dust grains and gas molecules which is undergoing collapse, and that had a non-zero initial angular velocity, will contract and its angular velocity increase. The balance between the gravitational pull and the centrifugal force in the particle reference frame will keep it in orbit around a central protostar, forming a keplerian disk (e.g., Hennebelle et al. 2004, Commerçon et al. 2008). However, the collapsing medium does not behave as a collection of particles, as its magnetic fields are coupled to charged material (ions and dust grains). Magnetic fields can transport angular momentum outwards in the system, thus causing particles to not have enough energy to stay in orbit and hinder the formation of a rotationally supported disk or truncate it to smaller radii (e.g., Basu & Mouschovias 1995, Galli et al. 2006, Hennebelle & Ciardi 2009). Observations seem to support such a scenario, since disks around young Class 0 sources have been constrained to be smaller than ∼50 au (see Maury et al. 2022 for a review). Since the strength of the magnetic field does

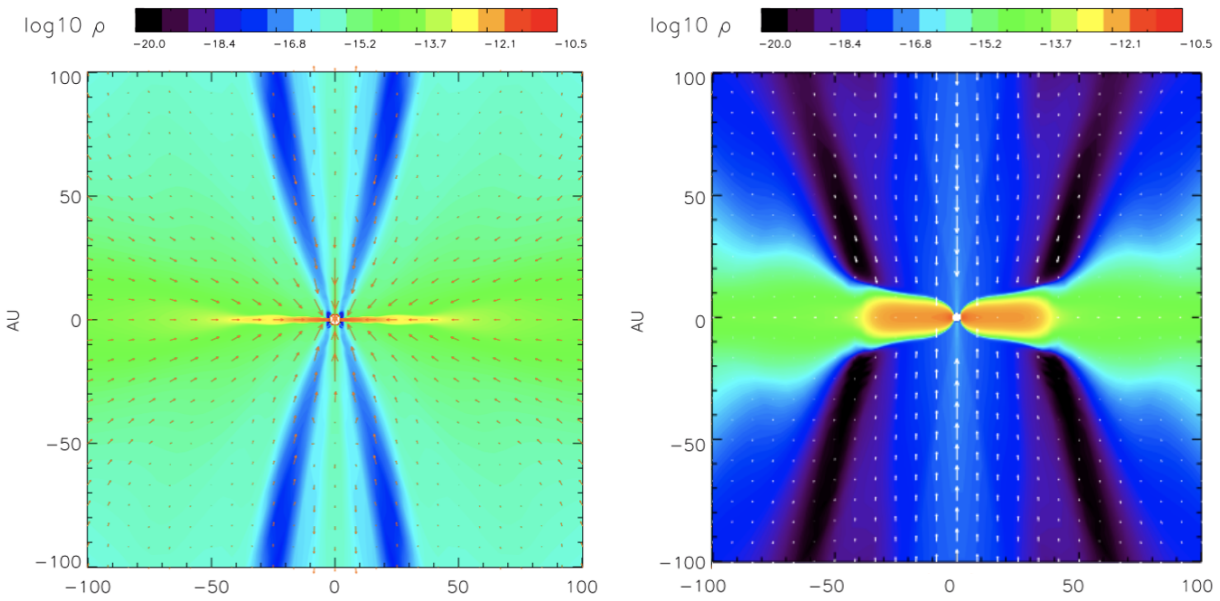

Figure 1.10: The density ρ of the inner envelope/disk system resulting from the 2D magnetohydrodyanmical simulations of Zhao et al. (2016). Both simulations started with a ionization rate of $10^{-17}s^{-1}$ but differ in their dust size distribution. On the left, an MNR distribution with $a_{min} = 0.005\mu$m is considered. On the right, a truncated MRN distribution is characterized by $a_{min} = 0.1\mu$m. The case where the very small grains are removed forms a larger disk due to lowered efficiency of the magnetic braking (see also Section 1.4.3).

not need to be large, this discovery came to be known as "magnetic braking catastrophe", as disk formation chances seemed to drastically thin. Because the transport of angular momentum depends on the efficiency of the coupling between the magnetic fields and the dragged material, the presence and characteristics of ionised gas and charged grains play a central role in this matter. In particular, it has been shown that small dust grains (10-100 Å) are responsible for efficient coupling, being the most charged ones, and thus that their removal from the collapsing envelopes is key to decrease the efficiency of magnetic braking and allow the formation of disks of tens of astronomical units (Fig. 1.10, and e.g., Zhao et al. 2016, Marchand et al. 2020). Finally, if planets are to be formed starting by

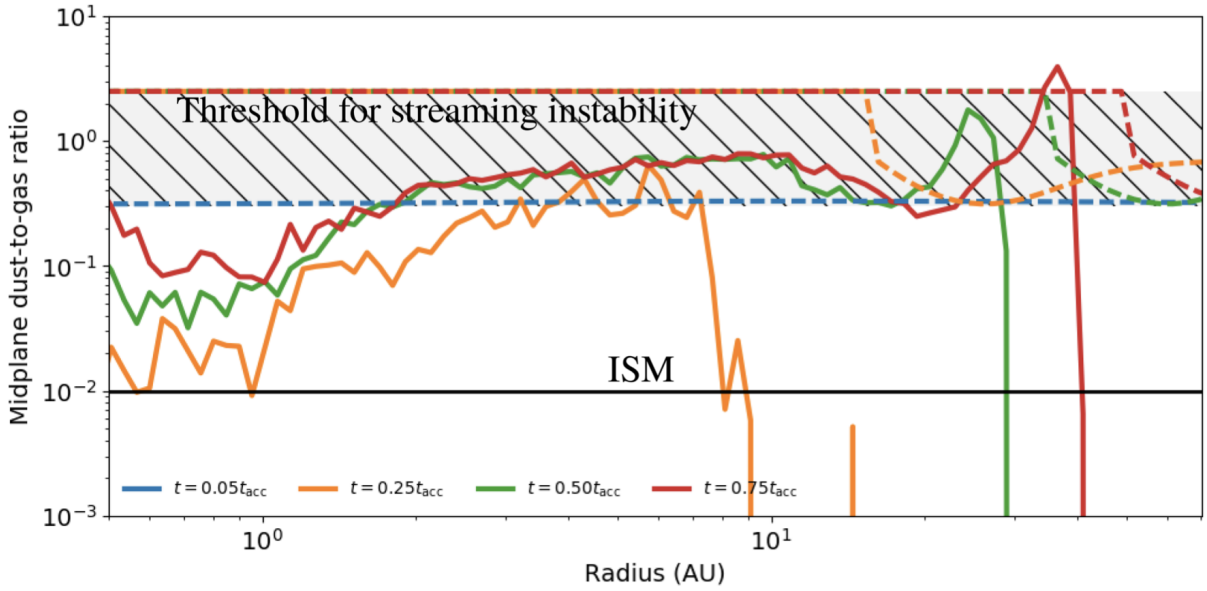

Figure 1.11: Midplane dust-to-gas ratio of the model of envelope collapse onto a young disk performed in Cridland et al. (2022). One can appreciate how the midplane d/g rises above unity at about 40au in the disk due to differential replenishment of dust and gas from the envelope, ultimately caused by the decoupling of the large ($\sim 30\mu$m) grains from the gas in the envelope.

the sub-micron particles observed in the ISM, it is clear that a process of dust growth across roughly sixteen orders of magnitudes must be followed from the collapse of dense cores, throughout the disk phase, and until protoplanetary disk dispersal. Importantly in this context, Cridland et al. (2022) found that differential gas and dust replenishment of a protoplanetary disk from its surrounding envelope sets favorable conditions for planetesimal formation. In fact, if dust grains from the envelope fall faster that the gas, an enhanced dust-to-gas ratio will build up in the young disk. Such an increase is a favorable condition for one of the mechanisms today thought to rapidly form planetesimals, i.e. streaming instability (Youdin & Goodman, 2005). Dust grains that are moderately coupled to the gas (>30 μm) are required to meet the streaming instability conditions that lead to the

birth of these planetary embryos (Fig. 1.11). However, it remains today unclear to what extent and in which conditions dust grows in different media in its path to the formation sites of planets, and in particular in protostellar envelopes, a problem at the centre of this Thesis work.

1.4.1 Evolution of dust during core collapse

All of the reasons just described make of dust grains a central component of the ISM, dense cores, protostellar envelopes, protoplanetary disks and finally exoplanets. And all of the above mentioned roles of dust during star and planet formation depend on the characteristics of individual grains and on the overall size distribution of dust. For this reason, constraining the properties and the evolution of dust in its trail from the diffuse interstellar medium to dense disks is of uttermost importance to understand how the collapse of clouds proceeds to produce the birth places of planets, and planets themselves. In order to understand how dust evolves during star and planet formation, we first need to understand how dust dynamics work as it describes the relative velocities among grains which drive the outcomes of their collisions. Dust dynamics is regulated by the interaction of grains with gas, magnetic fields, radiation pressure, and others. Which one among these interactions mediates the main force acting upon dust, depends on the environment conditions in which the interaction happens.

1.4.2 Dust-gas dynamics

When it comes to dust-gas interaction, if the mean free-path for grain-grain collision is much longer than the gas-grain ones, the dynamics of dust is largely controlled by the interaction between dust grains and gas molecules, and thus by the drag force between the two:

$$\overrightarrow{F}_{drag} = -m_g \frac{\Delta \overrightarrow{v}}{t_s} \tag{1.18}$$

where m_g is the grain mass, Δv the differential grain-gas velocity and t_s the stopping time, i.e. the time for a grain to adjust to velocity changes in the gas. The mathematical form of this force, in turn, depends on whether the Epstein or Stokes regime are valid. The first is valid when the grain size is small compared to the gas mean free-path ($a_g < 4/9\lambda_g$), while the second is relevant in the opposite case. Thus, the Epstein regime holds in the ISM, where the relevant stopping time is given by:

$$t_s = \frac{\rho_g a_g}{\rho_{gas} w_{th}}, \tag{1.19}$$

where ρ_g is the grain density, ρ_{gas} the gas one, a_g the grain size, and w_{th} the gas thermal speed. Thus the force in the Epstein regime is:

$$\overrightarrow{F}_{drag} = \frac{4}{3}\pi a^2 \rho_{gas} < v_{gas} > \Delta v, \tag{1.20}$$

where the 4/3 term comes from integration of velocities over many directions. The Epstein regime is equivalent to interpret the interaction as a discrete bombardment of dust particles by the gas ones. On the other hand, the Stokes regime becomes important in denser media, where the particles are not much smaller than the mean free-path of gas molecules and the experienced drag force becomes:

$$\overrightarrow{F}_{drag} = \frac{-1}{2} C_{drag} \rho_g \pi a_g^2 \Delta \overrightarrow{v} \tag{1.21}$$

where C_{drag} depends on the Reynolds number, Re = 2 a_g Δv / ν, with ν the kinematic viscosity of the medium. In the Stokes regime, the particle is seen as embedded in a continuous fluid. Conveniently, a parameter known as Stokes number can be defined which is independent on the details of grain porosity and composition, and indicates how well coupled a dust grain is to a gas distribution:

$$St = \frac{t_s}{t_{dyn}} \tag{1.22}$$

the ratio between the stopping time and a dynamical timescale, thus indicating strong coupling if St << 1 and no coupling if St >> 1. For example, in the case of a protoplanetary disk in which the dynamical timescale is given by the period of a keplerian orbit:

$$St = \sqrt{\frac{\pi\gamma}{8}} \frac{\rho_g a_g}{\rho_{gas} c_s} \Omega_K. \tag{1.23}$$

Defining a typical power-law density profile for the disk ($\rho_{gas} \propto R^{-2}$), and $c_s = H\Omega_K$, where H is the disk aspect ratio, then one can show that:

$$St = 2 \times 10^{-2} \Big(\frac{\rho_g}{2gcm^{-3}}\Big)\Big(\frac{a_g}{1cm}\Big)\Big(\frac{R}{1au}\Big), \tag{1.24}$$

assuming H$\sim$0.05. Thus, centimeter particles in disks are relatively well coupled. In the case of collapsing cores, the dynamical timescale can be considered to be the free-fall timescale, which yields:

$$St = \sqrt{\frac{32G\gamma}{8}} \frac{\rho_g a_g}{\sqrt{\mu_g m_H} c_s} \frac{1}{\sqrt{n_g}} \tag{1.25}$$

which in typical conditions yield:

$$St = 1 \times 10^{-2} \Big(\frac{\rho_g}{2gcm^{-3}}\Big)\Big(\frac{a_g}{1\mu m}\Big)\Big(\frac{n_g}{10^5 cm^{-3}}\Big) \tag{1.26}$$

meaning that smaller grains are well coupled to the much more diffuse medium.

Whether grains are well coupled to the medium in which they are embedded or not has in turn important consequences, and it is thus a fundamental concept in star and planet formation. For example, grains that are coupled to the gas in protoplanetary disks

(the largest grains) feel a strong headwind which causes a loss of angular momentum of the solid particle which drift inwards. This "radial drift" is of fundamental importance as - together with gas pressure gradients - plays a role in trapping dust in ring-like structures in which enhancements of dust-to-gas ratio could lead to planetesimals formation (e.g., Jiang & Ormel 2023, Lau et al. 2024). Similarly, in a collapsing envelope, if grains are large enough to decouple from the infalling gas, they will collapse faster, thus enriching the protoplanetary disk with dust and gas differentially in time. This will lead to an enhanced dust-to-gas ratio which can have the effect of onsetting the very early formation of planetary cores via streaming instabilities (Cridland et al., 2022).

Not only is gas inducing such systematic drifts in the dust population, but its turbulent and Brownian motions induce diffusion of the grains.

The former describes the relative velocities of particles trapped in eddies and, depending on the grains stopping time, the interaction between turbulence and grains is described by three types of vortices (known as class I, II or III vortices), leading to different relative velocities (Ormel & Cuzzi, 2007):

$$\Delta v_{turb,i,j} = \begin{cases} V_g^2 \frac{St_i - St_j}{St_i + St_j} \left(\frac{St_i^2}{St_i + 1/\sqrt{(Re)}} + \frac{St_j^2}{St_j + 1/\sqrt{(Re)}} \right), & \text{for } t_{s,i} < t_n \\ V_g^2 \beta_{i,j} St_i, & \text{for } t_\eta \leq t_{s,i} < t_{ff} \\ V_g^2 \left(\frac{1}{St_i + 1} + \frac{1}{St_j + 1} \right), & \text{otherwise} \end{cases} \tag{1.27}$$

where $V_g = \sqrt{(3/2)} c_s$ and $\beta_{i,j} = 3.2 - (1 + x_{i,j}) + \frac{2}{1+x_{i,j}}(1/2.6 + \frac{x^3}{1.6+x_{i,j}})$, with $x_{i,j} = St_i/St_j$ (Guillet et al., 2020). On the other hand, Brownian motions can be parametrized as:

$$\Delta v_{brownian,i,j} = \sqrt{\frac{8 k_B T}{m} \frac{m_i + m_j}{m_i m_j}}, \tag{1.28}$$

where k_B is the Boltzmann constant, m_i is the particles mass (Ormel & Cuzzi, 2007).

Finally, in order to fully describe the evolution of a dusty medium in the most general cases, one can use Euler equations for a system in which dust and gas co-exist and are treated as a fluid. This approximation is valid if the grain-grain collisions mean free-paths are long enough when compared to the gas-grain ones. The equations include mass conservation for both gas and dust, momentum conservation for both and energy conservation for the gas (since the dust is pressureless):

$$
\begin{aligned}
&\frac{\partial \rho_{\mathrm{g}}}{\partial t} + \nabla \cdot \rho_{\mathrm{g}} \vec{v}_{\mathrm{g}} = 0 \\
&\frac{\partial \rho_{\mathrm{d}}}{\partial t} + \nabla \cdot \rho_{\mathrm{d}} \vec{v}_{\mathrm{d}} = 0 \\
&\frac{\partial \rho_{\mathrm{g}} \vec{v}_{\mathrm{g}}}{\partial t} + \nabla \left(\rho_{\mathrm{g}} \vec{v}_{\mathrm{g}} \otimes \vec{v}_{\mathrm{g}} + P_{\mathrm{g}} \partial \right) = \rho_{\mathrm{g}} \vec{f} + \frac{\rho_d}{t_s} \overrightarrow{\Delta v} \\
&\frac{\partial \rho_{\mathrm{d}} \vec{v}_{\mathrm{d}}}{\partial t} + \nabla \rho_{\mathrm{d}} \vec{v}_{\mathrm{d}} \otimes \vec{v}_{\mathrm{d}} = \rho_{\mathrm{d}} \vec{f} - \frac{\rho_d}{t_s} \overrightarrow{\Delta v} \\
&\frac{\partial E_{\mathrm{g}}}{\partial t} + \nabla \cdot \left(E_{\mathrm{g}} + P_{\mathrm{g}} \right) \vec{v}_{\mathrm{g}} = \frac{\rho_d}{t_{\mathrm{c}}} \overrightarrow{\Delta v} \cdot \overrightarrow{\Delta v}
\end{aligned}
\tag{1.29}
$$

1.4.3 Dust dynamics in the presence of a $\overrightarrow{B}$ field

Since dust grains are generally charged in the interstellar medium - because of collisions with ions, electrons and cosmic rays (e.g., Guillet et al. 2007) - they will interact with magnetic fields. One can thus generalize the hydrodynamic equations of motion by adding a Lorentz force. By including the additional term to the fourth Equation of 1.29, one can prove (Kunz & Mouschovias, 2009) that - in the approximation that grains are very small and thus do not have inertia - the following equation holds:

$$
c\vec{E}_b = \eta_o \nabla \times \vec{B} - \frac{\eta_A}{|\vec{B}|^2}((\nabla \times \vec{B}) \times \vec{B}) \times \vec{B} + \frac{\eta_H}{|\vec{B}|^2}(\nabla \times \vec{B}) \times \vec{B}, \tag{1.30}
$$

where $\vec{E}_b = \vec{v}/c \times \vec{B}$. This is Ohm's law, where each term is the product of a resistivity η_i with a current term, and the sum of which yields the electric field value at a given location. The resistivities involed are respectively called "ohmic", "ambipolar" and "Hall" resistivity. The first is due to collisions between electrons and neutral particles, the second is due to collisions between ions and neutral particles, and the third is given by a drift between negatively and positively charged particles due to opposite coupling to $\vec{B}$. Using Maxwell's third equation ($c\nabla \times E = \frac{\partial \vec{B}}{\partial t}$), and expressing one can get to:

$$
\frac{\partial \vec{B}}{\partial t} + \nabla \times (\vec{v} \times \vec{B}) = \nabla \times \left[\eta_o \nabla \times \vec{B}\right] - \nabla \times \left[\frac{\eta_A}{|\vec{B}|^2}((\nabla \times \vec{B}) \times \vec{B}) \times \vec{B}\right] + \nabla \times \left[\frac{\eta_H}{|\vec{B}|^2}(\nabla \times \vec{B}) \times \vec{B}\right] \tag{1.31}
$$

which is known as an induction equation, and relates the magnetic field and velocity of the conductive fluid. Each of its terms partly describes the dynamic of charged dust particles in a magnetized medium. The first right-hand term is the "advection", which describes the bulk motion of dust grains as a fluid. The second right-hand term is the "ohmic dissipation", which describes the effect of electron adsorption on dust grains and thus the removal of charged particles from the gas distribution, lowering its coupling to the magnetic field. The second term is known as "ambipolar diffusion", which describes the differential diffusion of neutral particles with respect to the charged ions due to different coupling to the magnetic field. Interestingly, different charge usually means different grain sizes (as grain charging depends on cross sections) and thus ambipolar diffusion can be a way to cluster grains

of different sizes in a traffic jam which might aid grain growth in magnetized media. The last term is the "Hall effect", and describes the differential drift of differently charged particles due to their different coupling to the magnetic field. These resistivities are important because they can lower the efficiency of magnetic fields to transport angular momentum out of the system and thus they prevent or hinder the magnetic braking catastrophe (Lebreuilly et al. 2023, Vallucci-Goy et al. 2024) allowing for the formation of the observed rotationally supported protoplanetary disks (Maury et al., 2019). It is important to note that it is thus the value of the resistivities to drive whether magnetic braking will be efficient or not. Since the resistivities also depend on the grain size distribution, several works have explored the effect of grain growth and fragmentation on their values as a function of core, envelope and disk physical parameters (Fig. 1.12 and e.g., Zhao et al. 2016, Marchand et al. 2020, Tsukamoto et al. 2023).

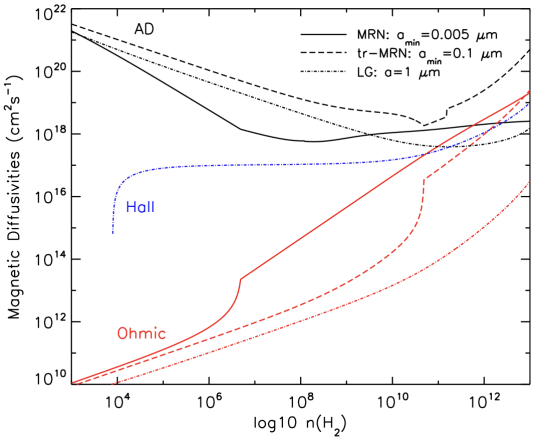

Figure 1.12: Dependence of the dust magnetic resistivities on the grain size distribution. The removal of very small grains ($a_{min} = 0.1\mu$m) from the medium changes the values of the resistivities at play, and enhances ambipolar diffusion (AD). This, in turn, lowers the efficiency of magnetic braking. Figure from Zhao et al. (2016).

1.4.4 Grain growth and fragmentation

The dynamics we described above are responsible for dust grains acceleration and deceleration, and thus govern their relative speed. The relative speed among dust grains, along with their physical properties, is what in turn drives the possible outcomes of grain-grain collisions and thus whether dust grains tend to grow or fragment in a dust distribution. The size of dust grains will thus evolve based on the involved exchange of kinetic energy and on its frequency, which is in turn dependent on the grain cross-sections. Moreover, this evolution process involves a distribution of different dust grains. Thus, the equation describing such evolution will contain derivatives in time and integrals over the distribution of mass:

$$\frac{\partial n(m)}{\partial t} = \int\int K(m, m_1, m_2) R(m_1, m_2) n(m_1) n(m_2) dm_1 dm_2 - n(m) \int R(m, m_1) n(m_1) dm_1 \quad (1.32)$$

which describes the variation of grains in a mass bin in time (left term) when the grains collide with a certain rate $R(m_1,m_2)n(m_1)n(m_2)$ and for collisions with outcomes described by $K(m,m_1,m_2)$. Equation 1.32 is known as Smoluchowski equation (Smoluchowski, 1916) and has been here written in the form presented in Stammler & Birnstiel (2022). The major complications of this equation resides in modeling the possible outcomes of the collisions

and the fact that they are velocity dependent. A summary of possible outcomes for bare silicates grain-grain collisions as a function of grain size and relative velocity is presented in Fig.1.13, and based on laboratory experiments.

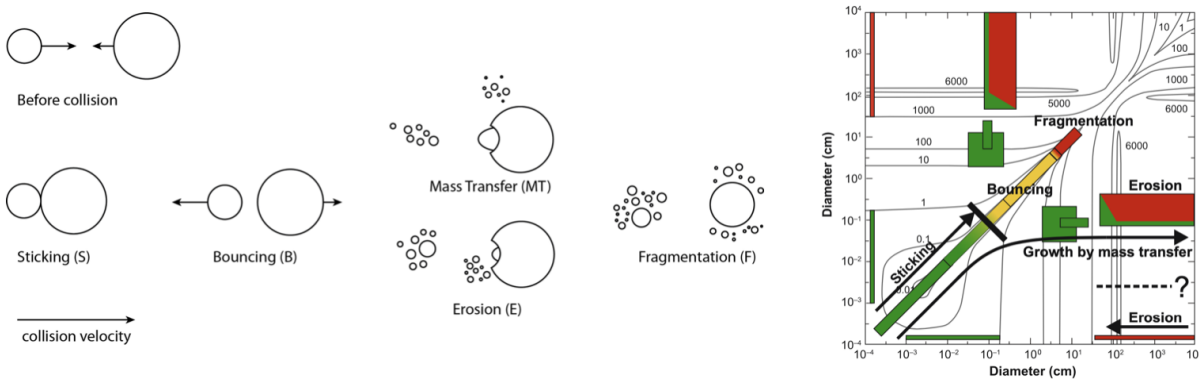

Figure 1.13: Schematic representation of the outcomes of dust collisions in protoplanetary disks (left, credits: Windmark, F.). Quantitative overview of the outcomes for grains of different sizes (right, Testi et al. 2014). The black contours are relative velocities in cm/s, colors represent thresholds for grain sticking (green), bouncing (yellow) and fragmentation (red).

1.5 The role of this Thesis

The main aim of this Thesis is to understand the properties of interstellar dust grains and their evolution during the collapse of cores via envelopes onto protoplanetary disks. As I introduced in the previous sections, the study of dust properties in the ISM has seen a tremendous evolution from the 1700s until today's most recent models. However, many questions remain open in the denser regions of collapse, where only modern radio-interferometers can shed light on dust evolution. More stringent constraint than the ones available today about dust properties during collapse can be obtained analysing more and diverse young sources, by means of refined analyses techniques, and thanks to higher data quality.

1.5.1 State-of-the-art simulations of dusty collapse

In order to understand whether dust evolves during the collapse of dense cores into protostars, the simulation approach is a critical milestone to be pursued as it needs to be compared to observations to look for tensions and/or agreements, and thus adjust our understanding of the problem as a whole. Simulations of collapse of gas and dust can be purely hydrodynamical, or account for magnetic fields and their coupling to charged particles; they can include dust grains as fixed ensembles of grains of different sizes, or even

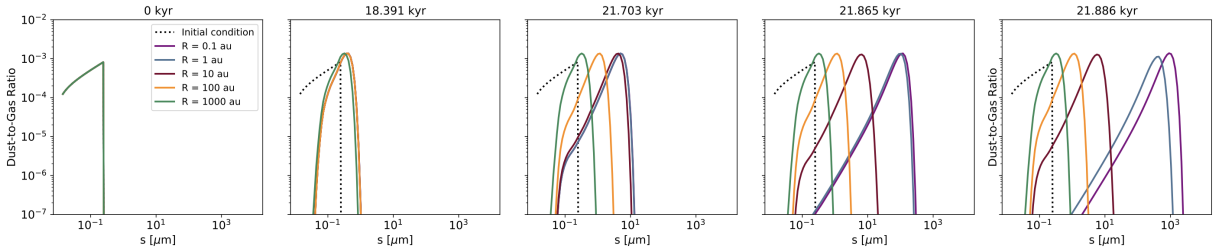

Figure 1.14: From Lebreuilly et al. (2023), the time evolution of the dust-to-gas mass ratio (y-axis) and maximum grain size of the distribution (x-axis) for a model of collapse. The initial conditions are displayed as a dotted line, and the evolution of the quantities at different scales are shown with colored lines.

follow the full evolution of dust by solving the Smoluchowski equation (Eq. 1.32). For example, the numerical simulations of Ormel et al. (2009) consisted of a two step model in which a part would simulate the collision between two grains and one would describe coagulation of the dust size distribution with time. In that study, dust evolution would take place in a static cloud of fixed temperature and the model run for about 10^7 yr. Ormel et al. (2009) found that if dust evolution happens on free-fall timescales, coagulation is only minor and the peak of the size distribution does not shift much with respect to the MRN one. However, if the cloud is somehow supported against collapse, and if grains are wrapped by ices which enhance the fragmentation thresholds dust aggregates of $\sim 100\mu$m can be formed. This only happens on timescales of 10^7 yr, which is longer even than disk timescales, let alone of protostellar envelopes or cores. In another attempt, Bate (2022) performed 3D hydrodynamical calculations of the collapse of cloud cores with a treatment of dust grain growth but not fragmentation. They start from a typical MRN distribution and evolve collapsing and rotating core models in an smoothed particle hydrodynamics (SPH) framework. They found that the peak distribution of the dust grains remains at the initial value of $\sim 0.25\mu$m at envelope scales (hundreds of au) and grains of 10-100 μm are only formed in the very inner core/disk (< 10au) due to higher densities which promote grain collisions and sticking. Moreover, Lebreuilly et al. (2023) solved the gas-dust hydrodynamics of collapse in spherical geometry and followed both the coagulation and fragmentation of dust grains via the Smoluchowski equation at each step. They included models which start from a typical MRN distribution, as for Bate (2022), but also one in which dust grains are "pre-grown" up to a micron in size, with the aim of exploring whether ISM dust pre-evolution could contribute to the overall dust distribution after first collapse (see Fig. 1.14), however finding similar results of largest grains up to $\sim 2\mu$m. Finally, Silsbee et al. (2022) proposed a simpler, analytical model to place strict upper bounds on the maximum grain size that can be reached in extended protostellar envelopes. They considered a coagulation model for the growth of spherical, yet fractal grains whose relative motions are driven by turbulence and the fragmentation of which happens for velocities above a quite generous threshold of $v_{rel} = 10$ m/s. Considering that the optical properties of dust grains depended on the product of their radius (a) with a filling factor (or porosity)

ϕ, they find that it is not possible to grow grains with an optical radius $a_{opt} = a\phi$ of 1 millimeter, in typical protostellar envelope conditions. They find that, in the 10^5 yr lifetime of a typical class 0 source whose volume density is approximately 10^7 cm^{-3}, grains grow up to only about 2 μm.

While different in the details, the simulations and analytical prescriptions described above have all shown that it is very unlikely that solid dust grains could grow larger than about 1 μm at the typical densities and free-fall timescales of cores, and for a usually assumed dust-to-gas ratio of 1%. While these theoretical works disfavor the in situ growth of (sub)millimeter dust grains in the envelopes of young objects, it is important to keep in mind that they all make use of the original coagulation/fragmentation scheme of Ormel & Cuzzi (2007), Ormel et al. (2009) and thus the fact that they reach similar conclusions comes perhaps with no big surprise. However, usually disregarded effects might be important to change the fate of these simulations, i.e. the importance of local clumping of dust across cores or envelopes, and grain charges which couple the particles to magnetic fields causing more sources of relative velocity between small and large particles, thus increasing their relative sticking - an effect of ambipolar diffusion. The exploration of some of these effects have recently started to grasp the attention of new research and are being included in new simulations which find possible pathways to form tens or hundreds μm grains given peculiar conditions of dust-to-gas ratio and magnetic coupling (Hennebelle & Lebreuilly 2023b, Vallucci-Goy et al. 2024).

1.5.2 After the collapse: dust lofting in outflows

When dust collapses onto young disks, it might not settle in it indefinitely. Or, at least, not at first. The collapse of gas and dust from envelopes on a central core requires ways for young protostellar systems to get rid of angular momentum excess. Not all of it, in fact, will support the protoplanetary disk and newly born exoplanetary systems. An efficient way in which large amounts of angular momentum are transported out of the system is via outflows and jets, bipolar ejections that carry material away from the disk at velocities of 10-100 km/s (Bally, 2016). Observationally, jets and outflows are differentiated based on their opening angles, the first being much more collimated than the latter; and by their velocities which, in the case of jets, are so high that trigger shocks in the surrounding ISM that are mostly unseen along slower outflows. Most of the ejected material is gas which can be observed in the submillimetre, especially with CO observations in the 0.8, 1 and 3 mm atmospheric windows (e.g. Podio et al. 2021, Hsieh et al. 2023); or in the visual and near-infrared, where the outflows are traced by H_2 emission lines and forbidden transitions of ionized atomic species like oxygen [OI], [OII], [OIII] (e.g. Le Gouellec et al. 2024). However, as dust grains can be coupled to the gas, it is expected that they will be entrained by these "winds". The extent up to which dust grains are lifted from bipolar prostellar winds has been studied with both analytical and numerical ways. Analytical studies were originally presented in Shu et al. (1996) and Shu et al. (2001), who suggested the possibility of dust lifting through winds to explain the mixing of thermal processed and pristine materials in

the outer Solar System, where no crystalline material would be expected otherwise. More recently, Wong et al. (2016) and Giacalone et al. (2019), with the aim of finding simple prescriptions that would provide the maximum size of lifted grains. The main forces at play in their formulations were the gravity of the central star, that tends to keep the grains on the plane of the disk, and the drag force exerted by the outflowing gas on the dust particles (see also Chapter 4). At typical Class 0 conditions (stellar mass, mass loss rates, gas temperatures), both studies find that relatively large dust grains ($\sim 100\mu$m) can be lifted by winds. Similar conclusions were reached by numerical computations as the ones presented in Lebreuilly et al. (2020) and Tsukamoto et al. (2021), where magneto-hydrodynamical simulations would follow the evolution of dust during collapse in the very early stages of star formation (the first few tens of kyr), with dust coagulation/fragmentation (the former) and just by including several bin in sizes (the latter). They both found that grains of a fraction of a millimeter could be lifted by outflows and jets away from the inner disk. In a more recent work, Bhandare et al. (2024) performed 2D radiation hydrodynamic simulations of core collapse and included dust to follow its path during the event (fixed grains of 1, 10, 100 μm). They found that 100 μm grains are efficiently lifted since well coupled with the gas in these stages of collapse and that, at the last snapshot of their simulation, had reach heights of several tens of au ($\sim$ 60au) above the disk.

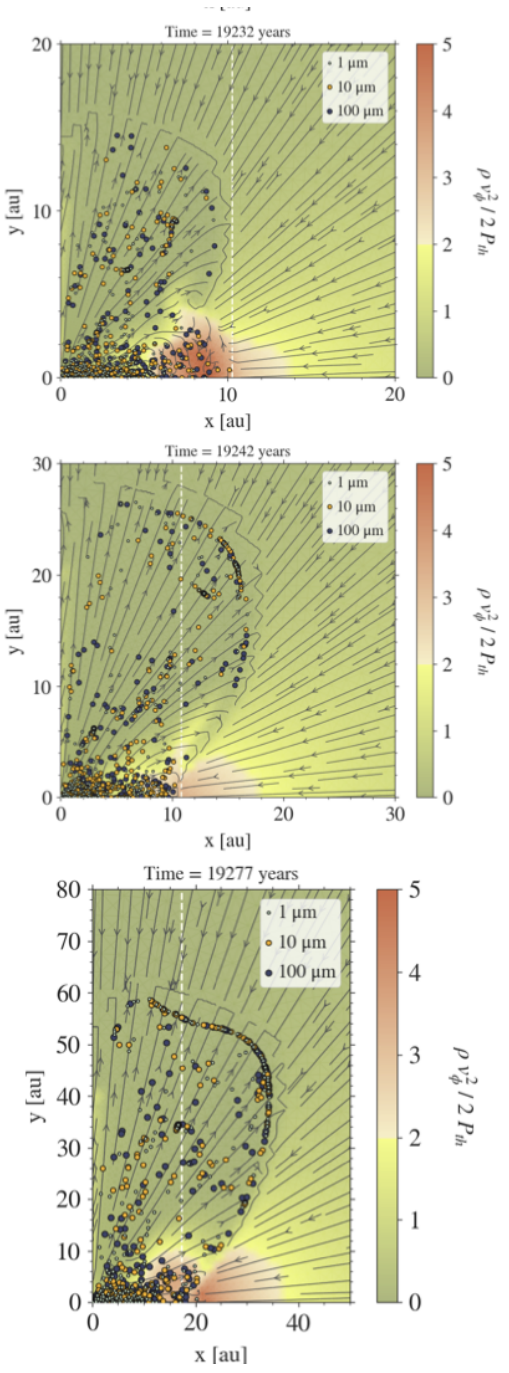

Figure 1.15: Core collapse simulations of Bhandare et al. (2024). After the onset of an outflow, dust grains of 1, 10, 100 μm are lifted from the disk towards the envelope.

However, the simulation lasted 55 yr after outflow launching because of computational time constraints being the simulation at very high angular resolution (10^{-4} au), and thus it remains unclear whether higher altitudes could be reached in time. Moreover the effect of a sublimation barrier, which

might destroy some of the "lifted" grains in the first place, was neglected at this stage. While the transport of dust grains has been considered and explored in the simulations of which above, no observational study has directly focused on the possibility of seeking connections between the evolution of infalling envelopes dust and these bipolar ejections. A tentative attempt at doing this has been carried out in this Thesis work and presented in Chapter 4. It is worth to note that, since that work, tentative observations have presented evidence for the presence of dust along the cavity walls of outflows in young stellar objects (Duchene et al. 2023, Sabatini et al. 2024, and Chapter 5), however their interpretation remains vague as it is not clear whether the observed emission comes from infalling envelope dust that is compressed because of the outflow and thus brighter, or whether the observations are tracing transport of dust from disks upwards. Future works will have to constrain the dust properties along the observed cavity walls either by careful modeling of the emission taking into account the 3D temperature structure of the cavity walls or by seeking to discern disk from envelope dust in terms of composition.

1.5.3 State-of-the-art observations of dusty collapse

Observationally, the properties of dust from the ISM to protoplanetary disks have been explored across a wide range of wavelengths, in order to trace extinction, scattering and emission depending on the density of the environment. Based on extinction observations at UV, optical and infrared wavelengths, a dust size distribution for the diffuse interstellar medium has been measured and is today usually described as a MRN law (Mathis et al., 1977), a power law in which the number of particles in size bins is described as $n(a)da \propto a^{-3.5}$ with minimum and maximum sizes of 5 and 250 nm (see also Section 1.2.2). In this kind of distribution, it can be shown, most of the mass is in the large grains (50% is in grains larger than 80 nm), while most grains in number are on the small-end (80% are smaller than 9.5 nm). However, already when transitioning from the diffuse ISM ($\sim 10^{21}$ cm^{-2}) to the denser regions of molecular clouds filaments (5-50 $\sim 10^{21}$ cm^{-2}), observations suggest that dust grains evolve. Roy et al. (2013), for example, studied the Orion molecular cloud A, and found that when going from regions with typical visual extinctions $A_V \sim 1$ to denser regions where $A_V \gtrsim 3$, the dust opacity at 1200 GHz (as observed with Herschel and 2MASS data) changes significantly. The observed increase in opacity indicates a change in the cross section of dust with respect to its interaction with light, possibly due to growth. Moreover, Pagani et al. (2010), Steinacker et al. (2010, 2015) studied even denser cores in the near- and mid-infrared, where they observed the so-called "coreshine" effect (Fig. 1.7), i.e., an enhancement of scattering from the dusty cores at the longer wavelengths they probed ($\sim 8 - 10\mu$m). As dust efficiently scatters light when its size is a fraction of the incident wavelengths, these studies seem to indicate the presence of 1-2 μm grains at 0.1 pc scales. Similar effects have been reported by Kandori et al. (2003) when studying the selective extinction (the ratio of V-I to B-V colors) in the dense core L1251, which presents a selective extinction $R_V = 3.1$ in the diffuse part of the cloud and $R_V = 6.5$ in the densest regions.Finally, recent works have been observing indications of the presence of micrometer size grains at cloude scales by means of JWST spectra. Dartois et al. (2024)

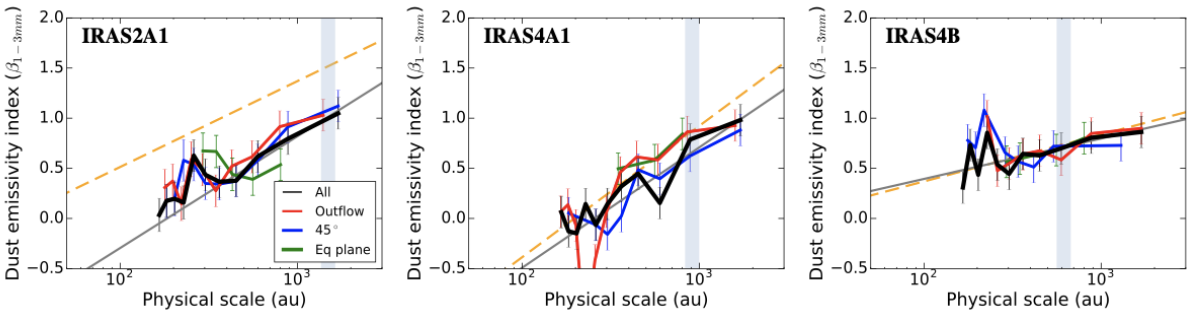

Figure 1.16: Examples of the dust opacity spectral index as measured by Galametz et al. (2019) in some sources of the PdBI CALYPSO sample. Each plot reports the azimuthally averaged measurement of β as a function of uv distance for each source (black line), along different angle ranges in the sky (RGB-colored), and after subtraction of a central optically thick component (orange dashed line).

modelled the shape of the $\sim 4.27\mu$m CO absorption band towards a couple of stellar sources in the background of the Chamaeleon cloud and found that grains of $\sim 1\mu$m are needed to explain a characteristic bump right before the line.

Unfortunately, while near- and mid-infrared can be used to probe dense cores, the very inner regions of the core, where protostars are forming via the collapse of even denser envelopes, are too extinguished to be observed in absorption. However, the presence of a central warm core heats up the surrounding dust, which will then emit at longer wavelenghts. It is for this reason that studying dust in collapsing envelopes requires radiointerferometers: these instruments can achieve the high resolutions needed to trace 100-10,000 au structures and at the same time recover its emission in the submillimetre. Dust thermal emission at these wavelengths can thus be used to measure the dust opacity spectral index (Eq. 3.7) as was done in, e.g. Kwon et al. (2009), Miotello et al. (2014), Agurto-Gangas et al. (2019a), Galametz et al. (2019). These works used observations at 1 and 3 mm of young protostars from interferometers like Australia Telescope Compact Array (ATCA), the Sub-Millimeter Array (SMA), the Plateau de Bure Interferometer (PdBI) in order to measure dust emission spectral indices. The results of these work are varied. Hints of potential grain growth were presented in Miotello et al. (2014), albeit with large uncertainties ($\beta = 0.8 \pm 0.7$ and $\beta = 0.6 \pm 0.3$ for two Class I YSOs). No grain growth signature was observed in Per-emb-50 by Agurto-Gangas et al. (2019a), who reported $\beta = 2.0 \pm 0.7$. Finally, the ten sources sample of Galametz et al. (2019) display β in a range from 0.4 to 1.5.

However pioneering, these works were conducted merging data from different observatories, each with their own calibration specifics; they were performed using two wavelengths; the interferometers at play were always made of 6-8 antennas, thereby jeopardizing the sensitivity of the observations; and finally the physical scales recovered by the observa-

tions were somewhat limited to within a few hundreds au and only down to about 200 au or worse in resolution. For these reason, each and every one of these studies recommended follow up observations and analysis of protostellar envelopes using higher sensitivity, better resolution data, and perhaps multi-wavelength analyses. Finally, it is worth mentioning that polarized observations of dust thermal emission are attracting more and more the attention of the community as they can provide independent constraints on the dust size distribution throughout planet formation environments, like envelopes and disks, with the advantage of not being necessarily limited by high optical depths, as is the case for unpolarized emission. In fact, the polarization fraction in envelopes - caused by alignments of dust grains with magnetic fields along a preferential axis - has been demonstrated to be correlated with the sizes of dust grains that populate the environment (Valdivia et al. 2019, Le Gouellec et al. 2020). Secondly, even in conditions of high optical depth, like for dense disks where polarized light is mainly caused by self scattering (dust grains that scatter thermal emission of other grains), multi-band polarized studies can constrain grain sizes in the range of a few tens to hundreds of μm (e.g. Kataoka et al. 2016). Naturally, as polarized emission is of the order of a few percent of the total emission, the main drawback of these observations is that they are much more time consuming of unpolarized ones and are harder to calibrate and analyse given the required level of precision needed to appreciate the signals and their variations in space or frequency.

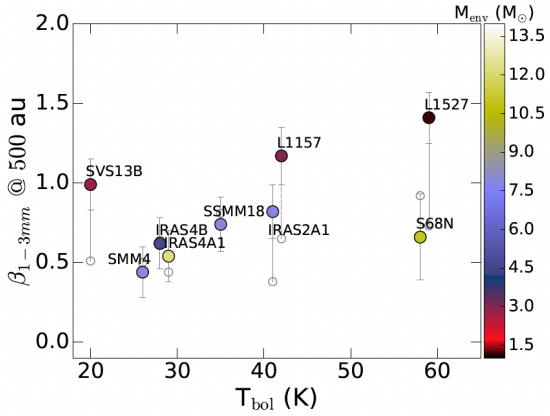

Figure 1.17: All the measured dust opacity spectral indices β of Galametz et al. (2019), as a function of bolometric temperature and envelope mass of the CALYPSO sample sources.

1.6 The structure of this Thesis

In the context presented within this Chapter, I started this Thesis work aiming at placing stronger observational constraints on our understanding of dust properties evolution in collapsing protostellar envelopes. To do so, I have made use of ALMA and PdBI data, which allowed me to (i) improve the methodologies that are needed to disentangle disk and envelope contribution in interferometric data sets; (ii) significantly decrease the error bars associated with the measurements that have been carried out when compared to literature works; (iii) increase the number of measurement of dust opacity spectral indices in protostellar envelopes; (iv) propose observational evidence for the transport of dust grains along protostellar outflows and jets; and (v) constrain for the first time the dust properties and dust mass in an asymmetric streamer impacting the history of a Class I

YSO.

In Chapter 2, I introduce the basics of radio interferometry, the technique on which most of this work is based. I briefly present the utilized instruments and discuss upon the specific needs of studies that aim at studying dust properties in infalling envelopes, requiring deep observations, modeling in the uv plane, and accurate data combination.

In Chapter 3, I present a pilot study on L1527 IRS. I aimed at extending previous studies spectral and spatial coverage of the observations in order to more robustly measure its spectral index profile. I find that observations are explained by variations of dust properties from being ISM-like at about 2000 au to resemble disk-like β in the inner envelope, at about 200 au. I call for the need of multi-scale, multi-wavelength observations of dusty envelopes, a practice that already became as critical as spread in the protoplanetary disk community for similar reasons.

In Chapter 4, I present tentative observational evidence for the transport of dust grains along protostellar outflows and jets. Re-interpreting the available PdBI β measurements of Galametz et al. (2019) and putting them in context with new measurements of jets and outflows mass loss rates based on data of the same program, I present a tentative correlation between the power of jets and outflows with the measured β. This correlation might suggest that more powerful outflows are lifting larger grains in the envelopes of young sources. Only further sample studies will tell us whether such a correlation is robust.

In Chapter 5, I utilize data from the ALMA FAUST Large Program in order to constrain the dust opacity spectral index for a new set of young Class 0 and Class I sources observed by the project. This study aims at increasing the number of measurements of dust properties, which is essentially limited to the ten objects presented in Galametz et al. (2019) based on the PdBI CALYPSO program. In this study, I find that most dust opacity spectral indices are ISM-like for the FAUST sources. I strengthen a correlation between such a quantity and the envelope mass of the source, first suggested in Galametz et al. (2019) and possibly hinting to high optical depth effects in inner massive envelopes. I measure for one of the first times the β index across the cavity walls of the outflow driven by a young protostar, IRAS15398-3359.

In Chapter 6, I present the first ever measurements of the dust opacity spectral index β in an infalling streamer onto a young Class I source in the dense Orion molecular cloud environment. While many streamers have recently been detected serendipitously in molecular gas emission, M512 represents the first case of a targeted study to measure dust properties and dust mass in such an environment and brought original constraints on this ever growing field of research. We found that the dust the streamer presents ISM-like properties across its full 4,000 au extent, and that its mass infall rate can significantly impact the inner system, even if only partially accreted. Whether this streamer is different than collapsing envelopes as it shows no variations, or if higher resolution observations of its very inner regions are needed to witness such an evolution, remains an open question

that we hope to tackle with further data.

Finally, in Chapter 7, I summarize my findings and discuss the future perspective of this work.

2

Instrumentation and methods

In this Chapter, I will review the basics of radiointerferometry and delve deeper into how instruments like ALMA or NOEMA are crucial when it comes to study the dust properties in dense protostellar environments. These telescopes are able to resolve celestial objects to sub-arcsecond scales and, at the same time, recover the dust thermal emission of their faint, extended envelopes. Both aspects are central to the research that was carried out and discussed in the rest of this Thesis.

2.1 Principles of radiointerferometry

In its simplest form, an interferometer is composed by two antennas that are wired to act similarly to a pair of slits when light passes through them. In both cases, an interference pattern is generated that carries information on the intensity and position of the light source, convolved with a "response function" dependent on the width of the individual slits and their mutual separation.

A plane parallel wave reaching two slits will be split into two new wavefronts at the slit locations, which will interfere when continuing along their path. If the waves reach a sensitive screen, they will impinge a fringe pattern onto it, the characteristics of which depend on the position of the light source, on the incoming radiation's wavelength and on the separation of the two slits (Fig. 2.1). The angular separation between maxima of the fringe pattern is in fact given by:

$$sin\theta = \frac{m\lambda}{d} \tag{2.1}$$

where d is the distance between the slits, λ is the wavelength of incoming radiation, and m is the "order" of the maximum (first maximum, second one, etc ...). Notice how closer slits imply larger separation between the fringes maxima, and viceversa.

In a radiointerferometer, antennas represent the slits and the fringe pattern is computed by electronically multiplying the signals received at each antenna in a supercomputer known as "correlator". An interferometer with closely spaced antennas will similarly generate a pattern with wide fringes, while finer and finer fringes will be achieved when positioning the antennas further away from each other. The distance between the antennas is called "baseline" and the fringe pattern computed correlating the two signals is called "dirty beam". From the dirty beam, one can obtain a "synthesized beam" by fitting a Gaussian the central region of the former (see Fig. 2.2). For an interferometer, the synthesized beam is the equivalent of the point spread function (PSF) of an optical

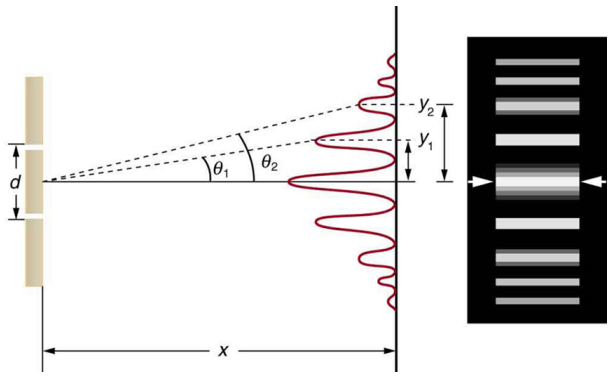

Figure 2.1: A wavefront is split by two fringes, interferes with itself and generates an interference pattern on a sensitive screen.

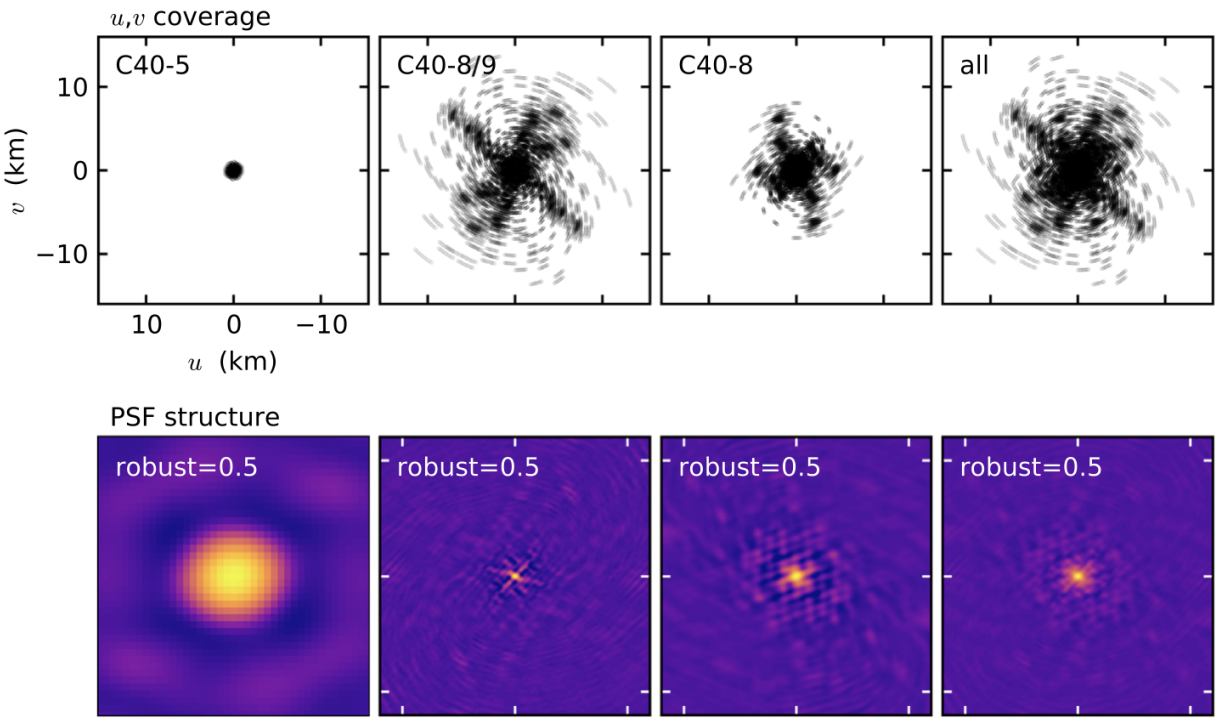

Figure 2.2: The "fringe pattern" of an interferometer, or its dirty beam, is the Fourier transform of the (u,v) coverage. As the (u,v) coverage (upper left panel) is very compact, the PSF is broad (lower left) and thus will be optimal to observe extended sources. As the antennas are distributed on longer baselines (second and third upper panels), the beam can be shrunk in order to resolve finer details of a source (second and third lower panels). Finally, combining compact and extended configurations can yield a balance (right upper and lower panels). Since the coverage is incomplete in all cases, the dirty beam displays complex structure and negative lobes. The synthesized beam is the gaussian that best fits the central dirty beam region. Image credits: Andrews et al. 2018.

telescope, thus representing the response of the instrument to a point-like light source on the sky. In particular, short baselines (wider fringes) are sensitive to extended sky brightness distributions. On the other hand, long baselines (narrower fringes) will be sensitive to smaller details in the sky brightness distribution, and will "filter out" flux, thus leading to the so called "missing flux problem". This happens because the sky brightness distribution (light source) is convolved with the telescope response, which is a strongly oscillating function in the case of long baselines, with many destructive-interference minima in the fringe pattern. Ideally, to reconstruct both the intensity and the morphology of a source with high "fidelity", one needs to combine many antennas in order to have both short and long baselines. The positions of these antennas as seen from the point of view of the source in the sky are referred to as "(u,v) coverage", where (u,v) are the coordinates of the antenna in this reference frame. While the synthesized beam of two antennas is a fringe pattern,

many antennas working together see the sky through a more complex pattern, which is the combination of all fringe patterns from all antenna pairs. However, if one sets up many antennas with a strategic distribution on a site, one can obtain a beam that is Gaussian-like as for the PSF of an optical telescope. Mathematically, it can be proven that the synthesized beam is the Fourier transform of the (u,v) coverage. The Fourier transform of a Gaussian of width σ is a Gaussian of width $1/\sigma$ and thus, if we approximate the antennas on short baselines to be distributed as a compact Gaussian, these will contribute to the synthesized beam as a broad Gaussian and be sensitive to large scales. On the other hand, antennas approximately distributed as a wide Gaussian on the (u,v) plane, i.e. on long baselines, will contribute as a compact Gaussian to the synthesized beam, thus recovering the fine details of the sky brightness distribution (Fig. 2.2). In reality, the (u,v) coverage is never perfect because we can only position a limited number of antennas and only down to a distance that corresponds to a physical limit imposed by their radius[1]. This will lead to an imperfect dirty beam, that will contain complicated destructive-interference patches, so called "side lobes" and need to be deconvolved from the observations when imaging (Fig. 2.2).

2.2 Interferometric data are visbilities

An interferometer measures the brightness of the sky by collecting two quantities, the amplitude of the signal and its phase. These can be combined and expressed in complex number, which we call a "visibility". The amplitude of a signal induced in a receiver of an antenna is intuitively proportional to the brightness of the source, while the phase at which the wave reaches the receiver depends on the relative positions of the antennas with respect to the source. In fact, since the antennas occupy different positions, the light path from the source to antenna 1 will be different than the light path between the source and antenna 2. Thus, if at given time the signal has an amplitude V_1 for antenna 1, it will be $V_2 = V_1 e^{2\pi i u l}$ on antenna 2, where $usin\alpha = ul$ is the extra path that the wavefront has to cover to reach antenna 2 (Fig. 2.3). The light path difference in time is called "delay" between the two signals, which is equivalent to a difference in the phase of the received wave. In order to compute the antenna response to the sky brightness distribution for a simple interferometer, the two signals are combined in the correlator:

$$< V_1 V_2 >= \int\int < V_1^2(l,m) > e^{2\pi i(ul+vm)} dldm \tag{2.2}$$

where the integration account for antenna relative positions in 2D. Then, since the squared voltage induced in the receiver is proportional to the power of the incoming radiation:

$$< V_1 V_2 > \propto \int\int I(l,m) e^{2\pi i(ul+vm)} dldm \tag{2.3}$$

meaning that the measured correlated signals are proportional to the Fourier transform of the sky brightness distribution. The hidden proportionality term is the primary beam of

[1] In practice, this is never done to avoid mechanical risks and shadowing between antenna plates.

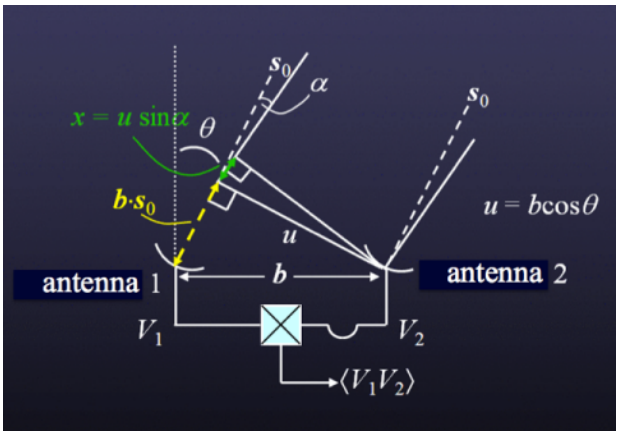

Figure 2.3: A simple, two-antenna interferometer. Image credits: ALMA Technical Handbook Cycle 10.

the antenna, i.e. the single antenna response to the sky A(l,m):

$$V(u,v) = \int\int A(l,m) I(l,m) e^{2\pi i(ul+vm)} dl dm. \tag{2.4}$$

The A(l,m) term describes how sensitive the antenna is off-center, which is especially important to note for extended sources. Indeed, an antenna is not sensitive in the same way along all directions, a characteristic called "directivity". This is usually well described by a Gaussian, the FWHM of which effectively represents the field of view of the observation.

2.3 ALMA: Atacama Large Millimeter Array

The Atacama Large Millimeter/submillimeter Array (ALMA) is a radiotelescope located in the Atacama Desert of northern Chile, and observations carried at that very facility have been central to this work. Its location, at an altitude of 5,050m, provides exceptionally dry and clear conditions, reducing the disturbance introduced by the atmosphere during observations. ALMA has been developed and it is operated by a collaboration involving the European Southern Observatory (ESO), the National Radio Astronomy Observatory (NRAO), and the National Astronomical Observatory of Japan (NAOJ), and called Joint ALMA Observatory (JAO). It is an instrument designed to observe in the millimeter and submillimeter wavelength range with ten receiver bands, from Band 1, targeting the 6-9 mm range, up to Band 10, targeting the 0.3-0.4 mm window.

The ALMA array consists of 66 high-precision antennas that can be configured in a range of possibilities, providing a range of observational capabilities. Among those 66 antennas, twelve are 7m in diameter and are distributed on short baselines in what is referred to as the Atacama Compact Array (ACA). This array, along with an additional four 12-m antennas that do not work in interferometry mode but provide zero-spacing

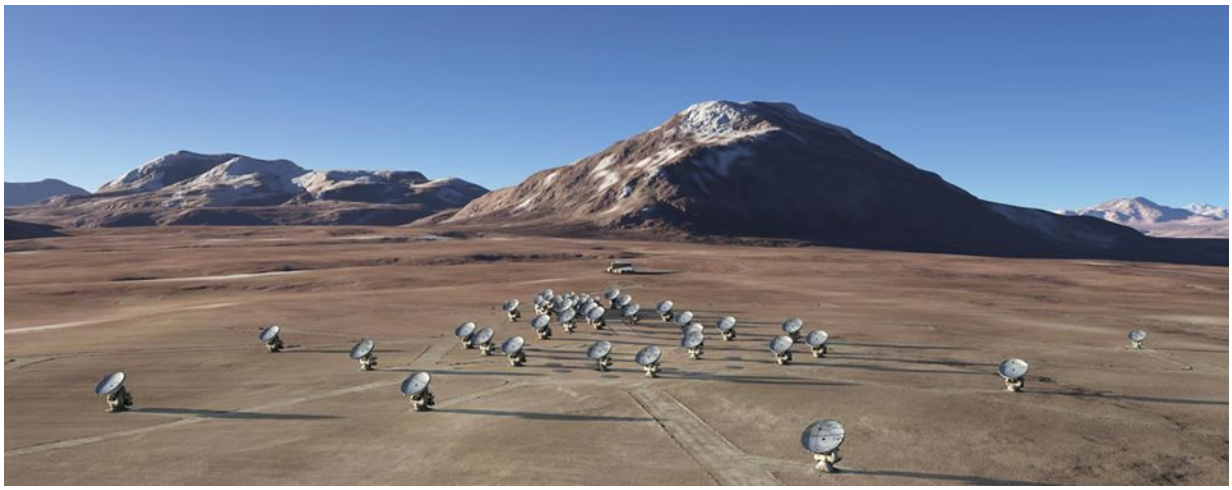

Figure 2.4: The Atacama Large Millimeter/Submillimeter Array on the Chajnantor Plateau, Chile.

observations, is used to recover the large-scale emission of extended sources. Finally, the remaining fifty antennas make up the extended array and can be allocated on stations the distances of which range from 15m to 16km, achieving sub-arcsecond resolution in all bands. The dynamic nature of ALMA antennas, moved on different pads at need using special transporters, ensures the most efficient (u,v) plane coverage among the world's radiointerferometers. This results in high fidelity images.

The ALMA correlator is the pivotal component within the Atacama Large Millimeter/submillimeter Array telescope, playing the crucial role in the synthesis of the signals collected by its extensive array of antennas (Eq. 2.2). The correlator can operate at the ALMA multiple frequency bands within the millimeter and submillimeter range. This versatility is needed to explore a diverse range of astronomical phenomena, each associated with distinct frequency signatures. The ALMA correlator can simultaneously process an extensive number of individual frequency channels (spectral resolution elements) over a given spectral window. ALMA can deliver data cubes with up to 7680 frequency channels. The width of these channels can range between 3.8 kHz and 15.6 MHz, while the total bandwidth cannot exceed 8 GHz and is sacrificed when very high spectral resolution is needed. At an observing frequency of 110 GHz, the highest spectral resolution implies a velocity resolution of 0.01 km/s. Finally, ALMA generates enormous data rates which enables state-of-the-art science ($\sim$ TBs/night) and this wealth of information is stored in an open access archive.

Figure 2.5: The NOrthern Extended Millimeter Array (NOEMA) on the Plateau de Bure, France.

2.4 NOEMA: NOrthern Extended Millimeter Array

The NOrthern Extended Millimeter Array (NOEMA) is a radiointerferometer located at 2550m on the Plateau de Bure, in southern France. Observations performed with its predecessor, the Plateau de Bure Interferometer (PdBI) - of which NOEMA is an extension for number of antennas and range of baselines - have been used in this work. NOEMA has been developed and it is operated by a collaboration involving the french Centre National de Recherche Scientifique (CNRS), the german Max-Planck-Gesellschaft (MPG), and the spanish Instituto Geográfico Nacional (IGN). It is an instrument designed to observe in the millimeter and submillimeter wavelength range with three receiver bands, targeting the 1, 2, and 3 mm atmospheric windows.

The NOEMA array consists of 12 high-precision antennas: the number doubled with respect to the original PdBI. The 12 antennas are all of 15m in diameter and can be configured in different ways thanks to "T"-shaped tracks along which the antennas can be moved on 32 different stations, providing a range of observational capabilities. The possible configurations range from A (0.″3 at 230 GHz) to D (1.″7 at 230 GHz). The NOEMA correlator, PolyFix, can process up to a total instantaneous bandwidth of 31 GHz for up to twelve antennas that is split up into two polarizations in each of the two available sidebands, the lower side band (LSB) and the upper one (USB). PolyFix offers a low frequency resolution mode (2 MHz) throughout the whole 16 GHz effective bandwidth, which is optimal for tunings that wish to include as many lines as possible in a setup; or a

high resolution mode with chunks of 62.5 kHz and up to 128 chunks in a spectral window.

2.5 Recovering faint emission: calibrations and self-calibration

When carrying out observations, atmospheric and instrumental effects degrade the signal at all times. For this reason, the measured interferometric visibilities can be expressed as the ones that ideally represent the source convolved with such degrading effects, in its simplest form:

$$V^{ij}_{obs}(\nu, t) = G^{ij}(\nu, t) * V^{ij}_{ideal}(\nu, t). \tag{2.5}$$

The relation above is known as “measurement equation" and it needs to be solved for the degrading matrix in order for the data to be accurately interpreted and scientifically analysed. The matrix G^{ij} contains terms for each baseline between antennas i and j that describe the way atmosphere scatters the incoming waves detected by that pair, the way system amplifiers convert the incoming signal into an electric one, the response of the telescope as a function of bandpass, and other effects.

2.5.1 Basic calibrations

First, the response of the interferometer to the signal across the observing bandpass needs to be calibrated. Both measured amplitude and phase are affected by the bandpass response, meaning that they vary in function of frequency across the sensitive range of the used receiver. Calibrating the observations against bandpass means correcting for these instrument-driven variations. The bandpass calibration uses a bright source, usually a quasar, for which the spectrum in phase and amplitude is very well known. If the quasar has expected flat spectrum in the bandpass range and a phase of zero everywhere since it is unresolved, any observed variations must have been due to instrumental response. These can be quantified and applied to the science source as well.

The amplitude term of the observed visibilities also needs to be calibrated for instrumental gains. The incoming signal is converted into an electrical one in the receivers before being sent to the correlator. The conversion factor can be calibrated against an object for which we know extremely precisely the true flux, for example because of very precise observations and modeling. These calibrators are usually chosen to be solar system planets, for which we know the spectrum very precisely across the spectrum where interferometers operate. At times, quasars are chosen, but they are monitored and consistently calibrated on the planets. Correcting any observed deviations of the expected calibrator amplitude will result in a set of factors that can then be applied on source. It is important to keep in mind that due to the variability of the calibrators, the flux calibration can suffer relatively large uncertainties of up to $\sim 25\%$ (Francis et al., 2020a). Depending on the science goal, this uncertainties have to be taken into account and corrected where possible.

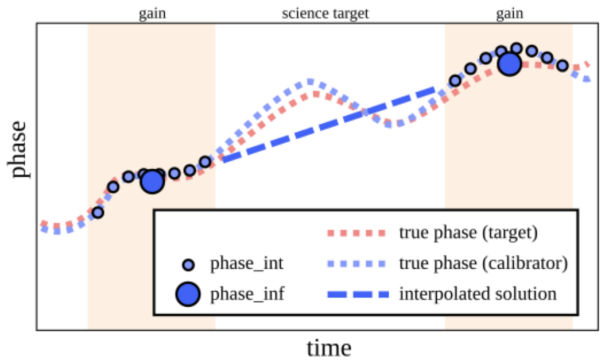

Figure 2.6: The gain calibration interpolates the phase of the gain calibrator over time. This approach can only be seen as an approximation for the true phase of your science target. Credits: Allegro ARC Node.

Finally, the phase term of measured visibilities can be degraded by the interaction of radiation with the atmosphere: a wavefront is scattered in its way from the top of the atmosphere to the receivers and thus its registered phase vary. This variation is stronger when weather conditions are bad and for higher frequencies, which are more subject to interactions with the atmosphere. Since the atmosphere vary on timescales of minutes, the phase of an observation needs to be corrected on the same scales. In order to perform the calibration, then, the interferometer is pointed towards a calibrator and the source in alternate fashion during an observing block. A bright calibrator is chosen such that it is close to the source in the sky (to trace the same atmospheric turbulence) and to be a point source. Since we expect the phase of a point source to be zero across all baselines, any detected phase offset of the calibrator observation is known to be originating from the atmosphere and the source can be corrected by inverting such an offset. However, note that since the interferometer alternates between science source and calibrator, it never samples the same exact atmosphere variations in time and also it does so at slightly different sky positions. For this reason, phase calibration is not perfect by construction, it only represents an approximation based on the assumption that the atmosphere varies linearly between two scans on the calibrator and interpolates a correction on the science target (Fig. 2.6). This situation can be improved using self-calibration.

2.5.2 Self-calibration

Self-calibration is a way to use the science target itself as a calibrator and can be used when the signal-to-noise ratio on the science source is high enough. This requirement on the signal strength is due to the necessity of using the source as a model to compare to the observed data. In order for the calibration solutions to be acceptable, a robust model is needed.

Self-calibration works as follows. First, the data is initially calibrated using stan-

dard techniques to correct for known instrumental effects and calibrate the antenna gains and phases as accurately as possible, as described before. Then, a model of the observed source is created. This model includes parameters such as the brightness distribution, positions, and flux densities of the sources. A model usually consists in a series of point-like sources, the sum of which approximates the sky brightness distribution. The model is then compared to the interferometric data and the residuals between the predicted and observed data are analyzed to identify discrepancies and errors. These residuals can indicate imperfections in the initial calibration, if the model is accurate. At this point, the calibration parameters and source model are adjusted to minimize the residuals. This adjustment can involve refining antenna gains and phases, as well as updating the source parameters such as positions and flux densities. Once the process converges, a final image of the observed source is reconstructed using the refined calibration parameters and model.

Self-calibration is a powerful technique that allows to retrieve high signal-to-noise ratio models for the faint protostellar envelopes that are at the centre of this study. More in particular, throughout this work, I have used self-calibration techniques to refine the quality of the data, which resulted in improvements on the signal-to-noise ratio of even 600% where self-calibration is most useful, i.e. at the high frequency bands where the atmospheric variations are quickest in time (for the details, see Chapters 5 and 6).

2.6 Protostellar disk-envelope systems in the image and (u,v) planes

We saw how Eq. 2.4 describes how the measured interferometric visibilities are proportional to the Fourier transform of the sky brightness distribution. Thus, it appears clear that, in order to image a radio source on the sky, one could invert the Fourier operation. Inverting Eq. 2.4 means evaluating an integral on the (u,v) plane:

$$I(u,v) = \int\int V(u,v) e^{-i2\pi(ul+vm)} du dv \tag{2.6}$$

However, u and v are not continuously sampled as we discussed in the previous Section. Rather, the antenna positions with respect to the source are discretely sampled and limited by the physical extent of the hardware. If we indicate with B(u,v) the distribution of the antennas in the u,v plane, then we can reconstruct the sky image as a "dirty image":

$$I_D(u,v) = \int\int B(u,v) V(u,v) e^{-i2\pi(ul+vm)} du dv. \tag{2.7}$$

Being incomplete, B(u,v) will cause a number of problems, such as spatial filtering (excluding the flux coming from scales much larger than the synthesized beam) and side lobes (negative sky response). Thus, to get a higher fidelity image of the sky source, we have to deconvolve the dirty image from the effects of the synthesized beam. In order to do so, several algorithms have been developed, and the most widely used is "CLEAN" (Högbom,

1974). The algorithm assumes that a radio image can be approximated by a number of point sources. It will iteratively find the peak value in the matrix image, subtract a certain fraction of this point source convolved with the synthesized beam of the observation, until the highest value is smaller than some threshold. Finally, it will convolve the model made of all the detected point sources to the beam and add the residuals. This final product is a model image of the sky brightness distribution.

In practice, when deconvolving, one can also assign "weights" to the visibilities to enhance a certain recovered scale, based on the science case. If one weighs more visibilities of shortly spaced antennas, one will be more sensitive to large scale emission, and viceversa. To do so, different weighting schemes have been introduced, such as "natural" (where visibilities are effectively not weighted, thus the density of baselines will determine the recovered flux and resolution), "uniform" where all scales receive the same weight, and "briggs" where one can tune whether more weight is given to the larger or smaller scales potentially finding a balance between the two. A certain balance can thus be reached, however, it is clear how such compromises do not allow a use of the data at its full. While this is mostly acceptable for studies focusing on a certain given physical scale, it becomes limiting for intrinsically multiscale analyses, such as the ones of this Thesis. In fact, if we were to generate images in which the lowest sensitivity is reached in order to recover the faint protostellar envelopes we are interested in, the image resolution would be very poor, thus blending together emission contributions from the envelope and the disk. On the other hand, if we were to boost the resolution, most of the envelope emission would be filtered out hindering the measurement of any related quantity. This way, measured protostellar envelopes spectral indices which carry dust information, would be either contaminated by the disk or impossible to measure due to lack of SNR, respectively.

Working in the (u,v) plane, one can stay clean of these compromises and use the data at its fullest. In the (u,v) plane, both the disk and envelope contribution are present at each point and can be disentangled using two-components models. Here, the long baselines mostly filter the envelope and trace the disk scales, while the short baselines display excesses due to the large scale envelope to which they are sensitive. It is mainly for this reason that working in the (u,v) plane becomes a priority in this Thesis, given the main goal of measuring dust properties across physical scales around young protostellar objects.

2.6.1 Modelling interferometric visibilities

Extracting geometrical and physical information from interferometric data requires modelling. This can be done generally in two ways: either by comparing a reconstructed image to a model image or by fitting models to the visibilities themselves. While the first option is more intuitive because it compares images that represent the sky brightness distribution, there is no single "right" image that can be obtained from the real data. Thus, fitting a model to an image effectively means fitting a model to a model. If the science goal is

intrinsically multi-scale, like following the evolution of dust from collapsing envelopes to disks, the problem gets worse (see previous section).

However, in the (u,v) plane, all contributions from all baselines have the same weight and thus can be modelled properly. The downsides of this approach are a loss in intuition of model visualization, as well as a higher degree of complexity when it comes to express a model as the Fourier transform of a brightness profile. Simple models are however often used to retrieve the geometrical parameters of sources observed via interferometry, like Gaussians, Gaussian rings, power laws, exponential cut offs. In order to compare model and observations, a series of steps can be applied. First, starting from a 1D brightness profile, one can generate a 2D matrix (model image) that needs to be Fourier transformed to make it comparable to the visibilities. Since the visibilities are scattered on the (u,v) plane, the result of the Fourier transform has to be sampled on the same (u,v) plane distribution. Only then can the model be compared to the data and a loss function, such as a χ^2, can be computed. Practically, in order to get the "best fit" parameters of a model from observations, a large number of parameter values are explored in certain ranges, perhaps based on some *a priori* knowledge of the source. This parameter space exploration is often conducted with Markov Chain Monte Carlo samplers. Calculating synthetic visibilities from a brightness profile thus involves many time-consuming matrix operations as Fourier transforms and interpolations. Moreover, interferometers produce large data rates as an N-antennas telescope will measure N(N-1)/2 visibilities at each time step of the observation. A typical high-resolution ALMA data set can easily reach a few hundred Gigabytes.

A widely used package to conduct such complex computations in order to fit parametric models to interferometric data is galario[2] (Tazzari et al., 2018), a computational library that exploits the power of graphical processing units (GPUs) to accelerate the analysis of radio observations. In concert with emcee (Foreman-Mackey et al., 2013), I have used galario in this Thesis work, to fit parametric models to interferometric visibilities. An example of how the code was used to speed up the fitting of data is in Section 3. These models account for a central protoplanetary disk with a certain peak flux, radius, inclination and position angle, and sum an extended spherical envelope to it, described by a broken power law profile. While this is a simplistic modelling approach, it robustly allows to account for both components as proved in (Maury et al. 2018, Tung et al. 2024). In Fig. 2.7, an example is shown to visualize how this model fits mock observations obtained from radiative transfer postprocessing of magnetohydrodynamical simulations. While the irregularities of collapsing envelopes cannot be fit with a generalized model, the value of the model lies in its capability to disentangle an inner gaussian region - perhaps a disk - from the rest of the emission. This is particularly valuable if one wants to disentangle the two contributions to study them separately, as is the case in this Thesis. It is noteworthy that non-parametric approaches to visibilities fitting are also possible, however not used throughout this Thesis work as they would not be useful to disentangle the emission from

[2]http://github.com/mtazzari/galario

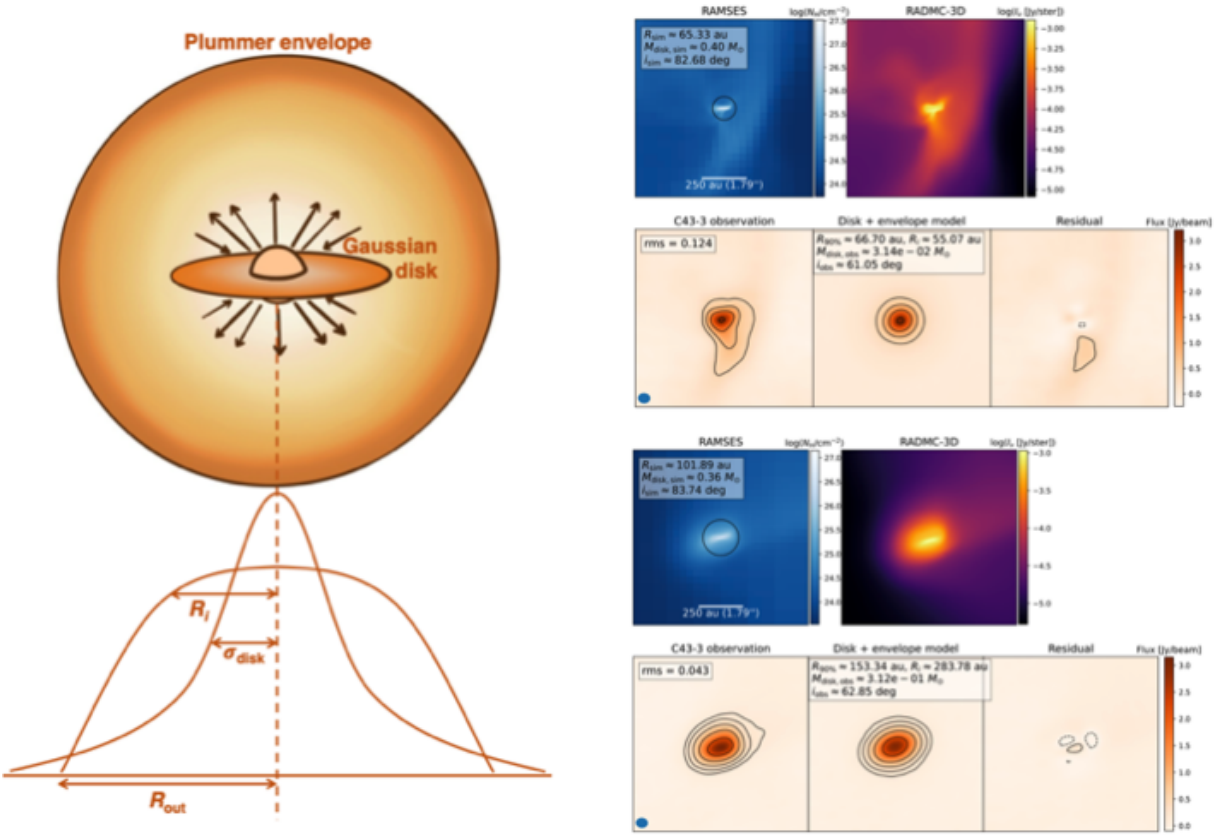

Figure 2.7: Left: visualization of the disk and envelope components of the modelling scheme largely applied throughout this Thesis work. Right: example of simulations of protostellar collapse (blue maps) that have been post-processed with the radiative transfer code RADMC3D at 0.88mm (plasma maps). Mock observations, their fit and residuals are shown in the three adjacent panels right below. Images are from Tung et al. (2024).

different components. An example of code that can fit interferometric data following this procedure is frankenstein (Jennings et al., 2020).

2.7 Recovering multi-scale, faint envelopes requires data combination

In order to be sensitive to the multiple scales involved in tracing dust properties from extended envelopes to disks, observing with just one configuration of an interferometer is not enough. As previously said, shortly-spaced antennas are sensitive to large scale emission in the sky, and viceversa. Thus, for a set of observations to be sensitive to both protostellar envelope (>1000 au) and disk (10 au) scales, a combination of array configurations must be employed. Moreover, it is imperative to consider configurations

of the array that provide the same resolution and largest angular scale recovery because the measured fluxes will be dependent on these quantities, and measuring spectral indices only makes sense comparing emission coming from the same portions of the sky. Data combination has thus been central to this Thesis and I here review the main considerations and lessons learnt in the process.

2.7.1 Calibrating relative data weights

First, combining data from different observation cycles requires care in making sure that the visibilities from each datasets are "weighted" properly. Each couple of antennas will produce a visibility point at each integration time, and this visibility point is naturally accompanied by an uncertainty, defined as:

$$\sigma_{ij}(Jy) = \frac{2\kappa}{\eta_q \eta_c A_{eff}} \sqrt{\frac{T_{sys,i} T_{sys,j}}{2\Delta\nu_{ch} t_{ij}}} \times 10^{26}, \tag{2.8}$$

where κ is Boltzmann's constant, A_{eff} is the effective antenna area, η_q and η_c are the quantization and correlator efficiencies, respectively. These have values of about 0.88 and 0.96, respectively[3]. Moreover, $T_{sys,i}$ is the system temperature for antenna i, and $T_{sys,j}$ is the system temperature for antenna j, $\Delta\nu_{ch}$ is the effective spectral channel frequency width, and t_{ij} is the integration time per visibility. A "visibility weight" is defined as $1/\sigma$ and it represents the relative importance of a visibility point when it comes to produce a model image, or fit a model to the data. While the weights can be changed to meet the science goals of a project (i.e., up-weighting short-baselines visibilities would help recover extended emission in a model image), it is important to keep in mind that this does not come for free (i.e., losing resolution in the example in parentheses above). For ALMA, weights were calculated differently in older versions of CASA (up to 4.2.1), with respect to what was done in CASA 4.2.2 and higher. In the older CASA versions, it was assumed that there weren't unflagged antennas with significantly low gain, and that all the antennas have similar efficiencies. This means that Eq.2.8 reduces to $\sigma = 1/\sqrt{2\Delta\nu\Delta t}$. While these are reasonable assumptions for an instrument like ALMA, successive versions of CASA correct the weights for both each baseline gains and antenna efficiency[4]. In general, it is a good practice to check the weights associated to each dataset when combining different datasets. This is because if, for any reason, a dataset has much higher weights than another one, it will drive most of the imaging or visibilities fitting results. In order to do this, one can plot the visibility weights of each data set against each other and compare. If unjustified large differences are present, one should fix the weights. This can be easily implemented in CASA with the `statwt` routine, which will improve the $\sigma = 1/\sqrt{2\Delta\nu\Delta t}$ approximation and compute the weight using the full Eq. 2.8.

[3]ALMA Techincal Handbook (Remjian et al., 2019)

[4]https://casaguides.nrao.edu/index.php/DataWeightsAndCombination

2.7.2 Source alignment across data sets

When combining multiple data sets in which a science source was observed, great care should be taken into aligning them since misalignment could cause blurring when making a model image and introduce spurious wiggles in the profiles of the real and imaginary parts of the visibilities. Thus, it is good norm to align the source emission with the phase center of the observations. Before further reduction and analysis of the data sets, we would thus make sure to align the source. First, a gaussian fit can be run on a first, simple image in order to get the peak coordinates. The CASA fixvis can then be used to recalculate (u, v, w) in an data set based on the antenna positions, time of observations and source position. The, fixvis also changes the phase center of visibilities. Finally, one can use fixplanets to correct the coordinates of the centre of the source in the metadata, which is considered by the concat routine at the moment of data sets concatenation - where a shift tolerance can be set to consider different pointings as on the same source.

2.7.3 Relative flux scaling

When the science goal of a radiointerferometric project is not limited to studying the morphology of the emission but includes measuring flux-dependent quantities like spectral indices or dust masses, accurate flux calibration must be performed. Achieving accurate flux calibrations is challenging because of the scarcity of bright calibrator sources in the sub-mm/mm sky, which are stable over time, a problem that worsens at higher frequencies. Solar system planets fluxes are known in the sub-millimeter to high accuracies but are not always visible in the sky, and thus are used as anchors to maintain a much larger catalog of calibrators whose fluxes are often (each 10-15 days) compared to the planets.

For example, while the 1σ ALMA nominal flux calibration uncertainty is 5% at longer wavelengths (Band 3, 4, 6) and 10% in Band 7, the actual uncertainty on a given data set could be worse if (i) outdated calibrator catalogs were used, (ii) a flare affected the latest quasar calibrator measurements or (iii) weather conditions were particularly bad (Francis et al., 2020a). These problems can be particularly accentuated when combining many data sets taken at different observing cycles, due to the evolution of the calibrator catalogues, and the stochastic chance of some data sets being affected by quasars time variability. Since data combination is central to some of the work done in this Thesis (Chapter 3), where data sets had to be combined to ensure recovering of faint envelope emission and of physical scales otherwise filtered by extended configurations, a solution to this problem had to be applied when needed.

In order to correct for any flux offset across datasets, we azimuthally averaged the visibilities and compared them across datasets in a range of (u,v) distances. We used the estimate_flux_scale and the rescale_flux routines implemented by the DSHARP Large Program Team and publicly available[5] (Andrews et al., 2018). With estimate_flux_scale,

[5] https://almascience.eso.org/almadata/lp/DSHARP/scripts/reduction_utils.py

we would first compute the flux ratio between two observations of a source in a range of baselines. The minimum baseline was chosen to be the longest among the shortest baselines of the single datasets.

The longest baseline was instead the shortest among the longest baselines in the individual datasets. This choice ensures the selection of a (u,v) distance range common to all involved data sets. This procedure returns a set of flux ratios in which one can identify the mean ALMA calibration uncertainty, which results below 10% for most datasets in all bands (see also Chapter 2). As a sanity check, we tested whether the rescaling factors were affected by decorrelation. Indeed, phase decorrelations can induce flux loss and thus a rapid decrease in the azimuthally averaged amplitude profile. If a data set is more decorrelated than others, its faster drop will mean the correcting factor is not a constant across baselines. We thus computed the rescaling factors as a function of baseline and ensured their stability. The second routine, rescale_flux, would then be used to rescale all individual data sets to a reference one, using the computed flux ratio and the CASA gencal task. We chose the reference dataset as follows: when most datasets fall within the ALMA calibration uncertainty, a median one is chosen in order to not bias the flux level towards the highest or lowest dataset. This rescaling was especially important for (rare) datasets that would fall beyond the nominal ALMA calibration error and that could have potentially strongly biased the final concatenation.

3

The dusty envelope of L1527 IRS A multi-scale, multi-wavelength ALMA study

This Chapter is based on "FAUST IX. Multi-band, multi-scale ALMA dust study of L1527. Dust properties variations in the envelope of a young class 0/I YSO" (Cacciapuoti et al., 2023, Astronomy & Astrophysics, Volume 676, id.A4, 18 pp.)

This Chapter was the result of my own writing. The data were reduced and analysed by me. I produced all the plots. The co-authors were involved in discussions and feedback.

Full authors list:
Luca Cacciapuoti; E. Macias; Maury, A. J.; Chandler, C. J.; Sakai, N.; Tychoniec, Ł. ; Viti, S.; Natta, A.; De Simone, M.; Miotello, A.; Codella, C.; Ceccarelli, C.; Podio, L.; Fedele, D.; Johnstone, D.; Shirley, Y.; Liu, B. J.; Bianchi, E.; Zhang, Z. E.; Pineda, J.; Loinard, L.; Ménard, F. ; Lebreuilly, U.; Klessen, R. S.; Hennebelle, P.; Molinari, S.; Testi, L.; Yamamoto, S.

Early dust grain growth in protostellar envelopes infalling on young disks has been suggested in recent studies, supporting the hypothesis that dust particles start to agglomerate already during the class 0/I phase of young stellar objects (YSOs). If this early evolution were confirmed, it would impact the usually assumed initial conditions of planet formation, where only particles with sizes $\lesssim 0.25\mu$m are usually considered for protostellar envelopes.

We aim to determine the maximum grain size of the dust population in the envelope of the class 0/I protostar L1527 IRS, located in the Taurus star-forming region (140 pc).

We use Atacama Large millimeter/submillimeter Array (ALMA) and Atacama Compact Array (ACA) archival data and present new observations, in an effort to both enhance the signal-to-noise ratio of the faint extended continuum emission and properly account for the compact emission from the inner disk. Using observations performed in four wavelength bands and extending the spatial range of previous studies, we aim to place tight constraints on the spectral (α) and dust emissivity (β) indices in the envelope of L1527 IRS.

We find a rather flat $\alpha \sim 3.0$ profile in the range 50-2000 au. Accounting for the envelope temperature profile, we derived values for the dust emissivity index, $0.9 < \beta < 1.6$, and reveal a tentative, positive outward gradient. This could be interpreted as a distribution of mainly interstellar medium (ISM) like grains at 2000 au, gradually progressing to (sub)millimeter-sized dust grains in the inner envelope, where at R = 300 au, $\beta = 1.1 \pm 0.1$. Our study supports a variation of the dust properties in the envelope of L1527 IRS. We discuss how this can be the result of in situ grain growth, dust differential collapse from the parent core, or upward transport of disk large grains.

3.1 Introduction

Circumstellar disks orbiting class II young stellar objects (YSOs) are also commonly referred to as protoplanetary disks even though a large fraction of them already display structures thought to be shaped by embedded planets (Andrews et al., 2018). Rings, gaps, and spirals have also been observed in younger (<1Myr) disks (ALMA Partnership et al. 2015, Sheehan & Eisner 2018, Segura-Cox et al. 2020a, Nakatani et al. 2020). Several mechanisms have been proposed to explain the formation of structures during the early stages of the disk lifetime, including gravitational instabilities (Takahashi & Inutsuka, 2014), disk winds (Johansen et al. 2009, Takahashi & Muto 2018), and the evolution of dust (Okuzumi et al., 2016). Along with these possibilities, the early formation of large planetesimals that gravitationally interact with the disk remains a viable explanation for the observations.

The early formation of planetary embryos is also suggested by the dust mass budget of evolved disks when compared to their younger progenitors (Testi et al. 2014, Ansdell et al. 2016). Manara et al. (2018) estimated that the solid (dust) mass observed in evolved class II disks of the Ophiuchus (Sanchis et al., 2020) and Lupus star-forming-region is 1 or 2 orders of magnitude lower than the mass of the expected exoplanet population. Conversely, the class 0/Is disks of Perseus contain roughly the same mass in solids as the known exoplanets (Williams et al. 2019, Tychoniec et al. 2020. One possible explanation is that the missing mass in the class II disks is the early conversion of class 0/I solids into planetesimals (e.g. Testi et al. 2022, Bernabò et al. 2022, Xu & Armitage 2023). In a separate study, Mulders et al. (2021) suggest that the solid masses in class II disks and in exoplanets might be of the same order of magnitude. Nevertheless, an unrealistic planet formation efficiency of 100% would be required to place the beginning of planet formation during the class II stage.

Direct observational evidence for early-formed, kilometer-sized planetesimals is out of reach for any radio interferometer and thus this problem remains open. Furthermore, observational constraints on the initial properties of the dust population are needed for simulations to reconstruct the pathways that lead to planetesimal formation, starting from submicron-sized interstellar medium (ISM) dust particle interactions in a core accretion paradigm (e.g., Safronov & Zvjagina 1969, Goldreich & Ward 1973, Ormel et al. 2009, Birnstiel et al. 2016, Drazkowska et al. 2022). Even more importantly in this context, in an effort to investigate planetesimal formation at early stages, Cridland et al. (2022) find that differential gas and dust replenishment of a protoplanetary disk from its surrounding envelope sets favorable conditions for planetesimal formation. However, grains that are moderately coupled to the gas (>30 μm) are required to meet the streaming instability conditions that lead to the birth of these planetary embryos (Youdin & Goodman, 2005). Moreover, constraining grain sizes during the protostellar collapse phase has proven to be important for understanding the role of magnetic breaking during the early stages of disk formation. Since small grains are the main charge carriers, their distribution is paramount

Table 3.1: Main properties of our target, L1527 IRS. The age of the object has been roughly estimated by [1] (Tobin et al., 2012) based on the mass loss rate of the source. The mass of the protostar has been estimated by means of kinematical analysis by [1] and [2] (Aso et al., 2017). The bolometric luminosity was reported by [3] (Karska et al., 2018) and might suffer up to a factor two uncertainty due to the high inclination of the disk (e.g., Whitney et al. 2003).The envelope mass was derived in [4] (Motte & André, 2001) based on the IRAM 30 m telescope and MPIfR bolometer arrays' 1.3 millimeter maps.

Alternative ID	IRAS 04368+2557
RA	04h 39m 53.88s
Dec	+26° 03'09.″56
Age [yr]	$< 3 \cdot 10^{5}$[1]
$M_*[M_\odot]$	0.2[1]-0.45[1,2]
$L_{bol}[L_\odot]$	1.6[3]
$M^{env}_{4200au}[M_\odot]$	0.8[4]

for the coupling of the infalling material with magnetic fields. In turn, such a coupling seems to regulate disk masses and sizes (Zhao et al. 2016, Lebreuilly et al. 2020).

An additional reason to investigate the properties of dust grains in these extended envelopes is to constrain the role that dust grains play as sites - and catalysts - of molecular reactions in diffuse environments. The most commonly accepted pathways to produce complex organic molecules all rely on the presence of icy mantles on dust grains to capture the building blocks of these complex molecules and facilitate reactions among them (e.g., Tielens & Hagen 1982).

One way to probe dust grain properties in protostellar environments relies on estimates of their spectral index (α), the slope of the spectral energy distribution (SED) across (sub)millimeter wavelengths. Specifically, if dust opacity scales as $\kappa \propto \nu^{\beta}$ and if the Rayleigh-Jeans (RJ) approximation holds, $\beta = \alpha - 2$ in the optically thin regime (e.g., Beckwith & Sargent 1991, Miyake & Nakagawa 1993, Natta et al. 2007). Typical spectral indices for the ISM - $\beta \sim 1.7$ - correspond to grain sizes in the range 100 Å – 0.3 μm (Weingartner & Draine, 2001). On the other hand, $\beta < 1$ has been observed in class II objects, suggesting the presence of larger grains ($a \geq 1$ mm) in more evolved disks (Beckwith & Sargent 1991 ,Testi et al. 2003, Ricci et al. 2010, Testi et al. 2014, Tazzari et al. 2021).

In the recent past, several works have attempted to measure the dust emissivity index β at the large scales of class 0/I protostellar envelopes to constrain whether dust growth might be significant at these very early stages of star and planet formation. Many have found surprisingly low β values (≤ 1) and interpreted this result as evidence for early dust growth (Kwon et al. 2009, Shirley et al. 2011, Chiang et al. 2012, Miotello et al. 2014, Le Gouellec et al. 2019b, Valdivia et al. 2019). Following similar methods, other works have not found hints of such growth (Agurto-Gangas et al., 2019b). And, in their sample study of ten CALYPSO (Maury et al., 2019) class 0/I sources, Galametz et al. (2019) found examples of both relatively low and large β values.

The hypothesis of early grain growth in the envelopes of class 0/Is has been considered to be challenging from a theoretical perspective: growth to millimeter-sized particles seems to require environments characterized by higher density and/or longer timescales than the average class 0/I envelope (e.g., Ormel et al. 2009, Guillet et al. 2020, Lebreuilly et al. 2023, Bate 2022 and Silsbee et al. 2022). Using both analytical models and numerical simulations, these authors find that dust particles cannot grow larger than $\sim 2\mu$m in collapsing envelopes. It will be crucial for next simulations to incorporate generally disregarded effects, like the dust back-reaction on the turbulence through gas-dust friction and dust-magnetic-field interaction. Early growth is not the only possible explanation for the mentioned observations. Lebreuilly et al. (2020) proposed a scenario in which the differential collapse of dust grains of different mass through the prestellar core leads to a stratification of the dust sizes since larger grains collapse faster. Finally, another possibility could be an uplifting of grown disk grains to the inner envelope by the protostellar outflows and/or jets (Wong et al. 2016, Tsukamoto et al. 2021).

It is thus imperative to characterize dust properties and evolution in the very early stage of star and planet formation.

In this paper we focus on a single source in Taurus, L1527 IRS, (140 pc, e.g., Torres et al. 2007, Zucker et al. 2019), hereafter L1527, to benchmark a dust continuum study across multiple frequencies and physical scales. Due to its distance and brightness, L1527 is one of the best studied class 0/I YSOs. The presence of an edge-on circumstellar disk was first suggested by Bontemps et al. (1996) and Ohashi et al. (1997) based on observations of the orientation of the bipolar outflow. It has been later confirmed by means of Spitzer and Gemini-North scattered light observations as an edge-on dark lane obscuring the central protostar (Tobin et al. 2008 and Tobin et al. 2010a, respectively) as well as high-resolution Submillimeter Array (SMA) and Combined Array for Research in Millimeter Astronomy (CARMA) interferometric observations of its continuum emission (Tobin et al., 2013). The Atacama Large Millimeter/submillimeter Array (ALMA) $C^{18}O$ kinematic detection of the disk was reported by Ohashi et al. (2014) and Aso et al. (2017). Furthermore, this edge-on, warped disk presents asymmetries at ~ 20 au that are consistent with spiral structures, the physical origin of which has been proposed to be gravitational instability (Sakai et al. 2019, Nakatani et al. 2020, Ohashi et al. 2022, Sheehan et al. 2022). Observations of L1527

Project Code	P.I.	Date	Integration (s)	Resolution	Frequency (GHz)	Rescale Factor	CASA version
			Band 3				
2015.1.00261.S	Ceccarelli, C.	01/03/2016	3113	2″	85-87	0.93	4.5.2
		02/03/2016		2.″4	90-92	0.92	4.5.2
2016.1.01245.S	Cox, E.	04/01/2017	907	2.″1	99-114	1.06	4.7.0-1
2016.1.01541.S	Harsono, D.	21/12/2016	635	1.″8	92-105	1.14	4.7.0
2017.1.00509.S	Sakai, N.	14/11/2017	6150	0.″09	85-99	1.000	5.1.1-5
		14/11/2017		0.″09	85-99	1.04	5.1.1-5
		14/11/2017		0.″09	85-99	1.04	5.1.1-5
2018.1.01205.L	Yamamoto, S.	4/01/2017	1783	1.″1	93-108	-	5.6.1-8
			Band 4				
2016.1.01203.S	Oya, Y.	19/11/2016	4697	0.″8	138-150	0.96	5.1.1
		03/09/2017		0.″1	138-150	0.92	5.1.1
2016.1.01541.S	Harsono, D.	10/03/2017	241	2.″1	144-154	0.97	4.7.0
		31/03/2017		2.″1	144-154	1.000	4.7.0
			Band 6				
2012.1.00647.S	Ohashi, N.	20/07/2014	2117	0.″4	218-233	1.000	4.2.1
		20/07/2014		0.″4	218-233	1.01	4.2.1
2013.1.01086.S	Koyamatsu, S.	24/05.2015	2902	0.″6	219-234	0.85	4.5.0
		20/09/2015		0.″2	219-234	0.99	4.5.0
2013.1.00858.S	Sakai, N.	18/07/2015	2388	0.″2	245-263	0.96	4.4.0
2012.1.00193.S	Tobin, J.	11/08/2015	7348	0.″2	244-260	0.94	4.3.1
		02/09/2015		0.″2	244-260	1.05	4.3.1
2017.1.01413.S	van 't Hoff, M.	10/09/2018	968	0.″3	226-240	1.05	5.4.0
		28/09/2018		0.″3	226-240	1.07	5.4.0
2011.0.00604.S	Sakai, N.	10/08/2012	4838	0.″6	245-262	1.14	4.2.1
		26/08/2014		0.″6	245-262	1.09	4.2.1
2011.0.00210.S	Ohashi, N.	26/08/2012	1663	0.″7	219-231	1.05	4.2.1
2013.1.01331.S	Sakai, N.	02/02/2015	1209.6	1.″2	216-235	0.97	4.3.0
2018.1.01205.L	Yamamoto, S.	26/10/2018	1360.8	0.″3	244-262	1.10	5.6.1-8
		17/03/2019	362.0	1.″1	244-262	1.10	5.6.1-8
		15/12/2019		1.″1	244-262	1.11	5.6.1-8
		26/10/2018	2358	0.″3	244-262	1.01	5.6.1-8
		07/03/2019	635.0	1.″1	244-262	1.004	5.6.1-8
			Band 7				
2012.1.00346.S	Evans, N.	14/06/2014	635	0.″3	343-357	1.11	4.2.1
2015.1.01549.S	Ohashi, N.	26/07/2016	847	0.″2	329-341	1.000	4.5.3
2016.A.00011.S	Sakai, N.	29/07/2017	3592	0.″075	339-352	0.95	4.7.2
		05/09/2017		0.″075	339-352	1.01	4.7.2
2011.0.00604.S	Sakai, N.	29/08/2012	4233	0.″5	338-352	1.12	4.2.1

Table 3.2: ALMA observations. For projects with more than one execution block, we only report the total integration time of the project. The rescaling factors are relative to the dataset whose factor is exactly 1.000.

also display a bipolar jets and outflows extending to 20000 au perpendicular to the disk plane, and carving a cavity in the collapsing envelope (Bontemps et al. 1996, Ohashi et al. 1997, Hogerheijde et al. 1998, Tobin et al. 2010a, Oya et al. 2015). Being this object in a late stage of accretion, its molecular jet and outflow are not very energetic (Podio et al., 2021). Table 3.1 summarizes the main properties of this young source.

We aim to study the dust continuum emission of L1527 using the Atacama Large millimeter/submillimeter Array (ALMA) and the Atacama Compact Array (ACA) to probe the outer (10^3 au) and inner (10^2 au) envelope, as well as the disk (10 au). We consider observations of our target in four different ALMA Bands (3, 4, 6, 7). Section 2 presents the ALMA and ACA observations that we have used throughout the analysis and the data

reduction process. In Section 3, we justify the uv-plane geometrical modeling used for the source. In Section 4, we analyze the spectral and dust emissivity indices of L1527 at different scales. We discuss our results in Section 5, and wrap up our conclusions in Section 6.

Project Code	P.I.	Date	Integration (s)	Resolution	Frequency (GHz)	Rescaling Factor	CASA version
			Band 3				
2016.1.01541.S	Harsono, D.	30/01/2018	907	13″.0	92-105	1.06	4.7.0
2018.1.00799.S	Pineda, J.	05/10/2018	5235	12″.0	92-107	1.06	5.4.0
		05/10/2020		12″.0	92-107	1.07	5.4.0
		06/10/2018		12″.0	92-107	1.05	5.4.0
		06/10/2018		12″.0	92-107	1.08	5.4.0
		06/10/2020		12″.0	92-107	1.06	5.4.0
			Band 4				
2016.1.01541.S	Harsono, D.	27/10/2016	302	9″.1	144-154	1.07	4.7.0
2016.2.00171.S	Harsono, D.	24/08/2017	6168	7″.8	144-154	1.03	4.7.2
		03/09/2017		7″.8	144-154	1.01	4.7.2
		04/09/2017		7″.8	144-154	0.93	4.7.2
		12/09/2017		7″.8	144-154	0.99	4.7.2
			Band 6				
2016.2.00117.S	Yoshida, K.	31/08/2017	26943	4″.3	230-245	1.12	4.7.2
		01/09/2017		4″.3	230-245	1.09	4.7.2
		15/09/2017		4″.3	225-245	1.11	4.7.2
		16/09/2017		4″.3	225-245	1.10	4.7.2
		16/09/2017		4″.3	225-245	1.02	4.7.2
		16/09/2017		4″.3	225-245	1.10	4.7.2
		17/09/2017		4″.3	225-245	1.03	4.7.2
		17/09/2017		4″.3	225-245	0.99	4.7.2
		17/09/2017		4″.3	225-245	0.95	4.7.2
2018.1.01205.L	Yamamoto, S.	24/10/2018	4474	5″.9	216-235	0.98	5.6.1-8
		20/10/2018		4″.8	245-262	1.07	5.6.1-8
			Band 7				
2016.2.00117.S	Yoshida, K.	15/09/2018	2782	3″.1	352-363	1.15	4.7.2

Table 3.3: ACA observations. The total integration times refer to the sum of the integration times within the entire project, in the cases with more than one execution block. The rescaling factors are relative to the 12m array dataset observed with the 12-m array, whose rescaling factor is 1.000 (cfr Table3.2).

3.2 ALMA observations

We here summarize the details of the observations used throughout this work. This source has been extensively studied with both the extended and compact arrays of ALMA. Archival data include high-resolution observations designed to detect disk substructure as well as lower-resolution, high-sensitivity observations of the extended envelope. We collect every available ALMA and ACA dataset suitable for our study of L1527, aiming to combine them in the deepest continuum analysis of the envelope so far. A summary of the datasets used in this work can be found in what follows and in Tables 3.2 and 3.3.

3.2.1 ALMA FAUST B3 and B6

Here, we present new B6 and B3 data from the ALMA Large Program Fifty AU Study of the chemistry in the disk/envelope system of Solar-like protostars (FAUST, PI: Yamamoto, S.). The main goal of FAUST is to investigate the gas chemical composition of the environments surrounding young, Sun-like protostars including their embedding envelopes, their outflows, and disks (see Codella et al. 2021 for further details).

The observations aimed at L1527 were centered at right ascension $\alpha(2000)$ = 04h39m53.878s and declination $\delta(2000) = +26°03'09.56''$. B3 observations were run on December 14, 2018 and August 25, 2019 with the 12m array in ALMA configurations C43-3 and C43-6, respectively. The baselines of these observations thus ranged 15-2500 meters. ALMA observed L1527 in the 93-95 and 104-108 GHz ranges. The source was observed for approximately 35 minutes in B3, for a continuum sensitivity of 0.025mJy. B6 observations were performed between October 20th, 2018 and December 15, 2019 with both the 7m and 12m arrays. The baselines of the 7m array ranged from 8.9 to 48.9 meters. The 12m array observations were taken in configurations C43-2 and C43-5, with baselines ranging from to 15-314 meters and 15-1400 meters, respectively. ALMA observed in the 244-247 and 258-262 GHz ranges with a spectral resolution of approximately 62.5 MHz. The source was observed for approximately 75 minutes in B6, for a continuum sensitivity of 0.026mJy.

The FAUST data were calibrated using a modified version of ALMA pipeline version 42866, using the Common Astronomical Software Applications (CASA, McMullin et al. 2007), version 5.6.1-8. This included a correction for errors introduced by the per-channel normalization of data by the ALMA correlator[1]. Line-free Local Standard of Rest Kinematic (LSRK) frequency ranges were identified by visual inspection and averaged per spectral window, and initial continuum images were produced for each separate ALMA configuration. These were then used as initial models for subsequent per-configuration phase-only self-calibration, followed by amplitude and phase self-calibration. Great care was taken to ensure that the models were as complete as possible to avoid changing the overall flux density scale of the data when doing amplitude self-calibration. L1527 is sufficiently strong that per-integration phase-only self-calibration was possible, while for amplitude self-calibration per-scan self-cal was used. The per-configuration datasets were then aligned across configurations in both phase and amplitude, again using a self-calibration technique. Corrections to the amplitude scale of up to 10% were found to be needed for some datasets. Improvements in the dynamic range (peak/RMS away from emission) of more than an order of magnitude for the final images were achieved using this technique for setup 1 and 2. The improvement for setup 3 was $\sim 35\%$. Finally, we imaged the visibilities with the CASA *tclean* function, using the hogbom deconvolver, a "briggs" weighting scheme with robust parameter set to 0.5. The resulting beam in B3 is $0''.44$x$0''.27$ wide with PA=-29°; while the synthesized beam in B6 is $0''.42$x$0''.28$, PA=19°. We present the new

[1]https://help.almascience.org/kb/articles/what-errors-could-originate-from-the-correlator-spectral-normalization-and-tsys-calibration

continuum maps in Fig. 3.1 and Fig. 3.2.

3.3 Additional observations

We gathered ALMA Band 3 (B3) observations of L1527 spanning from 2017 to 2020. Given the different scientific aims of the projects, the data collected with the 12-m array has a resolution between 0.″09 (project 2017.1.00509.S, PI: Sakai, N.) and 2.″4 (project 2015.1.00261.S, PI: Ceccarelli, C.). The sensitivity of the 12-m array observations that have been used in this work ranges from 0.03 to 0.06 mJy and the total time on source is ∼210 minutes. The frequency of the side bands ranges from 85 to 115 GHz.
The 7-m array has been pointed at L1527 in B3 for a total ∼102 minutes (projects: 2016.1.01541.S and 2018.1.00799.S; PIs: Harsono, D. and Pineda, J.). The observations have resolutions 12.″0 - 13.″2 and have been carried out in a range of frequencies from 92 to 105 GHz with sensitivities of 0.3-0.6 mJy.

L1527 has been observed in Band 4 (B4) throughout several months in 2016 and 2018. The data collected with the 12-m array has a resolution between 0.″1 (project 2016.1.01203.S, PI: Oya, Y.) and 2.″1 (project 2016.1.01541.S, PI: Harsono, D.). The sensitivity of the 12-m array data that have been used in this work ranges from 0.03 to 0.3 mJy and the total time on source is ∼82 minutes. The frequency of the side bands ranges from 138 to 154 GHz.
The 7-m array observed L1527 in B4 for a total ∼107 minutes (projects: 2016.1.01541.S and 2016.2.00171.S; PI: Harsono, D.). The observations have resolutions 7.″8 - 9.″1 and have been carried out in a range of frequencies from 144 to 154 GHz with sensitivities of 0.2-0.4 mJy.

ALMA Band 6 (B6) observations of L1527 span from 2013 and 2020. The data collected with the 12-m array has a resolution between 0.″2 (projects 2012.1.00193.S, 2013.1.00858.S and 2013.1.01086.S; PIs: Tobin, J.; Sakai, N. and Koyamatsu, S.) and 1.″1 (project 2018.1.01205.L; PI: Yamamoto, S.). The sensitivity of the 12-m array observations that have been used in this work ranges from 0.03 to 0.09 mJy and the total time on source is ∼403 minutes. The frequency of the side bands ranges from 218 to 263 GHz.
The 7-m array observed L1527 in B6 for a total ∼85 minutes. The observations have resolutions spanning 4.″3 - 5.″9 (projects: 2016.2.00117.S and 2018.1.01205.L; PIs: Yoshida, K. and Yamamoto, S.) and have been carried out in a range of frequencies from 216 to 262 GHz with sensitivities of 0.4-1.0 mJy.

In Band 7 (B7), L1527 has been observed from 2014 and 2018. The data collected with the 12-m array has a resolution between 0.″075 (project: 2016.A.00011.S, PI: Sakai, N.) and 0.″5 (project 2011.0.00604.S; PI: Sakai, N.). The sensitivity of the 12-m array observations that have been used in this work ranges from 0.06 to 0.2 mJy and the total time on source is ∼155 minutes. The frequency of the side bands ranges from 218 to 263 GHz.

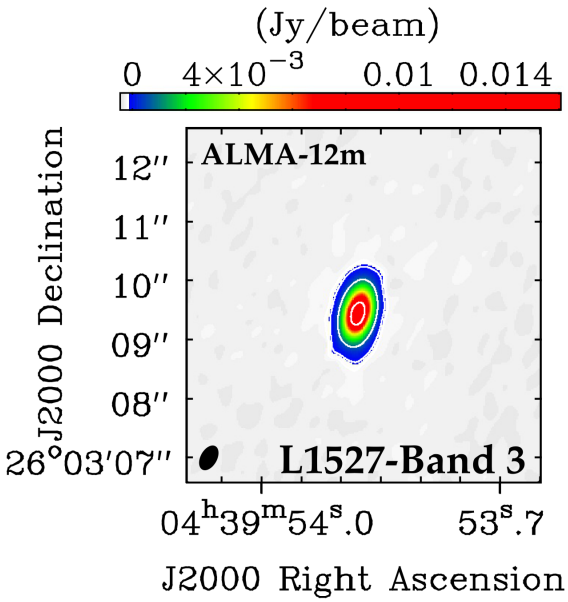

Figure 3.1: Zoom in to the inner 6.″0 of the ALMA B3 continuum of L1527 obtained with the 12m array setups of the FAUST Large Program. The color map shows only flux densities higher than $\sim 5\sigma$, with the white contours highlighting the $[5, 15, 30]\sigma$ levels. The ALMA synthesized beam is shown in black in the lower left corner.

The 7-m array observed L1527 in B6 for a total ∼46 minutes during project 2016.2.00117.S (PI: Yoshida, K.). The observations have resolutions 3.″1 and have been carried out in a range of frequencies from 352 to 363 GHz with sensitivity of 1.44 mJy.

3.3.1 Data reduction and self-calibration

Since we work with data taken at several frequencies, we avoid frequency smearing by splitting datasets with a relatively large frequency offset. This is especially important in B3. Thus, we split its datasets into two groups. This way, after calibration, we work with five final frequencies: 88, 100, 141, 249, and 348 GHz. These frequencies roughly correspond to 3.4, 3.0, 2.1, 1.2 and 0.88 mm wavelengths.

The first round of calibrations was performed using the standard CASA pipeline methods provided by the ALMA Regional Centers (ARC). Considering the data were acquired over a period of several years, different versions of CASA were used for these calibrations. The version used for each dataset is listed in Table 3.2. This first round includes system temperature, phase, amplitude, and bandpass calibration, along with corrections to account for atmospheric water vapor.

We carried out further data reduction and calibration steps using CASA version

6.2.1.7. First, the ALMA cubes for each execution block were inspected and additional flagging was applied when necessary, that is to mask out spectral lines. We are only interested in the continuum emission, thus, to speed up further operations, we channel-averaged the spectral windows of every execution block. We used a common width to level out the S/N among spectral windows and we were careful to avoid bandwidth smearing effects by limiting the averaging based on the maximum baselines and spectral window bandwidth (Bridle & Schwab, 1999). Before combining the datasets for the analysis, we performed several additional operations. First, we ran the *statwt* CASA routine in order to fix the visibility weights. This is especially important for datasets from old ALMA Cycles that have been reduced with CASA 4.2.1 or earlier versions[2]. We then imaged the averaged-channel visibilities with the *tclean* task and fitted a Gaussian with *imfit* to pinpoint the maximum of the emission. Next, we used the *fixvis* function to shift the phase center to the position of the peak of L1527 at the epoch of every observation. Since the

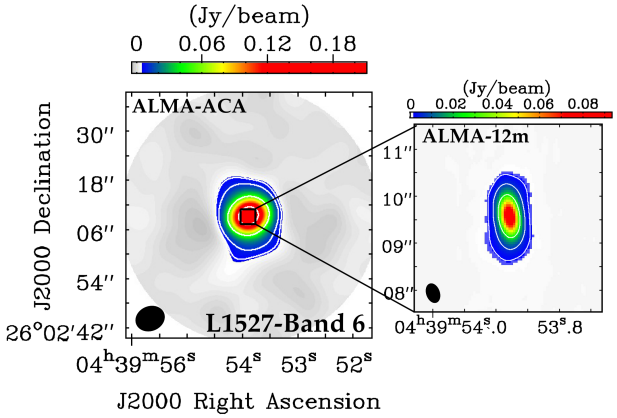

Figure 3.2: ALMA B6 continuum of map of L1527 obtained imaging the 7m array setup of the FAUST Large Program. The inner 4″.0 inset has been imaged using ALMA B6 FAUST 12-m array setup data. The color map for the ACA image shows only flux densities higher than 5σ, and the white [5, 10, 50, 150]σ level contours. The color map of the 12m-array image shows only flux densities higher than 20σ, and the white [20,60,100]σ level contours. The synthesized beams are shown in black in the lower left corner in both cases. We note that the colorbar is different for each map.

target coordinates were slighlty different across datasets, we also set the source sky position (in the metadata) to a common center across execution blocks using *fixplanets*. Once the coordinates of each dataset were phase-centered and aligned following this procedure, we rescaled the fluxes following the procedure of Andrews et al. (2018): for every frequency, selected a range of uv-distances where the uv coverage of two datasets overlaps, binned the visibilities in that range, and compared them to obtain a rescaling factor where the visibilities overlapped. The rescaling factors were in a 1-15% range for all execution blocks. The rescaling correction was then computed using the task *gencal* and the rescaling itself

[2]https://casaguides.nrao.edu/index.php/DataWeightsAndCombination

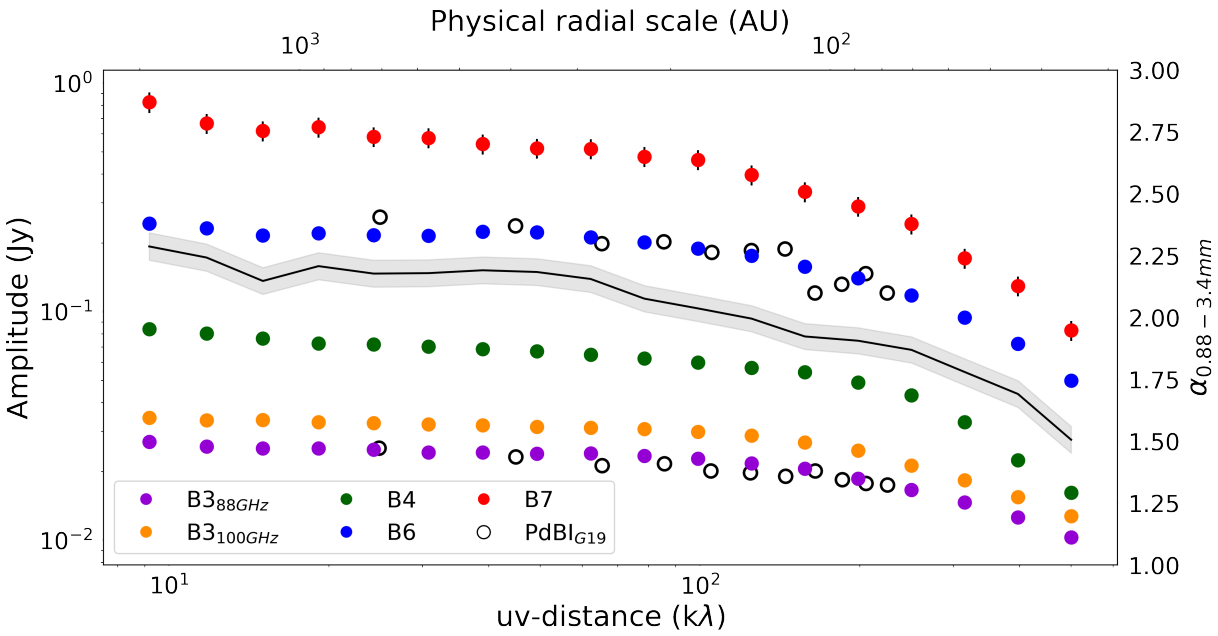

Figure 3.3: L1527 ALMA 88 GHz (purple), 100 GHz (orange), 141 GHz (green), 249 GHz (blue), 348GHz (red) visibility amplitudes up to 1000 kλ. We also compare the 94 and 231 GHz observations (white points) performed with the Plateau de Bure Interferometer (PdBI) and anlayzed in Galametz et al. (2019). The slope of our observed Spectral Energy Distribution (black line) has been obtained by fitting a line to the fluxes at all wavelengths in each uv-distance bin. While $1.5 < \alpha_{fit} < 2.5$, most of the contribution to the flux - and to α - at any uv-distance is due to the disk (see Section 3.5).

was achieved by applying the correction factors with *applycal*. We report the rescaling factors in Tables 3.2 and 3.3.

Imaging during self-calibration was performed using the CASA task *tclean* with the hogbom deconvolver (Högbom, 1974), and 'briggs' weighting with robust = 0.5, which yields an optimal combination of resolution and sensitivity. Based on this model, we then computed the phase corrections on each execution block using *gaincal* and applied them with *applycal*. This step aimed to correct phase errors between executions and between spectral windows. We repeated this procedure three times. In the first round, we set the solution interval of *gaincal* to *inf*, combined the scans within each execution block and set gaintype = "G", that is the gains were determined for each polarization and spectral window. In the second and third rounds, we combined the spectral windows of each block, shortened the solution intervals to 60 and 10 seconds, respectively, and set gaintype = "T", to obtain one solution for both polarizations. The self-calibration yielded peak S/N improvements in the range 10-500 % when evaluated on the images obtained with the combined datasets. We did not find any appreciable improvement in the noise and signal-to-noise properties for phase-only self-calibration steps with even smaller time intervals.

At this point, we combined the corrected datasets using the *concat* CASA task.

Since we analyze extended emission, we estimated the effect of the antennas primary beam (PB) correction on the recovered flux. In B7, the ALMA 7m and 12m antennas PB full width at half maximum is 33.″0 and 19.″0, respectively. This results in a loss of about 10% of flux at 20 kλ (1000 au scales), for the 12m antennas. This only marginally affects the recovered spectral index we are interested in, increasing it by a factor of <5% even at the largest scales.

3.3.2 L1527 as seen in the visibility space

The final binned visibility amplitudes obtained with our data reduction and self-calibration are illustrated in Fig. 3.3. We also show that the associated spectral index lies in the range $1.5 < \alpha_{0.88-3.4mm} < 2.4$. This low α is not surprising as the disk emission contribution dominates at every uv-distance (see Section 3.4), thus the total spectral index is strongly influenced by the optically thick disk (cfr. Section 3.5).

Among other class 0/Is of the CALYPSO survey, the continuum emission of the envelope infalling on L1527 has been studied in Galametz et al. (2019), hereafter G19, who used PdBI observations at 1.3 and 3.2 millimeter. The data they used spans a range in uv-distances from 20 to 200 kλ at both frequencies. Fig. 3.3 shows a comparison between the ALMA observations we used and G19's PdBI fluxes (white points).

We cut the ALMA datasets at the shortest common baseline, set by B7 at 9.8 kλ, hence a Maximum Recoverable Scale (MRS) of roughly 26.″0, or 3500 au at the distance of the source. We aim to more robustly determine the spectral and dust-emissivity indices of the source by extending the frequency range, that dominates the error on α (see Section 3.5). Furthermore, a denser sampling of frequencies is critical to understand the optical depth of the source across wavelengths, which is vital to constrain where the spectral index is a good proxy for dust grain sizes. On top of enriching the studied frequency range, we used a combination of ALMA and ACA data to study the dust continuum emission with high S/N at scales 2 times larger than G19, toward both shorter and longer baselines. In fact, although our primary attentions are devoted to the envelope, long-baseline visibilities are of great importance if we want to properly model the compact emission. G19 subtracted a constant amplitude ($F_{200k\lambda}$) from each visibility at the two frequencies, assuming an unresolved disk that would contribute a constant flux at baselines shorter than 200 kλ ($\sim$1.″0, or 140 au).

Considering the wider uv-coverage of the data we used (9.8-1000 kλ), we can more precisely model and subtract the compact emission by fitting a Gaussian component within a model that separately accounts for envelope and disk (see Section 3.4). This procedure also makes a significant difference when computing the errors on α and β, which in turn depend on the relative errors of the amplitudes. Since the PdBI amplitudes in G19 were roughly constant and only slightly above $F_{200k\lambda}$, the relative error on the fluxes after the

subtraction of $F_{200k\lambda}$ became large already at a uv-distance of $\sim$ 100 kλ. Given the high S/N of our combined datasets, the relative flux uncertainty remains relatively contained after disk subtraction (see Fig. 3.6). In the upcoming Section, we lay out the methods we followed to model the full visibilities and subtract the disk component to obtain an envelope-only spectral index.

3.4 Disentangling disk and envelope emission

To investigate dust properties in the envelope of L1527, we worked in the visibility (u, v) plane. This approach has the main advantage of keeping the analysis clear of the artifacts and non-linearity from which image reconstruction algorithms suffer.

The visibility amplitudes are the combined flux of disk and envelope at all uv distances. Since we are mainly interested in studying the spectral index of the envelope, we have to disentangle the compact emission flux from the extended one. Hence, we need to fit the data with a model appropriate for a compact disk that, at the same time, self-consistently accounts for excess emission at the shortest baselines (largest physical scales).

Brightness profiles of protostellar envelopes of diverse class 0/I YSOs have been found to be well fit by broken power laws with exponents in the (-2.5,-1) range (Plummer 1911, Motte & André 2001, Shirley et al. 2002, Maury et al. 2019). Thus, we consider a geometrical model in which a Gaussian, that will trace the compact emission, is summed to a power law (Plummer profile):

$$I_{TOT}(R) = rI_0 \cdot e^{-\frac{R^2}{2\sigma^2}} + \frac{(1-r)I_0}{\left(1+\left(\frac{R'}{R_i}\right)^2\right)^{\frac{p-1}{2}}}. \tag{3.1}$$

The Gaussian is defined by a peak $f_0' = rI_0$, a width σ, an inclination inc and position angle PA. The envelope power law has peak flux $f_0'' = (1-r)I_0$ and three free parameters: R_i, R_{out}, p. These are such that the envelope emission is constant within a radius R_i, it follows Eq. 5.1 between R_i and R_{out} and it is null beyond R_{out}. The peak fluxes of the extended and compact emission are modulated by the free parameter $0 < r < 1$. We have performed the fitting with `galario`, a library that exploits the power of modern graphical processing units (GPUs) to accelerate the analysis of observations from radio interferometers (Tazzari et al., 2018). In our framework, `galario` would compute a model image given our total profile, then it would Fourier-transform it into synthetic visibilities and sample them at the uv-points covered by the antenna configurations with which the observations were performed. Then, it would run a minimum-χ^2 fit between the data and the model visibilities. The 10 fit parameters were the flux amplitude I_0 and the r factor; the width σ, the inclination (inc) and position angle (PA) of the Gaussian; the inner and outer envelope radii, R_{in} and R_{out}, and the power law exponent p. Finally two parameters,

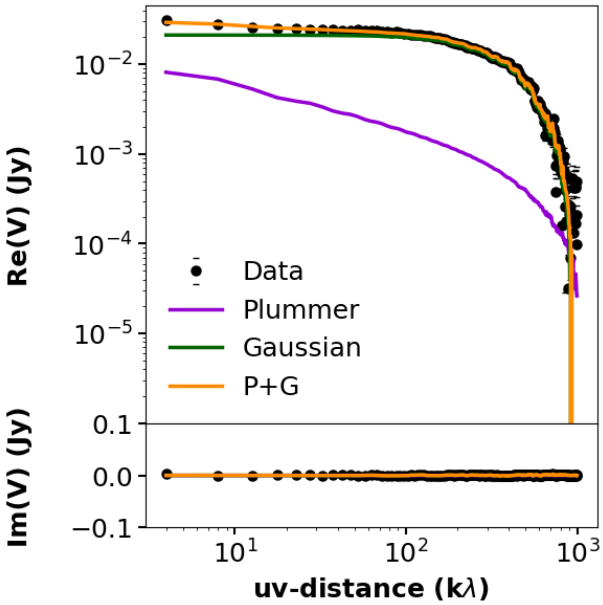

Figure 3.4: Final Plummer+Gaussian best fit (orange) is overplotted on the real part of the visibilities for the B3 (88 GHz) data (upper panel, black points). The fit on the imaginary is in the lower panel. The Plummer only (violet line) and Gaussian only (green line) components of the total model are also shown. In the case of the 88 GHz emission, the disk contributes up to 98% of the total emission. The wiggles in the model are due to its sampling on the uv points of the observations.

dRA and dDec, fit the offset of the peak from the phase center. For each fit, 80 walkers were set to run for 3,000 burn-in steps and 10,000 more steps after the burn-in stage. The best fit results are summarized in Table 3.8.3. We show, as an example, the single best-fit model for the B3 88 GHz data, decomposed in its power law and Gaussian components (Fig. 3.4). We report the rest of the fits in Figures 3.18, 3.19, 3.20, 3.21, along with the best fit parameters summary (Table 3.8.3) in Appendix 3.8.3. In particular, we find that the compact emission has a deprojected width of $0\farcs15 < \sigma_{fit} < 0\farcs28$ on the sky, depending on the Band. If we define the radius of the disk to be the 2σ contour of the Gaussian component, then $R_{disk} \sim 75$ au in B7, consistent with what was found in the kinematical analysis of Aso et al. (2017). In addition, the Gaussian component contributes to a minimum of 75% in B4, up to 98% in B3 (see Appendix 3.8.3 for the detail). The derived disk fluxes are listed in Table 3.4. This fitting procedure allows us to disentangle disk and envelope emission and study the spectral energy distribution of the disk and envelope separately in the next section.

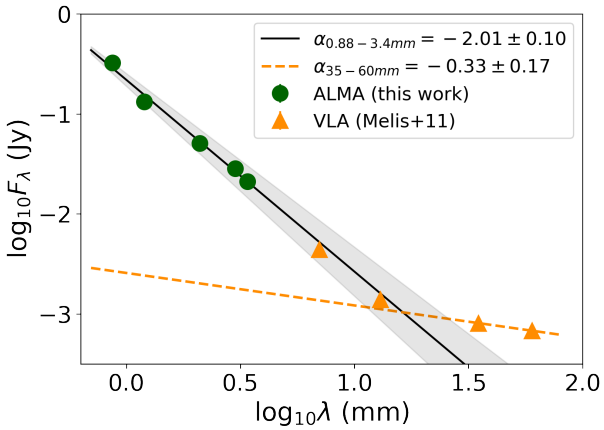

Figure 3.5: Spectral energy distribution of the circumstellar disk around L1527. Our galario best-fit total flux of the compact Gaussian component for each band, in green, along with longer wavelength VLA measurements from Melis et al. (2011) (see Table 3.4). The protoplanetary disk of L1527 is optically thick up to 3.4 mm ($\alpha_{B7-B3} \sim 2$), likely due to its edge-on nature.

3.5 Spectral and dust emissivity indices

In this Section, we first derive the spectral indices of the observed emission at both disk and envelope scales, then we discuss to what extent these can be used to evaluate dust grain properties.

3.5.1 The circumstellar disk

To study possible early dust grain growth in the envelope of L1527, we made use of long baseline data to properly model the compact emission to be subtracted from the short baseline amplitudes. In doing so, we obtained estimates of the flux of the compact ($0.15" < \sigma_{fit} < 0.27"$) emission of L1527 in four ALMA bands. We here show the spectral energy distribution of the disk we obtained by combining and modeling all suitable ALMA archival data for L1527 (Figure 3.5, Tab. 3.4). To offer a more comprehensive view to the reader, we extended the range of wavelengths by including literature Very Large Array (VLA) measurements from Melis et al. (2011), up to 6 cm.

Fitting the SED in the 0.88 to 7-millimeter range using our measurements along with the values of Melis et al. (2011), we find an optically thick disk with $\alpha = 2.1 \pm 0.1$. This is not surprising: the disk orbiting L1527 is very inclined ($i \sim 80°$), almost edge-on to the sky: this geometric factor contributes to increase its optical depth along our line of sight. Furthermore, Ohashi et al. (2022) used high-resolution, multiple frequency observations of the disk and found that the brightness temperature toward the mid-plane of the disk obtained by converting the flux at 0.88 mm (42 K) is much lower than that found at 2 and

3 mm (60 K and 90 K, respectively). This progressive increase in brightness temperature with wavelength means that the disk is at least partially optically thick at 0.88 and 2 mm.

The high optical depth of the circumstellar disk of L1527 prevents us from concluding anything about its dust grain properties based on the spectral index alone. Finally, the 3.5 and 6 cm fluxes can be used to estimate the free-free emission that affects the measurements at the shorter studied wavelengths. The slope at these longer wavelengths

Table 3.4: L1527 disk SED built with ALMA (this work) and VLA (Melis et al., 2011) observations.

ν (GHz)	λ (mm)	Flux density (mJy)	Reference
348	0.86	324 ± 29	this work
249	1.2	132 ± 9	this work
141	2.1	52 ± 3	this work
101	3.0	28 ± 0.6	this work
88	3.4	21 ± 0.5	this work
43.5	7.0	4.4 ± 0.6	Melis et al. (2011)
22.5	13.3	1.4 ± 0.1	Melis et al. (2011)
8.5	35.2	0.81 ± 0.03	Melis et al. (2011)
5	60	0.68 ± 0.04	Melis et al. (2011)

is $\alpha_{35-60} = 0.33 \pm 0.17$, as reported in Fig. 3.5 and is compatible with what is expected for free-free emission (Panagia & Felli, 1975). However, it is worth noting that Melis et al. (2011) showed how the 3.5 cm flux of L1527 is highly variable in time. Indeed, they listed eight measurements (references therein) at this wavelength taken between 1996 and 2010 where the 3.5 cm flux shows significant variations between 0.55 and 0.81 mJy, with errors of 1-5%. In Fig. 3.5, we show Melis et al. (2011) points taken at roughly simultaneous epochs (2010 July 30th). The contribution of the free-free emission is lower than 10% in B3 and lower than 1% in B7.

3.5.2 The envelope

We investigate changes in the spectral index throughout the spatial scales of the envelope in the visibility plane. Starting from the common shortest baseline of ~ 9 kλ, we log-uniformly bin the visibilities across the available uv-distances and then measure the spectral index in each bin. Since we are interested in studying the spectral index of the envelope, we have subtracted the galario best-fit Gaussian component of our model (see Section 3.4) from the data. This way, the remaining flux is the contribution of the extended emission only (Fig. 3.6).

Here, the amplitude and related error bars account for both statistical and calibration uncertainties. We set the latter to 10% for B7 and 5% for bands 3, 4 and 6, following

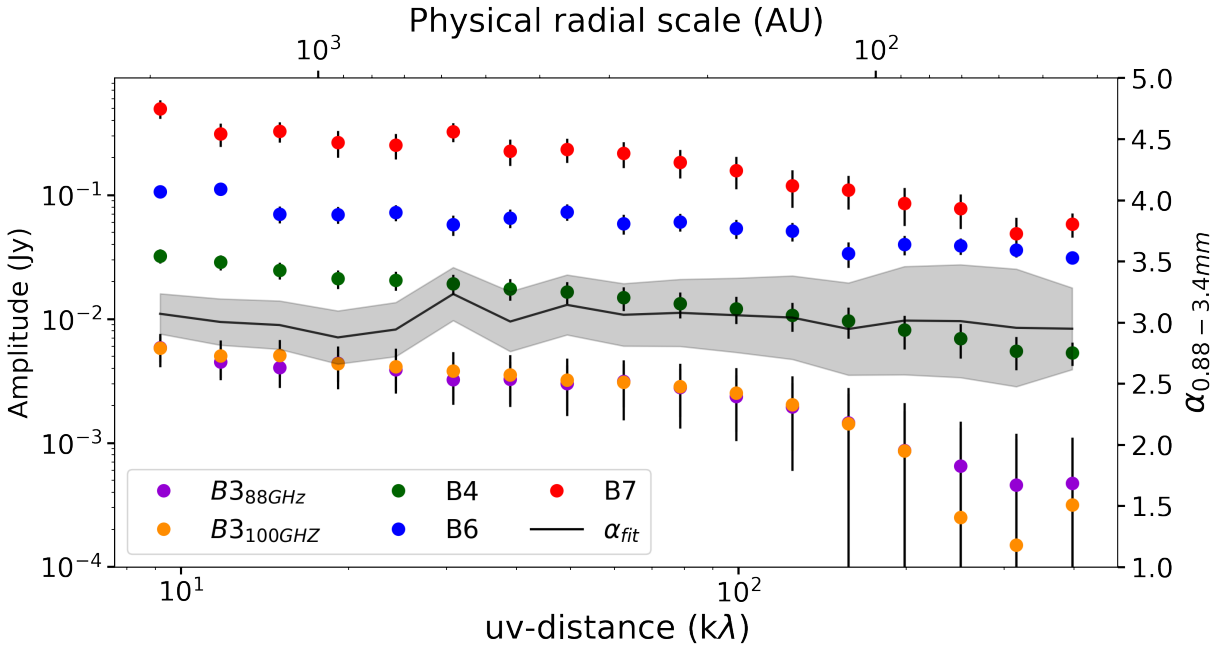

Figure 3.6: L1527 ALMA B3 (orange), 4 (green), 6 (blue), 7 (red) visibilities after removal of the fitted compact Gaussian component. The spectral index of the envelope emission (gray) has been obtained by fitting a line to the fluxes at all wavelengths in each uv-distance bin.

the prescriptions of the ALMA Handbook and on-sky analysis (respectively; Remjian et al., 2019; Francis et al., 2020b). While the error on α is dominated by flux calibration errors on the observed amplitudes (see Fig. 3.3), the relative amplitude error becomes important after the subtraction of the disk model. Not only is the relative error overall larger, it also visibly increases with uv-distance. This effect is clear in Fig. 3.6. Using almost every archival dataset for this source, we made an effort to maximize the S/N of the faint envelope of L1527 in what is its deepest continuum analysis.

To make the best use of our multiwavelength data, we fitted a line to the fluxes along all wavelengths in each uv-distance bin and we more robustly determined the spectral index. Since we combined a number of datasets for each band, the frequency of each flux point in each bin is taken to be the weighted average of the frequencies in that bin. The uncertainty on the spectral index obtained by fitting all bands is the error on the slope obtained with the weighted linear regression. Figure 3.6 shows that the fitted spectral index of the envelope of L1527 appears roughly flat in the studied range that spans from ~ 2000 down to 50 au, $\alpha \sim 3$. For completeness, we show the spectral indices computed between adjacent bands in Appendix 3.8.2. These are flat as well, although they show systematic differences in their average value, which clearly shows the need for a multifrequency (>2) approach.

Finally, we measured the spectral index in different angle bins on the sky, after removal of the compact component. We divided the uv-plane into three different regions: the envelope ($-20° < PA < 20°$), the outflow ($70° < PA < 110°$) and the cavity walls (the remaining zones). We do not observe any significant difference among the three spectral indices at scales larger than 200 au (Fig. 3.7).

3.5.3 Dust emissivity index

The simple link between the exponent of the dust opacity power law and the spectral index, $\beta = \alpha + 2$, only holds for optically thin emission when the RJ approximation is valid. Thus, before interpreting the values of the envelope's spectral index in terms of dust properties, we check whether these necessary conditions are met at the wavelengths we probe. First, we evaluate the optical thickness of the emission. The specific intensity I_λ, or flux per unit solid angle that we receive from the source (F_λ/Ω) can be generally expressed as an absorbed black body:

$$I_\lambda = \frac{\mathrm{F}_\lambda}{\Omega} = \left(1 - e^{-\tau_\lambda}\right) \cdot \mathrm{B}(\mathrm{T}_{dust}) \tag{3.2}$$

where the optical depth τ_λ modulates the difference between the observed flux and the optically thick black body emission. If $\tau_\lambda \ll 1$, then $F_\lambda/\Omega \sim \tau_\lambda B(T_{dust})$, while if $\tau_\lambda \gg 1$, then the observed emission tends to a black body spectrum.

To evaluate the optical thickness, we consider a typical dust temperature prescription for a centrally illuminated protostellar envelope (Shu 1977, Butner et al. 1990, Terebey et al. 1993, Motte & André 2001):

$$\mathrm{T(R)} = 38\mathrm{L}^{0.2}\left(\frac{R}{100au}\right)^{-0.4} \mathrm{K}. \tag{3.3}$$

Considering this relation and the range of scales that we probe, the temperature gets as low as 10 K in the outermost radii of the envelope ($\sim$ 2000 au). We find that, even at the shortest of our wavelengths, the envelope emission is optically thin at all scales as $F_{0.88mm}/\Omega < B(T_{dust})$ by a factor of 10 (Fig. 3.8). The optically thin regime is naturally satisfied at longer wavelengths.

Secondly, we check if the RJ approximation is valid. Based on the same temperature profile for the dust, in the cold outskirts of the envelope ($\sim$ 20 K at 500 au), $h\nu/k_BT \sim 0.8$ at our mean B7 frequency of 348 GHz. This violates the RJ condition $h\nu/k_BT \ll 1$. Thus, while the envelope of L1527 is in the optically thin emission regime, it does not satisfy the RJ approximation and $\beta \neq \alpha - 2$.

Thus, using the same profile, we can obtain a temperature-corrected β profile as:

$$\log_{10}\left[\frac{\mathrm{F}_\nu}{\mathrm{B}_\nu(\mathrm{T})}\right] = \beta \cdot \log_{10}(\nu) + \mathrm{A}, \tag{3.4}$$

where A is a constant (similarly to what done in G19, but for multiple frequencies). Figure 3.9 shows how the dust emissivity index is nearly $\alpha - 2$ for the smaller spatial scales, where T(R) is large enough, while it starts to show discrepancies after 200 au (where T$\sim$ 25 K). We also investigated the effects on β of changing the temperature profile's radial power law exponent. We found that exponents in the interval [-0.3,-0.6] do not affect our conclusions. We exclude steeper profiles as they lead to unreasonably low values of the temperature at the studied scales. The error on the dust emissivity index has been considered to be the same one that affects the spectral index since we are assuming an exact temperature profile, thus $\Delta\alpha = \Delta\beta$.

In Figure 3.9, we report the measured β as a function of uv-distance, and we overplot a linear fit to the points. We have run the fit by means of the Bayesian method described in Kelly (2007) and implemented in linmix[3]. The priors were uniformly distributed. We plot some single chain results in Fig. 3.9, along with the best fit model. We find evidence for an outward increasing β, rising from 0.8 to 1.6 between 50 and 2000 au radial scales:

$$\beta(\mathrm{R}_{au}) = 0.37^{+0.17}_{-0.16} \cdot \log_{10}(\mathrm{R}_{au}) - 0.23^{+0.45}_{-0.46}. \tag{3.5}$$

In turn, Eq. 3.5 yields:

$$\beta(\mathrm{R} = 300\mathrm{au}) = 1.15 \pm 0.08. \tag{3.6}$$

These measurements represent tentative evidence for dust optical properties variations throughout the envelope of L1527. Furthermore, low β at scales lower than $\sim$ 300 au are consistent with the presence of submillimeter sized grains in the inner envelope.

3.5.4 Literature comparison

G19 studied the envelope continuum emission of a few class 0/I sources, including L1527. Here, we briefly compare our findings to theirs. First, the wide uv-distance range of the datasets we used allowed us to model the disk emission spatial profile, while only a constant amplitude was subtracted in the amplitudes in G19, who assumed an unresolved compact disk. This spatial modeling is important to properly subtract the compact emission from the total amplitudes and work out the rest of the analysis on the flux of the envelope alone.

G19 reported a slope of β of 0.18 $\pm$ 0.39. Noticeably, this flat β profile of G19 is consistent with what we observe across the same region they studied, 70-700 au radii. Extending the studied scale by a factor 2, we are able to explore the outer envelope and determine the positive outward gradient of Eq. 3.5. At the outer probed radii ($\sim$ 2000 au), the derived values for β are consistent with typical ISM measurements. Secondly, G19 reported a fitted $\beta_{500au} = 1.41 \pm 0.16$ while we find $\beta_{500au} = 1.15 \pm 0.08$ based on Eq.3.4. These improvements have been obtained thanks to higher sensitivity data as well as the extension of the studied frequency ranges.

[3]https://github.com/jmeyers314/linmix

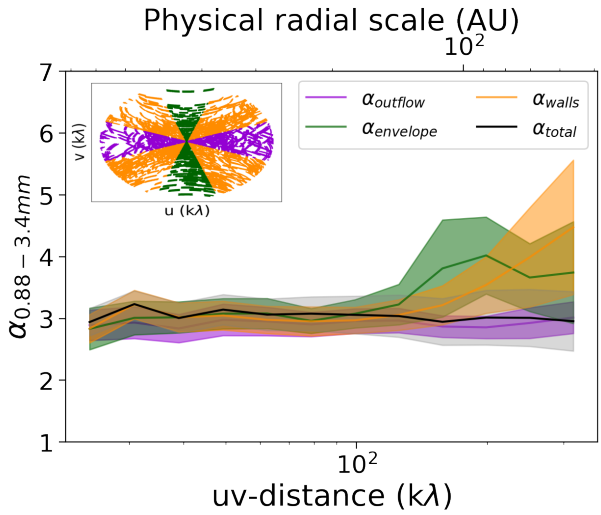

Figure 3.7: Spectral index of L1527 as measured along directions of the outflow (violet) and envelope (green), cavity walls (orange). The total α is also plotted (gray). The way the uv-coverage has been sampled is shown in the upper inset (B7 as an example). The scarce uv-coverage of the ACA B7 observations cause some bins to be undefined at the short baselines, hence the gaps. In all cases, α is only computed starting from 20 kλ.

3.6 Discussion

We here discuss our results in further detail, how they compare with existing theoretical and observational literature, and the caveats relevant to our analysis.

3.6.1 Dust growth in envelopes is challenging

The low β value we measured at scales of a few hundred au from L1527 is a tentative evidence for grown dust grains in the inner envelope of the class 0/I YSOs L1527. If solids indeed grew in the envelope, this would represent a shift in the usually assumed initial conditions for planet formation, which only include $< 0.25\mu$m grains at such scales. However, a challenge to our measurements rises when trying to link these low β with the in situ formation of relatively large dust grains in the envelope environment. Indeed, theoretical studies of grain agglomeration have not been able to reproduce such growth in envelope-like environments. The numerical simulations of Ormel et al. (2009), Lebreuilly et al. (2023) and Bate (2022) have shown that it is very unlikely that solid dust grains could grow larger than about 1 μm at the typical densities and timescales of envelopes such as the one infalling on L1527 and its young disk. These works included a thorough treatment of grain-grain collision energetics, accounting for relative grain velocities due to turbulence, Brownian motions, ambipolar diffusion and hydro-dynamical drift. Additionally, Silsbee et al. (2022) proposed a simpler, analytical model to place strict upper bounds on the maximum grain size that can be reached in extended protostellar envelopes. They considered a

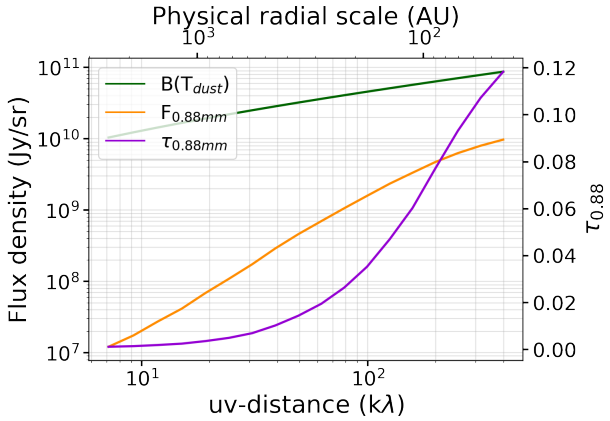

Figure 3.8: Flux density of the envelope emission in ALMA B7 (orange) is consistently lower by at least an order of magnitude than a black body spectrum of emitting dust with a radial temperature profile $T \propto r^{-0.4}$ (green). The optical depth (violet) is much smaller than 1 at all envelope scales, thus we can consider the envelope emission at 0.88 mm as optically thin.

coagulation model for the growth of spherical, yet fractal grains whose relative motions are driven by turbulence and the fragmentation of which happens for velocities above a quite generous threshold of $v_{rel} = 10$ m/s. Considering that the optical properties of dust grains depended on the product of their radius (a) with a filling factor (or porosity) ϕ, they find that it is not possible to grow grains with an optical radius $a_{opt} = a\phi$ of 1 millimeter, in typical protostellar envelope conditions. They find that, in the 10^5 yr lifetime of a typical class 0 source whose volume density is approximately 10^7 cm^{-3}, grains grow up to only about 2.5 μm.

3.6.2 Grain size, composition and temperature effects on dust opacity index

While these theoretical works strongly disfavor the in situ growth of (sub)millimeter dust grains in the envelopes of young objects, the observational evidence of the low dust emissivity indices found therein (Kwon et al. 2009, Miotello et al. 2014, Galametz et al. 2019) remains largely uncontested.

First, an objection to the link between low β and large grains might arise from the dependency of the dust-emissivity index on other dust properties. In fact, the dust emissivity index is sensitive to changes in dust composition, porosity and the presence (or absence) of an icy mantle (e.g., Beckwith & Sargent 1991, Testi et al. 2014). Although variations in β are evident and well-characterized across different grain properties, $\beta < 1$ remains a strong evidence for the presence of (sub)millimeter grains in the studied distribution (Natta & Testi 2004, Draine 2006, Natta et al. 2007, Testi et al. 2014 and Köhler

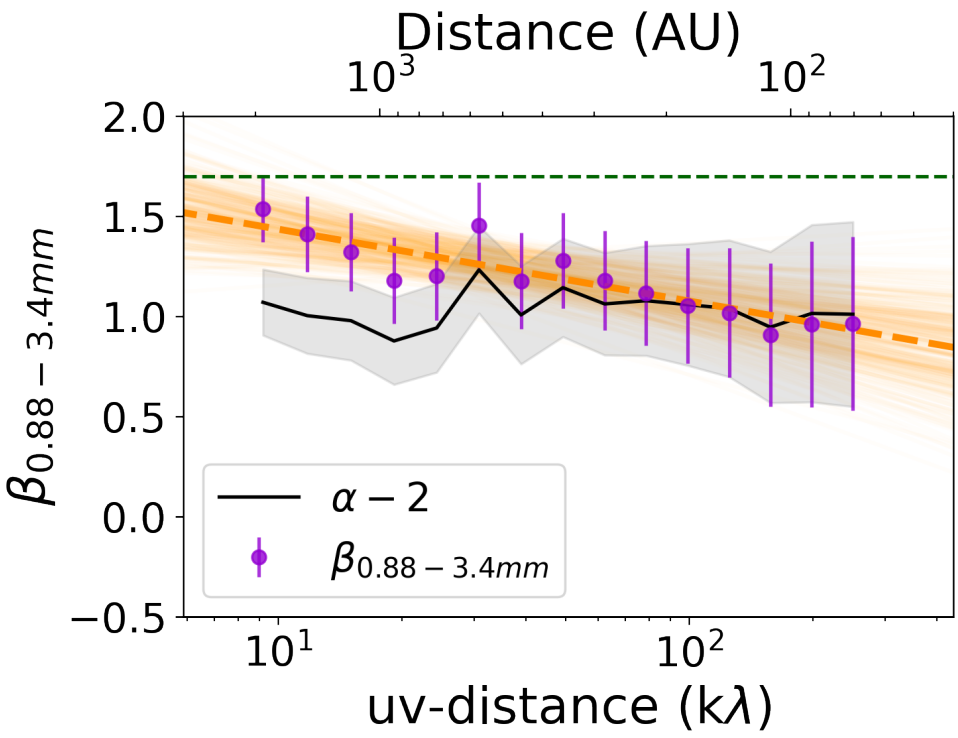

Figure 3.9: Dust emissivity index (purple dots) of the envelope of L1527 as a function of radial scales. The solid dots indicate the β computed fitting all available bands. The dashed orange line is the best model for the profile of β along scales, while the light orange lines are a subsample of the results of some chains of the fitting procedure. The black line shows the approximation in which $\beta = \alpha_{fit} - 2$, where α is the slope of the SED considering all available bands.

et al. 2015, Ysard et al. 2019). Thus, although further laboratory studies will be necessary to more precisely interpret β in terms of both grain sizes and compositions, dust particles significantly larger than what expected for the typical ISM grains (0.2-2 μm) remain a robust explanation for our observations.

Secondly, if the compact emission contribution is not properly subtracted from the visibilities, a bias can be introduced when determining the slope of the SED. Previous studies (e.g., Miotello et al. 2014 and G19) have subtracted the compact emission assuming unresolved disks that would only contribute an offset at all uv-distances. They determined this value by fitting a constant to the visibilities amplitudes after some arbitrary long baseline and subtracted it from the visibilities at shorter uv-distances. Here, we have tried to more properly model and subtract the disk emission as explained in Section 3.4.

Finally, perhaps the temperature correction discussed in Section 3.5.3 could be

revisited. If the emission is optically thin, Equation 3.4 reduces to:

$$\beta = \alpha - \frac{d\log(B_\nu(T))}{d\log(\nu)}, \tag{3.7}$$

where the second term is two in case the RJ approximation is satisfied. The temperature power law we consider (cfr. Eq.5.4) yields temperatures of about 25 K at 200 au, where we find $\beta \lesssim 1$. Here, the correction term of Eq.3.7 amounts to 1.85. If the true temperature of the medium at 300 au were lower than what is predicted with our simple power law, then the real β would be higher. However, to produce $\beta \sim 1.7$, the temperature of the envelope at 300 au would need to be lower than 5 K, which is far below a reasonable value for a protostellar envelope.

3.6.3 Alternatives: differential collapse or outflow transport

Although simulations predict so far that large grains cannot grow in situ, observations strongly hint to their presence in the inner few hundreds au of these protostellar envelopes. Different mechanisms that can justify their presence might be at play.

First, Lebreuilly et al. (2020) investigated how the distribution of dust grains of a prestellar core evolves during the early phases of the protostellar collapse and how this evolution depends on the initial conditions of the cloud and the dust distribution. They found a significant decoupling between gas and dust for grains of a few 10 μm. Moreover, observations of scattered light from molecular cloud cores in the 3-5 μm range ("coreshine") have provided evidences for the presence of grains larger than usually expected ISM ones: up to 10 μm compared to about 0.25 μm (Steinacker et al. 2010, Steinacker et al. 2014, Steinacker et al. 2015). These larger grains would tend to settle more efficiently in the first-core, leading to a radial stratification of dust properties that could reproduce a gradient of β as we observe here, but hardly explain the low β values at the inner envelope scales. Further refinement of this kind of model will require deeper knowledge of prestellar core dust properties.

A second scenario to explain large grains in the envelopes of class 0/I YSO was studied by Wong et al. (2016), who proposed that such grains might be transported to the envelope after the growth has happened in the disk in the very early stages of the system. Their model suggested that a typical protostellar outflow (T$\sim$ 10 K, v $\sim$ 10 km/s) could lift grains as large as 1 mm in the first 10^4 yr of the protostellar lifetime if the mass loss rate of the protostar was high enough ($\sim 10^{-6}\dot{M}_\odot$/yr). Among others, Brauer et al. (2008), Kawasaki et al. (2022), Bate (2022), Lebreuilly et al. (2023) all find that growth up to cm-sized pebbles is extremely fast (a few $\sim 10^3$ yr) at the high density of the disk environment, thus producing the large grains that the outflow would entrain in the first place. Based on three-dimensional magneto-hydro-dynamical simulations, Lebreuilly et al. (2020) and Tsukamoto et al. (2021) found that the large dust grains grown in the inner region of a disk can be entrained by an outflow up to the envelope scales (up to 100 μm

according to the first work, and even >1 mm for the second). These grains then decouple from the gas and are ejected from the outflow into the envelope itself, enriching its dust population before falling back to the disk.

Chen et al. (2016) found evidence for low β correlated with protostellar outflow locations in Perseus. More recently, G19 observed a correlation between β and the envelope mass of the CALYPSO sources, which might be in turn caused by a correlation between envelope mass and CO outflows fluxes (Bontemps et al., 1996). This two relationships together might support the scenario of disk dust transport into class 0/I protostellar envelopes.

While a more thorough treatment of this link for L1527 is outside of the scope of this work, we note that L1527 indeed hosts a large scale outflow structure in the east-west direction, perpendicular to the edge-on disk. Hogerheijde et al. (1998) observed the source with the James Clerk Maxwell Telescope and detected in ^{12}CO (J=3–2) line emission an outflow extending over about 20000 au. Moreover, Tobin et al. (2010a) imaged this source with the Gemini North telescope (in its L' band) and with the Infrared Array Camera (IRAC) on the Spitzer Space Telescope (2.15-8.0 μm), detecting the outflow cavity out to roughly 10000 au in both cases. Future investigations should consider whether the L1527 outflow can transport (sub)millimeter grains from the inner disk and lift them in the envelope. Such research is vital to our understanding the origin and consequences of relatively large grains at envelope scales, and may even shed light on this evolutionary stage of disk-based planet formation models.

3.6.4 Caveats

Although we aim to present a more robust way of measuring the spectral index of the faint extended emission from the envelope of class 0/I YSOs, our analysis is not free of caveats. Additional work remains to further improve the reliability of our claims.

First, while we present a study of the spectral- and dust emissivity indices as a function of uv-distance and physical source scales, we have to keep in mind that a particular baseline does not only probe an annular region at some distance from the center, rather it probes any physical structure within a scale given by $\theta \sim \lambda/B$. It is for this reason that we have to model and subtract the disk from the visibility amplitudes before evaluating the spectral index for the envelope and, for the same reason, the α and β we compute for the envelope at different scales represent a flux-weighted average over the relevant envelope spatial scales. If the inner envelope is much brighter than the outer one, as expected, the flux at even the shorter baselines will be dominated by the inner envelope. Thus, the spectral index value at these scales would still be mainly describing the inner region.

Second, in Section 3.5 we have calculated the dust emissivity index β of the envelope taking into account discrepancies from the RJ approximation, hence accounting for a temperature profile, $T \propto R^{-0.4}$. This power-law was derived for a dusty envelope illumi-

nated by a central protostar (e.g., Terebey et al. 1993). While the values we obtain using this proportionality are reasonable, as they do not reach values lower than typical cores temperatures at typical cores scales (10 K at 2000 au; e.g., Ferrière 2001), a more thorough treatment that accounts for the temperature structure and its associated uncertainties can be achieved by post-processing 3D envelope models with radiative transfer in order to.

3.7 Conclusions

We aim to characterize the maximum grain size of the dust distribution in the envelope of a class 0/I YSO: L1527 IRS, or L1527 for short. Given its vicinity (140 pc), this source has been extensively studied over decades with different types of data and methodologies to investigate its star, extended envelope, and circumstellar disk both in the dust continuum and line emission. In this context, we exploit the richness of data from the Atacama Large (sub)millimeter Array to greatly enhance the S/N of the extended emission in the continuum and determine the peak of the dust grain population in the envelope that surrounds and infalls onto the young circumstellar disk of L1527.

We find that:

- The spectral index of the compact disk, i.e. within a radius of ~ 75 au, is $\alpha_{0.88-3.4mm} = 2$, consistent with the expected high optical depth of its edge-on geometry. No dust grain properties information can be extracted in such a condition without thorough radiative transfer modelling, outside of the scope of this work.

- After subtraction of the inner disk emission and correction for the RJ approximation, we find tentative evidence for a positive outward gradient of the dust emissivity index of the envelope of L1527 ($\beta(R) \sim 0.37 \log(\mathrm{R}_{au})$, which can be interpreted as variations of dust properties from ISM-like particles ($\beta \sim 1.6$) at 2000 au down to grown grains below 300 au ($\beta \leq 1$).

- The implications of physical and chemical properties of dust grains on the values of β as well as the possible impact of the temperature profile used to calculate the correction for departure from the RJ approximation in computing the dust emissivity index (cfr Section 3.6.1) is carefully discussed. None of these possibilities alone are able to justify β values as low as 1 at hundreds of au, thus strengthening the hypothesis of submillimeter grains at these scales. While in situ formation seems disfavored by most theoretical studies, differential core dust collapse or outflow dust transport from the disk could explain our observations.

- We argue that a multiscale ($10^1 - 10^3$ au), multifrequency (n>2), and high-sensitivity study is necessary to tightly constrain the spectral- and dust emissivity index profiles of faint class 0/I YSO envelopes. Using ALMA B3, B4, B6 and B7 effectively halves the error bars of measurements made in previous studies that made use of two

wavelengths only.

ALMA has provided us with the necessary capabilities in terms of resolution, recoverable scales, sensitivity, and frequency ranges that are critical to the study of the continuum emission of faint, extended envelopes such as the one infalling onto the young protostar L1527. It is now the time to exploit this infrastructure to conduct sample studies of these objects with state-of-the-art data sets to finally pinpoint the initial conditions of grain growth and planet formation in both space and time.

Acknowledgments

This work was partly supported by the Italian Ministero dell'Istruzione, Università e Ricerca through the grant Progetti Premiali 2012-iALMA (CUP C52I13000140001), by the Deutsche Forschungsgemeinschaft (DFG, German Research Foundation) - Ref no. 325594231 FOR 2634/2 TE 1024/2-1, by the DFG Cluster of Excellence Origins (www.origins-cluster.de). This project has received funding from the European Union's Horizon 2020 research and innovation program under the Marie Sklodowska- Curie grant agreement No 823823 (DUSTBUSTERS) and from the European Research Council (ERC) via the ERC Synergy Grant ECOGAL (grant 855130). This research has received funding from the European Research Council (ERC) under the European Union's Horizon 2020 research and innovation programme (MagneticYSOS project, Grant Agreement No 679937). D.J. is supported by NRC Canada and by an NSERC discovery Grant. We thank the entire ALMA team for their dedication to provide us with the data we used for this work. This paper makes use of the following ALMA data: JAO.ALMA#2015.1.00261.S, JAO.ALMA#2016.1.01245.S, JAO.ALMA#2016.1.01541.S, JAO.ALMA#2017.1.00509.S, JAO.ALMA#2018.1.01205.L, JAO.ALMA#2016.1.01203.S, JAO.ALMA#2012.1.00647.S, JAO.ALMA#2013.1.01086.S, JAO.ALMA#2012.1.00193.S, JAO.ALMA#2017.1.01413.S, JAO.ALMA#2011.0.00604.S, JAO.ALMA#2011.0.00210.S, JAO.ALMA#2013.1.01331.S, JAO.ALMA#2012.1.00346.S, JAO.ALMA#2015.1.01549.S, JAO.ALMA#2016.A.00011.S, JAO.ALMA#2018.1.00799.S, JAO.ALMA#2016.2.00171.S, JAO.ALMA#2016.2.00117.S. ALMA is a partnership of ESO (representing its member states), NSF (USA) and NINS (Japan), together with NRC (Canada), MOST and ASIAA (Taiwan), and KASI (Republic of Korea), in cooperation with the Republic of Chile. The Joint ALMA Observatory is operated by ESO, AUI/NRAO and NAOJ. We thank M. Troisi for his sharp comments, which supported LC during this work. We thank the referee for their comments, which helped to improve the quality of this work.

3.8 Appendix

3.8.1 Continuum maps

While we have not conducted our analysis on the continuum maps, we have produced a set of images for each band during self-calibration, separately for the compact and extended array (see Section 3.2). We here report both large-scale (ACA 7m-array) and higher resolution (ALMA 12m-array) continuum maps of L1527 for the bands we used in this work.

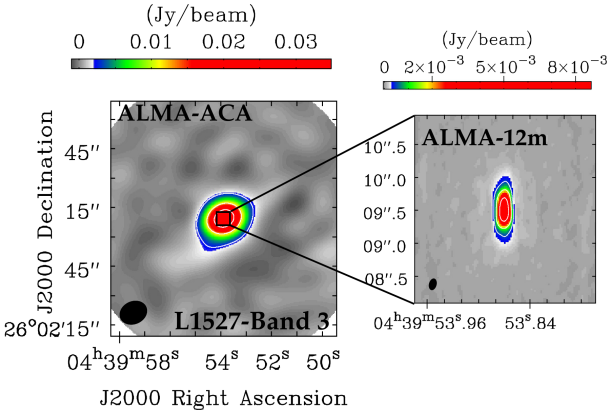

Figure 3.10: ALMA B3 continuum map of L1527 obtained imaging the 7m-array setups only (left) and the 12m-array only (right). The color map for the ACA image shows only flux densities higher than 10σ, and the white [50, 150]σ level contours. The color map of the 12m-array image shows only flux densities higher than 50σ, and the white [150, 500]σ level contours. The synthesized beams are shown in black in the lower left corner in both cases. We note that the colorbar is different for each map.

3.8.2 Adjacent bands spectral index

In this study, we have used multiple wavelengths to study the continuum emission of the envelope of L1527. This is critical to damp the possible systematic errors that occur when only using fluxes at two wavelengths. We show the importance of this approach in what follows. We computed α between pair of bands as follows:

$$\alpha = \frac{log_{10}F(\nu_2) - log_{10}F(\nu_1)}{log_{10}\nu_2 - log_{10}\nu_1}. \tag{3.8}$$

To evaluate the uncertainties on the spectral index between two wavelengths, we propagate the errors of Eq.3.8:

$$\Delta\alpha^2 = \left(\frac{1}{ln\nu_2 - ln\nu_1}\right)^2 \left(\frac{\sigma_1^2}{F_{\nu_1}^2} + \frac{\sigma_2^2}{F_{\nu_2}^2}\right), \tag{3.9}$$

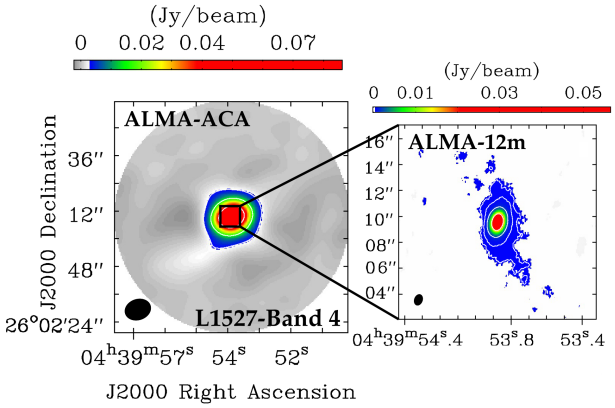

Figure 3.11: ALMA B4 continuum map of L1527 obtained imaging the 7m-array setups only (left) and the 12m-array only (right). The color map for the ACA image shows only flux densities higher than 10σ, the the white [50, 150]σ level contours. The color map of the 12m-array image shows only flux densities higher than 5σ, and the white [5, 10, 50, 500]σ level contours. The synthesized beams are shown in black in the lower left corner in both cases. We note that the colorbar is different for each map.

where σ_1 and σ_2 are the uncertainties on the amplitudes in each uv-distance bin:

$$\sigma_i = \sqrt{\left(\frac{\partial F_i}{\partial Re_i}\right)^2 dRe_i^2 + \left(\frac{\partial F_i}{\partial Im_i}\right)^2 dIm_i^2 + \left(F_i \cdot dC\right)^2}. \tag{3.10}$$

Here, Re and Im are the real and imaginary parts of the interferometric visibilities that make the amplitude as $F = \sqrt{(Re^2 + Im^2)}$, and dC is the flux calibration error. We set the latter to 10% for B7 and 5% for B3, B4 and B6, following the prescriptions of the ALMA Handbook (Remjian et al. 2019, Francis et al. 2020b). We here show the spectral index of the envelope of L1527 as computed between adjacent bands, plus the one between B3 and B6. Figures 3.14, 3.15, 3.16, 3.17 show how, given the statistical errors and the proximity of the adjacent bands, the error on α can be large at the longest baselines. Moreover, the spectral index α shows systematic differences among different combination of adjacent bands. Only using multiple bands (>2), one can robustly constrain the spectral index, damping the uncertainties that arise using only two frequencies (see Section 3.5).

3.8.3 Fit results

As explained in Section 3.4, we fit a composite model to the visibilities. The model consists of a Gaussian component to trace the compact emission and a power law to better describe the extended emission. The disk radius, defined as the 2σ level of the Gaussian component is approximately 75 au, consistent with what was found kinematically by Aso et al. (2017). The disk contributes to the flux up to a maximum of 98% in B3, highlighting the necessity to combine as many ALMA datasets as possible and selfcalibrate them in order to enhance

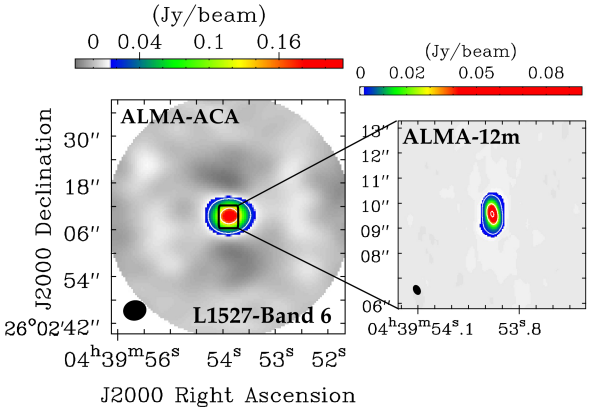

Figure 3.12: ALMA B6 continuum map of L1527 obtained imaging the 7m-array setups only (left) and the 12m-array only (right). The color map for the ACA image shows only flux densities higher than 10σ, and the white $[50, 150]\sigma$ level contours. The color map of the 12m-array image shows only flux densities higher than 5σ, and the white $[5, 50, 150]\sigma$ level contours. The synthesized beams are shown in black in the lower left corner in both cases. We note that the colorbar is different for each map.

the faint extended continuum emission. The disk results edge-on ($inc \sim 80°$), consistently with several results throughout the literature with a position angle $PA \sim 2°$, in a westward convention. The inner radius of the envelope is constrained to be in the range 0.01-0.15 arcseconds while the outer one is in the range 8-12 arcseconds, both depending on the band. Having phase-centered the datasets during the data calibration procedure, we find both dRA and dDec phase offsets consistent with zero. Finally, the power law exponent of the Plummer profile (p) is found to be in the range 2.6-3.1, roughly consistent with what was found by Ladd et al. (1991). We list the results of the fitting, that was carried out with galario, in Tab.3.8.3 and show the final model in Figures 3.4, 3.18, 3.19, 3.20, 3.21.

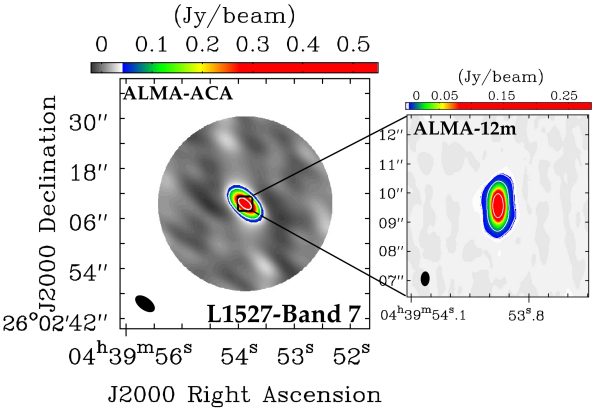

Figure 3.13: ALMA B7 continuum map of L1527 obtained imaging the 7m-array setups only (left) and the 12m-array only (right). The color map for the ACA image shows only flux densities higher than 10σ, and the white $[10, 50]\sigma$ level contours. The color map of the 12m-array image shows only flux densities higher than 10σ, and the white $[10, 50, 500]\sigma$ level contours. The synthesized beams are shown in black in the lower left corner in both cases. We note that the colorbar is different for each map.

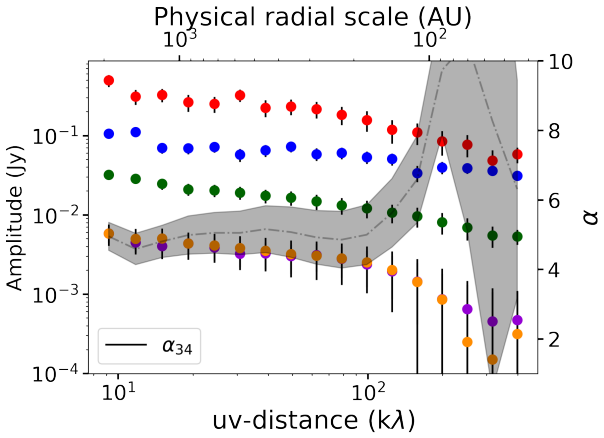

Figure 3.14: Same as Fig.3.6 but for B3 (100 GHz) - B4 spectral index.

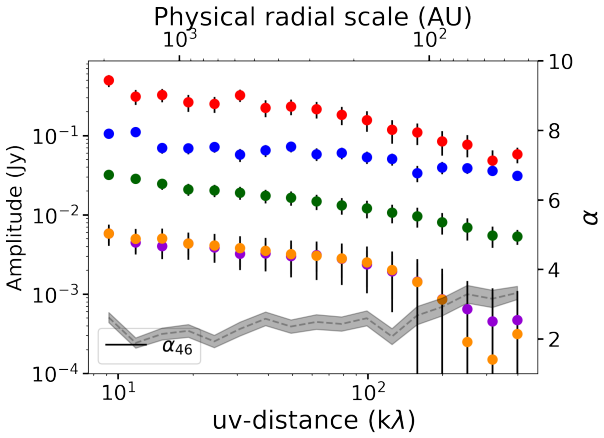

Figure 3.15: Same as Fig. 3.14 but for B4 and B6.

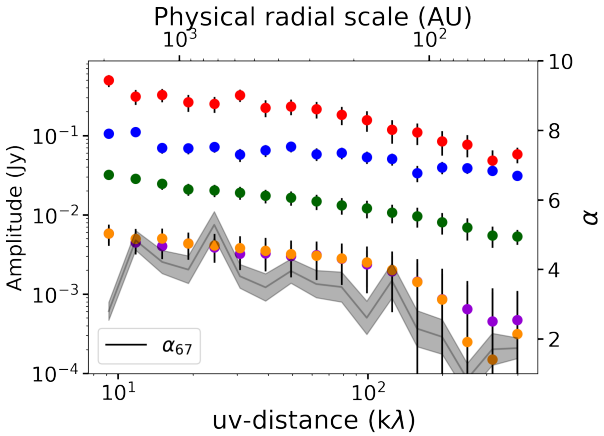

Figure 3.16: Same as Fig. 3.14 but for B6 and B7.

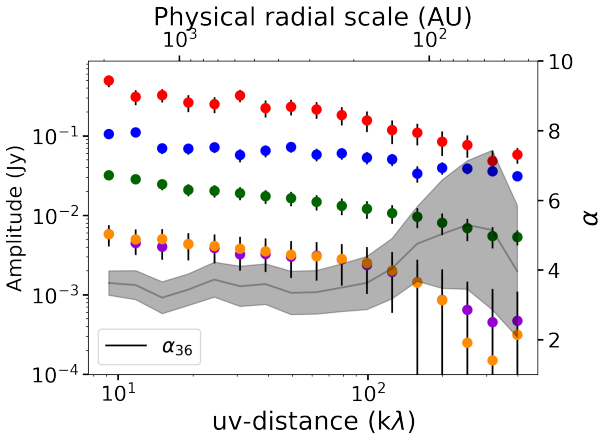

Figure 3.17: Same as Fig. 3.14 but for B3 and B6.

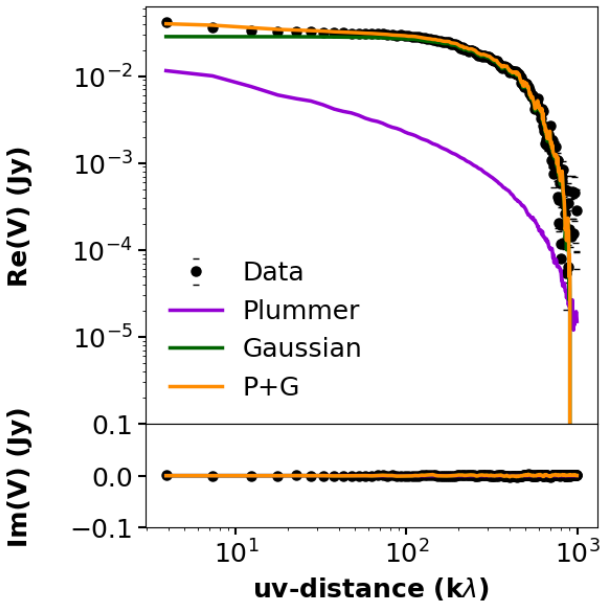

Figure 3.18: The `galario` fit of the B3 (100 GHz) real and imaginary part of the visibilities. The best model (orange) is composed of a compact Gaussian model (green) and an outer power law (violet). The wiggles in the plotted model are due to its sampling on the uv points of the observations.

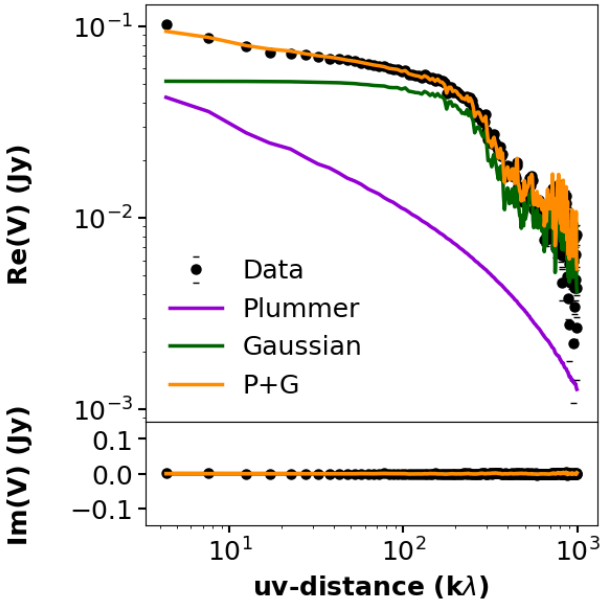

Figure 3.19: Same as Fig. 3.18 but for B4.

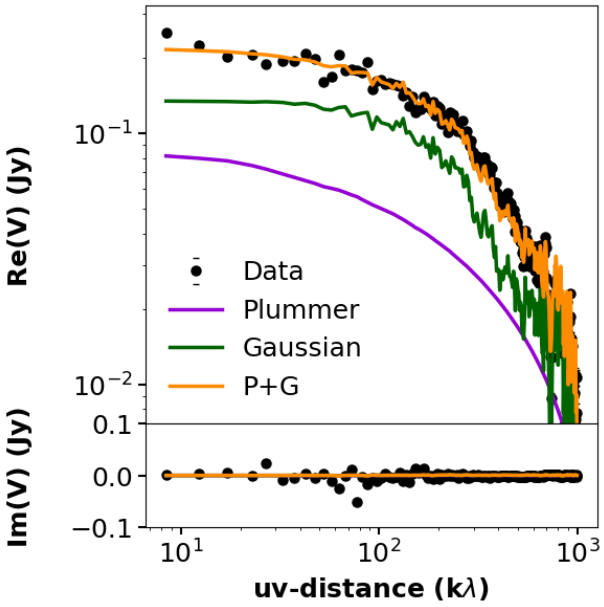

Figure 3.20: Same as Fig. 3.18 but for B6.

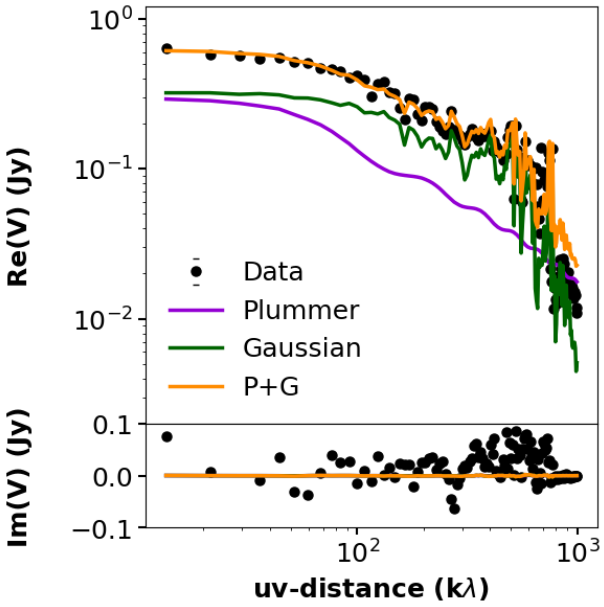

Figure 3.21: Same as Fig. 3.14 but for B7.

Parameter	Band 3 (88 GHz)	Band 3 (100 GHz)	Band 4	Band 6	Band 7
f_0 (Jy/sr)	10.47 ± 0.02	10.53 ± 0.01	10.79 ± 0.03	11.12 ± 0.01	11.51 ± 0.01
r	0.90 ± 0.01	0.98 ± 0.01	0.74 ± 0.01	0.72 ± 0.01	0.38 ± 0.01
σ (")	0.147 ± 0.007	0.151 ± 0.001	0.208 ± 0.004	0.270 ± 0.001	0.330 ± 0.001
inc (deg)	78 ± 1	80 ± 1	80 ± 1	82 ± 1	78 ± 1
PA (deg)	2.08 ± 0.6	2.27 ± 0.02	3.09 ± 0.05	2.3 ± 0.01	1.942 ± 0.007
R_{in} (")	0.03 ± 0.01	0.14 ± 0.01	0.04 ± 0.01	0.08 ± 0.02	0.03 ± 0.01
R_{out} (")	9.9 ± 0.1	9.9 ± 0.1	12.8 ± 0.1	4.4 ± 0.2	1.35 ± 0.1
p	2.62 ± 0.01	2.76 ± 0.03	2.75 ± 0.01	3.37 ± 0.01	2.54 ± 0.02
dRA (")	0.029 ± 0.001	0.029 ± 0.001	0.007 ± 0.001	0.001 ± 0.001	0.005 ± 0.001
dDec (")	-0.017 ± 0.002	-0.018 ± 0.001	-0.011 ± 0.001	0.008 ± 0.005	0.005 ± 0.003

Table 3.5: Best-fit parameters of the Gaussian plus power law model as obtained with galario, for each ALMA Band.

4

Dust transport from disks to envelopes via outflows

This chapter is based on "Protostellar chimney flues: are protostellar jets and outflows lifting submillimetre dust grains into envelopes?"
(Cacciapuoti et al. 2024, The Astrophysical Journal, Volume 961, Issue 1, id.90, 10 pp.)

The Chapter was the result of my own writing. The data were and analysed by me, except for the outflows mass loss rates, derived by L. Podio and C. Codella. The co-authors were involved in discussions and feedback.

Full authors list:
Luca Cacciapuoti; Testi, L.; Podio, L.; Codella, C.; Maury, A. J.; De Simone, M.; Hennebelle, P.; Lebreuilly, U.; Klessen, R. S.; Molinari, S.

Low dust opacity spectral indices ($\beta < 1$) measured in the inner envelopes of class 0/I young stellar objects (age $\sim 10^{4-5}$ yr) have been interpreted as the presence of (sub-)millimetre dust grains in these environments. The density conditions and the lifetimes of collapsing envelopes have proven unfavorable for the growth of solids up to millimetre sizes. As an alternative, magneto-hydrodynamical simulations suggest that protostellar jets and outflows might lift grains from circumstellar discs and diffuse them in the envelope. We reframe available data for the CALYPSO sample of Class 0/I sources and show tentative evidence for an anti-correlation between the value of β_{1-3mm} measured in the inner envelope and the mass loss rate of their jets and outflows, supporting a connection between the two. We discuss the implications that dust transport from the disc to the inner envelope might have for several aspects of planet formation. Finally, we urge for more accurate measurements of both correlated quantities and extension of this work to larger samples, necessary to further test the transport scenario.

4.1 Introduction

The formation of terrestrial planets and of the rocky cores of giant planets is thought to happen in a core-accretion scenario, a process spanning ten orders of magnitude in size, where interstellar medium, sub-micron dust grains grow into km-sized objects. While dust growth has been long thought to take place exclusively in isolated, evolved protoplanetary discs revolving around class II young stellar objects (YSOs), recent observations indicate that dust growth up to millimeter sizes might start in collapsing protostellar envelopes, thus much earlier and further away from host stars than previously thought. Observationally, the slope α of the spectral energy distribution (SED) across (sub-)millimetric wavelengths is a means to interpret interstellar dust properties and its size. Specifically, if (i) dust opacity scales as a power law ($\kappa \propto \nu^{\beta}$), (ii) the emission is optically thin, and (iii) the Rayleigh-Jeans (RJ) approximation holds, then $\beta = \alpha - 2$ (Natta et al. 2007, Testi et al. 2014). In turn, β depends on dust properties, and strongly on the maximum grain size of the dust population. For the interstellar medium, typically $\beta \sim 1.7$ (Weingartner & Draine, 2001). In Class II objects, $\beta < 1$ suggests the presence of millimetre dust grains (e.g., Testi et al. 2014, Tazzari et al. 2021, Macías et al. 2021).

Several authors measured low β values in the inner envelopes (a few 10^2 au) of Class 0/I sources (Kwon et al. 2009, Miotello et al. 2014, Galametz et al. 2019, Cacciapuoti et al. 2023). Although β also depends on grain composition and porosity, some of the observed values are too low ($\beta < 0.5$) to be explained without considering 100 μm - 1 mm grains (e.g., Köhler et al. 2015, Ysard et al. 2019). However, simulations have so far predicted that dust coagulation would be ineffective at the low densities ($n \sim 10^{5-7}$ cm^{-3}) and short timescales (a few 10^5 yr) that characterize these environments (Ormel et al. 2009, Lebreuilly et al. 2023, Silsbee et al. 2022). It will be crucial for next simulations to test the effects of generally disregarded processes, like the dust back-reaction on the turbulence through gas-dust friction and dust-magnetic-field interaction (Hennebelle & Lebreuilly, 2023a), to check whether growth remains a viable scenario.

Alternative or concomitant processes must be considered that could contribute to explain the observed low β. For example, Wong et al. (2016) first presented a simple analytical model to argue that millimetre dust from the disc could be entrained by protostellar outflows and transported to the envelope. Giacalone et al. (2019) also presented an analytical model for the entraiment of dust grains along magnetohydrodynamical (MHD) disc winds, and concluded that grains of $\sim$10 μm can be lifted by MHD winds and be transported outwards in the disc of T Tauri and Herbig Ae/Be objects. However, their model assumes typical evolved mass outflow rates of $\sim 10^{-8}$ M$_\odot$/yr. Since the maximum grain sizes lifted in the envelopes depend linearly on this quantity, it can be much larger in young Class 0/I objects, for which the mass loss rates are orders of magnitude higher. These findings might have found recent confirmation thanks to exquisite JWST observations of the Tau 042021 edge-on disc, for which Duchene et al. (2023) reported an X-shaped feature in dust scattered light whose spatial location is consistent with ALMA CO line emission trac-

Source	$\dot{M}_J$ (B)[a] (10^{-7} $M_\odot$/yr)	$\dot{M}_J$ (R)[a] (10^{-7} $M_\odot$/yr)	$\dot{M}_{OF}$ (B) (10^{-8} $M_\odot$/yr)	$\dot{M}_{OF}$ (R) (10^{-8} $M_\odot$/yr)	β^b_{500au}	M^b_{env} ($M_\odot$)
L1527	< 0.2	< 0.2	0.5	0.5	1.41 ± 0.16	1.2
L1157	1.6	2.9	2.5	1.9	1.17 ± 0.18	3.0
SVS13B	< 0.1	< 0.1	< 0.02	< 0.02	0.99 ± 0.16	2.8
IRAS2A1	> 6.7	< 0.1	2.4	1.5	0.82 ± 0.17	7.9
SerpS-MM18a	> 11.5	> 5.9	12.7	5.1	0.74 ± 0.16	5.4
SerpM-S68Na(1)	> 3.3	< 0.1	0.12	< 0.02	0.66 ± 0.27	11.0
IRAS4B1	1.2	2.3	3.6	1.0	0.62 ± 0.16	4.7
IRAS4A1	≥ 4.0	≥ 13.7	12.4	11.7	0.54 ± 0.16	12.2
L1448-C	9.7	13.8	7.3	10.1	0.41 ± 0.16	1.9

[a] from Podio et al. (2021) [b] from Galametz et al. (2019)

Table 4.1: Dust opacity spectral indices at 500 au (β_{500au}), envelope masses (M_{env}) and jets and outflows mass loss rates ($\dot{M}_J$ and $\dot{M}_{OF}$, respectively) from the selected Class 0 sources from the CALYPSO sample (Maury et al., 2019). The $\dot{M}_{OF}$ are measured in this work and are lower limits as the outflow LV emission is likely optically thick. We report upper limits if no jet/outflow was detected in the CALYPSO data. (1) We do not include SerpM-S68N in the correlation because its SiO $(5-4)$ transition prevents us from identifying high- and low-velocity ranges properly (we note, however, that the correlation is not affected by this point).

ing an outflow. Their observations suggest the entrainment of $\gtrsim 10\mu$m grains even beyond 300 au. Finally, the findings of these models are supported by Tsukamoto et al. (2021) and Lebreuilly et al. (2020), who arrived to consistent conclusions via three-dimensional MHD simulations. In particular, Tsukamoto et al. (2021) proposed the expression *ash-fall*[1], referring to the dust grains decoupling from the entrainment outflow and their subsequent fall back in the disc.

Thus, as outflows represent in principle a means to transport submillimetre grains to envelopes, we here explore the unique CALYPSO sample (Maury et al., 2019) to test whether a correlation holds between the observed power of jets and outflows in Class 0 protostars and the dust opacity index in their envelopes.

4.2 The sample

The sources that make up our sample are part of the Continuum And Lines in Young ProtoStellar Objects IRAM-PdBI Large Program (CALYPSO[2]; Maury et al. 2019). CALYPSO is a survey of 16 Class 0 sources, located in different star forming regions (d$\leq$450 pc), observed in three spectral setups (centered at $\sim$ 94, 219 and 231 GHz). The observations were carried out with the IRAM Plateu de Bure Interferometer (PdBI). See Maury

[1]Continuing Tsukamoto et al. (2021) nomenclature, we thus propose outflows as "chimney flues" in the title of this work.

[2]https://irfu.cea.fr/Projets/Calypso/Welcome.html

et al. (2019) for further details. Out of the sixteen sources, nine can be fully characterized for our purposes. Only for these, in fact, a reliable measure of β and of the jets/outflows mass loss rates could be performed ($\dot{M}_J$, $\dot{M}_{OF}$) (Table 4.1). Among the sources considered in this study, seven are in binary or multiple systems. We report considerations on their multiplicity in Appendix 4.8.1.

While this is a low number statistics, we note that CALYPSO is unique in its uniformity and is the only survey for which the SiO (5−4) transition is systematically targeted to detect the high-velocity jets of a sample of protostars (see Section 4.4). This allows us to perform the jets/outflows analysis as explained in Sect. 4.4 and have deep enough continuum datasets with which Galametz et al. (2019) measured dust optical properties. Finally, we note that the CALYPSO data for the sources we consider here have been self-calibrated as explained in Section 2 of Maury et al. (2019), and the self-calibrated data has been later used in Galametz et al. (2019) and Podio et al. (2021), i.e. the works that have measured the dust opacity spectral index β and the jets mass loss rates $\dot{M}_J$ that we also consider in this work.

4.3 The dust opacity spectral index

As stated in Section 4.1, the dust opacity spectral index β can be derived starting from the radio spectrum of a source and carries dependencies on the properties of interstellar dust, such as the maximum grain size of the distribution. Galametz et al. (2019) used CALYPSO 1.3 and 3.2 millimetre continuum observations to constrain β and infer the maximum dust grain sizes in the protostellar envelopes of the sources we consider in this work, up to ∼2000 au radial distances from the central protostars. While we report on the details of their measurements in Appendix 4.8.2 for completeness, we here briefly summarise them for the reader's convenience.

Galametz et al. (2019) measured β including a temperature correction that accounts for discrepancies from the Rayleigh-Jeans approximation due to low envelope temperatures:

$$\beta = \frac{log_{10}\left[\left(F_{\nu_2}/B_{\nu_2}(T)\right)/\left(F_{\nu_1}/B_{\nu_1}(T)\right)\right]}{log_{10}\nu_2 - log_{10}\nu_1} \tag{4.1}$$

where ν_2 = 231 GHz and ν_1= 94 GHz are the representative frequencies of the PdBI observations, F_ν is the flux at each frequency. The term $B_\nu(T)$ is the value of the Planck function at a temperature T that depends on the radial distance from the central protostar[3] ($T \propto r^{-0.4}$), evaluated at frequency ν_i. For each envelope, they measured β across scales and reported best-fit linear models to extrapolate β at any other scale. We report the final

[3]In brief, Galametz et al. (2019) assumed this temperature profile based on the radiative transfer post-processing of dusty envelopes from Motte & André (2001).

estimated envelope-onlyβ values at 500 au in Table 1. We note that β also depends on the extent of porosity and on the composition of both grain bulk and ice mantles (e.g., Natta et al. 2007). However, the lowest values observed by Galametz et al. (2019) are only reconcilable with laboratory experiments in which the sizes of the dust grains are $\gtrsim 100\mu$m, regardless of ice mantles properties (Köhler et al. 2015, Ysard et al. 2019). The effect of porosity would also not affect the interpretation of low β as due to large grain sizes (e.g., Birnstiel et al. 2018).

4.4 Jets and Outflows Mass Loss Rates

In this section, we report previous measurements of jets energetics for the CALYPSO sample and present new ones for their low-velocity outflow counterparts. We note that we are interested in the instantaneous mass loss rates of these components rather than their total ejected mass, hence we do not complement the CALYPSO observations with single dish data. This is the case because we aim to investigate a link between the presently observed low β values of Galametz et al. (2019) and the continuous flow of material along jets and outflows. The mass loss rates are constant along the jets/outflows extension since mass needs to be conserved, and we measure the latter (outflow) as Podio et al. (2021) measured the former (jet), i.e., at the first peak of the respective tracer emission, to minimize the contribution of possible gas entrained along the jet. The positions of these peaks are in Tab. 4 of Podio et al. (2021). For the reader's convenience, we note that the maximum recoverable scale of the observations is reported to be about 8$''$.0 (Podio et al., 2021). Based on the SiO (5−4) transition at the innermost knots of the blue- and red-shifted lobes, Podio et al. (2021) defined the high-velocity (HV) ranges, where the emission probes the jet, for all sources associated with SiO (see their Fig. C.1 and Table 4). In this work, we define the outflow as the emission on the complementary low-velocity (LV) ranges. In Fig. 4.1, we show the spatial distribution of CO (2−1) towards L1448-C, obtained integrating on the LV and HV ranges: HV CO traces the collimated jet, which is believed to originate from the inner disc region, while LV CO probes the wide-angle outflow, which is likely to arise from a more extended disc region. The HV ranges for all the CALYPSO sources are listed in Table 4 of Podio et al. (2021).

At this point, Podio et al. (2021) estimated the $\dot{M}_{\rm J}$, in the blue (B) and red (R) lobes. Here, we apply the same methodology to infer the LV outflows $\dot{M}_{\rm OF}$ of the sources in the CALYPSO sample, for the first time. The beam-averaged CO column densities in the jet and outflow, N_{CO}, are derived from the integrated line intensities on HV and LV, respectively. We assume local thermodynamic equilibrium (LTE) at a fixed excitation temperature, $T_K = 100$ K for HV jets (e.g., Cabrit et al., 2007), and $T_K = 20$ K for LV outflows (e.g., Bachiller et al., 2001), and that the emission is optically thin. The jet and outflow mass-loss rates are computed as (Lee et al. 2007, Podio et al. 2015):

$$\dot{M} = 1/\sqrt{C} \cdot m_{\rm H_2} \cdot (N_{CO}/X_{CO}) \cdot b_t \cdot V_{tan} \tag{4.2}$$

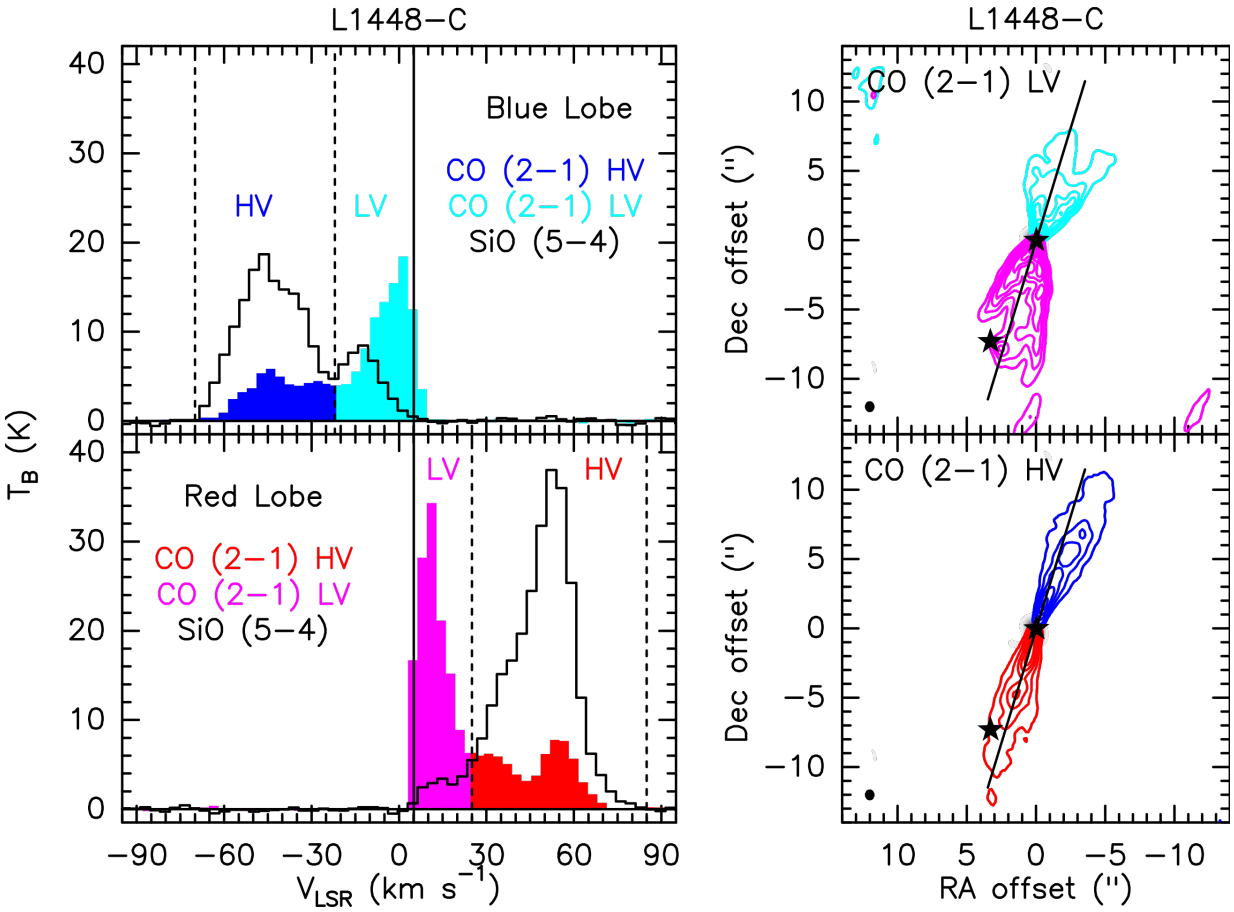

Figure 4.1: The L1448-C jet and the outflow, as imaged with PdBI in CO $(2-1)$ and SiO $(5-4)$. *Left panels:* CO (blue, cyan, magenta, and red) and SiO (black) spectra at the position of the blue-shifted and red-shifted SiO knots located closest to the driving source (from Podio et al., 2021). The horizontal and vertical solid lines indicate the baseline and systemic velocity, $V_{sys} = +5.1$ km s^{-1}, respectively. The vertical black dotted lines indicate the high-velocity (HV, blue/red) and low-velocity (LV, cyan/magenta) ranges, which trace the jet and the outflow, respectively. The definition of LV and HV ranges is based on the SiO $(5-4)$ emission (see text). *Right panels:* Maps of CO $(2-1)$, integrated on the LV (top panel) and HV (bottom panel) ranges. First contours and steps are 5σ, corresponding to 1 Jy km s^{-1} beam^{-1}. The black stars indicate the positions of the protostars L1448-C (at the center) and L1448-CS. The black solid line shows the jet/outflow PA (Podio et al., 2021). The beam size is in the bottom-left corner.

where $1/\sqrt{C}$ accounts for compression in the shocks ($C = 3$), m_{H_2} is the mass of molecular hydrogen, $X_{CO} = 10^{-4}$ the assumed CO abundance with respect to H_2, b_t the beam size perpendicular to the jet, and V_{tan} the tangential jet/outflow velocity. The latter is obtained by correcting for inclination the jet/outflow velocities, assumed to be 100 km s^{-1} for the HV jet, and 10 km s^{-1} for the LV outflow. The inclination is derived from the ratio between

the assumed jet velocity and its radial component from the HV spectra (see Table 4 of Podio et al. 2021).

For the HV jets, Podio et al. (2021) identified the sources for which $\dot{M}_{\rm J}$ is a lower limit by comparing CO and SiO spectra. The estimated rates carry a factor 3-10 of uncertainty due to the calibration of the parameters of Eq. 4.2. The LV outflow emission is likely optically thick, therefore, the estimated $\dot{M}_{\rm OF}$ must be considered as lower limits. We can estimate the uncertainty introduced by optical depth using ^{13}CO emission in the assumption that it is optically thin. For two sources only (IRAS 4A1 and IRAS 4B1), ^{13}CO is detected along the jet (see the maps in Maret et al. (2020)). For these two sources we can reliably estimate the ^{12}CO/^{13}CO ratio, hence opacity. We find $\tau^{(R)}_{IRAS4A1} = 6$, $\tau^{(B)}_{IRAS4A1} = 18$, $\tau^{(R)}_{IRAS4B1} = 15$, $\tau^{(B)}_{IRAS4B1} = 7$. These values imply $\dot{M}_{OF}$ higher by a factor at least ∼6-18. Since we cannot repeat this analysis for all sources, we here stress that the derived $\dot{M}_{OF}$ (in Table 4.1 and Fig. 4.2) are lower limits and we consider the jets to be a more robust proxy of the effective mass loss rates of each protostar. Observations of optically thin tracers of the low-velocity outflows will be key to further test the correlation we propose.

4.5 A tentative anti-correlation

Modern theoretical efforts have shown how growing dust grains in protostellar envelopes is problematic due to the lifetimes and densities of these environments (Ormel et al. 2009, Bate 2022, Silsbee et al. 2022, Lebreuilly et al. 2023). If millimeter dust, implied by recent measurements of low dust opacity spectral indices in envelopes (Miotello et al. 2014, Galametz et al. 2019), cannot grow at envelope scales, alternative processes might explain their presence therein. We here show a tentative anti-correlation between β with $\dot{M}_J$ and $\dot{M}_{OF}$, potentially supporting a scenario in which protostars launching powerful outflows can lift millimeter grains into their envelopes. Fig. 4.2 show the β indices found by Galametz et al. (2019) as a function of $\dot{M}_J$ and $\dot{M}_{OF}$ summed over the blue and red lobes (see Section 4.2). The values are reported in Table 4.1. We do not include SerpM-S68N because SiO $(5-4)$ emission in Podio et al. (2021) is only at low velocities, likely due to the system inclination, thus impeding the identification of the LV and HV. The resulting Pearson correlation coefficients are:

- $\rho_J \ = -0.73 \pm 0.27$ (β_{500au}, $\dot{M}^{R+B}_J$)
- $\rho_{OF} = -0.68 \pm 0.28$ (β_{500au}, $\dot{M}^{R+B}_{OF}$)

We evaluate the statistical significance of such a correlation by means of a two-tailed Student's t-test, where the null hypothesis is that $\rho = 0$ (against $\rho \neq 0$). We reject the null hypothesis at $p < 0.04$ level in the jet case, and at the $p < 0.06$ level for the outflows. These tentative correlations might support a dust transport scenario from young discs to their embedding envelopes.

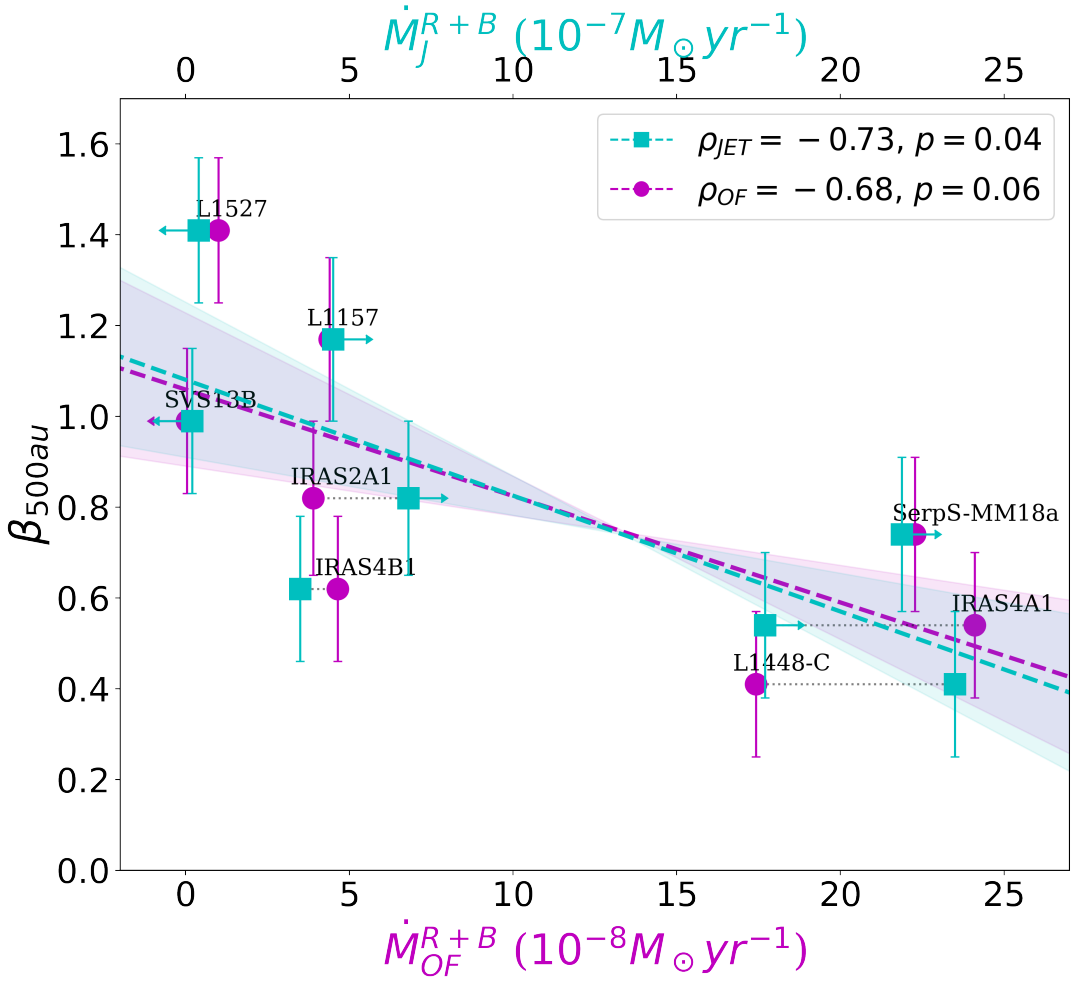

Figure 4.2: The total (red plus blue lobe) jet mass loss rates (cyan points, upper x-axis) and outflows mass loss rates (magenta points, lower x-axis) around young Class 0 sources anti-correlates with β (y-axis) of their inner envelopes (β_{500au}). For each source, a dotted gray line connects the corresponding jet and outflow rates. Source names are on top of the corresponding magenta point. The best-fit linear relations are shown in cyan and magenta, for outflows and jets respectively.

Alternative explanations to the observed tentative correlation are possible in case these two share correlations with other quantities. Bontemps et al. (1996) found a correlation between the envelope mass of Class 0/I YSOs and the CO momentum flux of their outflows. Since Galametz et al. (2019) observed a correlation between β and envelope mass of CALYPSO sources, then the tentative correlation we show in Fig. 4.2 might be the combined result of these underlying relationships. However, it remains unclear whether the fundamental causal correlation is the one between the dust opacity spectral index and envelope mass or the mass loss reates, as presented here. Moreover, the $\beta - \dot{M}_{OF}$

correlation in Fig.4.2 might be caused by an underlying $\dot{M}_J - \dot{M}_{OF}$ correlation. Such a correlation cannot be quantified here, given that the estimated $\dot{M}_{OF}$ are lower limits. To rule out possible contamination of the correlation from any dependence of the measured β and mass loss rates on the inclination of the source (disc/jet), we reject possible underlying correlations in Appendix 4.8.4.

4.6 Discussion

We here further discuss our findings, and the conditions that need to be met in order for the proposed dust transport to happen.

4.6.1 When and where do transported grains grow?

If outflows are lifting millimetre (or larger) dust grains into the envelopes of Class 0 objects, these must have first grown in the disc. Brauer et al. (2008) studied dust coagulation in the first 1 Myr of disc evolution at representative 1, 10 and 100 au scales and found that millimetre dust grains dominate the dust size distribution already after few 10^3 yr in the inner 1 au of the disc. Lebreuilly et al. (2023) considered several dust size distributions and simulated their early evolution during protostellar collapse under the effects of turbulent, brownian and radial motions. They found that millimetre grains are formed at ≤ 0.1 au scales in few years after the first Larson core formation start. Laboratory experiments have been performed to constrain the stickiness of dust grains in the disc inner regions. When heated at 1000 K, dust grains become *super-dry* and their stickiness can increase up to a factor 100, thus providing the conditions to grow even larger agglomerates (Bogdan et al. 2020, Pillich et al. 2021). These temperatures are typically reached in the inner ~ 0.1 au of low-mass protostellar discs. At these distances, both jets and outflows could lift grains. Indeed, the typical foot-point of jet is much closer to the star than the outflows'. For example, Lee et al. (2017) measured a $0.05 - 0.3$ au foot-point radius for the high-velocity SiO jet in the Class 0 HH212 source. Low-velocity outflows, instead, likely extend to a wider disc region out to radii of even $20 - 40$ au (Bjerkeli et al. 2016, Tabone et al. 2017, Lee et al. 2018), and thus could entrain grains from a larger reservoir.

4.6.2 Can outflows lift millimetre grains?

Wong et al. (2016) and Giacalone et al. (2019) presented an analytical treatment in which they explored the conditions for the uplifting of dust grains along outflows. Wong et al. (2016) presented the critical mass of the protostar for which, if $M_* < M_{cr}$, grains of a given size could be entrained against gravity (see their Eq. 7). Another analytical model, by Giacalone et al. (2019), reported an equation to compute the maximum grain size a_{max} that a given wind can uplift against the gravity of a star of mass M_*. We report the latter

for the reader's convenience:

$$a_{max} \approx 0.35\mu m \left(\frac{M_*}{M_\odot}\right)^{-1} \left(\frac{\dot{M}}{10^{-8} M_\odot/yr}\right) \left(\frac{T_{gas}}{200K}\right)^{0.5} \left(\frac{r}{au}\right)^{-0.25} \left(\frac{(z/r)}{0.06}\right)^{-1} \left(\frac{\log(r_+/r_-)}{10^3}\right)^{-1}, \tag{4.3}$$

where $\dot{M}_\odot/yr$ is the mass loss rate of the outflow, T_{gas} is the gas temperature, r is the launching footpoint, z/r the disc flaring ratio, r_+/r_- the ratio between disc's outer and inner edge. See Giacalone et al. (2019) for the details. We notice that the three sources of our sample with the largest outflows mass loss rates ($\gtrsim 2 \cdot 10^{-7} M_\odot/yr$) have $\beta < 0.8$. If we consider this value in Eq. 4.3, and we fix $M_* = 1 M_\odot$, $T_{gas} = 20$K at the outflow's base, r = 1 au, z/r = 0.1, $r_+ = 50$ au (typical Class 0 disc radius, e.g., Maury et al. 2022) and $r_- = 0.1$ au, we obtain $a_{max} \gtrsim 150\mu$m. Since outflows mass loss rates are lower limits due to optical depth effects, a_{max} could be higher by even an order of magnitude. We refrain from evaluating Eq. 4.3 source by source since it was derived for class II objects rather than class 0/I, and because most parameters suffer from large uncertainties for young sources. Thus, at face value, assuming standard parameters, grains larger than 100 μm could be lifted for the sources with highest mass loss rates (and lowest betas).

Similar findings for the maximum sizes of dust grains entrainable by outflows were reported by Lebreuilly et al. (2020) and Tsukamoto et al. (2021). They both performed magneto-hydrodynamical simulations. Lebreuilly et al. (2020) ran their setup including large grains to account for growth that might have happened at earlier times, while Tsukamoto et al. (2021) models dust coagulation. They both found that large grains in the inner region of disc (a few 100 μm to 1 cm) can be entrained. These grains then decouple from the gas and are ejected from the outflow into the envelope, before falling back into the disc like *ash fall*, as coined by Tsukamoto et al. (2021).

4.6.3 Do grains survive the transport?

Given their lower velocities and temperatures, as well as a wider entraining base, outflows seem to be the preferred mechanism to lift dust grains from protoplanetary discs to the inner envelopes of young protostars (Wong et al. 2016, Lebreuilly et al. 2020, Tsukamoto et al. 2021). The tentative $\beta - \dot{M}_{OF}$ correlation we present in Fig. 4.2 might support this scenario. The observed $\beta - \dot{M}_J$ correlation might either mean that jets are contributing to the mechanism or that they share an underlying correlation with the outflows. We thus here discuss if lifted dust grains would survive the transport along jets. Given the much lower speeds and temperatures of outflows, their survival to transport along the latter is a consequence.

The destruction of silicon-bearing dust grains in shocks has been identified as the mechanism that enriches SiO in the interstellar medium and makes of this molecule a key

jet tracer (e.g., Flower & Forêts, 1994; Caselli et al., 1997; Schilke et al., 1997). However, shock models predict that only a small fraction (< 10%) of grains is destroyed in the mild shocks along jets, with typical velocities of $20 - 50$ km s^{-1} and pre-shock gas densities of $10^4 - 10^6$ cm^{-3} (e.g., Gusdorf et al., 2008a,b; Guillet et al., 2011).

In the wide grid of models explored by Gusdorf et al. (2008a), where the shock velocities range 20 km s^{-1} $< v_s <$ 50 km s^{-1} and the pre-shock gas densities are in the interval 10^4 cm^{-3} $< n_H < 10^6$ cm^{-3}, no more than 5% of Si is released in the gas phase by sputtering. Taking into account shattering and vaporisation of the grains in grain-grain collisions may enhance the fraction of grains destroyed to $\sim 8\%$ (Guillet et al., 2011). These shock models reproduce the typical SiO abundances estimated in protostellar shocks which span from a few 10^{-8} and a few 10^{-7} (e.g., Gibb et al., 2004; Bachiller & Pérez Gutiérrez, 1997; Tafalla et al., 2010). Recent high angular resolution observations, e.g. in CALYPSO, indicate that SiO may reach abundances $> 5 \times 10^{-6}$ in jets, which requires either dust-free jets or the fraction of grains sputtered in shocks being larger than 10% (for $[\mathrm{Si/H}]_\odot \sim 3.5 \times 10^{-5}$, Holweger 2001).

Finally, Wong et al. (2016) studied whether (sub-)millimetre dust seeds would survive grain-grain collisions in the envelope, after reaching the transport limit velocity ($v \sim 0.5$ km/s), given by the gravity-drag equilibrium along the outflow. Making use of the shattering model of Kobayashi & Tanaka (2010), they concluded that millimetre-sized dust grains could survive in the envelope environment: only a fraction as small as 10% might be destroyed.

Thus, it seems reasonable that a large percentage of dust grains could survive the transport along outflows and even jets, being only partially eroded by collisions with both other grains and gas molecules in the latter. However, we note that there is a strong necessity for dust laboratory and modeling studies to assess the effects of high temperatures in the inner disc if submillimeter dust were lifted from inner outflows footpoints. In particular, it will be crucial to test whether the high temperatures would sublimate grain's mantles materials causing them to further shrink in size.

4.6.4 Potential implications

The possibility that protostellar outflows lift large millimetre grains from the disc into the envelopes of young stellar objects can have several implications for the evolution of dust throughout the system. The outwards transport of dust can extend the timescales of grain growth in discs, limited by the meter barrier problem; it can affect the physical properties of grains as they are transported upwards away from the optically thick disc; and it can contribute to explain mixing of the mineralogy of outer discs, like the one found in meteorites in the Solar System.

First, the orbital dynamics of dust grains orbiting in a disc depends on their stokes number, defined by their composition, density and size. When particles grow in size, they

experience a larger and larger headwind that slows them down and cause an inward orbit shift, known as radial drift. In a typical disc orbiting a 1 $M_\odot$ star, radial drift velocities of solids at 1 au reach a maximum for meter-sized boulders, thus causing intermediate solids to rapidly fall towards the central star in timescales much faster than the ones estimated for planet cores formation (Weidenschilling, 1977). At larger radii, this peak velocity is reached for even smaller pebbles. If outflows were uplifting grains in a continuous recycle of dust to the outer disc, this would setback grown millimetre grains in its outskirts and contribute to stretch the available time-span to form larger agglomerates, as already proposed by Tsukamoto et al. (2021). Moreover, if young protoplanetary discs harbor ring substructures that act like dust traps (as is the case for, e.g., GY91 from Sheehan & Eisner 2018 or IRS63 from Segura-Cox et al. 2020a), then outwards transported grains will be halted on their drift back towards the inner disc at one of these substructures, potential birthplaces of planetesimals via streaming instabilities (Chambers, 2021; Carrera et al., 2021).

Secondly, transported dust grains would undergo physical and chemical reprocessing once in the envelope. While they are partially shielded from the radiation of the star in the dense disc, they are going to be lifted in the much thinner envelope and the different energy and intensity of stellar radiation impinging onto them could change their structural and compositional properties. Furthermore, the grains would be transported from the warm inner disc to the colder envelopes where molecular freeze-out could form ice mantles.

Lastly, the uplifting and outward transport of inner disc grains represents a potential explanation for the discovery of cristalline grains in the outskirts of protoplanetary discs, where the temperatures are too low to explain spectral observations of silicate lines (e.g., Apai et al. 2005, Sargent et al. 2009). Along the same line, Trinquier et al. (2009) and Williams et al. (2020) observed anomalous abundances of ^{46}Ti, ^{50}Ti and ^{54}Cr isotopes in outer Solar System chondrules (mm-sized meteorite inclusions). Since Calcium-Aluminum Inclusions (CAIs), which formed in the inner Solar System, consistently show high abundances in both isotopes, they proposed a mixing of solar nebula material in the early stages of formation. In the same direction are the recent findings of Hellmann et al. (2023), who show that carbonaceous chondrites display correlation in different isotopes abundances which can be explained by mixing of refractory inclusions, chondrules, and chondrite-like matrix. They thus highlight the need for a mechanism to transport these constituents from the inner disc to its outskirts and trap them in rings where the meteorites would form. If dynamical barriers to outwards viscous transport were present, such as the core of a Jupiter-like planet, protostellar outflows might have played this transport role: the grains extracted by outflows from inner disc regions will later fall back onto the disc out to larger radii.

4.7 Conclusions

Recently, extremely low dust opacity indices have been observed at few hundred au scales in the envelopes of Class 0 sources, and have been interpreted as the presence of millimetric dust grains (Galametz et al., 2019). Since theoretical models seem to discard the possibility of growing millimetre grains at the densities typical of protostellar envelopes (e.g. Ormel et al. 2009, Silsbee et al. 2022), we propose here a possible observational test to an alternative explanation, the transport of dust from the disc into envelopes via protostellar outflows. The mechanism has been studied analytically by Wong et al. (2016) and Giacalone et al. (2019) and is supported by numerical simulations of Lebreuilly et al. (2020) and Tsukamoto et al. (2021).

We show a tentative anti-correlation between protostellar envelopes β and their mass loss rates driven by jets and outflows. Such a correlation can be interpreted as supporting a scenario in which protostellar outflows transport large disc grains into the envelopes of young sources.

If protostellar outflows are indeed lifting millimetre grains in the envelopes of young sources, implications are important for the meter-size barrier problem, the reprocessing of dust during its life cycle, and for material mixing throughout planetary systems, as already suggested for the Solar System (see Sect. 4.6). While further measurements of both dust opacity index and mass loss rates will be key in either confirming or disproving such a correlation, we here stress how we explored this possibility with a unique sample in this regard, for which uniform observations, reduction and analyses were carried out. ALMA and JWST synergies will be key to better constrain both dust properties and jets/outflows energetics in a larger sample of young sources.

Acknowledgments

This work was partly supported by the Italian Ministero dell'Istruzione, Università e Ricerca through the grant Progetti Premiali 2012-iALMA (CUP C52I13000140001), by the Deutsche Forschungsgemeinschaft (DFG, German Research Foundation) - Ref no. 325594231 FOR 2634/2 TE 1024/2-1, by the DFG Cluster of Excellence Origins (www.origins-cluster.de). This project has received funding from the European Union's Horizon 2020 research and innovation program under the Marie Sklodowska-Curie grant agreement No 823823 (DUSTBUSTERS) and from the European Research Council (ERC) via the ERC Synergy Grant "ECOGAL" (grant 855130) and from the ERC Starting Grant "MagneticYSOs" (grant 679937). CC and LP acknowledge the EC H2020 research and innovation programme for the project "Astro-Chemical Origins" (ACO, No 811312) and the PRIN-MUR 2020 MUR BEYOND-2p (Astrochemistry beyond the second period elements, Prot. 2020AFB3FX). RSK also acknowledges support from the Heidelberg Cluster of Excellence (EXC 2181 - 390900948) "STRUCTURES", funded by the German Excellence Strategy, and

from the German Ministry for Economic Affairs and Climate Action in project "MAINN" (funding ID 50OO2206). LC thank Chris Ormel and Sebastian Krijt for insightful discussions on this topic. We thank the referees for their helpful comments, which helped us improved the content and presentation of this work.

4.8 Appendix

4.8.1 Binary protostars

When stars form from the collapse of gas clouds, fragmentation of dense cores often leads to binary or multiple systems. It is estimated that the fraction of stars with at least one companion in the Galaxy is between ∼20% for M-type sources up to ∼90% for O-type ones (Offner et al., 2023). The protostars of the CALYPSO sample are no exception. The PdBI observations beam allowed Maury et al. (2019) to separate systems in the maps with separations larger than ∼60 au in Taurus, ∼90 au in Perseus and 132 au in Serpens South. For Serpens Main, the systems (SerpM-SMM4, SerpM-S68N) are probed down to distances smaller than 160 au. These spatial resolutions are based on distance measurements from Zucker et al. (2019) for Taurus (140 pc), Ortiz-León et al. (2018a) for Perseus (290 pc), Ortiz-León et al. (2023) for Serpens South (441 pc) and Ortiz-León et al. (2018b) for Serpens Main (436 pc). Moreover, on the large-scale end, they were sensitive to companions up to ∼1500-2800 au, depending on the region. They finally classified IRAM04191, L1521F, L1527, L1157, GF9-2, SerpS-MM22 as single sources. On the contrary, L1448-2A, L1448-N, L1448-C, IRAS4A, IRAS4B, SerpS-MM18, SVS13B, IRAS2A were classified as having a companion. For each protostar considered in this work, we report the distance of their comapnion(s), if any, in Table 4.2. We note that the tightest binary systems have not been considered here since either a measurement of β, $\dot{M}_J$, or $\dot{M}_{OF}$ was impractical in the studies of Galametz et al. (2019), Podio et al. (2021) or our own, respectively. While most sources of this study are well resolved binaries, their separation is usually closer than the extent of their envelopes, thus they share a common envelope. The only exceptions are SVS13B and IRAS4B1, for which the companion(s) have much wider separations. For all the sources considered in this work, and that enter the tentative correlation described in section 4.5, the source of jets and outflows was well resolved (e.g., see Fig. 4.1) and the measurement of β could be performed after model subtraction of the secondaries. Furthermore, we note that the low β of Galametz et al. (2019) are measured in the inner envelope of each protostar and thus far from possible contamination of the much larger common envelope (see section 4.3).

4.8.2 Details on β measurements of Galametz et al. (2019)

Galametz et al. (2019) measured the dust opacity spectral index in a sample of Class 0/I protostellar envelopes. First, for β to be a trustworthy proxy of the maximum grain size of a dust distribution, the emission over which the radio spectrum is sampled needs to be

Table 4.2: Stellar companions associated to the protostars considered in this work. The separations are reported in Maury et al. (2019). (a): Note that the physical separation of the SerpS-MM18 reported therein should instead be 4420 au, given the most up-to-date distance measurements of the Serpens South region Ortiz-León et al. 2023.

Source	Companion(s) name: distance
L1527	-
L1157	-
SVS13B	SVS13A: 3500au, SVS13C: 4500au
IRAS2A1	IRAS2-A2: 143au
SerpS-MM18a	SerpS-MM18b: 2600au[(a)]
SerpM-S68Na	SerpM-S68Nb: 5000au, SerpM-S68Nc: 8300au
IRAS4-B1	IRAS4-B2: 3500au
IRAS4-A1	IRAS4-A2: 420au
L1448-C	L1448-C(S): 2000au

optically thin. Hence, they estimated the envelopes optical depths and found τ well below 0.1 at few hundred au scales for every source (see their Fig. 2). To make sure the measured β would be representative of the envelope alone, Galametz et al. (2019) subtracted both the emission of binary companions (see Section 4.8.1) and circumstellar discs. The companions were subtracted by fitting and removing a gaussian model centered on the secondary sources from the visibilities (further details in Maury et al. (2019)). Secondly, the contribution of the circumstellar disc orbiting the target protostar was evaluated in the uv space as the mean of the amplitudes after 200 kλ and subtracted from the shorter-baseline visibilities. They test and comment on the robustness of such a correction in their Section 4, where they assess that considering the mean of the amplitudes in slightly different ranges of the long-baseline-end of the visibilities would not affect their results. Moreover, they subtracted the non-thermal dust contribution by extrapolating literature centimetre data for each source, as shown in their Table A.1.

4.8.3 Jets high velocity ranges

In Table 4.3, we report the velocity ranges in which we identify high and low velocity SiO line emission. These ranges were then used to derive mass loss rates from the CO line emission.

4.8.4 Inclination dependencies

As a sanity check for our correlations, we tested whether any underlying correlation exists between the reported (β, $\dot{M}_J$) or measured quantities ($\dot{M}_{OF}$) and the inclination of the sources of our sample. To derive the mass loss rates of outflows and jets, in fact, this work and Podio et al. (2021) assumed velocities of 10-100 km/s, respectively (see section

Table 4.3: Table of identified high-velocity ranges from the SiO jet emission for each source (from Tab.4 in Podio et al. (2021)). Based on these ranges, the high- and low-velocity emission of the CO is defined in order to derive the mass loss rates. Only the blue lobe is detected for IRAS2A1. For L1527, no SiO is detected. Therefore the LV range is defined based on the CO emission, while the HV range is assumed to extend +/-10 km/s with respect to the largest velocity detect in the LV.

Source	Lobe	HV range (km/s)	V_{sys} (km/s)
L1527	B	-21.8/-11.8 7	+5.7
	R	+17/+27	
L1157	B	-60/-20	+2.6
	R	+30/+70	
SVS13B	B	-37/+8.5	+8.5
	R	+8.5/+58	
IRAS2A1	B	-32/-9	+7.5
	R	-	
SerpS-MM18a	B	-17/-2	+8.1
	R	+21/+32	
SerpM-S68N	B	-7/+5	+9.2
	R	+12/+21	
IRAS4B1	B	-30/-5	+6.8
	R	+16/+50	
IRAS4A1	B	-30/-10	+6.3
	R	+30/+70	
L1448-C	B	-70/-22	+5.1
	R	+25/+85	

4.4. Such an approach ensures a uniform method to derive the rates, rather than making assumptions on the inclinations of the jets and outflows since current estimates are either unavailable or very uncertain. Thus, in this section, we check for potential correlation between the quantities involved in our proposed correlation. The inclinations we use have been collected from a number of works. Where more than one estimate was available based on different methods, we reported an average value. If no uncertainty was reported in the literature, for example because the estimate is only of qualitative nature (e.g., for IRAS2A1 reported by Codella et al. (2014)), we plot no error bar. Inclinations for IRAS4A and IRAS4B were reported by Yıldız et al. (2012) and Marvel et al. (2008). The inclination for the jet of SVS13B was reported to be ∼71° by Segura-Cox et al. (2016), while Podio et al. (2016) measured the one for L1157 at ∼73°. Yoshida et al. (2021) constrained the inclination of L1448-C to be ∼34 and ∼46 for the blue- and red-shifted lobes, respectively (in this case, we report the main value and scatter between the two). The inclination of L1527 is well constrained to be almost perpendicular to the sky plane (e.g., 85° in Ohashi et al. 1997). Finally, Plunkett et al. (2015) and Podio et al. (2021) independently and qualitatively assesed that the jet of SerpM-SMM18a lays in the plane of the sky, so we set it $i = 90°$. Figure 4.3 summarises the relationship between the inclinations and $\dot{M}_J$, $\dot{M}_{OF}$, or β for the CALYPSO sample. While a hint for a correlation is seen for the (β, inclination) pair, only a combination of underlying correlations for both β and mass loss rates with inclination would justify the correlation between β and mass loss rates. We thus conclude that possible inclination biases are not driving the correlation in Fig.4.2. 4.4).

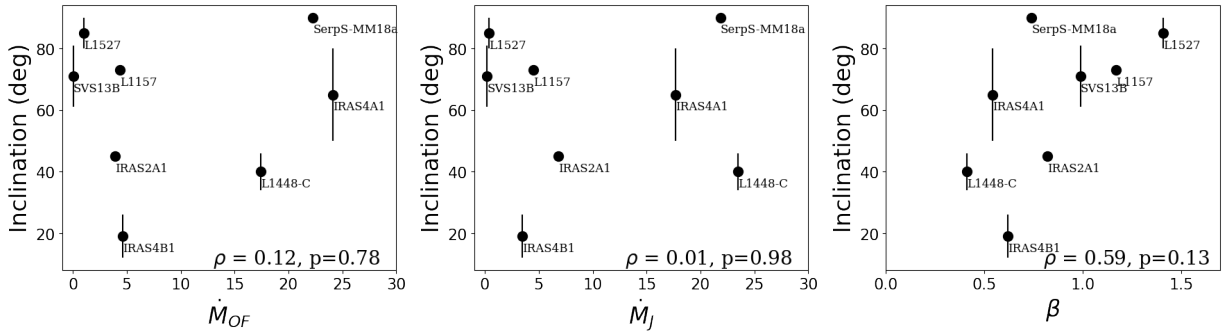

Figure 4.3: Scatter plot of the jets mass loss rates for the CALYPSO sample with inclinations of their jets (left), and same for the outflows mass loss rates (center) and dust opacity spectral index (right). The Pearson correlation coefficient and related p-value are reported in the lower right of each panel.

5

Not all Class 0/I protostars show signatures of early grain growth

This chapter is based on "FAUST XX. Not all class 0/I protostars show signatures of early grain growth"
(Cacciapuoti et al., in preparation)

The Chapter was the result of my own writing. The data were reduced by the FAUST working group, led by C. Chandler. I analysed the data and produced all the plots. The co-authors were involved in discussions and feedback.

Preliminary authors list:
Luca Cacciapuoti; Testi, L.; Maury, A. J.; Chandler, C. J.; Sakai, N.; Viti, S.; Codella, C.; Ceccarelli, C.; Klessen, R. S.; Hennebelle, P.; Molinari, S.; Yamamoto, S.; FAUST collaboration members; ECOGAL collaboration members

Measurements of the submillimetre continuum spectral index in protostellar envelopes are critical to constrain collapsing dust properties, and yet they are rare because of the need for multi-wavelength, multi-scale and low sensitivity data. So far, only the NOEMA CALYPSO Large Program was suitable to measure it at ∼500 au scales in the protostellar envelopes of ten Class 0/I sources across different star-forming regions. To progress in our understanding of the dust size distribution in these collapsing environments, we need to increase the number statistics of such measurements. We present dust continuum emission at 1.2 and 3.1 mm of the ALMA FAUST Large Program to constrain the dust opacity submillimetre spectral index around a new sample of twelve protostars. We combine the dual-band ALMA FAUST observations, sensitive to scales between 50 and 2000 au. We disentangle disk and envelope contributions in the uv-plane, and thus measure spectral indices for the envelopes by correcting for the optically thick emission of the inner regions. We observe a variety of morphologies in continuum: rather compact emission, inner flattened envelopes and bright dusty outflow cavity walls. We find that the central disk-like component of each source has a spectral index $\alpha \sim 2$, consistent with optically thick emission. More importantly, we increase by 60% the number of sources for which the dust opacity spectral index β has been measured so far at envelope scales in a resolved fashion. We find that the majority of the FAUST sources present an ISM-like $\beta \sim 1.6$. We find no correlation with evolutionary stage of the central object, but strengthen the correlation of β with envelope mass as was found by Galametz et al. (2019) for the CALYPSO sample. Our findings indicate that the dust size distribution in the envelopes of the young FAUST Class 0/I objects is consistent with having a maximum grain size below 100μm, consistently with models of dust collapse and evolution, except perhaps in the massive envelope of IRAS4A.

5.1 Introduction

Even if accounting for a mere percent of the material that permeates the interstellar medium, dust grains play several crucial roles in star and planet formation, and thus their evolution needs to be precisely constrained across space and time in star-forming regions.

From the slope of the submillimetre SED (α), the dust opacity spectral index (β) can be derived. The latter carries important information on cosmic dust: once over all, β anti-correlates with the maximum grain size of the distribution (e.g. Testi et al. 2014). In the diffuse end of the interstellar medium, the dust opacity spectral index has largely been characterized to be $\beta \sim 1.6$ (e.g., Schwartz 1982, Weingartner & Draine 2001, Li & Draine 2001). Moreover, large surveys to measure spectral indices in protoplanetary disks have been carried out in order to pinpoint the onset of planet formation, intended as the growth of dust into pebbles that will form planetesimals in disks. These surveys often yielded $\alpha < 3$ ($\beta < 1$) for the majority of disks (e.g., Ricci et al. 2010, Tazzari et al. 2021, Chung et al. 2024). Based on such studies, not only were important constraints derived on the evolution of dust in planet-forming enviornments, but also indirect evidence for protoplanetary disk substructures was suggested as the measured α could be explained by regions of enhancements in the dust surface brightness (Ricci et al. 2012, Delussu et al. 2024).

However, a gap is still open in our knowledge of the life cycle of dust from very diffuse ISM to very dense disks. Indeed, observations in different wavelength ranges have been challenging models of dust coagulation in the ISM, in denser cores, and even more so in collapsing protostellar envelopes. Dust models often assume the ISM dust distribution to be an MRN-lke distribution (Mathis et al., 1977) everywhere in the ISM, and thus with sizes in the [0.005, 0.1]μm range. Near-infrared observations have, on the contrary, hinted to the presence of micronic grains in denser regions of the ISM via extinction measurements (Roy et al., 2013), scattered light "coreshine" effect (e.g., Pagani et al. 2010, Steinacker et al. 2010, Steinacker et al. 2015), and even recent JWST spectroscopy (Dartois et al., 2024). Extinction-based studies can only be used to characterize dust up to visual extinctions of a few, after which the higher densities do not allow any background photon to escape the region and reach our detectors. Moreover, in order to study much denser regions than the ones considered in the above mentioned studies, high spatial resolution becomes a necessity. For these reasons, submillimetre interferometry has been used to constrain the properties of dust in the even denser environments, i.e. collapsing protostellar envelopes, which funnel ISM material onto young, forming stars and planets. Due to the time-consuming, needed observations, which are characterized by large maximum recoverable scales and low sensitivities, collapsing protostellar envelopes have never been largely surveyed to constrain their dust properties. Only a few works have attempted to do so and have found varied results. Kwon et al. (2009) and Miotello et al. (2014) measured low β values (≤ 1) in five combined objects, but with large relative uncertainties ($> 50\%$) due to the high sensitivity

Source Name	L_{bol} ($L_\odot$)	T_{bol} (K)	M_{env} ($M_\odot$)	inc (deg)	Class	Region
IRAS 15398-3359	$0.92^{(a)}$	$44^{(a)}$	$1.2^{(a)}$	$70^{(s)}$	0	Lup
CB68	$0.86^{(b)}$	$41^{(c)}$	$0.9^{(b)}$	$70^{(t)}$	0	Iso
L483	$9.0^{(d)}$	$50^{(a)}$	$4.4^{(d)}$	$83^{(u)}$	0	Aquila
Elias 29	$13.0^{(e)}$	$391^{(f)}$	$0.47^{(e)}$	$60^{(v)}$	I	Oph
VLA1623A	$2.6^{(g)}$	$55^{(h)}$	$0.8^{(h)}$	$55^{(w)}$	0	Oph
GSS30	$1.7^{(i)}$	$50^{(i)}$	$0.098^{(e)}$	$64^{(y)}$	I	Oph
RCra IRS7B	$5.1^{(i)}$	$88^{(i)}$	$6.3^{(l)}$	$65^{(z)}$	0/I	CrA
BHB07-11	$2.2^{(m)}$	$65^{(n)}$	$0.090^{(m)}$	$85^{(m)}$	0/I	Pipe
IRS63	$1.3^{(i)}$	$348^{(i)}$	$0.096^{(e)}$	$47^{(i)}$	I	Oph
NGC1333 IRAS4A	$9.1^{(o)}$	$29^{(p)}$	$12.2^{(p)}$	$65^{(x)}$	0	Per
NGC1333 IRAS4C	$1.1^{(q)}$	$31^{(q)}$	$1.2^{(q)}$	$75^{(xy)}$	0	Per
L1527 IRS*	$1.3^{(i)}$	$41^{(i)}$	$1.2^{(r)}$	$85^{(a)}$	0/I	Tau

Table 5.1: Main properties of the ALMA FAUST Large Program sources analysed in this work. *References:* [(a)] Jørgensen et al. 2013; [(b)] Vallée et al. 2000; [(c)] Launhardt et al. 2013; [(d)] Jørgensen et al. 2002; [(e)] Jørgensen et al. 2009; [(f)] Chen et al. 1995; [(g)] Froebrich 2005; [(h)] Myers et al. 1998; [(i)] Ohashi et al. 2023; [(l)] van Kempen et al. 2009; [(m)] Alves et al. 2017; [(n)] Evans et al. 2023; [(o)] André et al. 2010; [(p)] Sadavoy et al. 2014; [(q)] Mottram et al. 2017; [(r)] Motte & André 2001; [(s)] Okoda et al. 2018; [(t)] Imai et al. 2022; [(u)] Oya et al. 2018; [(v)] Miotello et al. 2014; [(w)] Sadavoy et al. 2019; [(y)] Santamaria-Miranda et al. 2024 ; [(z)] Takakuwa et al. 2024; [(x)] Yıldız et al. 2012; [(xy)] Segura-Cox et al. 2016. Note: (a) L1527 IRS was analysed in the pilot study of Cacciapuoti et al. 2023.

of the observations, the need to combine data from different facilities and the low effective light collecting area of the instruments at play. Following similar methods, other works have not found hints of such grain growth (Agurto-Gangas et al., 2019a). Finally, Galametz et al. (2019) (G19, hereafter) studied the CALYPSO sample of Class 0/I sources presented in Maury et al. (2018). For the ten sources for which they could measure β, they found examples of both relatively low and large β values, with a variety of gradients from the outer to inner envelope that would hint to the presence of submillimetre grains therein. However, simulations of dust evolution during collapse have a hard time reproducing such observations (e.g., Ormel et al. 2009, Bate 2022, Lebreuilly et al. 2023), and only find that grains can grow in envelopes up to $\sim 2\mu$m. Whether we are missing some fundamental aspect on how dust evolve during collapse, or if there are any biases causing the few measured low β, is a question that requires improving the number statistics of available measurements.

The evolution of dust grains in infalling envelopes can affect a set of conditions for star and planet formation. The infalling dust grains of protostellar envelopes will represent the initial distribution of solids in the planet-forming disks. Moreover, envelope dust grains are charged and thus couple with the protostar's magnetic fields: this leads to the well known magnetic braking effect which slows down collapse and regulates the formation of

rotationally-supported protoplanetary disks (Hennebelle & Ciardi 2009, Zhao et al. 2016, Vallucci-Goy et al. 2024). Finally, if grains are larger than expected in the envelopes, they might decouple from the gas and infall faster, leading to increases in the dust-to-gas ratio in the disks, critical to form early planetesimals (Cridland et al. 2022). Theoretical models are now longing for tighter constraints on the dust distribution of these early, large-scale objects to weigh their effect on systems evolution. To sum up, dust evolution at protostellar envelope scales should have significant effects on young systems evolution, and it is thus worth exploring further. In particular, it will be important to extend the sample of measurements of β, as well as independently constrain dust properties by means of near-infrared extinction (e.g., Ysard et al. 2019) or polarized thermal emission (e.g., Valdivia et al. 2019).

In this paper, we aim at improving the number statistics of measured dust opacity spectral indices from submillimetre thermal emission of dusty envelopes, by means of data from the ALMA FAUST Large Program. In Section 5.2, we present the sample and observations. In Section 5.3, we present the method with which we disentangle the disk and envelope emission in the uv-plane and constrain the spectral index. In Section 5.4, we present the measurements of spectral indices for each source. In Section **??**, we focus on the derived dust opacity spectral indices. We discuss our findings in Section 5.5 and sum up our conclusions and prospects in Section 5.6.

5.2 Observations and sample

In this work, we make us of data from the ALMA Large Program "Fifty AU Study of the chemistry in the disk/envelope system of Solar-like protostars" (FAUST, PI: Yamamoto, S.). The main goal of FAUST is to reveal and quantify the variety of the chemical composition of the envelope/disk system of Solar-like Class 0 and I protostars (see Codella et al. 2021 for further details). However, in that context, dust opacity ($\kappa \propto \nu^{\beta}$) is critical when studying line emission, and the only way to properly take it into account in chemistry studies is to spatially resolve the continuum emission at two or more frequencies, so that its brightness temperature can be compared to that expected from disk/envelope models with appropriate heating contributions from the central protostellar engine. FAUST, thus, has observed young sources in two wavelength ranges, nominally the 1.3 and 3.2 mm atmospheric windows. Moreover, FAUST observations cover a range of baselines that ensure a resolution of $0\farcs3$ and a maximum recoverable scale of $14\farcs4$ which, given typical distances of 150 pc for the sources, yield observations that are sensitive to physical scales in the range 50-2000 au. A summary of the main properties for the FAUST sources considered in this study is presented in Table 5.1. Among these, we note that L1527 IRS was analysed in the pilot study of Cacciapuoti et al. (2023), and L1551 IRS5 was excluded since its large-scale continuum is being studied in Sabatini et al., (in prep.).

5.2.1 Data calibration, reduction and imaging

The FAUST data were calibrated using a modified version of ALMA pipeline, using the Common Astronomical Software Applications (CASA, McMullin et al. 2007), version 5.6.1-8. This included a correction for errors introduced by the per-channel normalization of data by the ALMA correlator[1]. Line-free Local Standard of Rest Kinematic (LSRK) frequency ranges were identified by visual inspection and averaged per spectral window, and initial continuum images were produced for each separate ALMA configuration. These were then used as initial models for subsequent per-configuration phase-only self-calibration, followed by amplitude and phase self-calibration. Great care was taken to ensure that the models were as complete as possible to avoid changing the overall flux density scale of the data when doing amplitude self-calibration. The sources are sufficiently bright that per-integration phase-only self-calibration was possible, while for the amplitude self-calibration a per-scan self-cal was used. The per-configuration datasets were then aligned across configurations in both phase and amplitude, again using a self-calibration technique. Improvements in the dynamic range (peak/RMS away from emission) of more than an order of magnitude for the final images were often achieved using this technique for all setups. More details on the FAUST data calibration and reduction can be found in Chandler et al., (in prep.). The data was phase centred on the peak of the continuum emission in order to align the source across wavelengths. In this work, we imaged the continuum data products using a briggs weighting scheme with a robust parameter of 1 in order to highlight, where signal-to-noise allowed, the contribution of the large scale emission in which we are interested. We show the primary-beam-corrected images in Appendix 5.7.1.

5.2.2 Sources morphology

The continuum emission around the young protostars in the FAUST sample presents itself as quite diverse (see Figures 5.11, 5.12, 5.13, 5.14).

Some sources (CB68, L483, Elias 29, GSS30, IRS7B, IRS63, IRAS4C) appear very compact in nature, with small to no obvious extended emission displaying in the standardized images produced for this work (see previous section). However compact, the envelope emission becomes clearer in the uv-plane, where short-spacing (large-scale) emission is observed in excess of the compact component (see Section 5.7.2). Moreover, some of them present signs of more extended emission and this is detected in the form of outflow cavity walls at 1mm, while 3mm goes usually undetected because of signal-to-noise ratio. In one case, for IRAS15398-3359, the extended emission is very clearly associated with the cavity walls carved by the outflow of the central protostar, as observed already in Jørgensen et al. (2013) at 0.88 mm. However, we here detect these structures at both 1 and 3mm. (Fig. 5.11). Finally, for the compact Elias 29, extended dust emission is also detected southwards and likely associated with a reported S-shaped outflow (Fig. 5.13, and Bussmann

[1]https://help.almascience.org/kb/articles/what-errors-could-originate-from-the-correlator-spectral-normalization-and-tsys-calibration

et al. 2007).

On the other hand, another class of sources presents much more extended emission in the form of envelopes. BHB07-11 (Fig. 5.11) displays an inner circumbinary disk and a more extended flattened inner envelope structure, as already observed in Alves et al. (2017). A similar structure is observed for VLA1623A, in which a compact central component is associated with a somewhat similar flattened more disk-like structure that extends for a couple hundreds astronomical units and an even more extended envelope around it (Fig. 5.11). Finally, the protobinary IRAS4A (Fig. 5.14) shows a very bright envelope around both IRAS4A1 (centre) and IRAS4A2 (north-east).

5.3 Modelling in the (u, v) plane

As we are interested into measuring the dust opacity spectral index, and perhaps its gradient, across protostellar envelopes, a multi-scale approach needs to be taken. While very high resolution images across observing wavelengths of e.g., protoplanetary disks, have allowed the community to measure spectral indices reliably in the image plane, the need for a multi-scale (50-2000 au) study to trace dust evolution in envelopes calls for a different approach. Indeed, generating an image from interferometric visibilities is a modelling process in which a certain weighting scheme is associated to the data. Thus, the final model image will trace more compact structures or more extended emission based on which baselines were weighted more among the available ones. For this reason, making an image that ideally traces the source at high resolution and recovers the larger scale emission is challenging, especially when most of the emission comes from within the innermost regions. The result of this procedure is that it is hard in the image plane to disentangle the contributed of compact and extended structures and thus evaluate the contamination of one onto the other when measuring intensity-dependent quantities, like spectral indices. Moreover, an additional uncertainty can come from sparse uv-coverage since its uniformity and density also affect the recovered flux on the sky plane. For the reasons above, we mainly conduct our analysis in the uv-plane, where we aim to model the data with multiple components that trace the inner compact regions and the large scale envelopes. This approach has been benchmarked by e.g., Maury et al. (2018), Tung et al. (2024). The main goal of this kind of modelling is to isolate the central compact, usually optically thick, component. Once this is achieved, this component can be subtracted from the data, so that only the envelope flux contribution is left, which can then be used to compute an uncontaminated spectral index.

To fit the continuum emission visibilities of a system made of n components, we consider the total model to be the sum of the visibilities of the individual components. Thus, the number of parameters in our models varies based on the number of components needed to fit the data: e.g., a power-law envelope and/or one or more Gaussian disks. In particular, the brightness profile of typical protostellar envelopes have long been described by power laws (Plummer 1911, Motte & André 2001, Shirley et al. 2002, Maury et al.

2019):

$$\mathrm{I}^{P}_{\mathrm{TOT}}(\mathrm{R}) = \frac{\mathrm{I}_0}{\left[1 + \left(\frac{\mathrm{R'}}{\mathrm{R}_i}\right)^2\right]^{\frac{\mathrm{p}-1}{2}}}. \tag{5.1}$$

This envelope power law has peak flux I_0 and three free parameters: R_i, R_{out}, p. These are such that the envelope emission is constant within a radius R_i, it follows Eq. 5.1 between R_i and R_{out}, and it is null beyond R_{out}.

For the inner optically thick regions, dominated by a combination of disk and free-free emission, we instead use a Gaussian model (resolved disk). The Gaussian is defined by a peak I_0, a width σ, an inclination *inc* and position angle PA:

$$\mathrm{I}^{G}_{\mathrm{TOT}}(\mathrm{R}) = \mathrm{I}_0 \cdot e^{-\frac{\mathrm{R}^2}{2\sigma^2}} \tag{5.2}$$

In order to fit such models, we used `galario` (Tazzari et al., 2018). This publicly available python package computes a model image given a brightness profile, then it Fourier-transform it into synthetic visibilities and sample them at the uv-points covered by the antenna configurations with which the observations were performed. It samples the parameter space using `emcee` (Foreman-Mackey et al., 2013) and runs a minimum-χ^2 fit between the data and the model visibilities at each trial of parameters set.

We note that where more than one source was present in the field of view (see Figures 5.11 to 5.14), the central source was isolated by excluding the others with angle cuts in the uv-space that coincided with the quadrants where those sources are located ($\phi_{sky} = \mathrm{arctg}(u/v)$). For example, for VLA1623A, the visibilities where selected to avoid the regions where the other three sources appeared by selecting data in cones along the North-South direction. In the case of IRS7B, where the two central sources are very close to each other, a model of two Gaussians was preferred (and sufficient, since no envelope excess is detected, Fig. 5.24). Similarly, a simple Gaussian model fitted the data of GSS30 (Fig. 5.21), IRS63 (Fig. 5.22) and IRAS4C (Fig. 5.23) better than a combined one, since no envelope excess was detected at short spacings. Finally, for IRAS4A, the fit consisted of two Gaussian components and two Plummer envelopes, as the close binary and its extended envelope are clearly detected with high signal to noise ratio (Fig. 5.14). The best fit profiles are overplotted on the data in Figures 5.15, 5.16, 5.17, 5.18, 5.19, 5.20, 5.21, 5.22, 5.23, 5.24, 5.25.

It is noteworthy that, in almost all cases, the Gaussian emission contribution reaches its maximum in the uv-space at about 150-200 kλ, which was the baseline at which Galametz et al. (2019) assumed the compact emission to saturate and hence the one they subtracted at shorter baselines to isolate the envelope contribution in the uv-space. We thus confirm that their approach is robust in this regard.

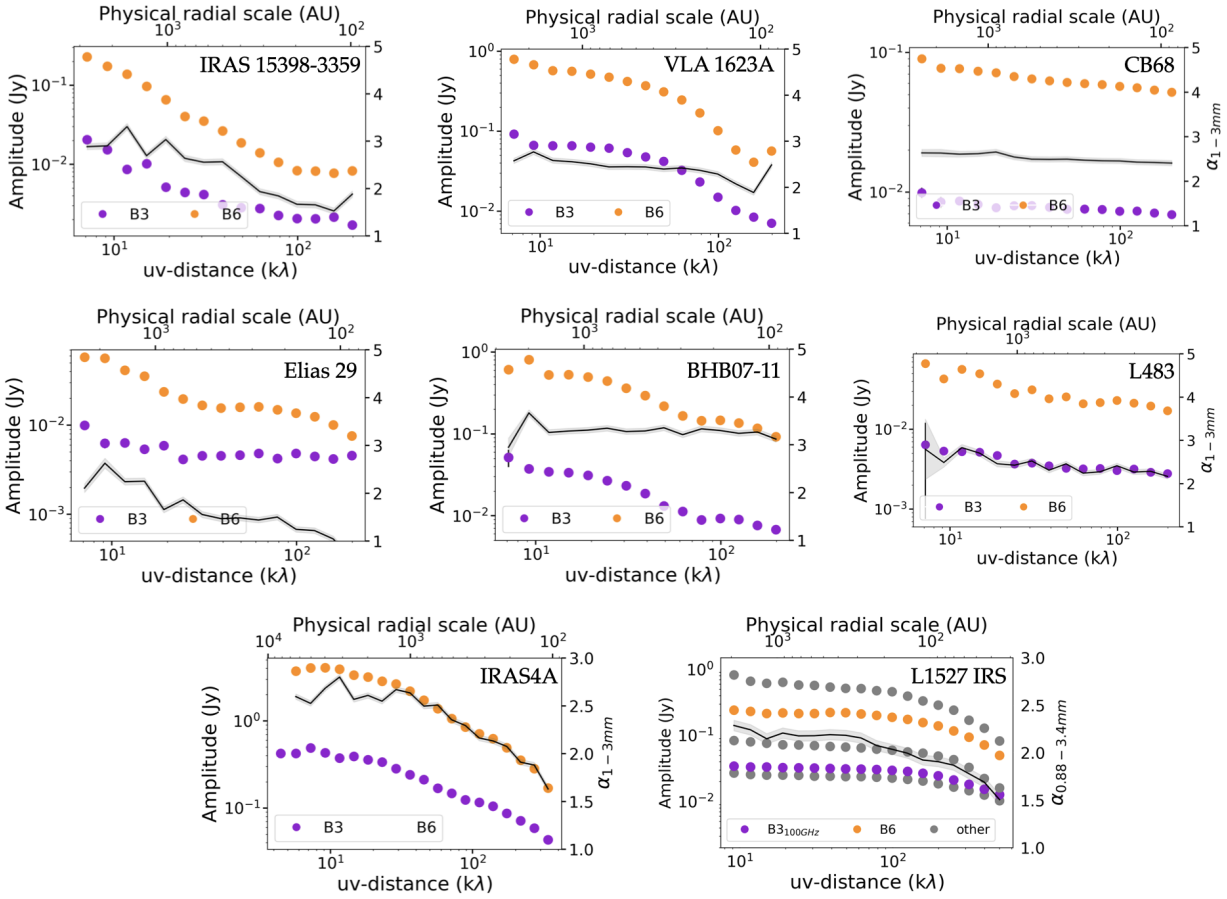

Figure 5.1: Spectral index (black line) of the total emission as a function of uv distance (bottom) or physical scale (top). The azimuthally averaged amplitude profiles in orange (B6) and violet (B3). Note: L1527 IRS is from Cacciapuoti et al. (2023), where only FAUST-like wavelengths have been colored uniformly to the other sources and the other frequencies are in gray.

5.4 Spectral index profiles

The spectral indices were computed in two ways: first, a profile of the spectral index:

$$\alpha = \frac{\log F_{\nu_2} - \log F_{\nu_1}}{\log \nu_2 - \log \nu_1} \tag{5.3}$$

as a function of the uv distance was computed on the total emission (Fig. 5.1). Since both disk and envelope contribute at all uv distances, this spectral index is not representative of one or the other individually, however it mainly traces the disk emission for most sources in which the compact emission is dominating in flux, especially at the long baselines where the envelope is resolved out and $\alpha \sim 2$. Indeed, these spectral indices profiles are consistent with the spectral index of the fitted compact component, as presented in Table 5.2.

Almost all spectral indices are around 2, except the ones of BHB07-11 ($\alpha \sim 2.7$, consistent with Alves et al. 2018) and Elias 29, for which a low $\alpha \sim 1.6$ is derived and could be caused by e.g., scattering effects (Liu, 2019). Then, we show α after the subtraction of

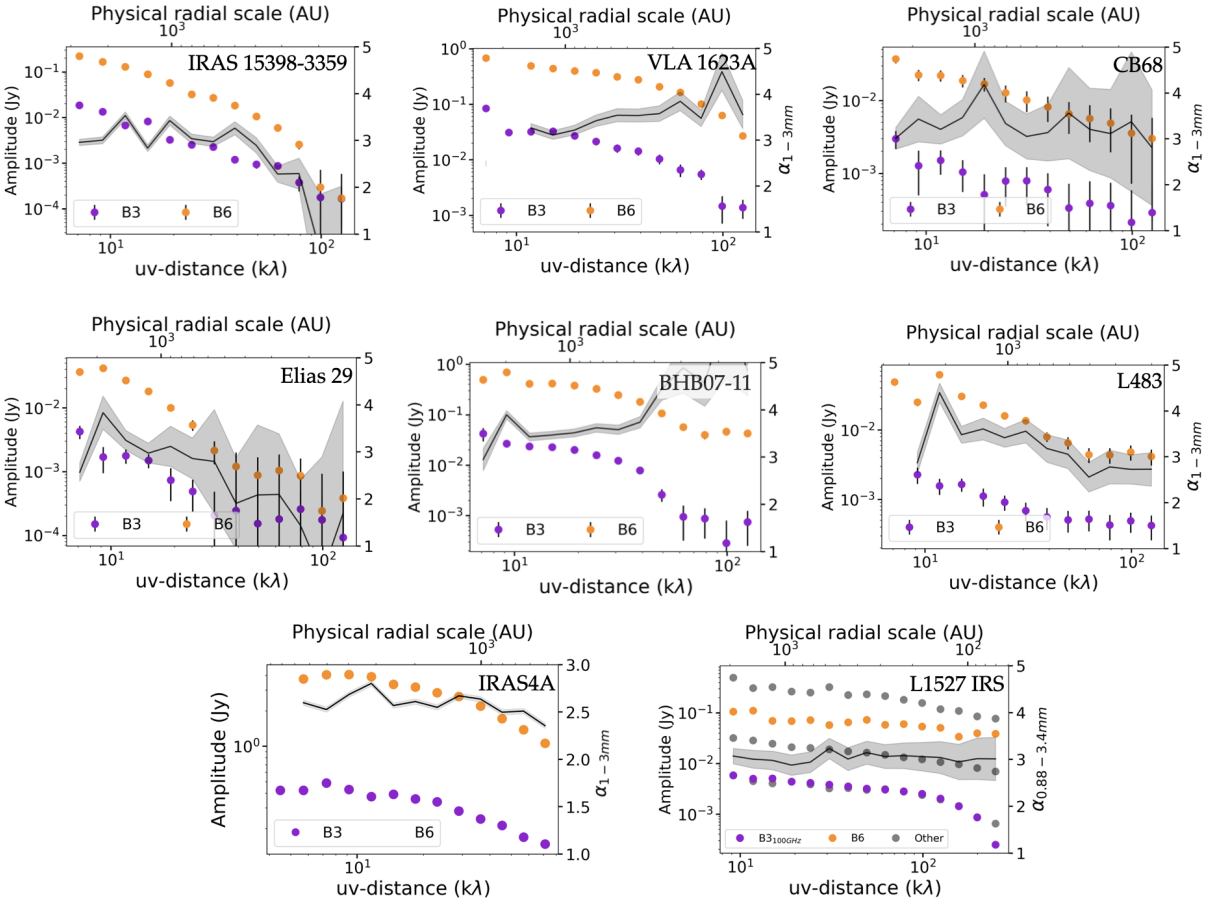

Figure 5.2: Spectral index (black line) of the emission after removal of the central region as a function of uv distance (bottom) or physical scale (top). The azimuthally averaged amplitude profiles in orange (B6) and violet (B3). Note: L1527 IRS is from the multi-wavelength analysis of Cacciapuoti et al. (2023), where only FAUST-like wavelengths have been colored uniformly to the other sources and the other frequencies are in gray.

the compact region emission (fitted as explained in Section 5.3). In this case, the spectral index characterizes the emission from the envelope alone (Fig. 5.2), and one can appreciate how $\alpha \sim 2.5 - 3$ is significantly larger than the total emission case. Finally, we computed the dust opacity spectral index β in the optically thin and Rayleigh-Jeans approximation, $\beta = \alpha - 2$, and in its full form $\beta = \alpha - \mathrm{d}\log \mathrm{B(T)}/\mathrm{d}\nu$, where we assumed a power law for the temperature profile (Adams & Shu 1985):

$$T(R) = 38 \times \left(\frac{\mathrm{L}}{\mathrm{L}_\odot}\right)^{0.2} \left(\frac{\mathrm{R}}{100\mathrm{au}}\right)^{-0.4} \mathrm{K}. \tag{5.4}$$

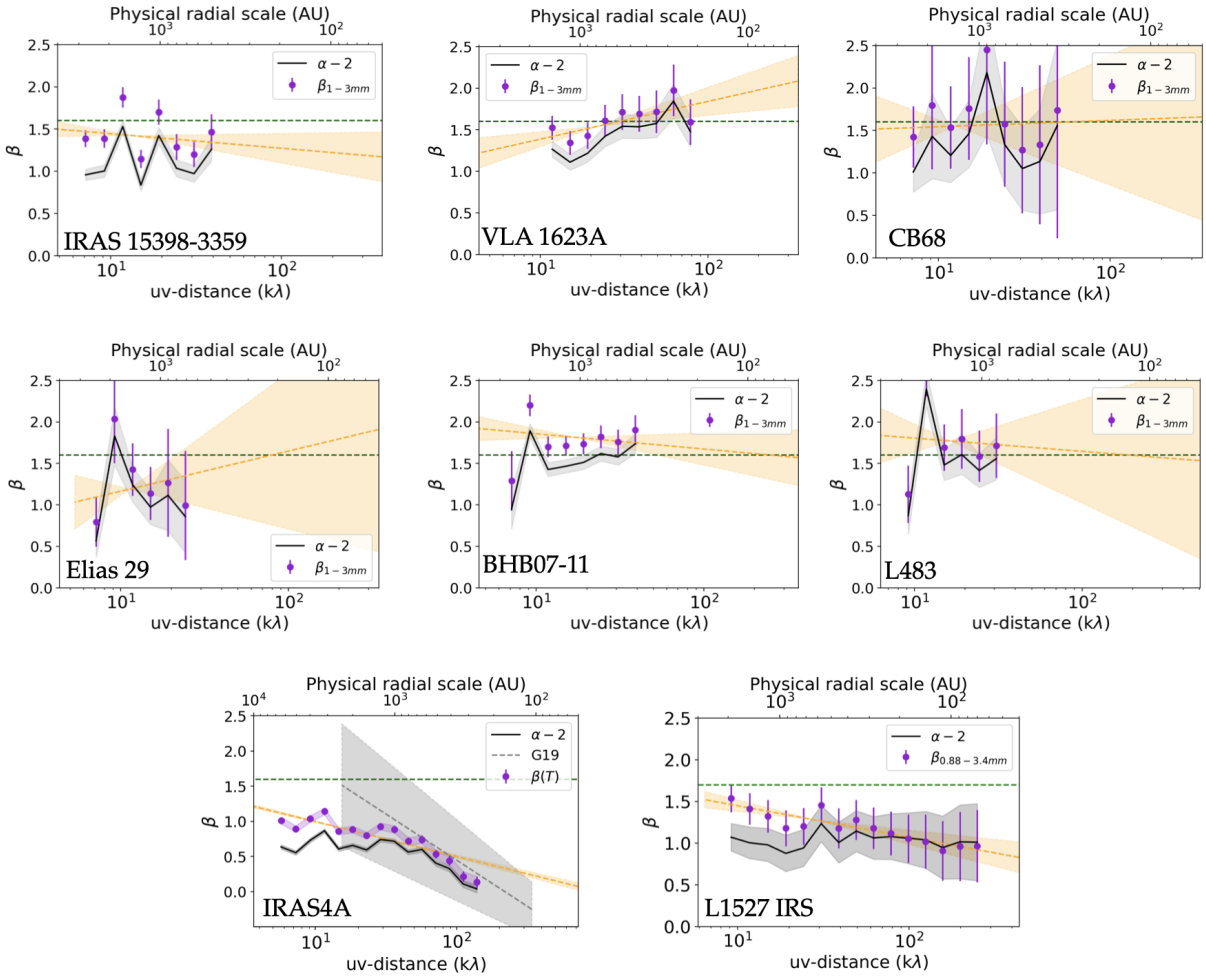

Figure 5.3: The derived dust opacity spectral indices for the sources studied in this work, as a function of uv distance (bottom) or traced physical scales (top). The black lines represent the $\beta = \alpha - 2$ approximation, while the purple dots are derived as $\beta = \alpha - \mathrm{d}\log \mathrm{B(T)}/\mathrm{d}\nu$ in each bin. The orange line is a linear plot to the purple points. The green dashed line is the typical ISM β value. Notes: (i) for IRAS4A we also report the measured β profile of Galametz et al. (2019), limited within the scales that their data probed (see Section 5.4.4); and (ii) the profile for L1527 IRS is from Cacciapuoti et al. (2023).

The resulting profiles of β are shown in Fig. 5.3, limited in a range of baselines over which the envelope contribution to the total emission is significant, i.e. usually within the first 100 kλ[2]. The uv-plane gradient of the profile in the envelope is simply defined by:

$$\beta^{env}(R_{au}) = \beta^{env}_{grad} \cdot \log_{10}(R_{au}) - a. \tag{5.5}$$

[2]After this range, the disk emission dominates and its subtraction translates into large error bars on the remaining flux bins.

Source	F_{3mm} (mJy)	F_{1mm} (mJy)	$\alpha^{compact}$
IRAS15398-3359	1.28	8.09	2.2 ± 0.2
VLA1623A	34.2	202	2.1 ± 0.2
CB68	7.2	55.0	2.4 ± 0.2
Elias 29	3.73	14.1	1.6 ± 0.2
BHB07-11	10.99	114.5	2.7 ± 0.2
L483	2.32	17.4	2.4 ± 0.2
IRAS4A1	31	200	2.2 ± 0.2
GSS30	21.8	106.8	1.9 ± 0.2
IRS7B	48.2	282.1	2.0 ± 0.2
IRS63	37.2	304.1	2.3 ± 0.2
IRAS4C	9.6	67.4	2.2 ± 0.2
L1527[(a)]	28.0	132.0	2.1 ± 0.2

Table 5.2: The 3mm and 1mm fluxes of the fitted compact component for each source. Almost spectral indices (third column) are consistent with optically thick emission (see text). Note: (a) is from Cacciapuoti et al. (2023).

5.4.1 No envelope excess for the Class I sources

Among the studied sources, four present no envelope excess at short spacings and are well fit by disk-like components alone, especially at 3mm. These are: GSS30 (Fig. 5.21), IRS63 (Fig. 5.22), IRAS4C (Fig. 5.23), IRS7B (Fig. 5.24). These sources thus do not appear further in the following discussion as we are here interested in envelopes properties. The main reason for the lack of a clear detection likely stands on the ground of the relatively high sensitivity of the data in combination with the evolutionary stage of these sources (all Class I, except the faint Class 0 IRAS4C), for which the envelope does not represent a dominant component of the system anymore. When comparing to available literature values for the retrieved disk radii of these sources, we find consistent results. Our fits yield a 3σ radius of 98 au for the disk of GSS30, which is consistent with the reported diameter from high resolution 1.3mm observations of the ALMA eDisk Large Program (198 au; Santamaria-Miranda et al. 2024). The fitted disk size of IRS63 is 78 au, in agreement with the continuum observations of Segura-Cox et al. (2020b). The radius of the disk of IRS7B was determined by means of PV diagram analyses by Lindberg et al. (2014), who reported a gas radius of 50 au, and we find a 2σ dust size of 36 au. Lastly, we find a 1σ 34 au radius for IRAS4C which, when taking into account the different model used for the disk emission, well compares to the radius found by Segura-Cox et al. (2016) of 28 au. It is worth mentioning that, using the integrated Gaussian component fluxes output by our modelling scheme, we derive spectral indices consistent with optically thick emission for all of these sources ($\alpha \sim 2$, Table 5.2).

Source	β^{env}_{grad}	β^{env} (500 au)
IRAS15398-3359	-0.17 ± 0.20	1.41 ± 0.09
VLA1623A	0.45 ± 0.25	1.63 ± 0.08
CB68	0.07 ± 0.84	1.58 ± 0.42
Elias 29	0.48 ± 0.99	1.42 ± 0.50
BHB07-11	-0.18 ± 0.25	1.80 ± 0.08
L483	-0.15 ± 0.79	1.69 ± 0.40
IRAS4A	0.76 ± 0.11	1.10 ± 0.03
L1527$^{(a)}$	0.39 ± 0.17	1.24 ± 0.06

Table 5.3: For each source for which extended emission was detected in both bands, we report the measured gradient of the dust opacity spectral index β^{env}_{grad} and a representative value of β^{env} at 500 au, after subtraction of the central compact component. The value of β is extrapolated from the uv-plane for all sources except for IRAS4A, where the image plane value was used (see Section 5.4.4). Note: (a) is from Cacciapuoti et al. (2023).

5.4.2 ISM-like dust across FAUST Class 0 sources

As opposite to what discussed in the previous section, we do detect extended emission for the rest of the sources, and thus we are able to perform our analysis to measure dust opacity spectral indices in the remaining envelopes. We find that for BHB07-11, VLA1623A, CB68, L483, the dust opacity spectral index profile is flat within 1σ and with values $\beta \sim 1.4-1.7$, and consistent within error bars with typical ISM values, indicating maximum grain sizes of the dust distribution below $\sim$100μm. IRAS4A represents a more complex case and it is discussed in Section 5.4.4. In Table 5.3, we report the measured β gradients and their values at a representative scale of 500 au, to enable comparison to the previous sample study of G19.

5.4.3 Dust emission along outflow cavity walls: IRAS15398-3359 and Elias 29

The protostar IRAS15398-3359 clearly displays dust emission along the cavity walls that its outflows are carving in the collapsing envelope (Fig. 5.11), as already observed by Jørgensen et al. (2013) at 0.88 mm. With the ALMA FAUST data, we can now measure the dust opacity spectral index as the cavity walls are detected at both 1 and 3 mm, which results to be $\beta \sim 1.45 \pm 0.1$, consistent with small dust grains. Thanks to the relatively high signal-to-noise ratio and the very extended nature of the emission around this source, we could produce a resolved map of the spectral index. We find that it varies in the range $\alpha \sim 3.5 - 4.2$ along the outflow. If one considers that $\beta = \alpha - 2$ as a first approximation, this values of α result consistent with our uv-plane analysis (Fig. 5.4).

Moreover, we note that the nature of the extended emission around Elias 29 also appears to be tightly linked to the S-shaped H_2 outflow detected by Bussmann et al.

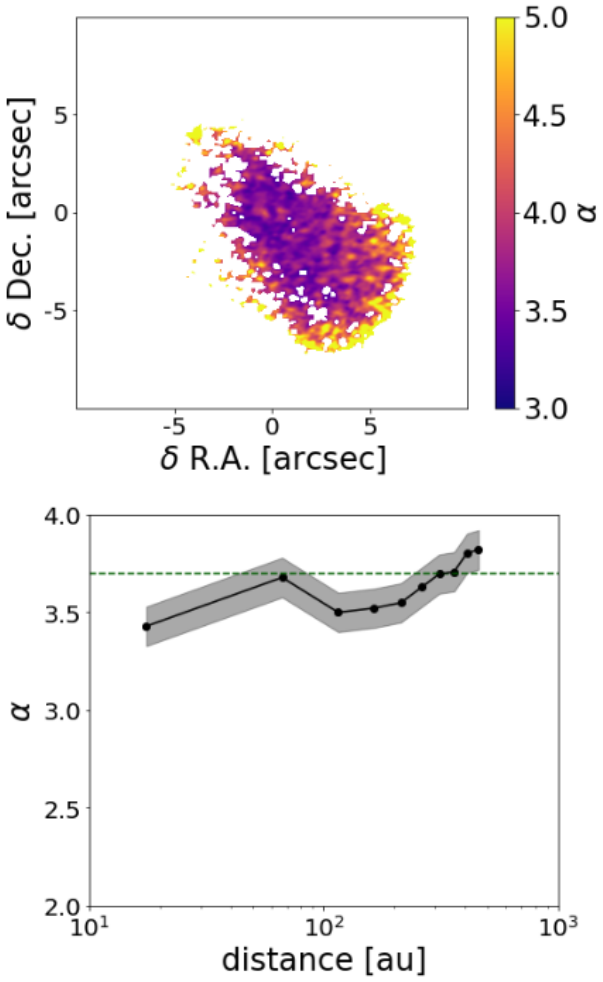

Figure 5.4: A 2D map of the spectral index α around the protostar IRAS15398-3359. Pixels are non-zero where both 1mm and 3mm emission is present at 3σ level, at least. The lower panel profile has been obtained by azimuthally averaging over the black annuli on the map, between 30 and 500 au. It shows a flat, ISM-like $\alpha \sim 3.7$ along the dusty cavity walls of IRAS15398-3359.

(2007), rather than to an infalling envelope. As this outflow appears to be encountering an ISM expanding bubble south of the source (Johnstone et al. 2000, Boogert et al. 2002), shocks might be brightening up the dust emission. It is thus not trivial to exclude that the observed emission and its spectral index $\alpha \sim 3$ is a combination of extended dust thermal emission and non-thermal processes. We thus caution about the grain growth interpretation of Miotello et al. (2014), who found an "envelope" dust opacity spectral index $\beta = 0.6 \pm 0.3$ with lower resolution observations, consistent within 1σ with the one found this work in the same range of uv-distances: $\beta = 1.0 \pm 0.3$ (Fig. 5.3). A more detailed interpretation of the continuum emission of this source lays out of the scope of this work.

We finally note that while only detected at 1 mm, a lower limit for the spectral index of the dusty cavity wall of IRAS4C was published by Sabatini et al. (2024) and that a more in-depth analysis of the cavity wall of L1551-IRS5 is undergoing (Sabatini et al., in prep.).

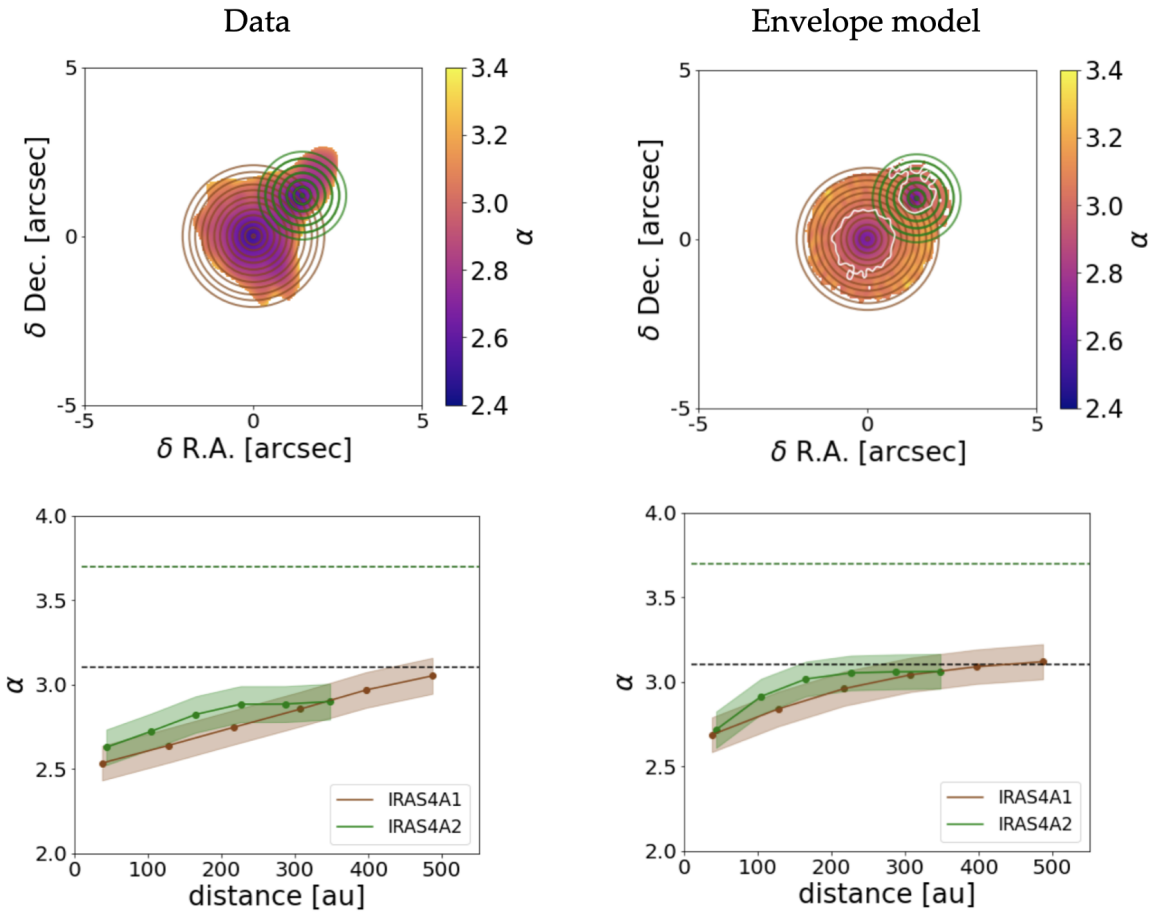

Figure 5.5: Azimuthally averaged spectral index profiles of the total observed emission around IRAS4A1 and IRAS4A2 (brown and green pattern respectively) as measured from the 2D map obtained by computing α pixel-by-pixel from the 5σ clipped images at 1 and 3 mm (upper panel). Same but for the best-fit envelope model component (right). The inner spectral index of the model is higher because the fitted compact component is not included, and it reaches the observed value $\alpha \sim 3.1$ at about 500 au.

5.4.4 The massive envelope of the IRAS4A proto-binary

As anticipated in Section 5.3, we fitted the IRAS4A source with a model that accounts for two disk-like components and two power laws, in order to capture the binary nature of this system (Fig. 5.14). The best fit solution yields remarkable agreement with the source morphology and flux in both bands (Fig. 5.26 and Fig. 5.27), and it is mainly dominated

by the very bright envelopes surrounding IRAS4A1 and IRAS4A2, as was already found by Maury et al. (2018). The resulting β profile in Fig. 5.3 is obtained after subtraction of the two fitted compact components, and thus traces a combination of the remaining contribution of the circumbinary envelope. The measured dust opacity spectral index is consistent with the one found by Galametz et al. (2019), varying between 0.5 and 1.1 across the same range of scales. However, by extending the available probed scales in this work, we can see how the gradient in the uv-plane profile (0.76 ± 0.11) is shallower than the one reported by them (1.31 ± 0.36), because we are able to observe how β saturates around 1.1 at shorter spacings (Fig. 5.3).

Since the envelope of IRAS4A appears very bright even at the high resolutions probed by the FAUST observations, we could produce a resolved map of its spectral index (Fig. 5.5). One can observe how the spectral index varies from $\alpha \sim 2.5$ in the inner 100 au all the way to $\alpha \sim 3.1$ at 500 au from IRAS4A1. It is necessary to highlight that these values are consistent with the ones we find the in the uv-plane, but seemingly at different scales. This appears to be the case because there is no one-to-one correspondence between the uv-distance and the distance from source centre on the sky. In other words, a given uv-distance corresponds to a certain recoverable scale on the sky via a Fourier transform, and not in a simple radial fashion. Indeed, one can see in Fig. 5.3 that, as the recoverable scale grows larger and larger, β saturates because the emission from the source is fully recovered at spacings below about 20 kλ. Nonetheless, since in this study we attempt to fully model the source, we can produce an image of the envelope model at the two bands and compute its spectral index map (Fig. 5.5) in order to retrieve the actual sky plane profile.

The model α map shows how the innermost regions of the envelope, both centered on IRAS4A1 and IRAS4A2, show a relatively higher spectral index $\alpha \sim 2.7$ with respect to the data, because of the absence of the compact Gaussian component. Further and further away from the centre of the sources, the spectral index increases and reaches $\alpha \sim 3.1$ at 500 au away from IRAS4A1, consistently with the α map obtained using the data. Moreover, as the temperatures obtained with Eq. 5.4 are relatively high for IRAS4A even at 500 au, β can be approximated as $\alpha - 2$. Thus, the envelope dust opacity spectral index $\beta \sim 0.5 - 1.1$ between 50 and 500 au. We finally note that, since the inner regions of this source could be partially optically thick given the considered temperature profile on Eq. 5.4 (Galametz et al. 2019), the low α in the inner 200 au could be tracing radiative transfer effects rather than exclusively dust optical properties. Independently, a temperature profile $T \propto r^{-1}$ has been derived for the inner envelope (20-100 au) of IRAS4A (Frediani et al., subm.), which is also consistent with an optically thick medium (Adams & Shu, 1985).

Finally, we note that the reader interested in a resolved spectral index study of the very inner regions (below 100 au) of IRAS4A should refer to Guerra-Alvarado et al. (2024).

5.5 Discussion

In Section 5.1, we discussed how dust grains infalling from protostellar envelopes onto protoplanetary disks: (i) represent the initial distribution of solids that will populate young disks; (ii) can act as regulators for the magnetic breaking efficiency, thus partially driving disk sizes; and (iii) trigger the conditions for planetesimals formation in the disk. These aspects, among others, justify the need to further constrain the dust size distribution in protostellar envelopes, and thus the following discussion.

5.5.1 A variety of spectral indices in protostellar envelopes

From the slope of the millimetre SED, α, the dust opacity index $\beta = \alpha - dlog(B_\nu(T))/dlog(\nu)$ can be derived. This index carries important information on cosmic dust, once over all the maximum grain size of the distribution (e.g., (Testi et al., 2014)). For this reason, large surveys to measure β have been conducted in planet-forming disks to understand when and where grain growth starts (e.g., Ricci et al. 2010, Tazzari et al. 2021). As planet formation has been shown to possibly onset at earlier stages of the star formation process (Manara et al. 2018, Tychoniec et al. 2020, Segura-Cox et al. 2020a), much more attention has been drawn upon the dust sizes distribution during these phases. Not only has there been a shift in time to try and look for the first hints of dust growth, a shift in space has also been suggested. In fact, Kwon et al. (2009), Miotello et al. (2014), and Galametz et al. (2019) underlined a possible gap in our understanding of the life cycle of dust from very diffuse ISM to very dense disks. They indeed measured low dust opacity spectral indices $\beta \leq 1$ in the collapsing envelopes of young protostars, indicating possible grain growth up to submillimetre sizes at scales of hundreds of astronomical units. On the contrary, simulations of dust evolution during collapse have a hard time reproducing such observations (e.g., Ormel et al. 2009, Bate 2022, Lebreuilly et al. 2023), and only find that grains can grow in envelopes up to about 1-2μm. There is thus a 2-3 orders of magnitude tension between the observational evidence and the theoretical predictions, so far.

However pioneering, the observational studies that triggered such a discussion were often based on data with limited spatial or spectral sampling and sub-optimal signal-to-noise ratio. Moreover, such studies would often utilize data from different facilities (such as SMA, ATCA, PdBI) and thus carry potential uncertainties related to the data calibration schemes, which are of the utmost importance when trying to constrain wavelength-dependent quantities like spectral indices (e.g., Francis et al. 2020a). For these reasons, we here decided to attempt to measure β in the uniformly observed sample of the ALMA FAUST Large Program.

5.5.2 The ALMA FAUST sample spectral indices

Among the 13 sources observed by FAUST, we here focused on 12 as an independent study is being carried out on L1551-IRS5 (Sabatini et al., in prep). Of these 13 sources,

we find 5 for which no envelope excess is retrieved at 3mm or in both bands, and thus our methodology cannot be applied. For the remaining 8 sources, we find mostly flat α and β at envelope scales, with values resembling the ones of the diffuse ISM, and thus not showing evidence for early grain growth. Only in the cases of IRAS4A (this work) and L1527 (pilot study of Cacciapuoti et al. 2023) we observe a β gradient. These two sources are in overlap with the CALYPSO sample and thus we can compare our results to the ones of Galametz et al. (2019). In particular, we find consistent values of α and β in the uv-plane for both. However, we can further constrain the gradient of IRAS4A thanks to spatially more extended data (Fig. 5.3): the uv-plane gradient of β flattens out with respect to the one found by Galametz et al. (2019) as β saturates to $\sim$1.1 at shorter and shorter spacings. Moreover, thanks to the overall higher sensitivity and resolution of the FAUST data, we could image the IRAS4A envelope and constrain its spectral index to vary between 2.5 and 3.1 between 50 and 500 au (Fig. 5.5 and Section 5.4.4). As the inner 200 au of IRAS4A are likely optically thick (see Section 5.4.4), this gradient might be shaped by optical depth effects. Even so, at 500 au, where the envelope seems to be optically thin, we find a relatively low $\alpha \sim 3.1$ ($\beta \sim 1.1$), which cannot rule the presence of sub-millimeter grains at those scales.

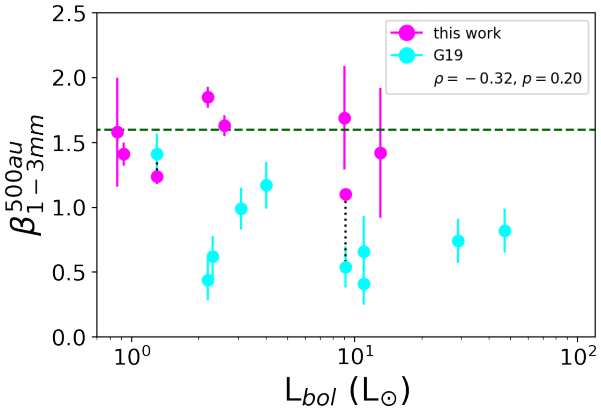

Figure 5.6: Dust opacity spectral index as a function of bolometric luminosity of the sources. A black dotted line connects the measured values for IRAS4A and L1527 IRS in this work and the one of Galametz et al. (2019), overlapping within the FAUST and CALYPSO samples.

5.5.3 The dust opacity spectral index and protostellar properties

In order to look for correlations between protostellar properties and dust opacity spectral indices in envelopes, we have put together the constraints derived in this work with the ones obtained by Galametz et al. (2019) for the CALYPSO sample. Figures 5.6 and 5.7 show the estimated β for all objects at a scale of 500 au as a function of protostellar bolometric luminosity L_{bol} and temperature T_{bol}. It is interesting to note that a correlation

with bolometric temperature might have indicated a link between the maximum inferred grain sizes and the evolutionary stage of the object, or in other words, the timescales over which dust might evolve. A correlation with the internal luminosity might have hinted to changes in β due to higher or lower temperatures in the envelope. Still, no correlation is found between any of the pairs. Finally, we checked whether the measured β correlate with

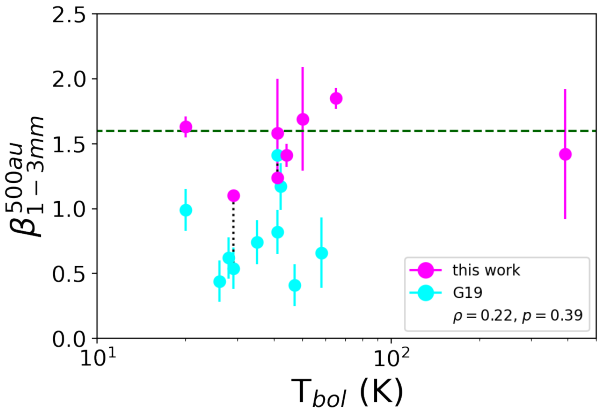

Figure 5.7: Same as Fig. 5.6, but for dust opacity spectral index as a function of bolometric temperature of the sources. Elias 29 is out of scale.

the inclination of the source. We collected sources inclination from the literature based on observations of the outflows geometry (see Table 5.1). We perform this check in order to explore whether more edge-on sources systematically show lower β, which could be caused by high optical depths due to a line-of-sight integration effect. We do not find any such effect, and actually observe many ISM-like β values even for high inclinations (Fig. 5.8).

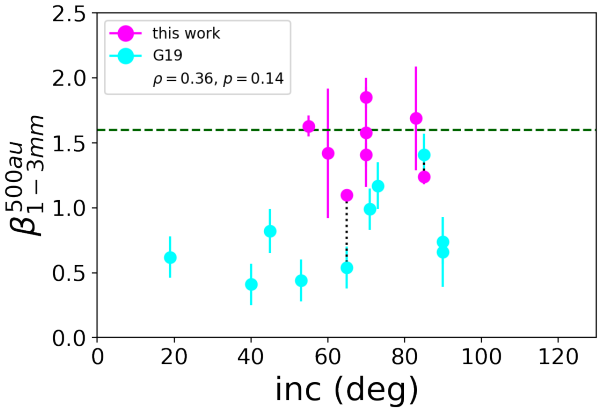

Figure 5.8: Same as Fig. 5.6, but for dust opacity spectral index as a function of inclination.

5.5.4 The dust opacity spectral index and protostellar envelope mass

While no link is evident with T_{bol}, L_{bol}, or source inclination, a significant correlation is found between β and the mass of the protostellar envelopes M_{env}, as well as between the latter and the gradient of the β profile (Fig. 5.9 and 5.10). Both correlations were already shown in Galametz et al. (2019), and here gain in statistical significance. Such correlations have been interpreted as a potential link between the derived β and the mass loss rates of outflows in Cacciapuoti et al. (2024). This scenario was proposed in order to explain the unexpected large grain sizes inferred in envelopes, which seem to be not justified by grain growth models in collapsing environments.

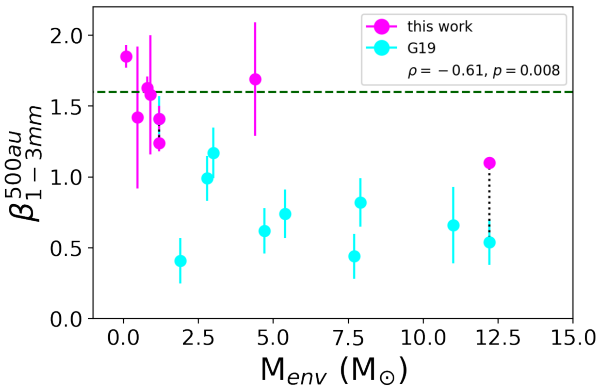

Figure 5.9: Same as Fig. 5.6, but for dust opacity spectral index as a function of envelope mass.

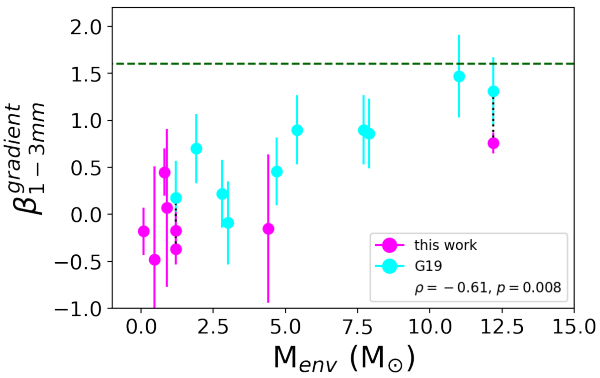

Figure 5.10: Same as Fig. 5.6, but for dust opacity spectral index gradient as a function of envelope mass.

Indeed, according to Bontemps et al. (1996), the envelope mass correlates with the CO flux measured in outflows because ejection and accretion are related in a way that

stronger accretion will lead to more powerful ejection events. Thus, Cacciapuoti et al. (2024) showed a correlation between the observed CALYPSO β values and the mass loss rates associated with their jets and outflows, suggesting it as a tentative evidence of the entraining of large grains from the disk towards the inner envelope. The possibility of such entraining acting at protostellar stages on submillimetre grains is backed up up by the simulations of, e.g., Tsukamoto et al. (2021), Bhandare et al. (2024). The ALMA FAUST program setups, however, do not include the SiO line which can be used to identify high velocity (HV) and low velocity (LV) ranges of ejection and thus we cannot accurately differentiate between LV outflows and HV jets as was uniformly done in Cacciapuoti et al. (2024) to measure the related mass loss rates. Still, we argue that, in light of the correlation found by Bontemps et al. (1996), the FAUST sources seem to be bound to possess low mass loss rates and thus that the high β values we measured for them would preserve (and strengthen) the correlation of Cacciapuoti et al. (2024). In order to further explore the transport scenario, new observations should try to constrain grain properties along outflows across wavelengths (e.g., Duchene et al. 2023, Sabatini et al. 2024).

A necessary note must, nonetheless, be made. Since we discuss the possible implications of high optical depth at the centre of a massive source like IRAS4A, which might contribute to shape the gradient in β (see Section 5.4.4), similar effects could be significant for the other sources of tha sample in Galametz et al. (2019) that hold massive envelopes and show low β values. Whether the relatively higher optical depth of the inner regions of massive protostaller envelopes can drive their inferred β profiles remains an open problem to be tackled with data and models accounting for multiple wavelengths.

5.5.5 Dusty cavity walls

As discussed in the Section above, new measurements of dust optical properties along outflows and outflow cavities will be necessary to constrain the dust size distribution that can be entrained from disks to envelopes. Here, we briefly discuss two sources for which we re tracing such structures.

As presented in Section 5.4.3, the extended emission of IRAS15398-3359 and Elias 29 seems to be tracing dust along the direction of outflows cavity walls. Both sources have $\beta^{grad} \sim 0$ and $\beta^{(500au)} \sim 1.4$ (Tab 5.3). These ISM-like values observed β values in IRAS15398-3359 and Elias 29 could then be interpreted in two ways. One, the observed dust grains are not lifted from the disk but rather are small envelope grains the brightness of which in the sub-millimetre regime is enhanced as they are compressed by the outflowing gas at the cavity walls. Two, that these sources drive relatively weak outflows and thus can only entrain the smallest grains from the disk atmosphere up towards their envelope. While no literature value is present for the mass loss rate of Elias 29, we do have evidence for a relatively weak $\dot{M} = 7 \times 10^{-8} M_{\odot}/yr$ in the case of IRAS15398-3359 (Bjerkeli et al., 2016).

5.6 Conclusions

We characterized the maximum grain size of the dust distribution in the envelopes of the ALMA FAUST Large Program sample of class 0/I protostars. We utilize methods to disentangle disk and envelope emission in order to accurately derive dust opacity spectral indices of the large scale emission. In this study, we increased the number statistics for the available measurements of β in protostellar envelopes, on the base of which we draw the following conclusions:

- the modelled central compact component of each source is always consistent with optically thick emission ($\alpha \sim 2.0$), except for the circumbinary disk of BHB07-11 ($\alpha \sim 2.7$). See Table 5.2.
- The large scale emission of most sources shows a flat profile ($\beta_{grad} \sim 0$) and ISM-like values, which indicate a dust size distribution with maximum grain sizes less than 100μm. This is the case for VLA1623A, CB68, L483, BHB07-11. See Table 5.3.
- The dust opacity spectral index of L1527 IRS and IRAS4A show spatial gradients. The first is discussed in Cacciapuoti et al. (2023). In the case of IRAS4A, β varies from 0.5 to 1.1 in the 50-500 au range. This gradient could potentially be attributed to a combination of grain optcal properties variation with the high optical depth of the innermost 200 au of this source. See Section 5.4.4.
- The extended continuum emission of IRAS15398-3359 and Elias 29 is co-spatial with previously identified outflows (Bjerkeli et al. 2016 and Bussmann et al. 2007, respectively). Both sources are characterized by a ISM-like spectral index, indicating small dust grains along the cavity walls carved by the outflows. Whether these grains are lifted from the disk or are pristine envelope grains detected at compressed cavity walls remains unclear. See Section 5.4.3.
- We find no correlation of β with source evolutionary stage, as identified by the bolometric temperature T_{bol}; nor with the internal source luminosity L_{bol} or source inclination. See Section 5.5.3.
- We strengthen the correlation already found by Galametz et al. (2019) between β (and its gradient β_{grad}) and envelope mass M_{env}. The fact that the inferred dust opacity spectral index lowers in more massive envelopes could potentially be tracing high optical depths at 1mm of the innermost regions of the more massive protostellar envelopes. See Sections 5.4.4 and 5.5.4.

Pushing the limits of ALMA in resolution, recoverable scales, sensitivity, and frequency ranges today allows us to isolate and study the continuum emission of relatively faint, extended envelopes infalling onto young protostars. Increasing the number of sources for which these measurements are performed and refine the methodologies to obtain such estimates is of critical importance to constrain the dust size distribution at the early stages

of collapse. Whether dust growth already starts at envelopes scales and if dust grains are lifted from young disks to envelopes via outflows remain open questions that will need even larger samples and a more thorough understanding of the temperature and optical depth profiles in the innermost regions of these environments. Not only more and better data in the sub-millimetre regime will be crucial. First, infrared data will significantly contribute to narrow the frame around envelope dust properties, by investigating extinction profiles and ices variations at these high densities, now within reach thanks to the sensitivity and resolution of JWST (e.g., McClure et al. 2023, Dartois et al. 2024). Second, polarimetric data could be used to further constrain dust properties as it is sensitive to intermediate dust sizes in the 10-100 μm range (e.g., Valdivia et al. 2019, Guillet et al. 2020).

Acknowledgments

This work was partly supported by the Italian Ministero dell'Istruzione, Università e Ricerca through the grant Progetti Premiali 2012-iALMA (CUP C52I13000140001), by the Deutsche Forschungsgemeinschaft (DFG, German Research Foundation) - Ref no. 325594231 FOR 2634/2 TE 1024/2-1, by the DFG Cluster of Excellence Origins (www.origins-cluster.de). This project has received funding from the European Union's Horizon 2020 research and innovation program under the Marie Sklodowska-Curie grant agreement No 823823 (DUSTBUSTERS) and from the European Research Council (ERC) via the ERC Synergy Grant ECOGAL (grant 855130). This research has received funding from the European Research Council (ERC) under the European Union's Horizon 2020 research and innovation programme (MagneticYSOS project, Grant Agreement No 679937). D.J. is supported by NRC Canada and by an NSERC diskovery Grant. We thank the entire ALMA team for their dedication to provide us with the data we used for this work. This paper makes use of the following ALMA data: ADS/JAO.ALMA#2018.1.01205.L, ADS/JAO.ALMA#2016.1.01203.S. ALMA is a partnership of ESO (representing its member states), NSF (USA) and NINS (Japan), together with NRC (Canada), MOST and ASIAA (Taiwan), and KASI (Republic of Korea), in cooperation with the Republic of Chile. The Joint ALMA Observatory is operated by ESO, AUI/NRAO and NAOJ.

5.7 Appendix

5.7.1 Continuum emission images

While our analysis was not conducted in the image plane, we here report the continuum emission maps for each source of the FAUST Large Program for completeness at both 1 and 3mm.

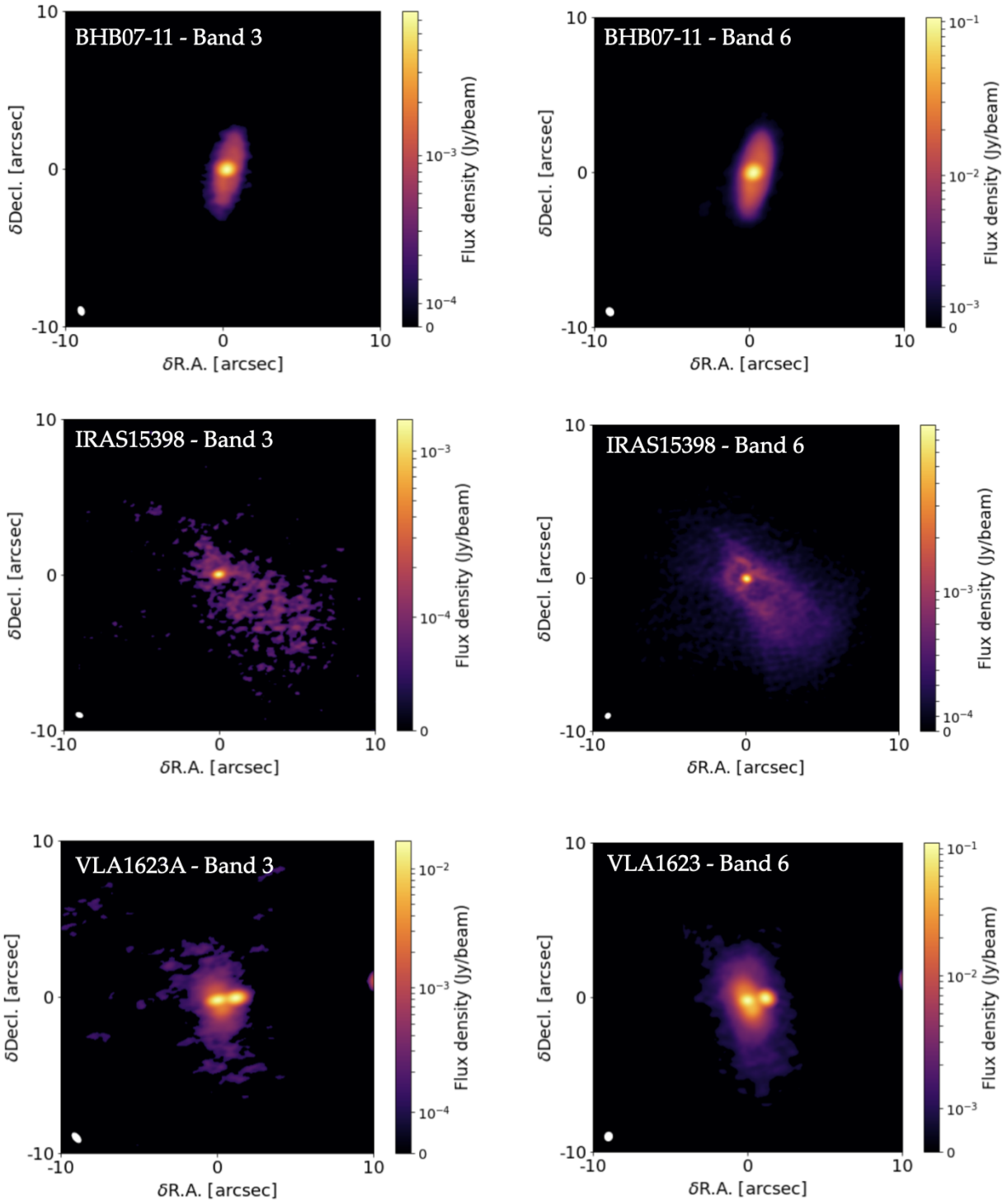

Figure 5.11: The dust continuum emission of BHB07-11 (top), IRAS15398-3359 (middle) and VLA1623 (bottom), as observed with ALMA at 3mm (left column) and 1mm (right column). The synthesized beam is plotted in the lower left in white.

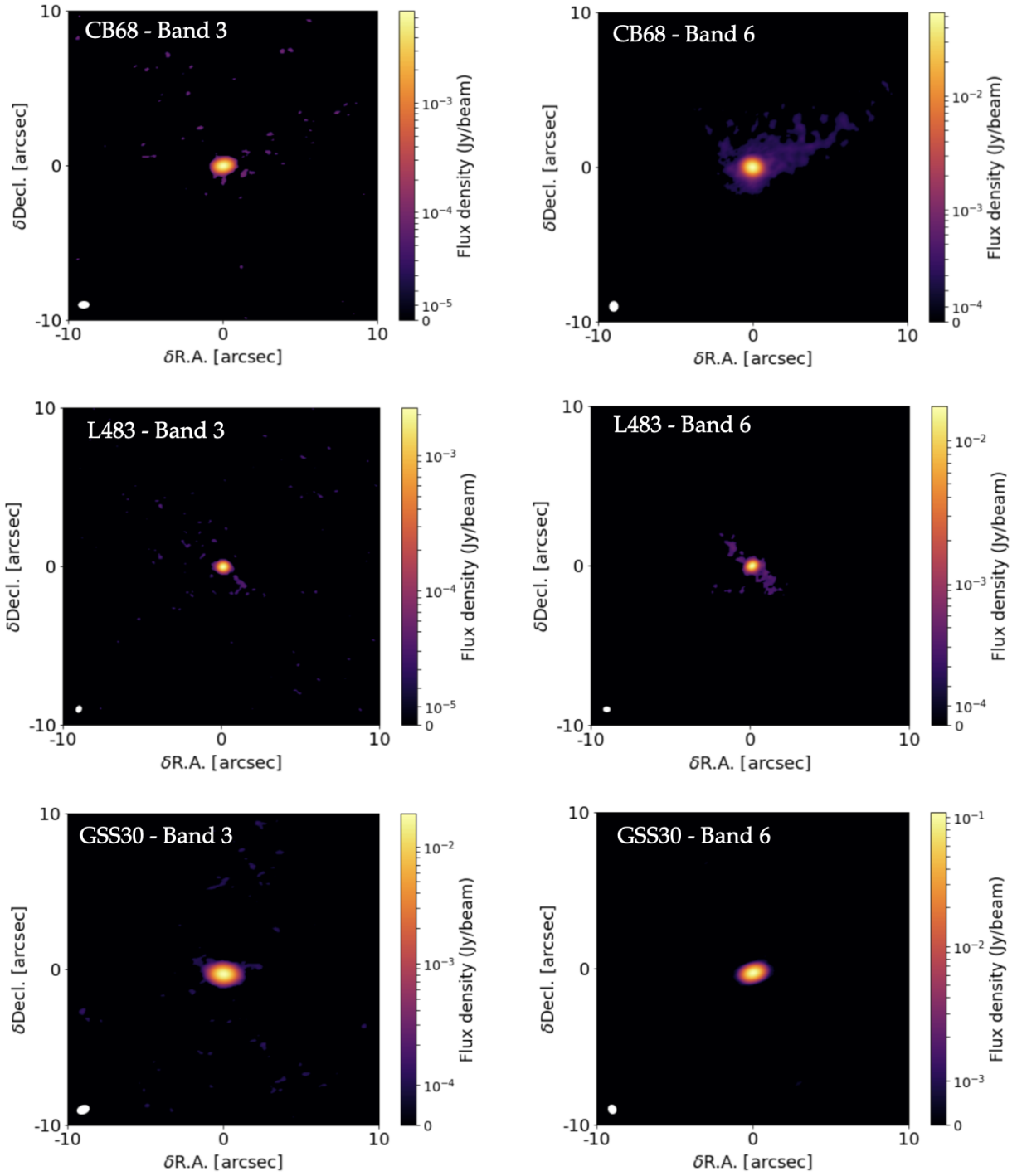

Figure 5.12: The dust continuum emission of CB68 (top), L483 (middle) and GSS30 (bottom), as observed with ALMA at 3mm (left column) and 1mm (right column). The synthesized beam is plotted in the lower left in white.

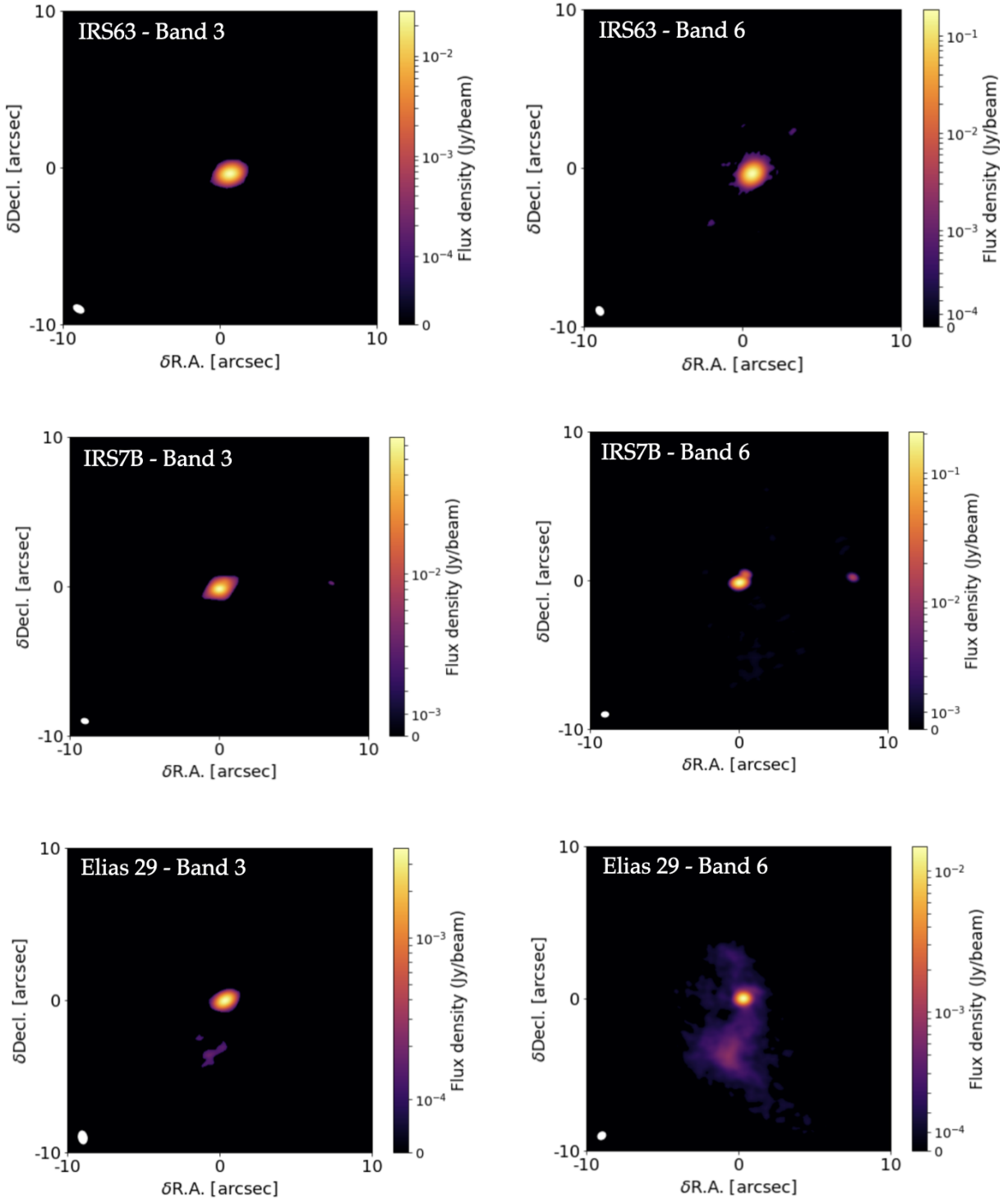

Figure 5.13: The dust continuum emission of IRS63 (top), IRS7B (middle) and Elias 29 (bottom), as observed with ALMA at 3mm (left column) and 1mm (right column). The synthesized beam is plotted in the lower left in white.

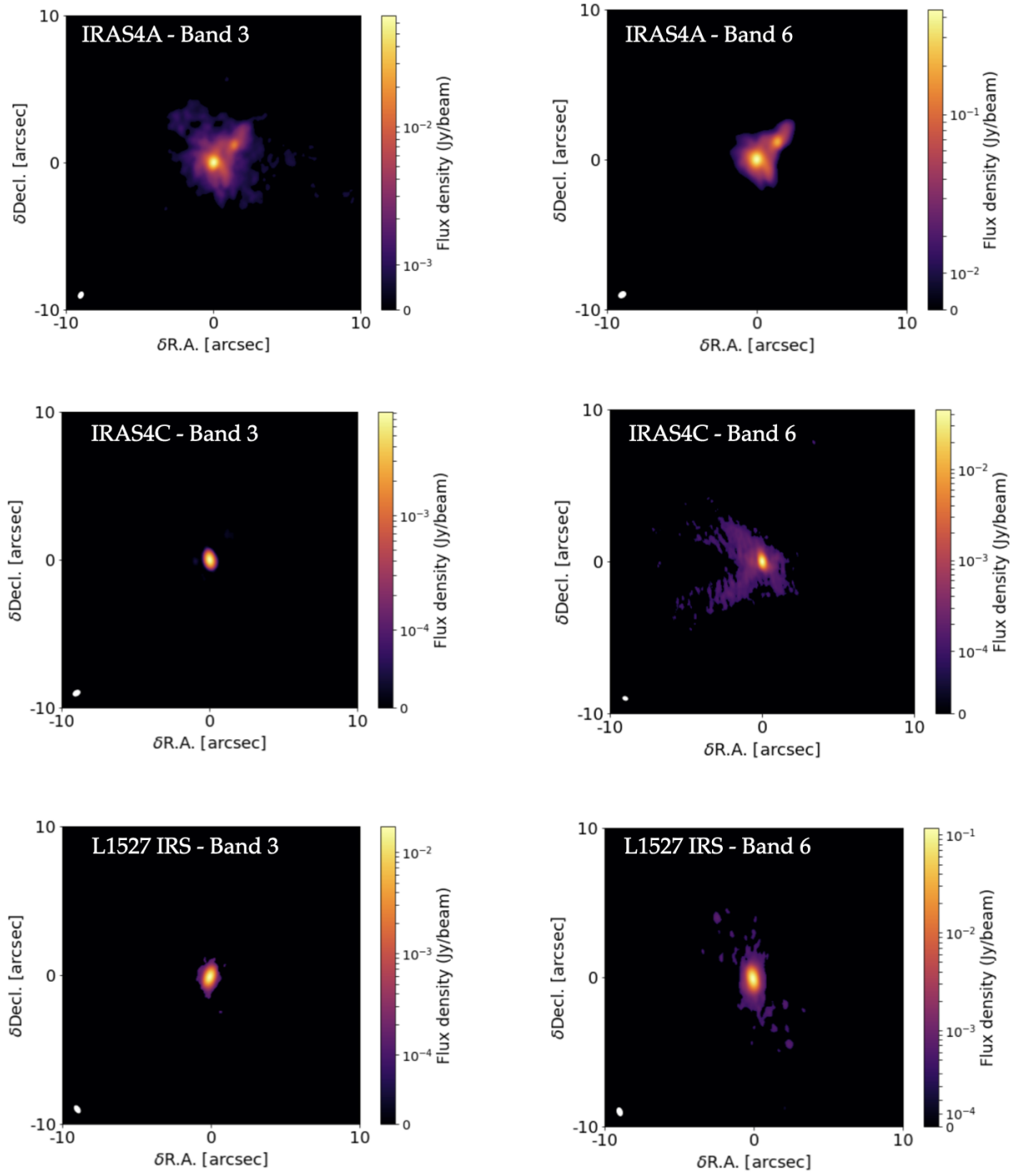

Figure 5.14: The dust continuum emission of IRAS4A (top), IRAS4C (middle), and L1527 IRS (bottom), as observed with ALMA at 3mm (left column) and 1mm (right column). The synthesized beam is plotted in the lower left in white.

5.7.2 Fits results

Here, we report the best-fit models in the (u,v) plane along with the residuals, for each of the analysed sources. The fits are shown on the real and imaginary parts of the visibilities and sampled over the covered (u,v) points, hence the visible wiggles at long baselines. The fits were performed with galario (Tazzari et al., 2018).

5.7.3 IRAS4A model images

Here, we report the imaged model and residuals for the protobinary IRAS4A. These are further discussed in Section 5.4.4.

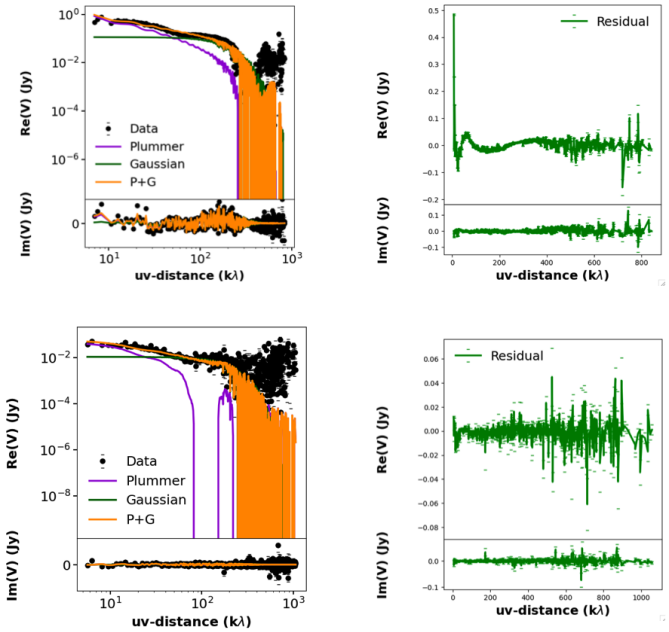

Figure 5.15: Plummer plus Gaussian best fit (orange) is overplotted on the real and imaginary parts of the visibilities for the B6 (upper panel, black points) and B3 (lower panel) observations of BHB07-11. The Plummer only (violet line) and Gaussian only (green line) components of the total model are also shown. The wiggles in the model are due to its sampling on the uv-points of the observations. the residuals of the model are shown in green at the side of each plot.

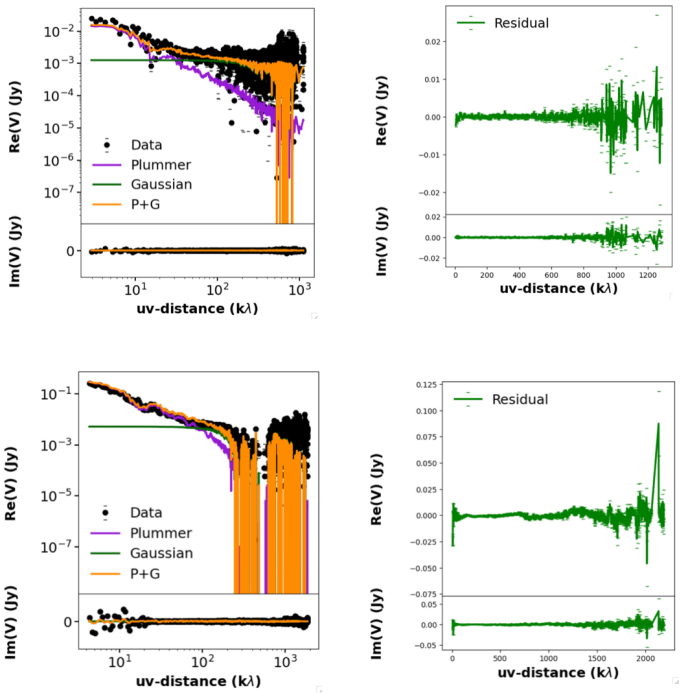

Figure 5.16: Same as Fig. 5.15, for IRAS15398-3359.

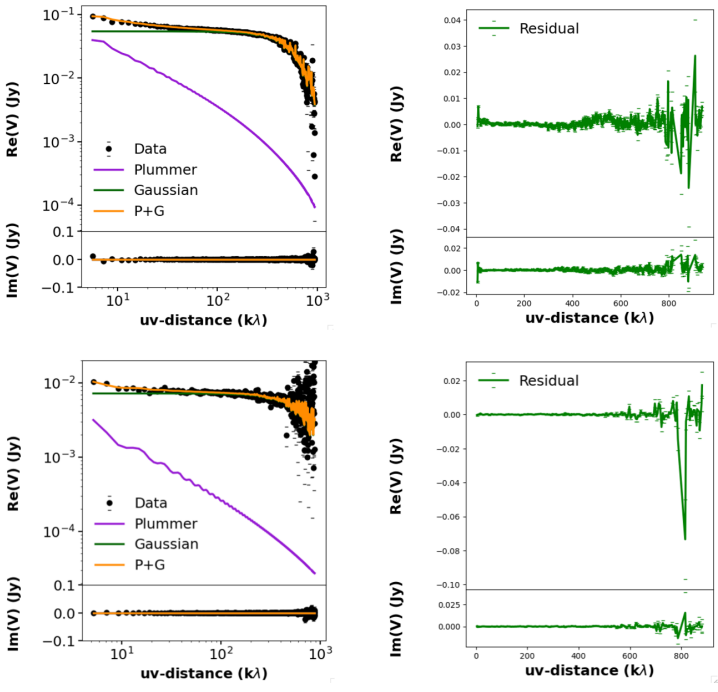

Figure 5.17: Same as Fig. 5.15, for CB68.

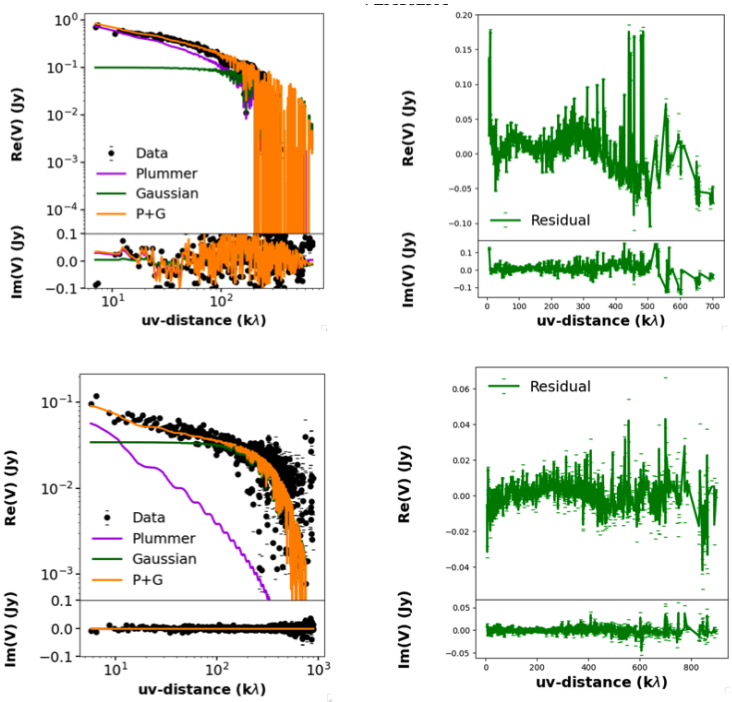

Figure 5.18: Same as Fig. 5.15, for VLA1623A.

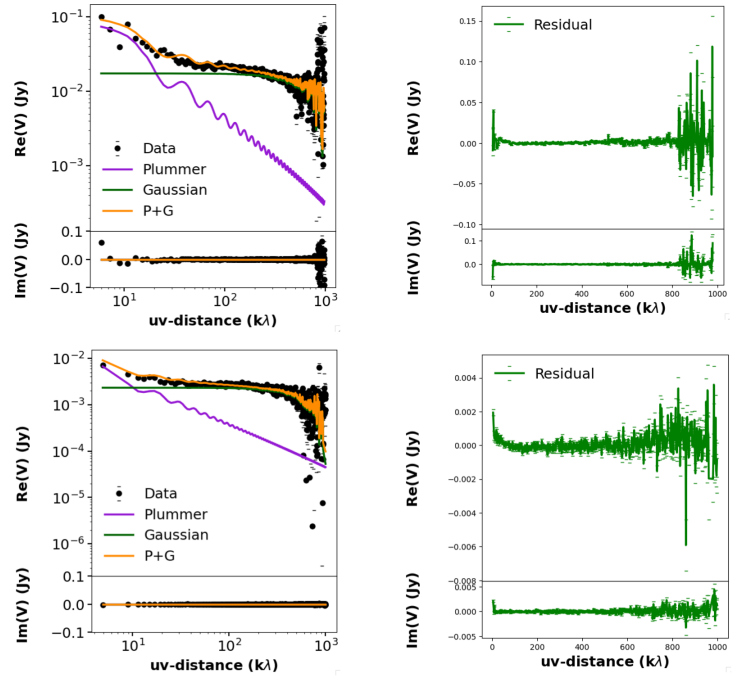

Figure 5.19: Same as Fig. 5.15, for L483.

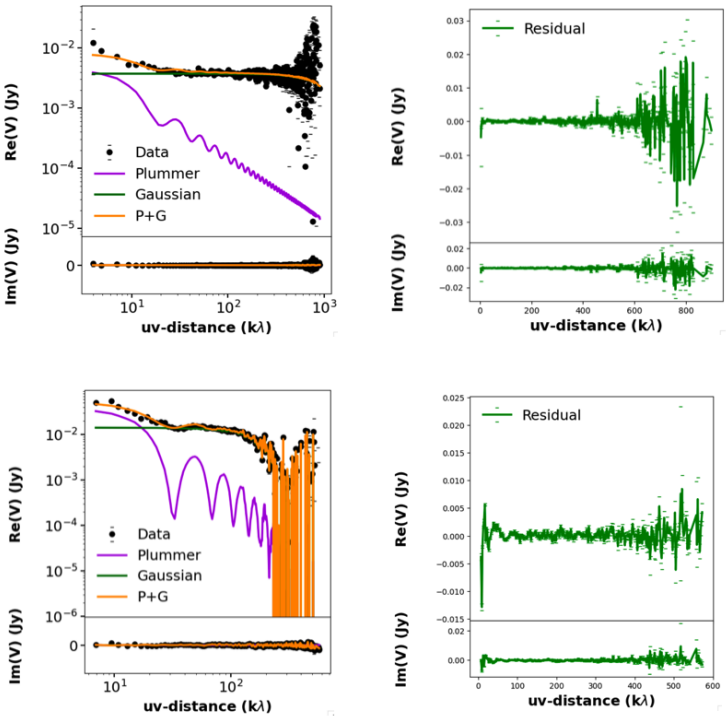

Figure 5.20: Same as Fig. 5.15, for Elias 29.

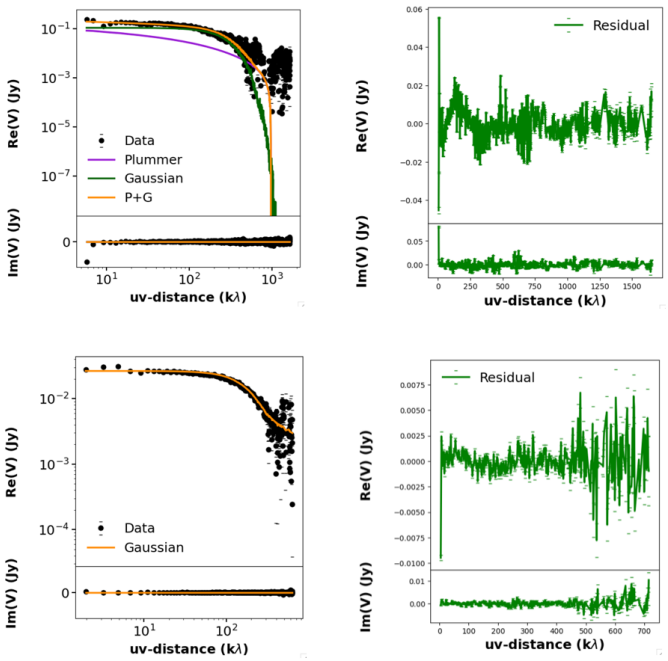

Figure 5.21: Same as Fig. 5.15, for GSS30. The 3mm emission is well fit by a Gaussian component alone.

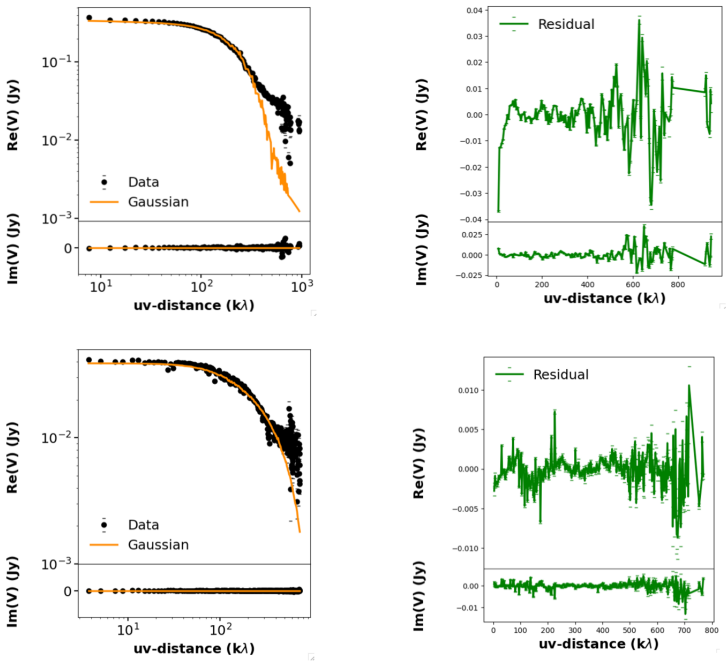

Figure 5.22: Same as Fig. 5.15, for IRS63. The 3mm emission is well fit by a Gaussian component alone. However, the long baselines show an excess emission from the Gaussian likely due to unresolved compact free-free emission. This is thus a preliminary fit that does not change our discussions or conclusions as no envelope emission is detected.

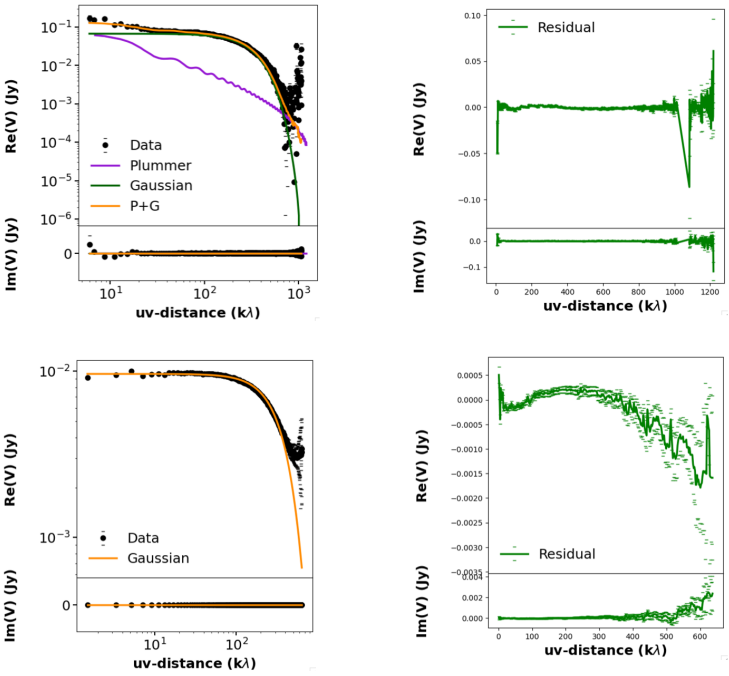

Figure 5.23: Same as Fig. 5.15, for IRAS4C. The 3mm emission is well fit by a Gaussian component alone.

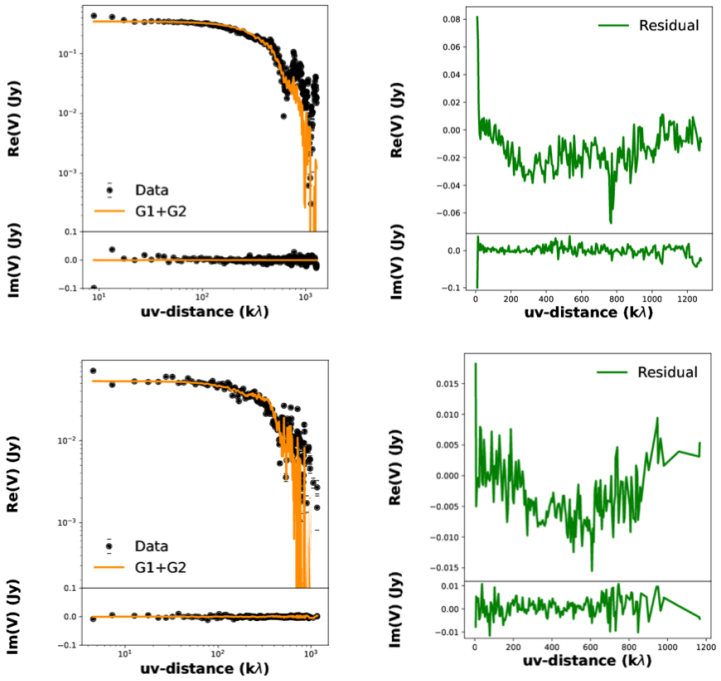

Figure 5.24: Same as Fig. 5.15, for IRS7B. The 1mm and 3mm emission is well fit by two compact Gaussians, consistently to what one can appreciate from the sky image in Fig. 5.13.

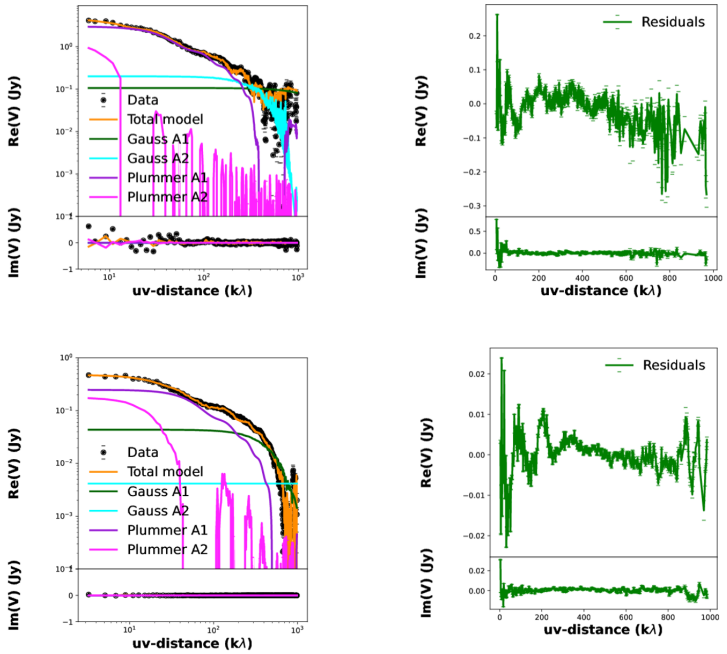

Figure 5.25: Same as Fig. 5.15, for IRAS4A. Here a model including two Gaussians (green and cyan) and two Plummer profiles (purple and magenta) is adopted to account for the binary nature of IRAS4A, consistently to what one can appreciate from the sky image in Fig. 5.14.

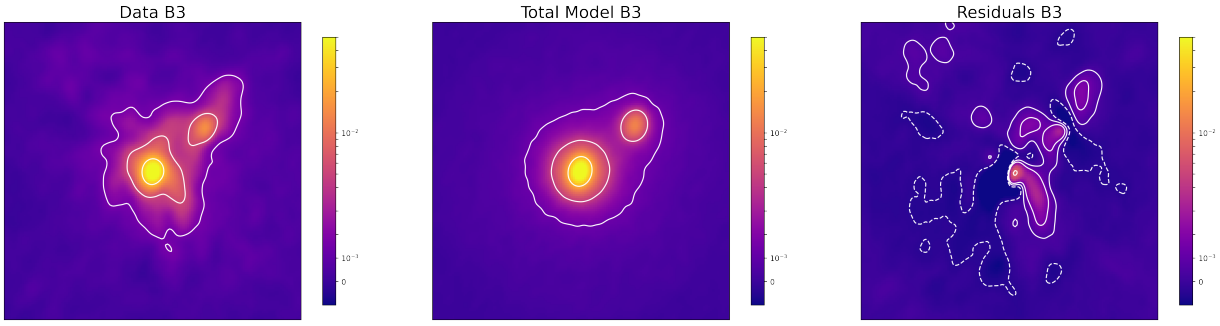

Figure 5.26: The data (left), best fit model (two Gaussians plus two Plummer envelopes) image (centre) and residuals (right). Contours show the [-3,3,10,50]σ levels. The inner components and extended envelope are well captured, while the non-axissymmetric spirals on both IRAS4A1 and IRAS4A2 are seen in the residuals.

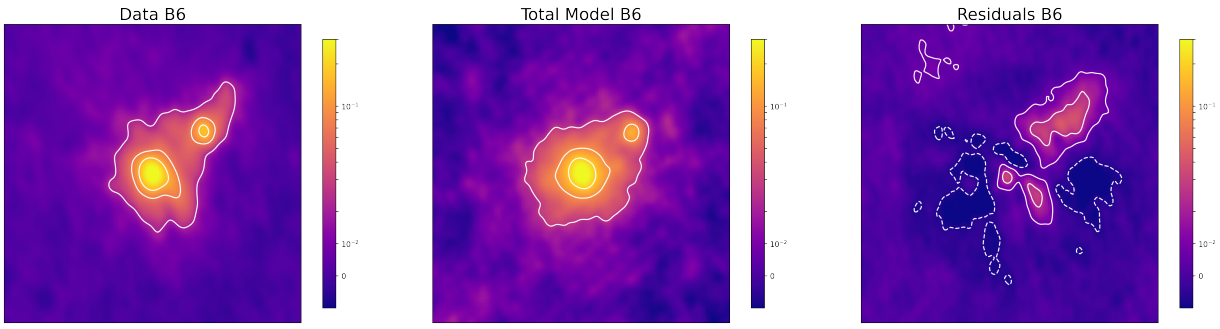

Figure 5.27: Same as Fig. 5.26 but for B6.

6

First measurements of dust properties along an infalling streamer

This chapter is based on "A dusty streamer infalling onto the disk of a class I protostar. ALMA dual-band constraints on grain properties and the mass-infall rate". (Cacciapuoti et al., 2024, Astronomy & Astrophysics, Volume 682, id.A61, 13 pp.)

The Chapter was the result of my own writing. The data were reduced and analysed by me. The kinematic model of Section 6.3 was run by A.Gupta. I produced all the plots. The co-authors were involved in discussions and feedback.

Full authors list:
Luca Cacciapuoti; Macias, E.; Gupta, A.; Testi, L.; Miotello, A.; Espaillat, C.; Küffmeier, M.; van Terwisga, S.; Tobin, J.; Grant, S.; Manara, C. F.; Segura-Cox, D.; Wendeborn, J.; Klessen, R. S.; Maury, A. J.; Lebreuilly, U.; Hennebelle, P.; Molinari, S.

Observations of interstellar material infalling onto star- and planet-forming systems have become increasingly common thanks to recent advancements in radio interferometry. These structures have the potential to alter the dynamics of protoplanetary disks significantly by triggering the formation of substructures, inducing shocks, and modifying their physical and chemical properties. Moreover, the protoplanetary disks are replenished with new material, which increases the overall mass budget for planet formation. In this study, we combine new ALMA band 3 and archival band 6 observations to characterize the dust content and infall rate of a 4,000 au arc-like structure that is infalling onto [MGM2012] 512 (hereafter M512), a class I young stellar object located in the Lynds 1641 region of the Orion A molecular cloud. We detected the extended dust emission from this structure in both ALMA bands. We tested whether the velocity pattern of the streamer is consistent with infalling trajectories by means of analytical streamline models. We measured spectral index maps for the first time and derived a dust opacity-index profile along a streamer. We constrained its grain properties and mass. We find that the arc structure is consistent with infalling motions. We measure a spectral index $\alpha \sim 3.2$ across the entire structure and a dust opacity index $\beta \sim 1.6$. Considering grain properties consistent with the measured β, the structure can host up to 245 $M_\oplus$ of dust, which exceeds or is comparable to the mass of the inner unresolved 600 au, which contains the protoplanetary disk of M512. Assuming a typical dust-to-gas ratio of 1% for the streamer, the free-fall timescales (50 kyr) imply total mass-infall rates up to $1.5 \cdot 10^{-6}$ $M_\odot$/yr. M512 has been classified as an outbursting source with multi-epoch WISE photometry. It is thus an interesting case study for exploring the possible connection between infalling streamers and accretion outbursts. M512 is a unique source for which dust continuum emission of an arc-like streamer extending out to 4,000 au can be characterized in a dual-band

analysis. The dust properties are similar to those in the interstellar medium and imply a high dust mass. A massive streamer like this can affect the evolution of the star- and planet-forming inner system strongly.

6.1 Introduction

Star and planet formation takes place in highly dynamical environments in which the accretion history of these stars and planets can be far from being driven by the traditionally assumed symmetric collapse. Young stellar objects experience episodic anisotropic accretion as they travel through the interstellar medium and gravitationally interact with it (e.g., Lebreuilly et al., 2021; Kuffmeier et al., 2023). Modern radiointerferometers have recently revealed large-scale gaseous structures extending from young stars and their protoplanetary disks at various evolutionary stages. These structures are more commonly observed in near-infrared (NIR) scattered light (Ginski et al., 2021) or submillimeter molecular lines, such as CO (Yen et al., 2019), HCO^+ (Akiyama et al., 2019), H_2CO (Valdivia-Mena et al., 2022), and HC_3N (Valdivia-Mena et al., 2023). Some of them are associated with infall of material as a stream from the surrounding environment (e.g., Tobin et al., 2010b; Alves et al., 2020; Yen et al., 2014, 2019; Garufi et al., 2022; Pineda et al., 2022), via gravitational capture of a nearby cloud fragment during a close encounter (e.g., Scicluna et al., 2014; Dullemond et al., 2019; Ginski et al., 2021; Gupta et al., 2023), or as the result of material that is stripped through stellar flyby events (e.g., Cabrit et al., 2006; Dai et al., 2015; Kurtovic et al., 2018; Winter et al., 2018a; Ménard et al., 2020; Dong et al., 2022).

These so-called streamers have earned significant interest due to their potential impact on the inner star- and planet-forming system. Infalling material might induce perturbations in the disk, triggering instabilities (e.g., Bae et al. 2015, Hennebelle et al. 2017, Kuznetsova et al. 2022). These instabilities could then generate exponentially growing vortices, which act as traps for dust particles, where efficient planetesimal formation might begin (Barge & Sommeria, 1995). Massive infall can also induce inner-to-outer disk misalignments (Kuffmeier et al., 2018, 2021; Ginski et al., 2021), generate spiral waves (Thies et al., 2011; Hennebelle et al., 2017), induce accretion outbursts (e.g., Bonnell & Bastien, 1992; Aspin & Reipurth, 2003), and it can result in shocks with the disk material, leading to localized and significant alterations in the physical and chemical conditions of the disk (Garufi et al., 2022; Kuznetsova et al., 2022). These variations can in turn have a substantial impact on the structural and chemical evolution of the disk. Moreover, the infall of interstellar material can deliver significant amounts of mass to the central protostar and its protoplanetary disk, and this might help to reconcile the discrepancy between protoplanetary disk masses and exoplanet masses (Manara et al. 2018, Mulders et al. 2021). The simulations of Kuffmeier et al. (2023) provided an example of how protostars can sweep up material while moving through their natal clouds, and how they accrete substantial fractions of their final mass in regions that lie even tens of thousands au away from the positions at which we observe them today. In summary, infalling streamers are expected to dramatically influence the evolution of the involved star- and planet-forming systems. However, detecting and characterizing examples of these events is critical for constraining their frequency and magnitude, about which little is known so far.

Recently, Grant et al. (2021) reported the detection of extended continuum and

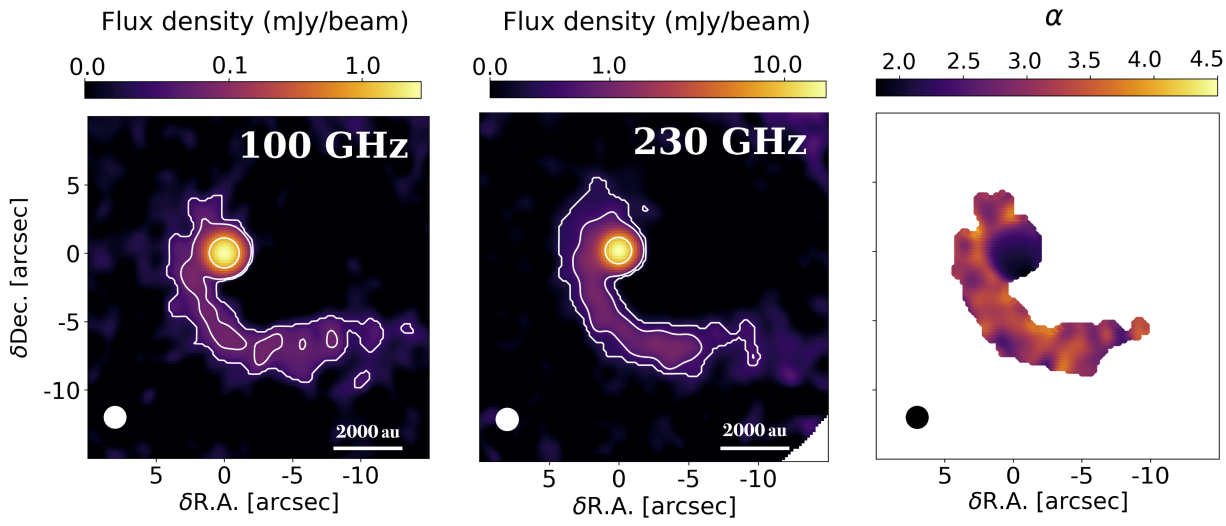

Figure 6.1: ALMA Band 3 (100 GHz) continuum emission of M512 with [3, 7, 100]σ contours overplotted in white (left). ALMA Band 6 (230 GHz) with [3, 10, 100]σ contours overplotted in white (center). The spectral index as measured from Eq. 6.1 using only pixels with flux above the 3σ noise level (right). The x- and y-axes report the offset from the central source in arcseconds. The color bars represent the flux density (mJy/beam) for the ALMA observations (left, center) and the value of the spectral index (right). The images have been created applying a uv taper to the visibilities, with Briggs weighting and robust = 1. Then we have smoothed them to the same resolution of 1$''$.6, which is roughly the width of the extended emission. The beam is reported in the lower left corner.

molecular millimeter emission around [MGM12] 512 (RA = 05h40m13.789s, Dec = -07d32m16.02s). Hereafter, we refer to the source as M512 for consistency with Grant et al. (2021). This young source is located in the Lynds 1641 region of the Orion A molecular cloud at a distance of $\sim$ 420 pc, based on the Gaia DR3 parallax p $\sim$ 2$''$.379 (Gaia Collaboration et al., 2022). This distance is consistent with very long baseline interferometry estimates for Orion nebula cluster (e.g., 414$\pm$7 pc; Menten et al. 2007). In this work, we assume d = 420 pc. The source was classified as class I based on the 2$-$25μm slope of the spectral energy distribution, $\alpha_{2-25\mu m} \sim 0.33$ (Caratti o Garatti et al. 2012 and Megeath et al. 2012). Finally, the main physical properties of M512 were reported by Caratti o Garatti et al. (2012) based on near-infrared spectroscopic measurements, and we summarize them in Table 6.1.

Here, we present new ALMA Band 3 (B3) observations M512 and combine them with archival ALMA Band 6 (B6) data to constrain the dust properties and mass of the extended structure. In Sect. 6.2, we describe the observations, in Sect. 6.3 we discuss the infalling nature of the extended arc around M512, and in Sect. 6.4, we measure the spectral index and derive a profile of the spectral index of the dust opacity. We discuss the results and the possible origins of this structure in Sect. 6.5 and summarize our conclusions in

Table 6.1: Stellar parameters of M512 as reported by Caratti o Garatti et al. (2012), based on its spectral energy distribution and SofI near-infrared spectra.

Alternative ID	IRAS 05377-0733
RA	05h40m13.789s
Dec	-07d32m16.02s
SpT	M7.5 ± 1.5
T_{eff} [K]	2800 ± 200
R_* [$R_\odot$]	3.71
M_* [$M_\odot$]	0.15
L_* [$L_\odot$]	0.9

Sect. 6.6.

6.2 Observations

M512 was observed with ALMA in B6 on 27 November 2019 (2019.1.01813.S, PI: van Terwisga, S.) and on 12 December 2019 (2019.1.00951.S, PI: Grant, S.). Both programs achieved a resolution of approximately 1″.14 and a reported maximum recoverable scale of roughly 11″.7. We refer to Grant et al. (2021) and van Terwisga et al. (2022) for further details and report the main characteristics of their observations in Tab. 6.2.

We here present new ALMA B3 observations of M512 taken on 16 January 2023 (program 2022.1.00126.S, PI: Wendeborn, J.). These were designed to retrieve the 3 mm continuum flux of the extended emission around M512 that was first reported by Grant et al. (2021) at 1.3 mm, with a similar resolution. The bandpass and flux calibrator was J0423-0120, and the phase calibrator was J0542-0913 (see Tab. 6.2).

The B3 data were initially calibrated by ALMA staff using the Cycle 9 ALMA interferometric pipeline (Hunter et al., 2023) within the Common Astronomical Software Applications (CASA; version 6.4.1-12). The B6 data were instead calibrated by the ALMA staff using CASA version 5.6.1-8 for both programs. We carried out further data reduction and calibration steps in both bands using CASA version 6.2.1.7. First, the ALMA cubes for each execution block were inspected and additional flagging was applied when necessary, for instance, to mask out all spectral lines. Among these lines , we note that the same arc-like structure is clearly detected in DCO+ (216.11 GHz) and N_2D+ (231.32 GHz). These lines are not spectrally resolved and thus could not be used in our kinematic analysis (Sect. 6.3).

We then channel-averaged the spectral windows of every execution block. First, we imaged the channel-averaged visibilities with the *tclean* CASA task and fit a Gaussian with *imfit* to identify the emission peak. Next, we used the *fixvis* function to shift the phase center to the position of the peak of M512 at the epoch of every observation. We

are interested in measuring spectral indices, and we therefore checked for potential offsets among the visibility amplitudes of different execution blocks and found none above 3%.

We then phase-self-calibrated the data. We computed the phase corrections on the continuum spectral windows of each execution block using *gaincal* and applied them with *applycal*. This step aimed to correct phase errors between executions and between spectral windows. We repeated this procedure three times, progressively shortening the solution interval. In the first round, we set the solution interval of *gaincal* to *inf*, combined the scans within each execution block, and set gaintype = "G", that is, the gains were determined for each polarization and spectral window. In the second and third rounds, we combined the spectral windows of each block, shortened the solution intervals to 60 and 10 seconds, respectively, and set gaintype = "T" to obtain one solution for both polarizations. At each round, we split and applied the table computed at the previous steps to each execution block. The self-calibration yielded peak S/N improvements of about 15% as the phase of the visibilities were already well constrained. We did not find any appreciable improvement in the properties of the noise and signal-to-noise ratio for phase-only self-calibration steps with even smaller time intervals. The final peak signal-to-noise ratio of the B3 image is 355, and it is 218 for the B6 image.

Finally, we imaged the visibilities to carry out the rest of the analysis. Because the emission is extended, we ran the *tclean* routine setting *pbcor = True* in order to correct for the primary beam attenuation. We deconvolved the images using the hogbom algorithm (Högbom, 1974) with the Briggs weighting scheme, and we tried a number of robust parameter choices to find the optimal balance between resolution and sensitivity. We finally carried out the analysis on images with robust = 1, a pixel size of 0.″2 (84 au at the distance of M512, one-seventh of the synthesized beam) and an image size of 300 pixels. When running *tclean*, we manually masked the emission, which is comprised of both the bright inner disk and the extended streamer, and CLEANed down to 1.5 times the image rms. Because we wish to compare emission that traces the same physical scales, we used a *uvtaper* to weight the visibilities in order to obtain similar synthesized beams for the two bands (1.″5 x 1.″2, PA = 72°). Finally, we smoothed the images to the same resolution of 1.″6, which is roughly equal to the width of the extended emission at the 3σ level recovered by Grant et al. (2021) with robust = 0.5 (see their Fig. 13). We recovered an arc-like structure that extends radially to about 4,000 au. We note that the length of the streamer as observed in this study is to be considered a lower limit because the interferometric observations might have filtered out larger-scale emission. Moreover, we report a $C^{18}O$ $J = 2 - 1$ transition moment-one map of M512 obtained with the observations of ALMA program 2019.1.00951.S (Fig. 6.2). In what follows, we focus on characterizing the kinematics and the dust content of this extended structure, to which we refer as "streamer" hereafter.

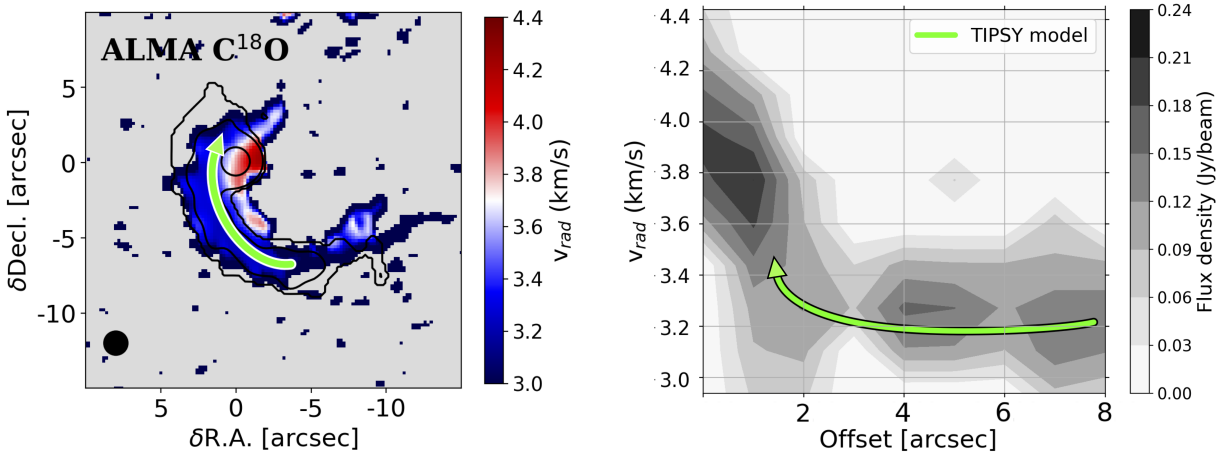

Figure 6.2: Moment-one map of the ^{18}CO J = 2 − 1 transition ($> 2\sigma$) around M512 (*left*). The black contours are the B6 continuum [3, 10, 100]σ levels. The green line is the TIPSY model trajectory for M = 0.15 $M_\odot$ and v_{sys} = 3.25 km/s. The position-velocity diagram of the streamer emission (grey contours) is extracted along the TIPSY trajectory and includes the inner protostellar region (*right*). The TIPSY fit to the radial velocities is reported as a green line.

6.3 Streamer kinematics

Whether extended structures such as the one linked to M512 are actually infalling on the central protoplanetary disks is a problem that requires precise constraints on the geometry and physical properties of the system. In our case, the unknown details of the geometry of the inner disk, due to somewhat limited spatial resolution, introduce uncertainties in the interpretation of the velocity structure around the source. To complicate the problem further, both the mass and system velocity are uncertain. The former is affected by the precision to which spectral types are determined by near-infrared spectra (Caratti o Garatti et al., 2012), the high extinction of this region (e.g., Gutermuth et al. 2011), and the contribution of the inner embedding material connected to an envelope remnant or to the streamer itself. Furthermore, the limited spectral resolution and the potentially high optical depth of the CO isotopologs limits the accuracy with which we can estimate the system velocity. In this section, we analyze the C^{18}O J=2-1 transition that was presented in Grant et al. (2021). Among the other isotopologs, we chose this transition because its emission is optically thinner than that of ^{12}CO and ^{13}CO and it is less affected by foreground absorption. We imaged the spectral cube containing the spectral window of the line with the same scheme of the continuum dataset. During the cleaning, we masked the emission manually, channel-by-channel, in order to capture its complex morphology.

The moment-one map shows an arc-like feature consistent with the 1.3mm dust continuum emission region, and it is characterized by a progression from lower to higher velocities when approaching the protostar from afar (Fig. 6.2). This gradient may be in-

dicative of infalling motions toward the inner object (as observed in, e.g., Per-emb 2; Pineda et al. 2020, Per-emb 50 Valdivia-Mena et al. 2022). The velocity transition between the streamer and the inner material might also indicate rotation of the innermost embedding material. We attempted to model the $C^{18}O$ kinematics to constrain whether the data are consistent with infalling motion. We analyzed the spectral cube with the code called *trajectory of infalling particles in streamers around young stars* (TIPSY; Gupta et al., 2023). The input for the code were the mass of the central object and its line-of-sight velocity (v_{sys}). We set the former to 0.15 $M_\odot$, as reported in Table 6.1. We note that the inner envelope mass and even the streamer mass might contribute significantly to influencing the ballistic motion of a particle. For the latter, we explored a range of systemic velocities consistent with the observed $C^{18}O$ spectral line, between 2.9 and 3.9 km/s. Based on these constraints, TIPSY solved analytical kinematics equations for an infalling parcel of gas that feels the gravity of a central source from Mendoza et al. (2009) and computed its trajectory throughout the region over which we detect emission, as well as the kinetic gravitational (and thus total E_{tot}) energy of the parcel and its infall timescale. We overplot a TIPSY fit model to the moment-one map in Fig.6.2 to show that the arc-like feature around M512 is consistent with the infall of material. The available data are consistent with infall for velocities in the explored range of v_{sys}, but the material is only loosely bound ($E_{tot} \lesssim 0$) for $v_{sys} \gtrsim 3.7 km/s$. The TIPSY model constrains the infall timescales to about 50 kyr. We overplot the radial velocities as fit by TIPSY in a position-velocity diagram (PVD; Fig.6.2) obtained using pvextractor (Ginsburg et al., 2016). The PVD was extracted along the infalling trajectory shown in Fig.6.2, and it includes the inner region. The width of the selected path is equivalent to the beam, 1.″6. The TIPSY model is consistent with the radial velocities of the observed emission. New observations will be key to constraining the geometry, the system velocity, and the effect of the streamer mass on the infall trajectories.

In Sect. 6.5 we discuss further qualitative arguments that support the infall scenario against alternatives such as stripping due to a flyby or the cavity wall of an outflow. We thus tentatively suggest that the arc-like structure detected around M512 is an infalling streamer.

6.4 Spectral index

The slope of the radio spectrum

$$\alpha = \frac{\log_{10} \mathrm{F}(\nu_2) - \log_{10} \mathrm{F}(\nu_1)}{\log_{10} \nu_2 - \log_{10} \nu_1}, \tag{6.1}$$

where ν_i are the observed frequencies, can provide valuable insights into the properties of interstellar dust grains. Because the dust opacity follows a power-law relation $\kappa \propto \nu^\beta$ at the millimeter end of the spectrum, $\beta = \alpha - 2$ in the optically thin regime and if the Rayleigh-Jeans (RJ) approximation holds (e.g., Draine 2006, Beckwith & Sargent 1991, Miyake & Nakagawa 1993, Natta et al. 2007). The typical dust opacity index observed for

the interstellar medium, $\beta \sim 1.6$, is usually interpreted to mean that the maximum grain sizes of the dust population range from 100 Å to 0.3 μm (Weingartner & Draine, 2001). In contrast, a value $\beta < 1$, which is often measured in class II objects, indicates the presence of larger grains, with sizes $a \geq 1$ mm, in more evolved disks (Beckwith & Sargent 1991, Ricci et al. 2010, Testi et al. 2014, Macías et al. 2021).

In the following analysis, we present maps of the spectral index α and the profile of the dust opacity spectral index β in the emission region of M512 and its streamer.

6.4.1 Spectral index maps

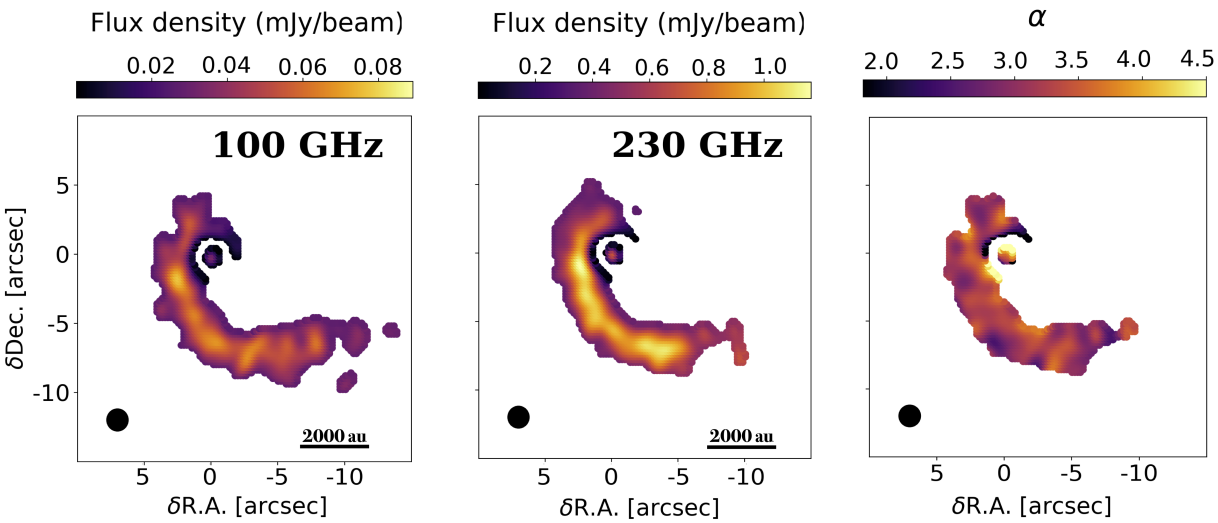

Figure 6.3: Same as Fig. 6.1, but after subtraction of the inner optically thick region. Only the pixels with flux above 3σ are shown for each inset.

Using the ALMA B3 and B6 maps, we calculated the spectral index α at each pixel in our smoothed maps. This procedure yielded the spectral index map shown in Fig. 6.1. Within the inner ∼600 au region, centered on the protoplanetary disk of this young source, the spectral index is approximately $\alpha \sim 2$, which indicates optically thick emission (Beckwith & Sargent, 1991). The high optical depth of this compact region suggests an optically thick disk that is diluted in a more extended sky area by the finite resolution of the observations. To ensure that the spectral index of the inner end of the streamer was not contaminated by this central emission, we modeled and subtracted the contribution of the latter. We fit a 2D Gaussian to the inner region in the image plane. The fitting results are provided in Table 6.3, and the model and residuals are displayed in Appendix 6.7.2. The compact emission extends for 1.″4 (2σ, 574 au) and might comprise a combination of the inner end of the streamer, remnants of the original envelope of M512, and a more compact protoplanetary disk. Higher-resolution observations will be key to discern the extent of the inner disk. We then subtracted the Gaussian model from the image to isolate the contribution of the streamer (Fig. 6.3). Finally, we computed the spectral index of

the streamer emission, α_S (see Fig. 6.1 and Fig. 6.3). We observe a spectral index of approximately $\alpha_S \sim 3.2$ along the entire streamer, which indicates optically thin emission. Because of the dust temperature profile we considered to derive the spectral index of the dust opacity (see Eq.6.1), we derive $\tau = -\ln(1 - I_\nu/B_\nu(T)) < 0.05$ in B6 along the full arc. As a sanity check, we ran a similar analysis in the uv plane, where we subtracted a point source from the visibilities and then computed the spectral index as a function of uv distance. We obtained consistent results (see Appendix 6.7.2).

6.4.2 Dust opacity spectral index

To investigate whether and how the optical properties of the dust change along the streamer M512, we divided the streamer into spatial bins and derived the spectral index of the dust opacity β within each bin. In order to select the bins, we used a logarithmic spiral with manually tuned parameters to adapt it to the shape of the streamer. We then selected points along the spiral as centers for circular apertures as large as the streamer width (see Fig. 6.4). The aperture radius is twice the beam aperture, and each aperture contained roughly 160 pixels. When we assume that the main heating mechanism for the dust is the irradiation from the central source, we can use the radial temperature profile that Motte & André (2001) derived for spherical dusty envelopes as a first approximation,

$$\mathrm{T(r)} = 38\mathrm{K}\left(\frac{\mathrm{L}}{\mathrm{L}_\odot}\right)^{0.2}\left(\frac{\mathrm{r}}{100\mathrm{au}}\right)^{-0.4}. \tag{6.2}$$

This equation yields temperatures in the range of 21 to 8 K across the scales of the streamer, that is, 600 to 4,000 au. We note that these distances from the central source assume that the streamer lies in the plane of the sky. At $\lambda = 1.3$ mm, the temperature T = 8 K implies that the RJ approximation is not valid ($h\nu/\mathrm{k}_B\mathrm{T} \sim 1$). We thus introduced a correction to the simple $\alpha = \beta - 2$ case for the low temperatures that would otherwise artificially lower the derived β, which we then derive as

$$\beta = \frac{\log\left[\left(\mathrm{F}_{\nu_2}(r)/\mathrm{F}_{\nu_1}(r)\right)/\left(\mathrm{B}_{\nu_1}(\mathrm{T_d}(r))/\mathrm{B}_{\nu_2}(\mathrm{T_d}(r))\right)\right]}{\log(\nu_2/\nu_1)}, \tag{6.3}$$

where the ALMA B6 and B3 representative frequencies are $\nu_2 = 230$ GHz, $\nu_1 = 100$ GHz, T_d is the temperature of the dust, and $\mathrm{B}_{\nu_i}(\mathrm{T}_d)$ is the Planck function value at the two frequencies.

Finally, we computed the statistical error on the spectral index as

$$\delta\alpha^2 (= \delta\beta^2) = \left(\frac{1}{ln\nu_2 - ln\nu_1}\right)^2 \left(\frac{\sigma_1^2}{\mathrm{F}_{\nu_1}^2} + \frac{\sigma_2^2}{\mathrm{F}_{\nu_2}^2}\right), \tag{6.4}$$

where σ_i, $F^2_{\nu_i}$ are the primary-beam-corrected rms and fluxes in each distance bin for the two bands. We considered the same error for β because we assumed an exact value for the temperature in Eq. 6.3. In addition to the statistical error, the systematic calibration uncertainty on the B3 and B6 fluxes for ALMA of $1\sigma = 5\%$ (Remjian et al., 2019) should be considered. Within the same bins, we also computed α using Eq. 6.1, and we show the resulting $\beta = \alpha - 2$ proxy and the β(T) profile in Fig. 6.4.

We find a mean $\beta = 1.62 \pm 0.04$ throughout the whole structure. Finally, we tested the two extreme scenarios in which the temperature is fixed at 21 or 8 K for the whole structure. The arc might self-shield against the internal radiation and might therefore be colder on average, or conversely, significant external irradiation from Orion OB stars might lead to higher temperatures in the outer arc (Haworth, 2021)[1]. In any case, the β measured with both fixed temperatures only changes by <10% with respect to the β obtained using the temperature profile.

6.5 Discussion

We discuss the interpretation of the derived dust-opacity index, estimate the mass of the surrounding material, and weigh the implications of such an event on a planet-forming system, as well as its possible origins.

6.5.1 Dust properties of the streamer

The retrieved continuum flux of the streamer around M512 implies a relatively high dust mass that can either be distributed in large numbers of small grains or in smaller numbers of large grains. It is thus important to constrain the maximum grain size of the distribution in order to constrain its mass content.

In the case of a distribution of spherical compact grains, the Mie scattering theory predicts that the derived $\beta \sim 1.6$ (Fig. 6.4) is consistent with a dust population for which the maximum grain size is submicron (Draine, 2006). If the grains were instead porous, $\beta \sim 1.6$ could be consistent with a dust distribution where the maximum grain size lies in a smoother range from submicron to one millimeter (e.g. Birnstiel et al. 2018).

It has recently been suggested that dust can grow up to millimeter sizes even in protostellar envelopes. β values lower than ~ 1.6 have been measured in the inner envelopes of a sample of class 0/I objects (e.g., Kwon et al., 2009; Miotello et al., 2014; Galametz et al., 2019; Cacciapuoti et al., 2023). However, models show that dust cannot grow more than a few μm in more diffuse molecular clouds cores (e.g., Ormel et al., 2009; Lebreuilly et al., 2023), where the submillimeter-dust opacity spectral index $\beta \sim 1.6$ (Draine, 2006). Scattered-light observations of these environments have also independently

[1]However, M512 lays in a region where the UV irradiation field is too low to induce such an effect (van Terwisga & Hacar, 2023).

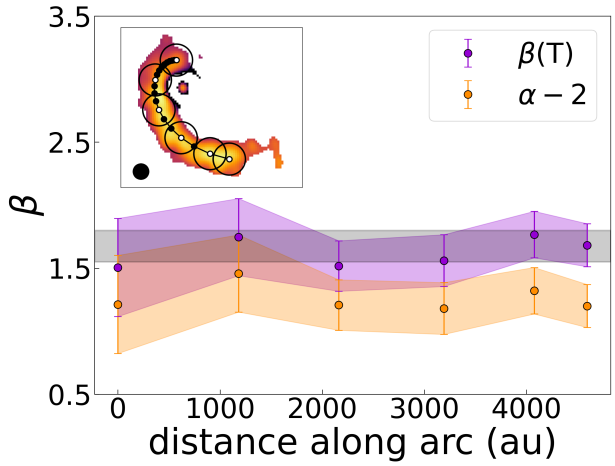

Figure 6.4: Profile of the spectral index β of the dust opacity along the length of the streamer. The approximation $\beta = \alpha - 2$ is shown as the orange line, and β, corrected for the deviation from the RJ approximation, is shown as the violet line. This profile has been obtained starting from the maps in Fig. 6.3, where the central emission had been modeled and subtracted. The centers of the selected apertures in which we derive β are highlighted in white among all the points that sample the manually defined logarithmic spiral in the B6 map as an example (upper inset). Throughout the whole structure, $\beta \sim 1.6$. The gray band represents ISM-like β.

been interpreted as the presence of grains up to only ~ 10 μm (e.g., Steinacker et al., 2010, 2014, 2015). Thus, the $\beta = 1.6$ measured for the streamer of M512 is consistent with the properties of ISM-like dust grains.

6.5.2 Mass constraints and infall rate

The delivery rate of mass onto M512 is critical to assess the implications that the event might have for the subsequent evolution of the system. In the optically thin regime, the dust mass of the observed streamer can be derived as (Hildebrand, 1983):

$$\mathrm{M} = \frac{\mathrm{d}^2 \mathrm{F}_\nu}{\kappa_\nu \mathrm{B}_\nu(\mathrm{T_d})}, \tag{6.5}$$

where d is the distance to the source, F_ν is the flux density of the structure, κ_ν is the dust opacity, and $\mathrm{B}_\nu(\mathrm{T}_d)$ is the value of the Planck function at a frequency ν. We considered a distance of 420 pc (see Section 6.1), and the temperature was given by Eq. 6.2. In order to measure the mass of the streamer and take the expected temperature variation along the arc into account, we considered the logarithmic spiral we mentioned in Sect. 6.5.1 that is shown in Fig. 6.4. For each selected aperture on the spiral, we assigned each pixel above the 3σ threshold to the closest aperture center, measured the total flux in the bin so defined, and computed the temperature with Eq. 6.2, where r is the projected radial distance of each aperture center from the source.

When we assume DSHARP dust properties (Birnstiel et al., 2018), the absorption opacity of a dust grain distribution that is characterized by ISM-like spectral indices such as we measure for the streamer of M512, and a typical power-law $n(a) \propto a^{-3.5}$, is $\kappa_{1.3mm} = 0.4$ g/cm^{-2}. The solid mass of the streamer thus amounts to $M_{dust}^{streamer} = 245 \pm 25$ M$_\oplus$. On the other hand, considering the usual assumptions for protoplanetary disks to derive the mass of the inner region (e.g., Andrews et al. 2013, Pascucci et al. 2016, Ansdell et al. 2016), that is, a temperature of 20 K and an absorption opacity $\kappa_{1.3mm} = 2.25$ g/cm^{-2}, we obtain $M_{dust}^{inner} = 58 \pm 6$ M$_\oplus$, given the integrated flux in Tab. 6.3. The reported uncertainties on the derived masses only reflect the dominant flux calibration error of 10%. We note that because the compact inner emission is optically thick, the mass estimates for the inner region can be off by a factor up to ∼5 (Ballering & Eisner 2019, Ribas et al. 2020, Macías et al. 2021, Xin et al. 2023, Rilinger et al. 2023), and a further underestimate of the millimeter-derived mass can be due to scattering effects in the very inner optically thick region (Zhu et al. 2019, Liu 2019). Taking all of this into account, we find that the mass of the streamer seems to exceed or be comparable to the mass of the inner region. Based on the resolution of the observations, this mass does not correspond to the mass of the protoplanetary disk alone, but also accounts for contribution from the inner infalling material.

Finally, we can constrain the infall rate onto M512 and its disk. Considering the typical free-fall timescale, $t_{ff} \propto \sqrt{r^3/GM}$, a particle with null initial velocity would fall from 4000 au onto the 0.15 $M_\odot$ protostar in roughly 50 kyr. This estimate is consistent with the TIPSY outputs ran in Sect. 6.3. Thus, when we assume that the whole streamer will infall onto the inner system and when we assume a typical dust-to-gas ratio of 0.01, the total mass infall rate is $\dot{M} = 1.5 \cdot 10^{-6}$ M$_\odot$/yr.

However, it is imperative to bear in mind that the infall rate may be lower if the streamer does not interact in its entirety with the inner protoplanetary disk. Consequently, while we discuss the implications of our study under the assumption that the entire streamer ultimately infalls on the inner disk, we emphasize the sensitivity of these outcomes on the mass that is actually captured by the source. Observations with higher spatial and spectral resolution are needed to remove the remaining sources of uncertainty of the analysis: The geometry of the inner system, the line-of-sight velocity of the star, and the impact of the infall via shock tracers such as SO (e.g., Garufi et al. 2022). It is noteworthy that outbursts observed for young stellar objects have been proposed to be triggered by massive accretion events (e.g., Bonnell & Bastien, 1992; Aspin & Reipurth, 2003). M512 might represent a rare case for which we witness a late-infall event that delivers mass at a significantly high rate. When we assume infall of the entire structure and outburst durations of ∼100 yr, these rates would imply a possible future accretion event of $7.5{\cdot}10^{-4}$ M$_\odot$/yr, or a series of smaller events. For example, if accretion were to build up material in the disk for 10 kyr[2], this would imply FUOr-like accretion (∼10^{-4} M$_\odot$/yr, Kenyon et al. 1988), which might then cause outbursts. The accretion rate of M512 has

[2]The typical duration interval between subsequent outbursts for FUOr events (Scholz et al., 2013).

been characterized as being in a quite ordinary accretion state, that is, $L_{acc} < L_*$, with $\dot{M} \sim 2 \cdot 10^{-7}$ $M_\odot$/yr, based on single-epoch observations (Caratti o Garatti et al., 2012). However, M512 has been classified as a bursting source based on multi-epoch WISE 3.4μm and 4.6μm photometry by Park et al. (2021). Over the course of 6.5 yr and with a time resolution of 0.5 yr, Park et al. (2021) observed three sharp increases in the flux by a factor $\sim$2.5 in both bands. This source represents an exciting case for exploring the possible link between infalling streamers and accretion outbursts.

Furthermore, the mass-infall rate onto M512 is similar to the rate used, for instance, by Bae et al. (2015) and Kuznetsova et al. (2022) in their simulations, in which they found that material infalling at these high rates on protoplanetary disks has the power to drive significant substructures. M512 thus represents a unique source for probing whether infall can drive substructures, which are often regarded as birthplaces of planets.

We note that an additional source of uncertainty for the derived masses comes from the chosen dust opacities. While we considered DSHARP opacities so far, other works made use of different prescriptions, such as the DIANA opacities (Min et al., 2016) or opacities constrained from Solar System observations (Pollack et al., 1994). These alternative choices would imply absorption opacities that are systematically higher in the submillimeter regime, up to about three or ten times those of the DSHARP, respectively. The mass derived through them would therefore be up to ten times lower both for the streamer and the inner disk. We point out that consistent choices of opacities imply the same ratio of the streamer and the disk mass.

6.5.3 Origins and frequency

The origin of streamers is still a matter of debate. Some authors have proposed that streamers are a channeled inflow of material from protostellar envelopes or even from beyond the scales of prestellar cores (e.g., Yen et al. 2014, Yen et al. 2019, Pineda et al. 2020). The streamer in the surroundings of M512 discussed here, however, is not reminiscent of irregular envelopes, and it is infalling in an apparently ordered, arc-like manner (see Sect. 6.3). Moreover, CO observations seem to indicate that M512 lost most of its initial envelope (Grant et al., 2021). Other explanations involve the interaction of M512 with close-by objects, such as a flyby with another stellar object or interactions with close interstellar clouds.

Flyby events might be quite common in star-forming regions, especially during the protostellar stages, where stars form close to each other in clusters (Pfalzner 2013, Winter et al. 2018, Lebreuilly et al. 2021, Offner et al. 2022). In this sense, the morphology of M512 is reminiscent of the stages observed for RW Aurigae (Cabrit et al. 2006, Dai et al. 2015, Rodriguez et al. 2018), AS 205 (Kurtovic et al., 2018), UX Tau (Ménard et al., 2020), and Z CMa (Dong et al., 2022), binary-star systems for which a long molecular arm extends from the primary star and points toward a secondary object. In Appendix 6.7.3 we discuss that a close encounter might have occurred between M512 and another source

a few hundred thousand years ago. This is much longer than most flyby events for which we still observe stripped material. Simulations indeed suggest that the re-circularization of material happens in a few thousand years (e.g., Cuello et al. 2023), making the observation of such an event extremely unlikely. Moreover, spirals excited due to stellar flybys are usually of the same order of magnitude of the outer radius of the stripped disk ($\lesssim 3$ R_{out}; Smallwood et al. 2023), while the arc we observe extends for thousands of astronomical units. The flyby scenario is thus hard to reconcile with our observations. We expand on our arguments in Appendix 6.7.3.

The velocity gradient we observe in the arc of M512 (see Fig.6.2) is also consistent with the capture of material from a nearby cloud with a nonzero initial velocity. The material is then accelerated toward the central star. Scicluna et al. (2014) and Dullemond et al. (2019) explored the possibility that forming protostars might capture material from nearby small clouds as they travel within their natal environment. Because of its non-null initial angular momentum, the material in this scenario does not fall directly onto the protostar, but feeds the disk, or even forms a new one. This capture process has been proposed to explain the observed infrared excess around very evolved $\geq$10 Myr old stars (e.g., Beccari et al., 2010; De Marchi et al., 2013a,b) and the $M_* - \dot{M}$ correlation in pre-main-sequence stars (e.g., Padoan et al., 2005; Throop & Bally, 2008; Padoan et al., 2014). Examples of objects that might be undergoing scenarios like this are AB Aur (Nakajima & Golimowski, 1995; Grady et al., 1999) and HD 100546 (Ardila et al., 2007). The hydrodynamics simulations of Dullemond et al. (2019) and Kuffmeier et al. (2020) demonstrated that the capture of cloud fragments would lead to the formation of arc-shaped structures much like the one observed in M512 (Scicluna et al. 2014, Dullemond et al. 2019). Additionally, Scicluna et al. (2014) computed the probability of cloudlet capture by a stellar object in different density conditions of the environment. Scicluna et al. (2014) found that for a region in which dense clumps occupy a fraction f_V of the total volume, the number of stars that is expected to be observed as cloudlet-capture accretors at a given time is larger by an order of magnitude than the volume filling-factor of dense clumps. Thus, if dense clumps only occupy a volume fraction as small as $f_V = 10^{-4}$, we expect one in a thousand objects to show late accretion. We note that M512 is one of three objects showing extended continuum emission in the Survey of Orion Disks with ALMA (SODA) (van Terwisga et al., 2022), which includes 873 objects. The overall median accreted mass in all the simulation grids explored in this survey is $0.01 M_\odot$. Scicluna et al. (2014) also demonstrated that the structures formed due to capture can last for even 10^4-10^5 yr (see their Section 2). These values are comparable to the streamer mass of M512 and to its free-fall timescale. Furthermore, we note that dust grains in ISM clouds should not exceed a few tenths of microns (e.g., (Mathis et al., 1977)), which further supports a scenario in which the $\beta \sim 1.6$ measured in Sect. 6.5.1 indicates ISM-like grains. Larger-scale maps than available at present would be helpful to link the streaming material around M512 with the neighboring environment, and to understand whether the observed streamer presented in this work is replenished by the surrounding environment or if it represents the full extent of the mass that will be delivered to the disk of M512.

Last, continuum emission has sometimes been detected along the cavity walls of protostellar outflows, where the dust might be brighter because the temperatures are higher (e.g., Maury et al. 2018, Le Gouellec et al. 2023). In the case of M512, however, the arc-like emission is quite bent and not reminiscent of more cone-like outflow cavities (e.g., Garufi et al. 2021, Hsieh et al. 2023). Additionally, CO emission is optically thick, and the $C^{18}O$ line profile indicates low velocities, about 500-700 m/s, and we observe both redshifted and blueshifted emission within the same arc (Fig. 6.2). Finally, M512 is a class I very low mass star, implying that such a large outflow would be unlikely. It is thus not straightforward to reconcile our observations with the outflow scenario. We also note that our mass estimates would still be valid with the caveat that at the cavity wall of a low-velocity outflow, temperatures would be slightly higher than what we assumed for the cold-streamer case (e.g., Flores-Rivera et al. 2021). This would imply a mass that is a factor of a few lower, and thus still a significantly high dust mass ($M_{dust} \gtrsim 50$ $M_\oplus$). When we consider typical class I outflow mass-loss rates of a few 10^{-8} $M_\odot$/yr (Fiorellino et al., 2021), it would take over 1 Myr yr to lift $M_{dust} \gtrsim 50$ $M_\oplus$, while the mass-loss rates quickly decline over the first $\sim 10^5$ yr of star formation. We thus tentatively discard this scenario. However, nonisotropic accretion from the envelope to the central source has been suggested to occur along the cavity walls of outflows (Le Gouellec et al. 2019a, Cabedo et al. 2021). Observations of bright and optically thin outflow tracers will help to clarify this case, together with higher-resolution observations of the central source to resolve the geometry of the disk and thus the direction along which an outflow could be launched.

In summary, given the constraints of Sect. 6.3 and the qualitative arguments laid out in this section, we repeat our suggestion that the arc-like structure around M512 is an infalling streamer, possibly caused by a cloudlet-capture event.

6.5.4 Implications for planet formation

Streamers can have significant implications for planet formation and for the evolution of a protoplanetary disk. M512 represents a unique case for which dust continuum emission is detected in two ALMA bands, thus enabling us to better constrain its dust properties and mass content. The structure we observe delivers a substantial amount of mass to the inner disk of M512, carrying several significant implications that we discuss below. In what follows, we assume that the whole streamer will infall onto the central disk, consistently with the bound solutions found in the kinematical analysis we laid out in Sect. 6.3. However, it is possible that only a fraction of the detected structure will infall onto the inner system, and the infall rate might therefore be lower by a factor of a few.

To begin with, the streamer replenishes the system with an amount of mass that exceeds or is comparable to the mass of the protoplanetary disk. If the infalling dust were captured by a nearby cloudlet in which the maximum grain sizes are 1-10 μm (see 6.5.1), a total mass of up to 0.075 $M_\odot$ might infall on the disk of M512. The infall can potentially double the mass available for planet formation in the system. The mass budget problem,

that is, the apparent lack of mass that is required to form known exoplanetary systems starting from the class II protoplanetary disks we observe in the Galaxy (e.g., Testi et al. 2016, Manara et al. 2018, Williams et al. 2019, Sanchis et al. 2020, Tychoniec et al. 2020), could thus be partially bridged by late infall of material onto evolved disks. Additionally, the supply of material around low-mass stars such as M512 could represent a possibility for the formation of gas giants around this type of object. While exoplanets like this are detected, if rarely (e.g., Morales et al. 2019, Bryant et al. 2023), their formation pathways remain unclear (Liu et al., 2020).

Additionally, M512 is a candidate on which to study the origin of substructures in evolved disks. Infall of material onto disks has been proposed to be one of the mechanisms that can trigger such substructures (Thies et al., 2011; Hennebelle et al., 2017; Kuffmeier et al., 2018; Ginski et al., 2021). Bae et al. (2015) and Kuznetsova et al. (2022) demonstrated that infall can drive the formation of rings and gaps in disks with infall rates that are consistent with what we find for M512. A possible instance of this process was detected by Segura-Cox et al. (2020b), who observed rings and gaps in in the protoplanetary disk around Oph IRS63, which was recently shown to be subject to anisotropic infall (Flores et al., 2023). Another example is HL Tau, where both disk structures and an infalling streamer were observed (ALMA Partnership et al. 2015, Yen et al. 2019). The study of the impact of streamers on disks that display substructures can inform us about the necessity, or lack thereof, of invoking planets that carve out these structures at the early stages of star and planet formation. Moreover, the formation of substructures and the induction of turbulence in the disk can alter the timescales of grain growth because the clumping of grains is more efficient under these conditions. Higher-resolution observations of M512 will be key to unveiling the geometry of its inner disk and to searching for potential substructures.

Last, the infalling material will impact the disk at some radius and will potentially shock its surroundings. In the vicinity of the shock, the disk temperature will rise (Garufi et al., 2022). Thus, the streamer will change the physical and chemical properties of the disk, as shown for example for HL Tau in (Garufi et al., 2022). M512 is known to undergo outbursts (Park et al., 2021) that can greatly alter the physical and chemical properties of protoplanetary disks by influencing both the evolution of dust (Houge & Krijt, 2023) and gas (Owen & Jacquet, 2014; Wiebe et al., 2019). To determine whether these properties are linked to the infalling streamer is an exciting matter for further studies.

6.6 Conclusions

We have presented new ALMA B3 observations of M512 in the Lynds 1641 region of the Orion A molecular cloud and combined them with archival ALMA B6 data to constrain the dust properties of a 4,000 au arc-like structure extending from the central source. Our conclusions are listed below.

- The structure is characterized by a velocity gradient consistent with infall (see Fig. 6.2).

The morphology of the extended emission and the velocity gradient are consistent with the capture and infall of material from a nearby cloudlet.

- The compact ($\sim$ 600 au) region surrounding M512 is optically thick at the wavelengths considered here ($\alpha \sim 2$). Higher-resolution observations will be key for studying this inner region and for constraining its geometry and the impact of the infall event, which we cannot probe with current observations.

- The streamer is optically thin with $\alpha_S \sim 3.2$ throughout the whole structure. Accounting for the low temperatures expected at its scales, we obtain a spectral index of the dust opacity $\beta = 1.62 \pm 0.04$, which is typical of ISM-like dust (Sect. 6.5.1).

- We constrain the dust mass of the streamer to be $\sim 250 M_\oplus$[3] (see Sect. 6.5.2). Based on typical free-fall timescales, the streamer might deliver up to $1.5 \cdot 10^{-6}$ $M_\odot$/yr onto the inner disk, and it might last about 50 kyr. We note that these estimates assume that the whole structure will infall.

- We discuss the possible origins and impact that this event can have on the planet-forming disk of M512, including the replenishment of mass, the formation of substructures, and changes in the physical and chemical conditions due to shocks and/or accretion outbursts (Sect. 6.5.4).

Streamer observations are a new window for insight into star and planet formation. They remind us that this process is not isolated and is highly dynamic within star-forming regions. Further observations are necessary to link streamers to their potential large-scale progenitors and to test the impact that streamers have on planet-forming disks on smaller scales. M512 is a unique source that will play a crucial role in these studies. This target is a rare opportunity for studying both gas and dust in their physical properties and dynamics, which would enable a comprehensive comparison to dedicated models.

Acknowledgments

This work was partly supported by the Italian Ministero dell'Istruzione, Università e Ricerca through the grant Progetti Premiali 2012-iALMA (CUP C52I13000140001), by the Deutsche Forschungsgemeinschaft (DFG, German Research Foundation) - Ref no. 325594231 FOR 2634/2 TE 1024/2-1, by the DFG Cluster of Excellence Origins (www.origins-cluster.de). This project has received funding from the European Union's Horizon 2020 research and innovation program under the Marie Sklodowska- Curie grant agreement No 823823 (DUSTBUSTERS) and from the European Research Council (ERC) via the ERC Synergy Grant ECOGAL (grant 855130). Funded by the European Union (ERC, WANDA, 101039452). Views and opinions expressed are however those of the author(s)

[3]This value is obtained when considering the opacities for ISM-like grains of Birnstiel et al. (2018), thus $\kappa_{1.3mm} = 0.4$ g/cm^{-2}, and the temperature profile give in Eq.6.2.

only and do not necessarily reflect those of the European Union or the European Research Council Executive Agency. Neither the European Union nor the granting authority can be held responsible for them. This work benefited from the Core2disk-III residential program of Institut Pascal at Université Paris-Saclay, with the support of the program "Investissements d'avenir" ANR-11-IDEX-0003-01. This paper makes use of the following ALMA data: ADS/JAO.ALMA#2019.1.01813.S, ADS/JAO.ALMA#2019.1.00951.S, ADS/JAO.ALMA#2022.1.00126.S. ALMA is a partnership of ESO (representing its member states), NSF (USA) and NINS (Japan), together with NRC (Canada), MOST and ASIAA (Taiwan), and KASI (Republic of Korea), in cooperation with the Republic of Chile. The Joint ALMA Observatory is operated by ESO, AUI/NRAO and NAOJ. We thank the entire ALMA team for their dedication to provide us with the data we used for this work. We thank Nicolas Cuello for helpful insights and discussion. We thank the referee for their insightful comments, which helped us to improve the quality of this work.

6.7 Appendix

6.7.1 Datasets

We report a summary of the datasets used in this work in Table 6.2.

Table 6.2: Summary of the datasets.

Project Code	P.I.	Date	Integration (s)	Resolution (arcsec)	Frequency (GHz)	CASA version
			Band 3			
2022.1.00126.S	Wendeborn, J.	2023/01/16	7529	1.05	89-105	6.4.1-12
			Band 6			
2019.1.01813.S	van Terwisga, S.	2019/11/27	32	1.13	223-243	5.6.1-8
2019.1.00951.S	Grant, S,	2019/12/12	72	1.15	216-233	5.6.1-8

6.7.2 Modeling the compact emission

In order to measure α and β along the streamer free of flux contamination from the inner optically thick region, we subtracted the compact contribution centered on the source in two ways.

First, we fit a Gaussian model to the central region in the image plane. Figures 6.5 and 6.6 show the data, the model, and the residuals of the fit. Table 6.3 summarizes the fitted parameters for the models in the two bands. The spectral index α and the spectral index of the dust opacity β were measured after the optically thick region was modeled out (Sect. 6.4). As a robustness check, we tested whether our results were robust against a different modeling scheme. We used the *uvmodelfit* CASA routine to fit a point-source component to the visibilities because the disc is unresolved at the resolution of our observations. The function fits for an offset from the phase center and the flux of the

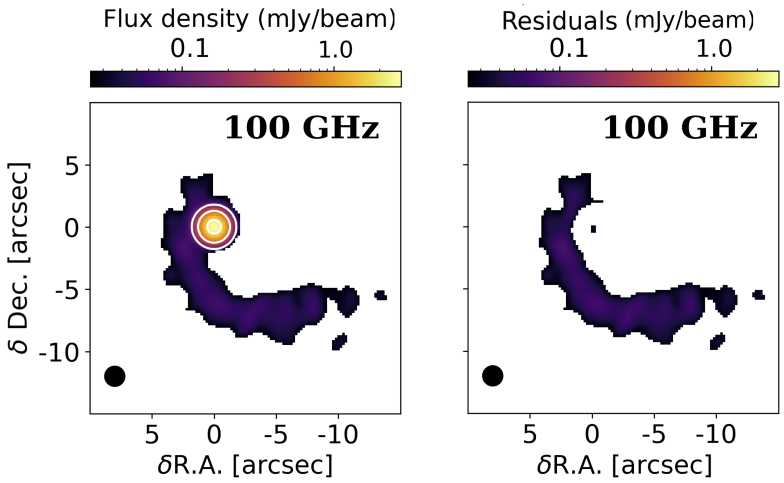

Figure 6.5: Contour levels (white) of the Gaussian model on top of the ALMA B3 (100 GHz) data of M512 (left). The color bar reports the flux values of the original image. The residuals of the model are shown on the right, and their color bar lies in the same range of values as the original emission to facilitate the comparison.

point source. We find the same offset from the center as for the Gaussian fit and a total integrated flux density of 16.1 mJy in B6 and 2.6 mJy in B3. We then subtracted this contribution from the visibility amplitudes (A = $\sqrt{Re^2 + Im^2}$) at all scales, and we binned them. In each bin, the uncertainty is given by the combined uncertainties on the real and imaginary parts of the visibilities, together with the ALMA calibration error ($1\sigma = 5\%$, Remjian et al. 2019). We finally computed the spectral and dust opacity indices using Eq. 6.1 and 6.3 as a function of uv distance after the subtraction, as shown in Fig. 6.7. The bump at the short uv distances is caused by the combination of the asymmetric shape of the streamer with the uv coverage of the observations. The large scatter in amplitude at these scales also causes a larger error around the mean, and thus, a larger uncertainty on α and β. The very first bin (at the shortest common uv distance) shows $\beta \sim 2$ because of an increase in the B6 visibility amplitudes that is not observed in B3 due to the uv coverage. Shorter baselines, and thus, observations on larger recoverable scales, are needed to measure β in the outskirts of the streamer more reliably. The higher β would still agree with the conclusion of small ISM-like grains. Finally, the two azimuthally averaged spectral indices are consistent with what was found in the image plane: $\alpha_S = 3.1 \pm 0.1$, and $\beta = 1.55 \pm 0.05$.

Table 6.3: Results of the Gaussian fit to the compact unresolved region around M512.

Band	Shift from source coordinates (arcsec)	Integrated flux density (mJy)	σ_x x σ_y (arcsec)
3	(0.060 ± 0.003, 0.080 ± 0.003)	2.8 ± 0.1	(0.696 ± 0.002) x (0.691 ± 0.002)
6	(0.020 ± 0.008, 0.020 ± 0.008)	19.4 ± 0.2	(0.740 ± 0.008) x (0.723 ± 0.007)

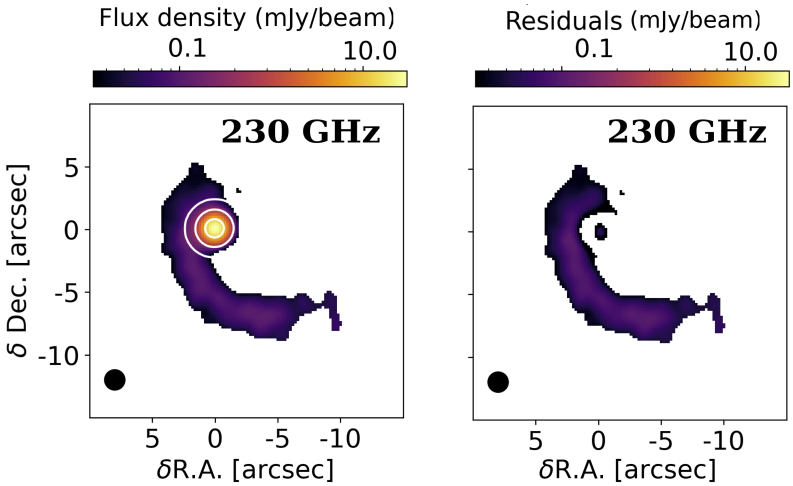

Figure 6.6: Same as Fig. 6.5, but for B6 (230 GHz) data.

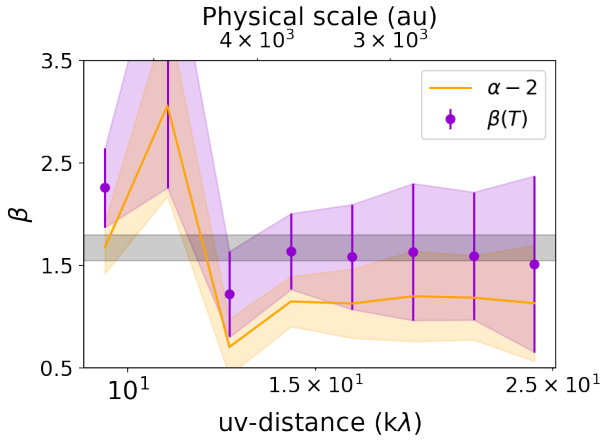

Figure 6.7: Spectral (orange) and dust opacity (violet) indices as measured across the probed uv distances after subtraction of a point-like source. The mean values $\alpha \sim 3.1$ and $\beta \sim 1.6$ are consistent with what was found across the scale of the streamer in the image-plane analysis.

6.7.3 Possible flyby candidates

We here note the presence of a class II young stellar object ($\alpha_{2-25\mu m} = -1$; Megeath et al. 2012) at a projected distance of 100″ (41,000 au) from M512. This source, 2MASS J05401156-0730409, was studied in continuum by van Terwisga et al. (2022), who reported a integrated 1.3mm flux of 1.65 ± 0.06 mJy and a dust mass estimate of 8.1 ± 0.3 $M_\oplus$, assuming optically thin emission, a dust temperature of 20 K, and a dust absorption opacity of 2.3 cm^2/g. Gaia DR3 Gaia Collaboration et al. (2022) reported a parallax of 2.54 ± 0.18 for the latter, indicating that it lies at a distance consistent with M512 (but still different from it), whose Gaia DR3 parallax is 2.37 ± 0.12. The measured Gaia DR3 proper motion in declination of the secondary object is pmDec = −0.18 ± 0.15 mas/yr and the proper motion in right ascension is pmRA = 0.14 ± 0.16 mas/yr. M512 moves in the plane of the sky with pmDec = −0.50 ± 0.10 mas/yr and pmRA = 0.15 ± 0.11. Considering that the relative motion of the sources is −0.32 ± 0.18 mas/yr in declination and δpmRA = 0.01 ± 0.19 in right ascension, the relative proper motions are consistent with a close encounter of the two objects between 200 and 700 kyr ago (1σ range) in the plane of the sky. However, considering the error bars on the Gaia proper motion and parallax measurements, it is possible that no flyby occurred at all. We report the 2MASS sky map in Figure 6.8.

The spatial scale and the timescale both yield major counterarguments for this scenario. For a disk with a size R_{disc} that is perturbed by a star during a close encounter $R_{flyby} \sim R_{disc}$, simulations suggest that the induced arc-like spirals would have a spatial extent of about three times R_{disc} at most (see Cuello et al. (2019)). The streamer around M512, however, is 4,000 au or longer (depending on projection effects and interferometric filtering), and would require an unreasonably extended protoplanetary disk that we would have resolved with our observations. Additionally, even in the earliest case that is compatible with Gaia constraints, a close encounter could have occurred between 200-700kyr ago, within 1sigma confidence. The typical freefall timescale $t_{ff} \propto \sqrt{r^3/Gm}$ for a particle that is infalling from 4,000 au onto a 0.15 $M_\odot$ star is roughly 50 kyr, which means that the material should already have fallen onto the star. If the observed streamer were a flyby-induced spiral, its survival time would be a few times the orbital period at most at the outer edge of the disk (Smallwood et al., 2023). The arc would therefore have been dispersed in a few thousand years, which means that it is highly improbable that it would have been observed. Last, the derived masses for the streamer around M512 and its inner region suggest that a flyby should have stripped away a significant portion of the disk (see Sect. 6.5.2). Pfalzner et al. (2005) demonstrated that even encounters with a similar-mass object and with a periastron of about the disk radius would only strip up to about 50% of the mass of the perturbed disk[4]. Finally, we inspected ALMA archival data for this nearby source (ID 2019.1.01813.S) and found no evidence for extended emission.

As a cautionary argument, however, we note that flybys for which the stripped material has been observed in a structure exceeding three times R_{disc} (RW Aur) and for

[4]Although this argument relies on the systematically uncertain dust-mass constraints.

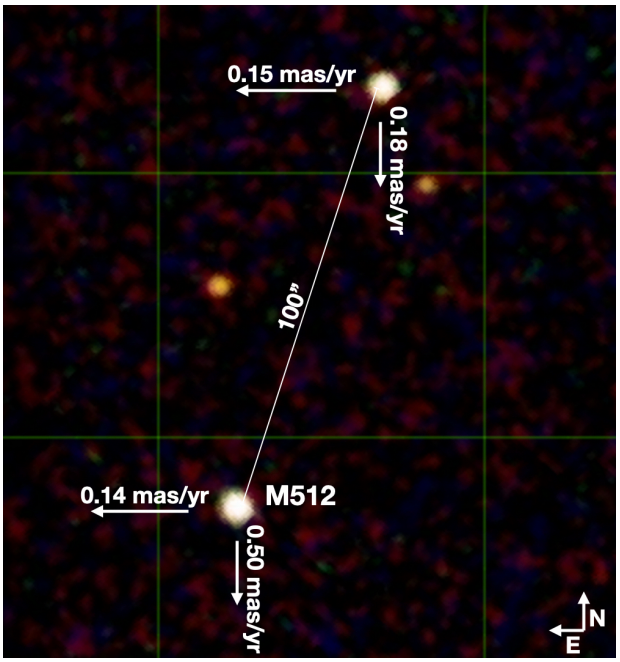

Figure 6.8: 2MASS map of the surroundings of M512, whose arc extends westward. A young stellar object (2MASS J05401156-0730409) lies at a projected distance of approximately 41,000 au from M512. The Gaia DR3 mean proper motion components are overlaid as arrows, and their magnitude is reported in milliarcseconds per year. A close encounter might have occurred, but only a few hundred thousand years ago. Each box of the grid is 1’x1’.

which the re-circularization timescales seem to exceed a few thousand years (HV Tau and DO Tau) have been observed in Rodriguez et al. (2018) and Winter et al. (2018b), respectively. Overall, we suggest that a flyby of M512 on 2MASS J05401156-0730409 appears to be harder to reconcile with the observed extended and massive arc than the streamer scenario, but it cannot be completely ruled out at this stage.

7

Summary and prospects

7.1 This Thesis main achievements

At the end of Chapter 1, I highlighted how previous literature studies that aimed at constraining the dust size distribution in protostellar envelopes (e.g., Miotello et al. 2014, Galametz et al. 2019) recommended follow-up analyses on larger numbers of sources by using higher sensitivity, higher resolution data, and perhaps multi-wavelength analyses. Here I summarize the main achievements and findings of this Thesis, and I discuss some possible follow-up investigations to this work.

Studies of dust properties have been largely conducted in the diffuse ISM via extinction studies in the UV, optical and infrared regimes; and in much denser protoplanetary disks by analysing their strong submillimetre thermal emission. However, the realm of environments with intermediate densities have proven challenging due to the lack of background sources to conduct extinction measurements, and due to a lack in resolution and sensitivity in the thermal emission where these environments can be observed in the submillimetre. For this reason, while robust measurements and established knowledge about dust properties characterizes the diffuse ISM and the very compact disks, a gap in the evolution of dust remains at the intermediate scales. In particular, the dust properties of protostellar envelopes, the infalling reservoirs of material that build up a nascent protostar and its disk, have only been rarely targeted. However hard to study, characterizing dust in envelopes is critical to (i) constrain the dust distribution that falls onto young disks; (ii) understand the magnetic breaking effect, according to which the coupling of charged dust grains with the magnetic field can lead to drive the extent of protoplanetary disks due to angular momentum removal from the system; (iii) characterize the composition of dust grains which will deliver volatiles to the planet-forming disks.

In this Thesis, I have demonstrated how a multi-scale, multi-wavelength approach to measure spectral and dust opacity indices in envelopes can yield far more robust results than what previously done, setting tighter constraints on the dust opacity spectral index and its gradient throughout the probed scales around protostars (Chapter 3). This kind of study aims at constraining the dust optical properties in the collapsing environments and has led to indications of grain growth in protostellar envelopes (e.g., Miotello et al. 2014, Galametz et al. 2019). However, since dust growth appears complicated by the lifetimes and densities of envelopes, I have explored the possibility that instead it is a transport of large dust grains from the denser circumstellar disk along outflows and jets that could explain the same observations (Chapter 4). Moreover, I have contributed to significantly increase the number of protostellar envelopes for which constraints on dust properties, in terms of their submillimetre thermal emission, have been carried out (Chapter 5). Finally, for the first time, I have presented measurements of submillimetre dust properties in an infalling streamer, an asymmetric and episodic event of accretion onto a young source, perhaps due to the capture of a pocket of ISM material from a young protostar and its disk (Chapter 6).

The main results of these works can be summarized in the following statements:

1. Multi-band and multi-scale radiointerferometric data can be utilized to robustly constrain the profile of dust opacity spectral index β across collapsing protostellar envelopes by means of uv plane modelling, in which disk and envelope contributions can be isolated and analysed (Chapters 2, 3, 5, 6).

2. A variety of β profiles characterize these environments, some flatter than others and with values ranging from 0.4 to 2.0 (Miotello et al. 2014, Galametz et al. 2019, Agurto-Gangas et al. 2019a, Chapter 5). This would suggest some degree of dust evolution in envelopes, with larger and larger grains from outer to inner envelope.

3. A tight correlation between β (or its gradient) and the mass of the protostellar envelopes, previously reported in Galametz et al. (2019), is confirmed and reinforced (Chapter 5). In Chapter 5, I discuss how this correlation might arise from the high optical depths of very massive inner envelopes of Class 0 protostars, using IRAS4A as an example.

4. If, on the other hand, the observed gradients of β in envelopes are driven by radial changes in dust optical properties from outer to inner envelope, it is possible that lifting of submillimetre grains from disks via outflows contributes to the dust grain size distribution in envelopes (Chapter 4). Moreover, one of the first ever measurements of β along the resolved cavity walls of an outflow indicates an ISM-like dust size distribution around the Class 0 IRAS 15398-3359. Whether this dust is entrained from the disk or not remains to be further explored (Chapter 5).

5. The optical properties of dust in the only known "dusty" streamer observed to date resemble the ones of the ISM, which could be the case if the arc infalling on the studied young source is caused by capture of an ISM cloudlet of pristine material. The mass budget of an inner young system can be significantly enhanced by these kind of events (Chapter 6).

7.2 Possible follow-up to this Thesis

After this Thesis work, a number of questions remain open and will therefore be topics for further research:

- How do dust properties (β) and their radial gradient distribute across large samples of protostellar envelopes?

- How can we extend our studies to ranges of the dust size distribution to which we are blind with submillimetre observations?

- To what extent compositional changes play a role in the dust properties variations

we measure in protostellar envelopes?

7.2.1 A need for larger samples

The dust continuum emission of protostellar envelopes has been studied for only a few sources and with limited spatial and wavelength coverage. In Chapters 3 and 5, I increased our ensemble of β measurements in envelopes and demonstrated how extending these studies in covered physical scales and wavelength range, I could cut previous error bars by a factor of ~ 3, and potentially reveal previously unseen gradients in β. I now plan to uniformly study dust properties for larger samples of envelopes. I will combine data from large collaborations of which I am part of, together with complements from the ALMA archive. In order to try and constrain the distribution of β in protostellar envelopes, deep observations of many envelopes have to be performed. Within the duration of this Thesis, I took part in the first steps of the "ENYGMA" Large Survey, obtained with the NOEMA interferometer. ENYGMA consists of deep, polarization-mode observations of bright and well known protostellar envelopes across different regions with a resolution of $1\farcs0$, for which the 3 mm window is targeted. The program will achieve very high SNR observations of the dust thermal emission in total intensity, along with robust observations of its polarized fraction. ALMA and NOEMA archival data can be combined with this new 3mm data to constrain the dust opacity spectral index distribution for many envelopes.

7.2.2 The potential of polarized emission observations

Studies of dust thermal emission by itself is not likely to provide us with all the answers. The dust opacity spectral index in fact suffers from its own limitations, like its dependence on also grain chemistry and porosity, thus leaving a degeneracy in how we interpret it as a function of grain sizes. Moreover, submillimetre spectral indices are sensitive to the submillimtere range of sizes of a dust distribution and saturate when grains are much smaller or much larger than that (Fig. 1.8). For this reason, complementary information will be central to unveil the evolution history of dust in these environments. We know that when dust grains are aligned along a preferential direction, their thermal emission is polarized up to a certain fraction. In protostellar envelopes, such an alignment can be guaranteed by a combination of photon bombardment of grains and protostellar magnetic fields - as explained by the RAT theory (Lazarian & Hoang, 2007). Since the RAT mechanism allows to align grains of sizes similar to the wavelengths of the photons with which they are irradiated, the polarized emission is correlated to dust grain sizes. Valdivia et al. (2019) demonstrated how the polarization fractions in protostellar envelopes can provide independent constraints on the dust grain sizes in these dense environments. Thus, constraining the fraction of polarized light at submillimetre wavelengths represents another venue significantly constrain the presence of dust grains with sizes of 10μm and up to a few hundreds of microns. Besides, polarized emission observations at different wavelengths can probe the even larger grains population, as the polarization angle can undergo a switch in sign across bands probed by modern interferometers, like ALMA (Guillet et al., 2020).

Once again, these goals can be achieved with the ENYGMA program. In the near future, we will work on this survey of dusty envelopes that aims at constraining dust properties based on both polarized and unpolarized emission, which promises to be the first of its kind. Beyond dust properties themselves, ENYGMA will naturally allow us to study the morphology and intensity of magnetic fields at core/envelope scales, which are a fundamental aspect of the formation of protostars and their protoplanetary disk (e.g. Maury et al. 2022).

7.2.3 Beyond the submillimetre

Not only can we probe a different phase space of dust properties with polarized thermal emission but, if we are to break the degeneracies of dust grain sizes with porosity and composition, near- and mid-infrared studies will be key to do so. While observed low $\beta < 1$ in protostellar envelopes cannot be explained with mere changes in dust composition (e.g., Ysard et al. 2019), much can be learned about the bulk and mantle properties of dust grains by observing their extinction properties as function of wavelength. The coagulation of grains strongly depends on their physical and chemical properties as well as the ones of the medium in which they are embedded (e.g., Ormel et al. 2009). Thus, characterizing the conditions of dust grains along their collapse is necessary to constrain the timescales and efficiency of planet formation. However, to probe the full extent of the dust size distribution and its composition, a multi-wavelength approach is key. The near-infrared offers a window on the small-end ($\lesssim 1\mu$m) of dust properties and allows to constrain dust composition via spectral features. A pioneering work when it comes to constrain dust properties in infalling envelopes was attempted with VLT-ISAAC L-band spectra in the 2.84-4.15 μm range. Pontoppidan et al. (2004) mapped the distribution of the water ice mantles absorption band in the Serpens South star forming region, using bright background sources. The lines of sight were scattered across the region, with one of them possibly intersecting the outer envelope of the protostar SerpS-SMM4. Along this line of sight, Pontoppidan et al. (2004) found a sharp rise in the water ice abundance, possibly marking very different dust properties in the envelope when compared to the surrounding ISM. However novel, this work was limited by the instrumental capabilities of the time. Today, JWST has proven to offer an unprecedented opportunity to extend such studies by far, thanks to its high spatial resolution (necessary to resolve envelopes), and sensitivity (necessary to probe very dense lines of sight). (McClure et al., 2023) has indeed initiated what will surely be a series of work on probing very high density lines of sight ($A_V \sim 90$), comparable to the ones of protostellar envelopes. Another JWST program, ID 1611 has targeted the Serpens South densely populated star forming region in order to extend the above cited work of Pontoppidan et al. (2004). In particular, it will be possible to extract the broad water ice band at 3μm, the CO_2 ice band at 4.26μm, and the silicate bands at 10 and 18 μm, which will inform the community about the bulk composition of dust grains and their mantles. It is noteworthy that the shape of the CO_2 ice band will be an independent indicator for grain sizes, as it presents a bump if micronic grains are present in the medium (Dartois et al. 2022, Dartois et al. 2024). Moreover, infrared surveys like the

ESO VISTA "VISIONS" survey (Meingast et al., 2023) or the VLT/SPHERE DESTYNYS program (Ginski et al. 2020, Garufi et al. 2024) recently targeted star-forming regions in the infrared to study the dust properties at several scales. For example, the former is a complete and deep photometric survey in the J, H, I bands and suitable to measure dust extinction in the outer envelopes of several young sources. For these sources, VISIONS will thus be an opportunity to probe the universality of the near-infrared extinction law and possible deviations from it at densities that have not been proved before in this wavelength range.

Bibliography

Adams, F. C. & Shu, F. H. 1985, ApJ, 296, 655

Agurto-Gangas, C., Pineda, J. E., Szűcs, L., et al. 2019a, A&A, 623, A147

Agurto-Gangas, C., Pineda, J. E., Szűcs, L., et al. 2019b, A&A, 623, A147

Ahmad, A. A., González, M., Hennebelle, P., & Commerçon, B. 2024, arXiv e-prints, arXiv:2404.14496

Akiyama, E., Vorobyov, E. I., Liu, H. B., et al. 2019, AJ, 157, 165

ALMA Partnership, Brogan, C. L., Pérez, L. M., et al. 2015, ApJ, 808, L3

Alves, F. O., Cleeves, L. I., Girart, J. M., et al. 2020, ApJ, 904, L6

Alves, F. O., Girart, J. M., Caselli, P., et al. 2017, A&A, 603, L3

Alves, F. O., Girart, J. M., Padovani, M., et al. 2018, A&A, 616, A56

André, P., Men'shchikov, A., Bontemps, S., et al. 2010, A&A, 518, L102

Andre, P., Ward-Thompson, D., & Barsony, M. 1993, ApJ, 406, 122

Andrews, S. M., Huang, J., Pérez, L. M., et al. 2018, ApJ, 869, L41

Andrews, S. M., Rosenfeld, K. A., Kraus, A. L., & Wilner, D. J. 2013, ApJ, 771, 129

Ansdell, M., Williams, J. P., van der Marel, N., et al. 2016, ApJ, 828, 46

Apai, D., Pascucci, I., Bouwman, J., et al. 2005, Science, 310, 834

Ardila, D. R., Golimowski, D. A., Krist, J. E., et al. 2007, ApJ, 665, 512

Aso, Y., Ohashi, N., Aikawa, Y., et al. 2017, ApJ, 849, 56

Aspin, C. & Reipurth, B. 2003, AJ, 126, 2936

Bachiller, R. & Pérez Gutiérrez, M. 1997, ApJ, 487, L93

Bachiller, R., Pérez Gutiérrez, M., Kumar, M. S. N., & Tafalla, M. 2001, A&A, 372, 899

Bae, J., Hartmann, L., & Zhu, Z. 2015, ApJ, 805, 15

Ballering, N. P. & Eisner, J. A. 2019, AJ, 157, 144

Bally, J. 2016, ARA&A, 54, 491

Barge, P. & Sommeria, J. 1995, A&A, 295, L1

Barnard, E. E. 1919, ApJ, 49, 1

Basu, S. & Mouschovias, T. C. 1995, ApJ, 452, 386

Bate, M. R. 2022, MNRAS, 514, 2145

Beccari, G., Spezzi, L., De Marchi, G., et al. 2010, ApJ, 720, 1108

Beckwith, S. V. W. & Sargent, A. I. 1991, ApJ, 381, 250

Bernabò, L. M., Turrini, D., Testi, L., Marzari, F., & Polychroni, D. 2022, ApJ, 927, L22

Bhandare, A., Commerçon, B., Laibe, G., et al. 2024, arXiv e-prints, arXiv:2404.09257

Bianchi, E., López-Sepulcre, A., Ceccarelli, C., et al. 2023, Faraday Discussions, 245, 164

Birnstiel, T., Dullemond, C. P., Zhu, Z., et al. 2018, ApJ, 869, L45

Birnstiel, T., Fang, M., & Johansen, A. 2016, Space Sci. Rev., 205, 41

Bjerkeli, P., Jørgensen, J. K., & Brinch, C. 2016, A&A, 587, A145

Bogdan, T., Pillich, C., Landers, J., Wende, H., & Wurm, G. 2020, A&A, 638, A151

Bonnell, I. & Bastien, P. 1992, ApJ, 401, L31

Bontemps, S., Andre, P., Terebey, S., & Cabrit, S. 1996, A&A, 311, 858

Boogert, A. C. A., Gerakines, P. A., & Whittet, D. C. B. 2015, ARA&A, 53, 541

Boogert, A. C. A., Hogerheijde, M. R., Ceccarelli, C., et al. 2002, ApJ, 570, 708

Brauer, F., Dullemond, C. P., & Henning, T. 2008, A&A, 480, 859

Bridle, A. H. & Schwab, F. R. 1999, in Astronomical Society of the Pacific Conference Series, Vol. 180, Synthesis Imaging in Radio Astronomy II, ed. G. B. Taylor, C. L. Carilli, & R. A. Perley, 371

Bryant, E. M., Bayliss, D., & Van Eylen, V. 2023, MNRAS, 521, 3663

Bussmann, R. S., Wong, T. W., Hedden, A. S., Kulesa, C. A., & Walker, C. K. 2007, ApJ, 657, L33

Butner, H. M., Evans, Neal J., I., Harvey, P. M., et al. 1990, ApJ, 364, 164

Cabedo, V., Maury, A., Girart, J. M., & Padovani, M. 2021, A&A, 653, A166

Cabrit, S., Codella, C., Gueth, F., et al. 2007, A&A, 468, L29

Cabrit, S., Pety, J., Pesenti, N., & Dougados, C. 2006, A&A, 452, 897

Cacciapuoti, L., Macias, E., Maury, A. J., et al. 2023, A&A, 676, A4

Cacciapuoti, L., Testi, L., Podio, L., et al. 2024, ApJ, 961, 90

Caratti o Garatti, A., Garcia Lopez, R., Antoniucci, S., et al. 2012, A&A, 538, A64

Cardelli, J. A., Clayton, G. C., & Mathis, J. S. 1989, ApJ, 345, 245

Carrera, D., Simon, J. B., Li, R., Kretke, K. A., & Klahr, H. 2021, AJ, 161, 96

Caselli, P., Hartquist, T. W., & Havnes, O. 1997, A&A, 322, 296

Ceccarelli, C., Codella, C., Balucani, N., et al. 2022, arXiv e-prints, arXiv:2206.13270

Chambers, J. 2021, ApJ, 914, 102

Chen, H., Myers, P. C., Ladd, E. F., & Wood, D. O. S. 1995, ApJ, 445, 377

Chen, M. C.-Y., Di Francesco, J., Johnstone, D., et al. 2016, ApJ, 826, 95

Chiang, H.-F., Looney, L. W., & Tobin, J. J. 2012, ApJ, 756, 168

Chung, C.-Y., Andrews, S. M., Gurwell, M. A., et al. 2024, arXiv e-prints, arXiv:2405.19867

Codella, C., Ceccarelli, C., Chandler, C., et al. 2021, Frontiers in Astronomy and Space Sciences, 8, 227

Codella, C., Maury, A. J., Gueth, F., et al. 2014, A&A, 563, L3

Commerçon, B., Hennebelle, P., Audit, E., Chabrier, G., & Teyssier, R. 2008, A&A, 482, 371

Cridland, A. J., Rosotti, G. P., Tabone, B., et al. 2022, A&A, 662, A90

Cuello, N., Dipierro, G., Mentiplay, D., et al. 2019, MNRAS, 483, 4114

Cuello, N., Ménard, F., & Price, D. J. 2023, European Physical Journal Plus, 138, 11

Curone, P., Testi, L., Macías, E., et al. 2023, A&A, 677, A118

Dai, F., Facchini, S., Clarke, C. J., & Haworth, T. J. 2015, MNRAS, 449, 1996

Dartois, E., Noble, J. A., Caselli, P., et al. 2024, Nature Astronomy, 8, 359

Dartois, E., Noble, J. A., Ysard, N., Demyk, K., & Chabot, M. 2022, A&A, 666, A153

De Marchi, G., Beccari, G., & Panagia, N. 2013a, ApJ, 775, 68

De Marchi, G., Panagia, N., Guarcello, M. G., & Bonito, R. 2013b, MNRAS, 435, 3058

Delussu, L., Birnstiel, T., Miotello, A., et al. 2024, arXiv e-prints, arXiv:2405.14501

Demyk, K., Jones, A. P., Dartois, E., Cox, P., & D'Hendecourt, L. 1999, A&A, 349, 267

Desert, F. X., Boulanger, F., & Puget, J. L. 1990, A&A, 237, 215

Dolginov, A. Z. & Mitrofanov, I. G. 1976, Ap&SS, 43, 291

Dong, R., Liu, H. B., Cuello, N., et al. 2022, Nature Astronomy, 6, 331

Donn, B. 1968, ApJ, 152, L129

Draine, B. T. 2006, ApJ, 636, 1114

Draine, B. T. & Li, A. 2007, ApJ, 657, 810

Drazkowska, J., Bitsch, B., Lambrechts, M., et al. 2022, arXiv e-prints, arXiv:2203.09759

Drążkowska, J. & Dullemond, C. P. 2018, A&A, 614, A62

Duchene, G., Menard, F., Stapelfeldt, K., et al. 2023, arXiv e-prints, arXiv:2309.07040

Dullemond, C. P., Küffmeier, M., Goicovic, F., et al. 2019, A&A, 628, A20

Dunham, M. M., Allen, L. E., Evans, Neal J., I., et al. 2015, ApJS, 220, 11

Dunham, M. M., Stutz, A. M., Allen, L. E., et al. 2014, in Protostars and Planets VI, ed. H. Beuther, R. S. Klessen, C. P. Dullemond, & T. Henning, 195–218

Evans, L., Vastel, C., Fontani, F., et al. 2023, A&A, 678, A160

Ferrière, K. M. 2001, Reviews of Modern Physics, 73, 1031

Fiorellino, E., Manara, C. F., Nisini, B., et al. 2021, A&A, 650, A43

Flores, C., Ohashi, N., Tobin, J. J., et al. 2023, arXiv e-prints, arXiv:2310.14617

Flores-Rivera, L., Terebey, S., Willacy, K., et al. 2021, ApJ, 908, 108

Flower, D. R. & Forêts, G. P. d. 1994, Monthly Notices of the Royal Astronomical Society, 268, 724

Foreman-Mackey, D., Hogg, D. W., Lang, D., & Goodman, J. 2013, PASP, 125, 306

Francis, L., Johnstone, D., Herczeg, G., Hunter, T. R., & Harsono, D. 2020a, AJ, 160, 270

Francis, L., Johnstone, D., Herczeg, G., Hunter, T. R., & Harsono, D. 2020b, AJ, 160, 270

Froebrich, D. 2005, ApJS, 156, 169

Gaia Collaboration, Klioner, S. A., Lindegren, L., et al. 2022, A&A, 667, A148

Galametz, M., Maury, A., Girart, J. M., et al. 2018, A&A, 616, A139

Galametz, M., Maury, A. J., Valdivia, V., et al. 2019, A&A, 632, A5

Galli, D., Lizano, S., Shu, F. H., & Allen, A. 2006, ApJ, 647, 374

Galliano, F. 2022, Habilitation Thesis, 1

Garufi, A., Ginski, C., van Holstein, R. G., et al. 2024, A&A, 685, A53

Garufi, A., Podio, L., Codella, C., et al. 2021, A&A, 645, A145

Garufi, A., Podio, L., Codella, C., et al. 2022, A&A, 658, A104

Giacalone, S., Teitler, S., Königl, A., Krijt, S., & Ciesla, F. J. 2019, ApJ, 882, 33

Gibb, A. G., Richer, J. S., Chandler, C. J., & Davis, C. J. 2004, ApJ, 603, 198

Ginsburg, A., Robitaille, T., & Beaumont, C. 2016, pvextractor: Position-Velocity Diagram Extractor, Astrophysics Source Code Library, record ascl:1608.010

Ginski, C., Facchini, S., Huang, J., et al. 2021, ApJ, 908, L25

Ginski, C., Gratton, R., Bohn, A., et al. 2022, A&A, 662, A74

Ginski, C., Ménard, F., Rab, C., et al. 2020, A&A, 642, A119

Girart, J. M., Rao, R., & Marrone, D. P. 2008, Ap&SS, 313, 87

Goldreich, P. & Ward, W. R. 1973, ApJ, 183, 1051

Grady, C. A., Woodgate, B., Bruhweiler, F. C., et al. 1999, ApJ, 523, L151

Grant, S. L., Espaillat, C. C., Wendeborn, J., et al. 2021, ApJ, 913, 123

Guerra-Alvarado, O. M., van der Marel, N., Di Francesco, J., et al. 2024, A&A, 681, A82

Guidi, G., Isella, A., Testi, L., et al. 2022, A&A, 664, A137

Guillet, V., Fanciullo, L., Verstraete, L., et al. 2018, A&A, 610, A16

Guillet, V., Hennebelle, P., Pineau des Forêts, G., et al. 2020, A&A, 643, A17

Guillet, V., Pineau Des Forêts, G., & Jones, A. P. 2007, A&A, 476, 263

Guillet, V., Pineau Des Forêts, G., & Jones, A. P. 2011, A&A, 527, A123

Gupta, A., Miotello, A., Manara, C. F., et al. 2023, A&A, 670, L8

Gusdorf, A., Cabrit, S., Flower, D. R., & Pineau Des Forêts, G. 2008a, A&A, 482, 809

Gusdorf, A., Pineau Des Forêts, G., Cabrit, S., & Flower, D. R. 2008b, A&A, 490, 695

Gutermuth, R. A., Pipher, J. L., Megeath, S. T., et al. 2011, ApJ, 739, 84

Haworth, T. J. 2021, MNRAS, 503, 4172

Hellmann, J. L., Schneider, J. M., Wölfer, E., et al. 2023, ApJ, 946, L34

Hennebelle, P. & Ciardi, A. 2009, A&A, 506, L29

Hennebelle, P. & Lebreuilly, U. 2023a, arXiv e-prints, arXiv:2303.09883

Hennebelle, P. & Lebreuilly, U. 2023b, A&A, 674, A149

Hennebelle, P., Lesur, G., & Fromang, S. 2017, A&A, 599, A86

Hennebelle, P., Whitworth, A. P., Cha, S. H., & Goodwin, S. P. 2004, MNRAS, 348, 687

Hildebrand, R. H. 1983, QJRAS, 24, 267

Hoang, T., Tram, L. N., Minh Phan, V. H., et al. 2022, AJ, 164, 248

Högbom, J. A. 1974, A&AS, 15, 417

Hogerheijde, M. R., van Dishoeck, E. F., Blake, G. A., & van Langevelde, H. J. 1998, ApJ, 502, 315

Holweger, H. 2001, in American Institute of Physics Conference Series, Vol. 598, Joint SOHO/ACE workshop "Solar and Galactic Composition", ed. R. F. Wimmer-Schweingruber, 23–30

Houge, A. & Krijt, S. 2023, Monthly Notices of the Royal Astronomical Society, 521, 5826

Hsieh, C.-H., Arce, H. G., Li, Z.-Y., et al. 2023, ApJ, 947, 25

Hunter, T. R., Indebetouw, R., Brogan, C. L., et al. 2023, PASP, 135, 074501

Imai, M., Oya, Y., Svoboda, B., et al. 2022, ApJ, 934, 70

Isella, A., Carpenter, J. M., & Sargent, A. I. 2009, ApJ, 701, 260

Jeans, J. H. 1902, Philosophical Transactions of the Royal Society of London Series A, 199, 1

Jennings, J., Booth, R. A., Tazzari, M., Rosotti, G. P., & Clarke, C. J. 2020, MNRAS, 495, 3209

Jiang, H. & Ormel, C. W. 2023, MNRAS, 518, 3877

Johansen, A., Youdin, A., & Klahr, H. 2009, ApJ, 697, 1269

Johnstone, D., Wilson, C. D., Moriarty-Schieven, G., et al. 2000, ApJ, 545, 327

Jørgensen, J. K., Schöier, F. L., & van Dishoeck, E. F. 2002, A&A, 389, 908

Jørgensen, J. K., van Dishoeck, E. F., Visser, R., et al. 2009, A&A, 507, 861

Jørgensen, J. K., Visser, R., Sakai, N., et al. 2013, ApJ, 779, L22

Kandori, R., Dobashi, K., Uehara, H., Sato, F., & Yanagisawa, K. 2003, AJ, 126, 1888

Karska, A., Kaufman, M. J., Kristensen, L. E., et al. 2018, ApJS, 235, 30

Kataoka, A., Muto, T., Momose, M., Tsukagoshi, T., & Dullemond, C. P. 2016, ApJ, 820, 54

Kawasaki, Y., Koga, S., & Machida, M. N. 2022, MNRAS, 515, 2072

Kelly, B. C. 2007, ApJ, 665, 1489

Kenyon, S. J., Hartmann, L., & Hewett, R. 1988, ApJ, 325, 231

Kobayashi, H. & Tanaka, H. 2010, Icarus, 206, 735

Köhler, M., Ysard, N., & Jones, A. P. 2015, A&A, 579, A15

Krist, J. E., Stapelfeldt, K. R., Ménard, F., Padgett, D. L., & Burrows, C. J. 2000, ApJ, 538, 793

Kuffmeier, M. 2024, arXiv e-prints, arXiv:2406.10901

Kuffmeier, M., Dullemond, C. P., Reissl, S., & Goicovic, F. G. 2021, A&A, 656, A161

Kuffmeier, M., Frimann, S., Jensen, S. S., & Haugbølle, T. 2018, MNRAS, 475, 2642

Kuffmeier, M., Goicovic, F. G., & Dullemond, C. P. 2020, A&A, 633, A3

Kuffmeier, M., Jensen, S. S., & Haugbølle, T. 2023, European Physical Journal Plus, 138, 272

Kunz, M. W. & Mouschovias, T. C. 2009, MNRAS, 399, L94

Kurtovic, N. T., Pérez, L. M., Benisty, M., et al. 2018, ApJ, 869, L44

Kuznetsova, A., Bae, J., Hartmann, L., & Mac Low, M.-M. 2022, ApJ, 928, 92

Kwon, W., Looney, L. W., Mundy, L. G., Chiang, H.-F., & Kemball, A. J. 2009, ApJ, 696, 841

Lada, C. J. 1987, in Star Forming Regions, ed. M. Peimbert & J. Jugaku, Vol. 115, 1

Ladd, E. F., Adams, F. C., Casey, S., et al. 1991, ApJ, 382, 555

Lau, T. C. H., Birnstiel, T., Drążkowska, J., & Stammler, S. 2024, arXiv e-prints, arXiv:2406.12340

Launhardt, R., Stutz, A. M., Schmiedeke, A., et al. 2013, A&A, 551, A98

Lazarian, A. & Hoang, T. 2007, ApJ, 669, L77

Le Gouellec, V. J. M., Greene, T. P., Hillenbrand, L. A., & Yates, Z. 2024, ApJ, 966, 91

Le Gouellec, V. J. M., Hull, C. L. H., Maury, A. J., et al. 2019a, ApJ, 885, 106

Le Gouellec, V. J. M., Hull, C. L. H., Maury, A. J., et al. 2019b, ApJ, 885, 106

Le Gouellec, V. J. M., Maury, A. J., Guillet, V., et al. 2020, A&A, 644, A11

Le Gouellec, V. J. M., Maury, A. J., & Hull, C. L. H. 2023, A&A, 671, A167

Lebreuilly, U., Commerçon, B., & Laibe, G. 2020, A&A, 641, A112

Lebreuilly, U., Hennebelle, P., Colman, T., et al. 2021, ApJ, 917, L10

Lebreuilly, U., Mac Low, M. M., Commerçon, B., & Ebel, D. S. 2023, A&A, 675, A38

Lee, C.-F., Ho, P. T. P., Li, Z.-Y., et al. 2017, Nature Astronomy, 1, 0152

Lee, C.-F., Ho, P. T. P., Palau, A., et al. 2007, ApJ, 670, 1188

Lee, C.-F., Li, Z.-Y., Hirano, N., et al. 2018, ApJ, 863, 94

Li, A. & Draine, B. T. 2001, ApJ, 554, 778

Li, P. S., Lopez-Rodriguez, E., Soam, A., & Klein, R. I. 2022, MNRAS, 514, 3024

Lin, S.-J., Lai, S.-P., Pattle, K., et al. 2024a, ApJ, 961, 117

Lin, Z.-Y., Li, Z.-Y., & Tobin, J. 2024b, in American Astronomical Society Meeting Abstracts, Vol. 243, American Astronomical Society Meeting Abstracts, 155.04D

Lin, Z.-Y. D., Li, Z.-Y., Stephens, I. W., et al. 2024c, MNRAS, 528, 843

Lindberg, J. E., Jørgensen, J. K., Brinch, C., et al. 2014, A&A, 566, A74

Liu, B., Lambrechts, M., Johansen, A., Pascucci, I., & Henning, T. 2020, A&A, 638, A88

Liu, H. B. 2019, ApJ, 877, L22

Longarini, C., Lodato, G., Clarke, C. J., et al. 2024, A&A, 686, L6

Macías, E., Guerra-Alvarado, O., Carrasco-González, C., et al. 2021, A&A, 648, A33

Maercker, M., Vlemmings, W. H. T., Brunner, M., et al. 2016, A&A, 586, A5

Manara, C. F., Morbidelli, A., & Guillot, T. 2018, A&A, 618, L3

Marchand, P., Tomida, K., Tanaka, K. E. I., Commerçon, B., & Chabrier, G. 2020, ApJ, 900, 180

Maret, S., Maury, A. J., Belloche, A., et al. 2020, A&A, 635, A15

Marvel, K. B., Wilking, B. A., Claussen, M. J., & Wootten, A. 2008, ApJ, 685, 285

Mathis, J. S., Rumpl, W., & Nordsieck, K. H. 1977, ApJ, 217, 425

Maury, A., Hennebelle, P., & Girart, J. M. 2022, Frontiers in Astronomy and Space Sciences, 9, 949223

Maury, A. J., André, P., Testi, L., et al. 2019, A&A, 621, A76

Maury, A. J., Girart, J. M., Zhang, Q., et al. 2018, MNRAS, 477, 2760

McCarthy, J. F., Forrest, W. J., Briotta, D. A., J., & Houck, J. R. 1980, ApJ, 242, 965

McClure, M. K., Rocha, W. R. M., Pontoppidan, K. M., et al. 2023, Nature Astronomy, 7, 431

McMullin, J. P., Waters, B., Schiebel, D., Young, W., & Golap, K. 2007, in Astronomical Society of the Pacific Conference Series, Vol. 376, Astronomical Data Analysis Software and Systems XVI, ed. R. A. Shaw, F. Hill, & D. J. Bell, 127

Megeath, S. T., Gutermuth, R., Muzerolle, J., et al. 2012, AJ, 144, 192

Meingast, S., Alves, J., Bouy, H., et al. 2023, A&A, 673, A58

Melis, C., Duchêne, G., Chomiuk, L., et al. 2011, ApJ, 739, L7

Ménard, F., Cuello, N., Ginski, C., et al. 2020, A&A, 639, L1

Mendoza, S., Tejeda, E., & Nagel, E. 2009, MNRAS, 393, 579

Menten, K. M., Reid, M. J., Forbrich, J., & Brunthaler, A. 2007, A&A, 474, 515

Mie, G. 1908, Annalen der Physik, 330, 377

Min, M., Rab, C., Woitke, P., Dominik, C., & Ménard, F. 2016, A&A, 585, A13

Miotello, A., Testi, L., Lodato, G., et al. 2014, A&A, 567, A32

Miyake, K. & Nakagawa, Y. 1993, Icarus, 106, 20

Morales, J. C., Mustill, A. J., Ribas, I., et al. 2019, Science, 365, 1441

Motte, F. & André, P. 2001, A&A, 365, 440

Mottram, J. C., van Dishoeck, E. F., Kristensen, L. E., et al. 2017, A&A, 600, A99

Mouillet, D., Lagrange, A. M., Augereau, J. C., & Ménard, F. 2001, A&A, 372, L61

Mulders, G. D., Pascucci, I., Ciesla, F. J., & Fernandes, R. B. 2021, ApJ, 920, 66

Myers, P. C., Adams, F. C., Chen, H., & Schaff, E. 1998, ApJ, 492, 703

Nakajima, T. & Golimowski, D. A. 1995, AJ, 109, 1181

Nakatani, R., Liu, H. B., Ohashi, S., et al. 2020, ApJ, 895, L2

Natta, A. & Testi, L. 2004, in Astronomical Society of the Pacific Conference Series, Vol. 323, Star Formation in the Interstellar Medium: In Honor of David Hollenbach, ed. D. Johnstone, F. C. Adams, D. N. C. Lin, D. A. Neufeeld, & E. C. Ostriker, 279

Natta, A., Testi, L., Calvet, N., et al. 2007, in Protostars and Planets V, ed. B. Reipurth, D. Jewitt, & K. Keil, 767

Oba, Y., Takano, Y., Naraoka, H., Watanabe, N., & Kouchi, A. 2019, Nature Communications, 10, 4413

Offner, S. S. R., Moe, M., Kratter, K. M., et al. 2022, arXiv e-prints, arXiv:2203.10066

Offner, S. S. R., Moe, M., Kratter, K. M., et al. 2023, in Astronomical Society of the Pacific Conference Series, Vol. 534, Protostars and Planets VII, ed. S. Inutsuka, Y. Aikawa, T. Muto, K. Tomida, & M. Tamura, 275

Ohashi, N., Hayashi, M., Ho, P. T. P., & Momose, M. 1997, ApJ, 475, 211

Ohashi, N., Saigo, K., Aso, Y., et al. 2014, ApJ, 796, 131

Ohashi, N., Tobin, J. J., Jørgensen, J. K., et al. 2023, ApJ, 951, 8

Ohashi, S., Nakatani, R., Liu, H. B., et al. 2022, ApJ, 934, 163

Okoda, Y., Oya, Y., Sakai, N., et al. 2018, ApJ, 864, L25

Okuzumi, S., Momose, M., Sirono, S.-i., Kobayashi, H., & Tanaka, H. 2016, ApJ, 821, 82

Oort, J. H. & van de Hulst, H. C. 1946, Bull. Astron. Inst. Netherlands, 10, 187

Ormel, C. W. & Cuzzi, J. N. 2007, A&A, 466, 413

Ormel, C. W., Liu, B., & Schoonenberg, D. 2017, A&A, 604, A1

Ormel, C. W., Paszun, D., Dominik, C., & Tielens, A. G. G. M. 2009, A&A, 502, 845

Ortiz-León, G. N., Dzib, S. A., Loinard, L., et al. 2023, A&A, 673, L1

Ortiz-León, G. N., Loinard, L., Dzib, S. A., et al. 2018a, ApJ, 865, 73

Ortiz-León, G. N., Loinard, L., Dzib, S. A., et al. 2018b, ApJ, 869, L33

Ossenkopf, V. 1993, A&A, 280, 617

Owen, J. E. & Jacquet, E. 2014, Monthly Notices of the Royal Astronomical Society, 446, 3285

Oya, Y., Sakai, N., Lefloch, B., et al. 2015, ApJ, 812, 59

Oya, Y., Sakai, N., Watanabe, Y., et al. 2018, ApJ, 863, 72

Padoan, P., Haugbølle, T., & Nordlund, Å. 2014, ApJ, 797, 32

Padoan, P., Kritsuk, A., Norman, M. L., & Nordlund, Å. 2005, ApJ, 622, L61

Pagani, L., Steinacker, J., Bacmann, A., Stutz, A., & Henning, T. 2010, Science, 329, 1622

Panagia, N. & Felli, M. 1975, A&A, 39, 1

Park, W., Lee, J.-E., Contreras Peña, C., et al. 2021, ApJ, 920, 132

Pascucci, I., Testi, L., Herczeg, G. J., et al. 2016, ApJ, 831, 125

Pelkonen, V.-M., Padoan, P., Juvela, M., Haugbølle, T., & Nordlund, Å. 2024, arXiv e-prints, arXiv:2405.06520

Pfalzner, S. 2013, A&A, 549, A82

Pfalzner, S., Dehghani, S., & Michel, A. 2022, ApJ, 939, L10

Pfalzner, S., Vogel, P., Scharwächter, J., & Olczak, C. 2005, A&A, 437, 967

Pillich, C., Bogdan, T., Landers, J., Wurm, G., & Wende, H. 2021, A&A, 652, A106

Pineda, J. E., Arzoumanian, D., André, P., et al. 2022, arXiv e-prints, arXiv:2205.03935

Pineda, J. E., Segura-Cox, D., Caselli, P., et al. 2020, Nature Astronomy, 4, 1158

Planck Collaboration, Adam, R., Ade, P. A. R., et al. 2016, A&A, 594, A1

Plummer, H. C. 1911, MNRAS, 71, 460

Plunkett, A. L., Arce, H. G., Corder, S. A., et al. 2015, ApJ, 803, 22

Podio, L., Codella, C., Gueth, F., et al. 2015, A&A, 581, A85

Podio, L., Codella, C., Gueth, F., et al. 2016, A&A, 593, L4

Podio, L., Tabone, B., Codella, C., et al. 2021, A&A, 648, A45

Pollack, J. B., Hollenbach, D., Beckwith, S., et al. 1994, ApJ, 421, 615

Pontoppidan, K. M., van Dishoeck, E. F., & Dartois, E. 2004, A&A, 426, 925

Remjian, A., Biggs, A., Cortes, P. A., et al. 2019, ALMA Technical Handbook,ALMA Doc. 7.3, ver. 1.1, 2019, ALMA Technical Handbook,ALMA Doc. 7.3, ver. 1.1ISBN 978-3-923524-66-2

Ribas, Á., Espaillat, C. C., Macías, E., & Sarro, L. M. 2020, A&A, 642, A171

Ribas, Á., Merín, B., Bouy, H., & Maud, L. T. 2014, A&A, 561, A54

Ricci, L., Testi, L., Natta, A., & Brooks, K. J. 2010, A&A, 521, A66

Ricci, L., Trotta, F., Testi, L., et al. 2012, A&A, 540, A6

Rilinger, A. M., Espaillat, C. C., Xin, Z., et al. 2023, ApJ, 944, 66

Rodriguez, J. E., Loomis, R., Cabrit, S., et al. 2018, ApJ, 859, 150

Rota, A. A., Meijerhof, J. D., van der Marel, N., et al. 2024, A&A, 684, A134

Roy, A., Martin, P. G., Polychroni, D., et al. 2013, ApJ, 763, 55

Russell, H. N. 1922, Proceedings of the National Academy of Science, 8, 115

Sabatini, G., Podio, L., Codella, C., et al. 2024, A&A, 684, L12

Sadavoy, S. I., Di Francesco, J., André, P., et al. 2014, ApJ, 787, L18

Sadavoy, S. I., Stephens, I. W., Myers, P. C., et al. 2019, ApJS, 245, 2

Safronov, V. S. & Zvjagina, E. V. 1969, Icarus, 10, 109

Sakai, N., Hanawa, T., Zhang, Y., et al. 2019, Nature, 565, 206

Sanchis, E., Testi, L., Natta, A., et al. 2020, A&A, 633, A114

Santamaria-Miranda, A., de Gregorio-Monsalvo, I., Ohashi, N., et al. 2024, arXiv e-prints, arXiv:2407.20885

Sargent, B. A., Forrest, W. J., Tayrien, C., et al. 2009, ApJ, 690, 1193

Schilke, P., Walmsley, C. M., Pineau des Forets, G., & Flower, D. R. 1997, A&A, 321, 293

Scholz, A., Froebrich, D., & Wood, K. 2013, MNRAS, 430, 2910

Schutte, W. A., Allamandola, L. J., & Sandford, S. A. 1992, Advances in Space Research, 12, 47

Schwartz, P. R. 1982, ApJ, 252, 589

Scicluna, P., Rosotti, G., Dale, J. E., & Testi, L. 2014, A&A, 566, L3

Segura-Cox, D. M., Harris, R. J., Tobin, J. J., et al. 2016, ApJ, 817, L14

Segura-Cox, D. M., Schmiedeke, A., Pineda, J. E., et al. 2020a, Nature, 586, 228

Segura-Cox, D. M., Schmiedeke, A., Pineda, J. E., et al. 2020b, Nature, 586, 228

Shahbandeh, M., Sarangi, A., Temim, T., et al. 2023, MNRAS, 523, 6048

Sheehan, P. D. & Eisner, J. A. 2018, ApJ, 857, 18

Sheehan, P. D., Tobin, J. J., Li, Z.-Y., et al. 2022, ApJ, 934, 95

Shirley, Y. L., Evans, Neal J., I., & Rawlings, J. M. C. 2002, ApJ, 575, 337

Shirley, Y. L., Mason, B. S., Mangum, J. G., et al. 2011, AJ, 141, 39

Shu, F. H. 1977, ApJ, 214, 488

Shu, F. H., Shang, H., Gounelle, M., Glassgold, A. E., & Lee, T. 2001, ApJ, 548, 1029

Shu, F. H., Shang, H., & Lee, T. 1996, Science, 271, 1545

Sierra, A. & Lizano, S. 2020, ApJ, 892, 136

Silsbee, K., Akimkin, V., Ivlev, A. V., et al. 2022, arXiv e-prints, arXiv:2210.01832

Smallwood, J. L., Yang, C.-C., Zhu, Z., et al. 2023, MNRAS, 521, 3500

Smoluchowski, M. V. 1916, Zeitschrift fur Physik, 17, 557

Soler, J. D., Alves, F., Boulanger, F., et al. 2016, A&A, 596, A93

Stammler, S. M. & Birnstiel, T. 2022, ApJ, 935, 35

Steinacker, J., Andersen, M., Thi, W. F., et al. 2015, A&A, 582, A70

Steinacker, J., Ormel, C. W., Andersen, M., & Bacmann, A. 2014, A&A, 564, A96

Steinacker, J., Pagani, L., Bacmann, A., & Guieu, S. 2010, A&A, 511, A9

Stephens, I. W., Lin, Z.-Y. D., Fernández-López, M., et al. 2023, Nature, 623, 705

Struve, F. G. W. 1847, Etudes d'Astronomie Stellaire: Sur la voie lactee et sur la distance des etoiles fixes

Tabone, B., Cabrit, S., Bianchi, E., et al. 2017, A&A, 607, L6

Tafalla, M., Santiago-García, J., Hacar, A., & Bachiller, R. 2010, A&A, 522, A91

Takahashi, S. Z. & Inutsuka, S.-i. 2014, ApJ, 794, 55

Takahashi, S. Z. & Muto, T. 2018, ApJ, 865, 102

Takakuwa, S., Saigo, K., Kido, M., et al. 2024, ApJ, 964, 24

Takami, M., Karr, J. L., Hashimoto, J., et al. 2013, ApJ, 772, 145

Tazzari, M., Beaujean, F., & Testi, L. 2018, MNRAS, 476, 4527

Tazzari, M., Clarke, C. J., Testi, L., et al. 2021, MNRAS, 506, 2804

Tazzari, M., Testi, L., Ercolano, B., et al. 2016, A&A, 588, A53

Terebey, S., Chandler, C. J., & Andre, P. 1993, ApJ, 414, 759

Terry, J. P., Hall, C., Longarini, C., et al. 2022, MNRAS, 510, 1671

Testi, L., Birnstiel, T., Ricci, L., et al. 2014, in Protostars and Planets VI, ed. H. Beuther, R. S. Klessen, C. P. Dullemond, & T. Henning, 339

Testi, L., Natta, A., Manara, C. F., et al. 2022, A&A, 663, A98

Testi, L., Natta, A., Scholz, A., et al. 2016, A&A, 593, A111

Testi, L., Natta, A., Shepherd, D. S., & Wilner, D. J. 2001, ApJ, 554, 1087

Testi, L., Natta, A., Shepherd, D. S., & Wilner, D. J. 2003, A&A, 403, 323

Thies, I., Kroupa, P., Goodwin, S. P., Stamatellos, D., & Whitworth, A. P. 2011, MNRAS, 417, 1817

Throop, H. B. & Bally, J. 2008, AJ, 135, 2380

Tielens, A. G. G. M. & Hagen, W. 1982, A&A, 114, 245

Tobin, J. J., Hartmann, L., Calvet, N., & D'Alessio, P. 2008, ApJ, 679, 1364

Tobin, J. J., Hartmann, L., Chiang, H.-F., et al. 2012, Nature, 492, 83

Tobin, J. J., Hartmann, L., Chiang, H.-F., et al. 2013, ApJ, 771, 48

Tobin, J. J., Hartmann, L., & Loinard, L. 2010a, ApJ, 722, L12

Tobin, J. J., Hartmann, L., Looney, L. W., & Chiang, H.-F. 2010b, ApJ, 712, 1010

Torres, R. M., Loinard, L., Mioduszewski, A. J., & Rodríguez, L. F. 2007, ApJ, 671, 1813

Trinquier, A., Elliott, T., Ulfbeck, D., et al. 2009, Science, 324, 374

Trumpler, R. J. 1930, Lick Observatory Bulletin, 420, 154

Tsukamoto, Y., Machida, M. N., & Inutsuka, S.-i. 2021, ApJ, 920, L35

Tsukamoto, Y., Machida, M. N., & Inutsuka, S.-i. 2023, PASJ, 75, 835

Tung, N.-D., Testi, L., Lebreuilly, U., et al. 2024, A&A, 684, A36

Tychoniec, Ł., Manara, C. F., Rosotti, G. P., et al. 2020, A&A, 640, A19

Valdivia, V., Maury, A., Brauer, R., et al. 2019, MNRAS, 488, 4897

Valdivia-Mena, M. T., Pineda, J. E., Segura-Cox, D. M., et al. 2022, A&A, 667, A12

Valdivia-Mena, M. T., Pineda, J. E., Segura-Cox, D. M., et al. 2023, A&A, 677, A92

Vallée, J. P., Bastien, P., & Greaves, J. S. 2000, ApJ, 542, 352

Vallucci-Goy, V., Lebreuilly, U., & Hennebelle, P. 2024, arXiv e-prints, arXiv:2406.00124

van de Hulst, H. C. 1946, Recherches Astronomiques de l'Observatoire d'Utrecht, 11, 2.i

van Kempen, T. A., van Dishoeck, E. F., Hogerheijde, M. R., & Güsten, R. 2009, A&A, 508, 259

van Terwisga, S. E. & Hacar, A. 2023, A&A, 673, L2

van Terwisga, S. E., Hacar, A., van Dishoeck, E. F., Oonk, R., & Portegies Zwart, S. 2022, A&A, 661, A53

Wakelam, V., Bron, E., Cazaux, S., et al. 2017, Molecular Astrophysics, 9, 1

Weidenschilling, S. J. 1977, MNRAS, 180, 57

Weingartner, J. C. & Draine, B. T. 2001, ApJ, 548, 296

Whitney, B. A., Wood, K., Bjorkman, J. E., & Cohen, M. 2003, ApJ, 598, 1079

Wiebe, D. S., Molyarova, T. S., Akimkin, V. V., Vorobyov, E. I., & Semenov, D. A. 2019, MNRAS, 485, 1843

Williams, C. D., Sanborn, M. E., Defouilloy, C., et al. 2020, Proceedings of the National Academy of Science, 117, 23426

Williams, J. P., Cieza, L., Hales, A., et al. 2019, ApJ, 875, L9

Winter, A. J., Benisty, M., & Andrews, S. M. 2024, arXiv e-prints, arXiv:2405.08451

Winter, A. J., Booth, R. A., & Clarke, C. J. 2018a, MNRAS, 479, 5522

Winter, A. J., Booth, R. A., & Clarke, C. J. 2018b, MNRAS, 479, 5522

Winter, A. J., Clarke, C. J., Rosotti, G., et al. 2018, Monthly Notices of the Royal Astronomical Society, 478, 2700

Wong, Y. H. V., Hirashita, H., & Li, Z.-Y. 2016, PASJ, 68, 67

Xin, Z., Espaillat, C. C., Rilinger, A. M., Ribas, Á., & Macías, E. 2023, ApJ, 942, 4

Xu, W. & Armitage, P. J. 2023, arXiv e-prints, arXiv:2302.04711

Yen, H.-W., Gu, P.-G., Hirano, N., et al. 2019, ApJ, 880, 69

Yen, H.-W., Takakuwa, S., Ohashi, N., et al. 2014, ApJ, 793, 1

Yıldız, U. A., Kristensen, L. E., van Dishoeck, E. F., et al. 2012, A&A, 542, A86

Yoshida, T., Hsieh, T.-H., Hirano, N., & Aso, Y. 2021, ApJ, 906, 112

Youdin, A. N. & Goodman, J. 2005, ApJ, 620, 459

Ysard, N., Koehler, M., Jimenez-Serra, I., Jones, A. P., & Verstraete, L. 2019, A&A, 631, A88

Zhao, B., Caselli, P., Li, Z.-Y., et al. 2016, MNRAS, 460, 2050

Zhu, Z., Zhang, S., Jiang, Y.-F., et al. 2019, ApJ, 877, L18

Zucker, C., Speagle, J. S., Schlafly, E. F., et al. 2019, ApJ, 879, 125

Danksagung

Qualche anno fa ho deciso di tentare un dottorato di ricerca all'estero, in una fra Francia, Svizzera e Germania. La Svizzera mi sembrava la scelta più adatta, una che potesse dare continuità alla ricerca di esopianeti che aveva catturato la mia attenzione e passione durante gli anni di università a Napoli. Oggi, sto scrivendo questi ringraziamenti nella mia piccola cucina di Monaco di Baviera, e non potrei essere più in disaccordo con il vecchio me. Ora ti dico perchè.

Quando si arriva ad ESO, al primo giorno di lavoro, i dottorandi più navigati offrono un tour dell'istituto alle matricole. Stephen ed Aish guidarono me, Pierrick e Tuts in giro per i corridoi, la biblioteca, ci mostrarono gli hangar in cui i telescopi del più grande telescopio mai costruito venivano testati. Vedemmo per la prima volta Eridanus, quella stanza in cui di lì in poi ogni venerdi mattina avremmo assistito ad innumerevoli presentazioni scientifiche da ogni membro dello staff, durante l'amato Journal Club. Vagando negli edifici di ESO, e più precisamente nel ponte che colleghi l'edificio "nuovo" a quello "vecchio", mi ricordo che pensai e dissi ad alta voce: "This is setting the bar way too high for what comes next" ("Tutto ciò alza troppo le aspettative rispetto a quello che verrà dopo"). ESO è stato il maggior punto di forza del mio dottorato. Quando ci si sceglie un lavoro il cui obiettivo quotidiano è letteralmente farsi dei problemi e cercarvi delle risposte, nulla è più importante del team, dell'ambiente, e delle persone di cui ci si circonda. Ed è qui che iniziano i miei ringraziamenti.

Ad ESO ho trovato fin dal primo giorno individui che mi hanno spinto a diventare la miglior versione di me stesso. Ogni lunedì, nelle riunioni di gruppo di formazione stellare e planetaria, gli studenti presentano il progresso fatto nelle ultime settimane di dottorato. Vedere il livello del lavoro di Teresa P.-C., Alice S., Andrés I.-C., Dominika I., Chi Yan L., Aashish G., Rik C., Pietro C., mi ha motivato a lavorare duro come letteralmente null'altro. Siete tutti degli eccellenti ricercatori, alla punta dei vostri rispettivi campi o sulla via verso essa. Mi avete indirettamente insegnato ad andare oltre i puntini standard di matplotlib; oltre in quello che leggo in un nuovo articolo; oltre le slides con bullet points da un lato e figure dall'altro; oltre la mia scienza. Mi avete ispirato con i vostri metodi e risultati, e supportato in momenti di stanchezza ed indecisione. Ve ne sono estremamente grato, e farete sempre parte del mio bagaglio scientifico. Viaggiare con voi durante questa

esperienza è stata fra le parti migliori del dottorato. Abbiamo visto insieme Firenze, Parigi, Grenoble, Cracovia, Santiago, Gargnano sul Garda, e varie altre. Grazie, ragazzi!

Al di là del gruppo di ricerca in sè, tre anni ad ESO hanno significato nuove amicizie, importanti tanto qui a Monaco quanto in giro per il mondo. Il legame creatosi anche con Victor A.A., Alvaro V., Alonso, Tuts, Alvaro M., Julio, Ivanna L., Joshiwa v. M., Marta D.S., Giulia R., Simon W., Amanda C., Pierrick V., Stephen M., Claudia T., è qualcosa che porterò con me con molta cura e nostalgia. Mi avete fatto ridere, migliorare, assaggiare prelibatezze, crescere, mi avete supportato ed incoraggiato. Siete speciali ed il dottorato non sarebbe stato divertente la metà senza voi. Mi sento fortunato ogni giorno. Un grazie speciale va a Nelma, con me (e noi) da prima del primo giorno dell'avventura, ai break in portoghese, per una semplice chiacchierata o per salvare letteralmente i piani del giorno.

Al mio secondo ufficio preferito, al terzo piano, con Teresa, Victor e Camila. Siete andati tutti via prima di me e scendere da voi, sedermi al davanzale a cazzeggiare, prendere un caffè e rilassarsi prima di tornare al lavoro mi manca come l'aria. Siete stati in quei mesi ed anni per me un porto sicuro con cui confrontarmi, lasciarmi andare e divertirmi. TerePaneque, quando sono arrivato ci siamo conosciuti al primo dei tanti "Beer Friday" e scherzai con te dicendoti di essere già un tuo fan e di voler andare oltre e diventare un amico. È incredibile pensare come tutto ciò sia poi venuto con estrema naturalezza e come continui nel tempo anche con una certa distanza che ci separa. Andrò a vivere nella tua città e lì mi troverai, oltre che in conferenze in giro per il mondo, per uscire a condividere una fetta di dolce (pannacotta, va bene!). Victor, non sei rimasto molto ad ESO ma hai poi preso affitto a lungo termine nei cuori di tutti. Sei una persona di una onestà, integrità e purezza disarmanti. Ogni volta che ci reincontriamo, mi ricordi tutto ciò e spero vivamente che ci vedremo spesso per poter godere della tua amicizia.

Camila, valeu por abrir a minha mente todo dias. Voce me ensinou a comunicar de um jeito que nem conhecia (alem em portugues!), com uma sensibilidade e respeito que eu nao sabia eu precisar. Obrigado por fazer me virar em uma pessoa melhor todo dia. Obrigado por ter ficado a meu lado enquanto trabalhava nessa locura aqui e por acreditar em mim quando eu mesmo não pude. Nao vejo a hora de começar o nosso novo capitulo lá em Santiago. A gente è muito foda pra chegar onde a gente chegou, muito sortuda pra cuidar de um tesouro como o Pastelzinho e da gente mesma e, simplesmente, muito fofa junta.

Se gli amici, gli altri studenti e le relazioni sono importanti a gestire le emozioni di un dottorato, il tuo supervisor gioca un ruolo central nel guidarti a portare avanti anni di ricerca quando sei alle prime armi. Leonardo, sei stato il mentore di cui avevo bisogno. Scientificamente, non c'è bisogno che io mi esprima dato che comunque non sarei in grado di enumerare tutti i contributi che hai portato alla ricerca italiana ed all'estero. Personalmente, sei stato un supervisor lungimirante, paziente, informale, e come si dice a Napoli: "componente". *Componente: dicesi di una persona atta ad inserirsi in eventi di*

gruppo, pianificati o non, con leggerezza e propositività. E.g.,: Uajù, 'o prufessor nuost s'è messo a cantà "Super Santos" e "L'alluvione" 'nda machin cu nuje manco fosse o karaoke. (Ragazzi!, il nostro supervisor ha cantato con noi grandi classici della musica folkloristica italiana in macchina come fosse al karaoke; ndr.). Ti ringrazio per avermi insegnato quello che sai di ALMA, di polveri, di metodo scientifico, di come si collabora. Ti ringrazio per non aver esitato ad ascoltare i miei desideri, ed anzi averli incoraggiati e pianificati con me, come quello di puntare al Cile per il post-dottorato. Oltre il tuo supporto, voglio ringraziare in tutta sincerità le altre personalità, ricercatori e ricercatrici esperte, che in questi anni mi hanno dato tanto in un modo o nell'altro: Carlo Manara, Anna Miotello, Enrique Macías, Antonella Natta, Anaëlle Maury, Claudio Codella, Linda Podio, Eleonora Bianchi, Jason Spyromilio, Michael Hilker, Amelia Bayo, Vincent Pietú, Greta Guidi, Nacho Añez Lopez, Michel Girart e Ramprasad Rao.

Ancora, se sono qui a scirvere queste righe è solo grazie a chi è venuto prima delle persone citate sin qui. L'università di Napoli con i suoi prof., menzione speciale al Prof. Covone, ed i suoi studenti con cui ho condiviso le avventure scientifiche precedenti e che mi hanno supportato durante il mio dottorato sebbene a distanza: grazie, Riccardo, Francesco, Marco, Fabrizio!

Grazie a chi crede in me da sempre e mi spinge ad essere il miglio essere umano che riesco ad essere, ogni giorno. I miei amici Pierluigi, Diego, Andreacarola, Crescenzo, Crescenzo, Willy, Luisa (no, non è un errore di battitura, è che sono due). Siete fra le prime persone che chiamo quando mi sento giù, quando mi sento al settimo cielo, quando mi sento insicuro o un leone. Siete a quelli ho cui ho raccontato aspetti dell'esperienza a Monaco che altri non hanno visto e che hanno saputo ascoltarmi e suggerirmi. Vi voglio bene, vi ringrazio.

Infine, grazie alla mia famiglia: Elisabetta, Carmine, Sara, Nadia. Quanto siete importanti lo dice il fatto (che solo io so ma che decido di scrivere per farvelo capire) che mi vengono le lacrime solo arrivato a questo punto. Senza di voi non sarei qui. Mi avete costruito, donato i valori che mi defniscono, insegnato a lavorare duro, a rispettare il diverso. È stato bellissimo vedervi a Monaco e sarebbe fantastico potervi opsitare nel prossimo passo della mia vita, in Cile, perchè senza voi non sarei giunto nè in uno nè nell'altro posto. Vi voglio bene.

PS: un grazie a me stesso grande quanto tutto il lavoro che faccio ogni giorno che si concretizza in cose tipo questa Tesi che rappresenta uno dei miei più grandi risultati fino a questo punto.